der Bundeswehr
Universität München

Variationally Consistent Approaches for Numerical Modeling of Membrane Wrinkling

Daobo Zhang

Vollständiger Abdruck der von der Fakultät für Bauingenieurwesen und Umweltwissenschaften der Universität der Bundeswehr München zur Erlangung des akademischen Grades eines

Doktor-Ingenieurs (Dr.-Ing.)

angenommenen Dissertation.

Gutachter/Gutachterin:

1. Univ. Prof. Dr.-Ing. Josef Kiendl, UniBw München
2. Univ. Prof. Dr.-Ing. habil. Ralf Müller, TU Darmstadt
3. Univ. Prof. Dr.-Ing. habil. Roland Wüchner, TU München

Die Dissertation wurde am 29.10.2025 bei der Universität der Bundeswehr München eingereicht und durch die Fakultät für Bauingenieurwesen und Umweltwissenschaften am 28.04.2026 angenommen. Die mündliche Prüfung fand am 05.05.2026 statt.

© Daobo Zhang

daobo.zhang@unibw.de; daobozhang92@gmail.com

Universität der Bundeswehr München
Institut für Mechanik und Statik
Werner-Heisenberg-Weg 39
85579 Neubiberg
www.unibw.de/mechanik-und-statik

Abstract

This work proposes various variationally consistent approaches based on spectral decomposition for the modeling of membrane wrinkling. These approaches are formulated within a unified framework that provides a compact representation capable of describing the taut, wrinkled, and slack states in a single expression, while avoiding both nested optimization relaxations and the explicit state switching commonly used in tension-field models. The general formulation is established by splitting the strain energy into tensile and compressive parts, with compressive contributions removed or reduced through a degradation factor, from which the stress tensor and the material constitutive tensor are derived consistently. In addition, wrinkle directions are obtained directly from the eigenvectors of the strain tensor, eliminating the need for additional identification procedures.

Three alternative definitions of the tensile–compressive split are investigated for membranes modeled with a St. Venant–Kirchhoff material, corresponding to the principal-strain, principal-stress, and mixed wrinkling criteria. Furthermore, building upon the same variational principle, a projection-based wrinkling model is developed for incompressible and compressible hyperelastic materials, providing a compact stress representation primarily governed by the second principal stress. Numerical studies are conducted for both linear elastic and hyperelastic materials under a wide range of loading scenarios, including static and dynamic cases. The results demonstrate that all proposed models are accurate and robust, with the mixed-criterion-based model achieving the best overall balance between accuracy and stability.

These developments therefore provide a unified, physically consistent, and computationally efficient basis for the numerical modeling of membrane wrinkling, with broad applicability in engineering analysis.

Kurzfassung

In dieser Arbeit werden verschiedene variationskonsistente Ansätze auf der Grundlage der Spektralzerlegung zur numerischen Modellierung der Membranfaltenbildung vorgestellt. Diese Ansätze sind innerhalb eines einheitlichen Rahmens formuliert, der eine kompakte Darstellung ermöglicht, mit der gespannte, gefaltete und erschlaffte Zustände in einem einzigen Ausdruck beschrieben werden können. Dabei werden sowohl verschachtelte Optimierungsrelaxationen als auch explizite Zustandsumschaltungen vermieden, wie sie für klassische Tension-Field-Modelle typisch sind. Die allgemeine Formulierung basiert auf der Aufspaltung der Verzerrungsenergie in Zug- und Druckanteile, wobei die Druckanteile durch einen Degradationsfaktor reduziert oder entfernt werden. Aus dieser Energieformulierung werden der Spannungstensor und der konstitutive Materialtensor konsistent abgeleitet. Zudem ergeben sich die Faltenrichtungen unmittelbar aus den Eigenvektoren des Verzerrungstensors (aus seiner Spektralzerlegung), sodass keine zusätzlichen Identifikationsverfahren erforderlich sind.

Drei alternative Definitionen der Zug-Druck-Aufspaltung werden für Membranen untersucht, die mit einem St.-Venant–Kirchhoff-Material modelliert sind. Diese entsprechen den Kriterien der Hauptdehnung, der Hauptspannung und einem gemischten Kriterium. Aufbauend auf demselben Variationsprinzip wird außerdem ein projektionsbasierter Ansatz für inkompressible und kompressible hyperelastische Materialien entwickelt, der eine kompakte Spannungsdarstellung liefert, die im Wesentlichen von der zweiten Hauptspannung bestimmt wird. Numerische Untersuchungen für sowohl linear-elastische als auch hyperelastische Materialien unter einer Vielzahl von Belastungsszenarien, einschließlich statischer und dynamischer Fälle, zeigen eine hohe Genauigkeit und Robustheit. Unter den betrachteten Modellen weist der auf dem gemischten Kriterium basierende Ansatz das beste Gesamtgleichgewicht zwischen Genauigkeit und Stabilität auf.

Damit bieten die entwickelten Ansätze eine einheitliche, physikalisch konsistente und numerisch effiziente Grundlage für die Modellierung der Membranfaltenbildung und verfügen über eine breite Anwendbarkeit in der ingenieurwissenschaftlichen Analyse.

Acknowledgments

This dissertation was completed between 2021 and 2025 during my time as a research associate at the Institute for Engineering Mechanics and Structural Analysis at the Universität der Bundeswehr München. I would like to express my sincere gratitude to Prof. Dr.-Ing. Josef Kiendl for his patient guidance and dedicated support throughout my doctoral studies. He not only helped me to continuously advance academically, but also fostered an open and supportive research atmosphere, which enabled me to experience a rewarding and fruitful doctoral journey.

I am also grateful to Prof. Dr.-Ing. Ralf Müller for his guidance during the early stages of my academic career, which laid a solid foundation for my subsequent research. My sincere thanks also go to him and to Prof. Dr.-Ing. habil. Roland Wüchner for serving as reviewers of this dissertation.

My doctoral journey was enriched by the support and companionship of my colleagues. I would like to thank Dr.-Ing. Georgios Michaloudis for our three years of collaboration in teaching the course Dynamik, and my office mate Michael Loibl for his support in both professional and personal matters. I also thank Julius Mader and Dagmar Bergel for the memorable hiking trips, and our secretary Anja Achner for her generous assistance with various administrative matters. I am equally thankful to all my colleagues for the many cheerful lunch breaks we shared. All of you have enriched my life in Germany and made it more memorable.

Finally, I would like to express my gratitude to my family far away in China for their constant understanding and unconditional support. I also wish to acknowledge myself for persevering throughout this decade-long journey in Germany, from undergraduate studies to the completion of my doctorate, without ever giving up or retreating.

Munich, September 2025 Daobo Zhang

Contents

1 Introduction **1**
1.1 Motivation 1
1.2 State of the Art 2
1.3 Objectives and Scope 7
1.4 Outline 8

2 Structural Mechanics of Membranes and Shells **11**
2.1 Differential Geometry of Surfaces 11
2.2 Fundamentals of Solid Continuum Mechanics 14
2.2.1 Kinematics 14
2.2.2 Constitutive Equations 16
2.2.3 Equilibrium 18
2.3 Membrane and Shell Formulations 19
2.3.1 Kinematics for Membranes and Shells 20
2.3.2 Stress Resultants and Recovery 23
2.3.3 Linearization and Discretization 25
2.4 Extension to Hyperelastic Materials 28
2.4.1 Incompressible Materials 30
2.4.2 Compressible Materials 32

3 Isogeometric Analysis **35**
3.1 Introduction 35
3.2 B-Spline Basis 35
3.3 NURBS Basis and Geometry 37
3.4 Refinement Strategies in Isogeometric Analysis 38
3.5 Static and Dynamic Solution Methods 40
3.5.1 Newton–Raphson Iteration Method 40
3.5.2 Generalized-α Method 42

4 Fundamentals of Tension-Field Wrinkling Models **45**
4.1 General Procedure of Wrinkling Models 45
4.2 Membrane States and Wrinkling Criteria 46
4.3 Uniaxial Tension Condition 49
4.4 Reference Model for Numerical Comparison 52
4.4.1 Kinematic Equation 52
4.4.2 Determination of Wrinkle Direction 53

4.4.3 Variational Formulation 54
4.4.4 Derivation of the Modified Material Tensor 55

5 Variationally Consistent Wrinkling Models 59
5.1 Spectral Decomposition Framework 59
5.2 Strain-Criterion-Based Wrinkling Model 60
5.3 Model Assessment and Development 64
5.3.1 Evaluation via Uniaxial Tension Condition 65
5.3.2 Stress- and Mixed-Criterion-Based Wrinkling Models 67
5.3.3 Regularity and Convexity Analysis 70
5.4 Generalization to Hyperelastic Membranes 73

6 Numerical Examples 77
6.1 Wrinkling in Elastic Membranes 77
6.1.1 In-Plane Bending of a Rectangular Membrane 77
6.1.2 Torsion of a Annual Membrane 85
6.1.3 Simple Shear of a Rectangular Membrane 89
6.1.4 Biaxial Corner Stretching of a Flat Membrane 94
6.1.5 Inflation of a Square Airbag 98
6.1.6 Free Fall of a Square Blanket 103
6.1.7 Dynamic Response of a Lice Skirt under Steady Towing 106
6.1.8 Influence of the Degradation Factor η 111
6.2 Wrinkling in Hyperelastic Membranes 114
6.2.1 Inflation of a Hyperelastic Airbag 114
6.2.2 Stretching of a Hyperelastic Rectangular Membrane 116
6.2.3 Shear Loading of a Hyperelastic Membrane 119
6.2.4 Twisting of a Prestretched Membrane 121

7 Conclusions and Outlook 125

A Appendix 129
A.1 Tensor Derivatives of Invariants 129
A.2 Static Condensation of E_{33} for Incompressible Materials 130
A.3 Discussion of the Wrinkle and Principal Directions 132

Bibliography 141

Chapter 1

Introduction

1.1 Motivation

Wrinkling is a ubiquitous localized instability in membranes. It occurs widely in nature and biological systems, for instance in algae, flowers, leaves, marine organisms, and biofilms (Figures 1.1(a)–(e)). Wrinkling is also observed in everyday materials such as stretched polymer films, adhesive tapes, elastic rings, and dielectric elastomers (Figures 1.1(f)–(i)). In advanced materials research, wrinkles in graphene films can significantly alter thermal conductivity and other material properties. Moreover, highly stretchable membranes are extensively employed in flexible electronics and biomedical systems, including epidermal sensors, photovoltaic modules, integrated circuits, and micro light-emitting devices, where controlling wrinkling is essential to ensure device functionality and reliability (Figures 1.1(j)–(m)). From an engineering perspective, wrinkling is equally critical for structural performance and reliability, as exemplified by parachutes, solar sails, airbags, and flexible floating platforms under wind and wave loading, where it may even trigger global instabilities.

At the mechanical level, wrinkling in membranes exhibits complex nonlinear behavior with diverse morphologies and has attracted broad attention over the past decades. Substantial progress has been made through theoretical, numerical, and experimental studies; however, accurate prediction and modeling of wrinkling behavior remain nontrivial. The underlying reason is that membranes have extremely low out-of-plane bending stiffness, proportional to the cube of the thickness, whereas their in-plane stretching stiffness scales approximately linearly with thickness; once compression arises, a membrane tends to relieve it via a localized out-of-plane instability that forms wrinkles. The accompanying changes in effective stiffness and stress state lead to pronounced nonlinearity and localization, posing challenges for stable modeling and numerical convergence. Given the ubiquity of this phenomenon and its implications for the performance and reliability of natural and engineered systems, continued research is warranted to deepen the mechanical understanding and to support more reliable analysis and design.

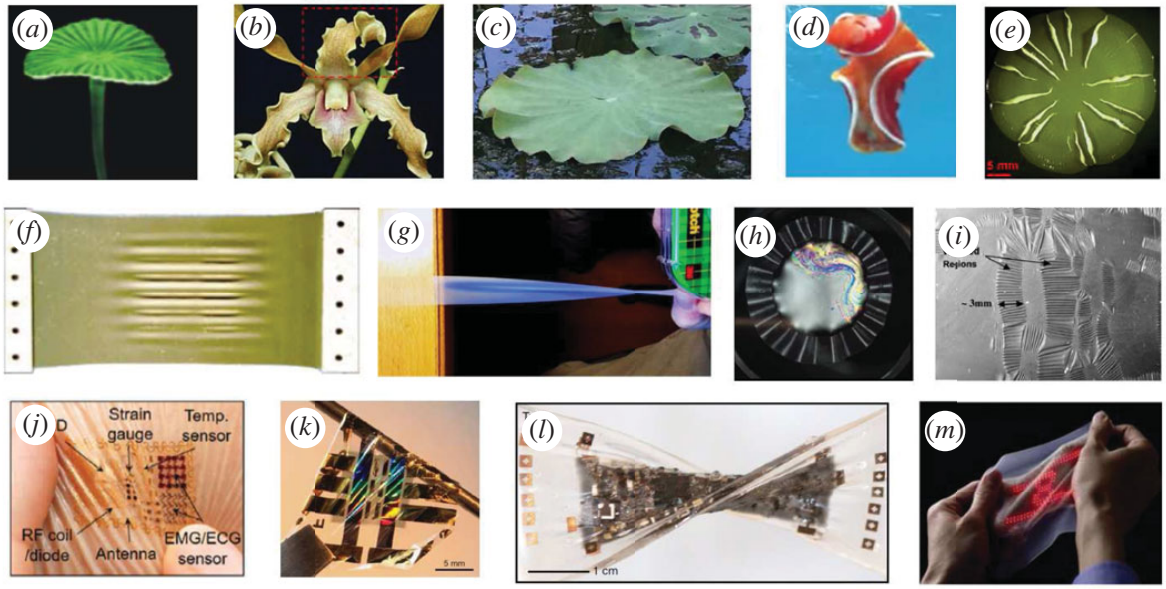

Figure 1.1.: Illustrative examples of wrinkling phenomena across different contexts and scales [1]: (a) buckling pattern observed in the stem of a green alga (Acetabularia schenckii); (b) undulated petal edge of Dendrobium helix orchid; (c) growth-induced marginal wrinkles in a lotus leaf; (d) body-surface folds of the free-swimming sea slug (Hexabranchus sanguineus); (e) surface morphology of E. coli AR3110 biofilm; (f) lateral wrinkling in a polyethylene film subjected to uniaxial stretching; (g) wavy patterns on adhesive tape generated by torsional loading; (h) time-dependent instability in an elastic ring under dynamic conditions; (i) pull-in-induced wrinkling of a dielectric elastomer membrane; (j) skin-mounted epidermal electronic sensor; (k) wrinkle formation in a photovoltaic thin film; (l) patterned deformations in a three-dimensional flexible integrated circuit; (m) microscale light-emitting diode device exhibiting surface instabilities.

1.2 State of the Art

Over the years, various methods have been developed. These are primarily based on two fundamental theoretical frameworks: plate and shell theory, and tension-field theory (TFT). These frameworks differ in their underlying assumptions, computational efficiency, resolution capabilities, and practical applicability, and form the basis for most models proposed to date.

In parallel, experimental investigations have contributed significantly to understanding the physical mechanisms of membrane wrinkling. Since the emphasis here is on modeling approaches, a detailed review of experimental studies is beyond the scope of this work. For further reading on experimental observation, particularly in stretch-induced wrinkling, the reader is referred to the recent overview by [1], as well as other comprehensive reviews [2–6].

Plate- and Shell-Theory-Based Approaches

Among the two frameworks, the plate- and shell-theory-based approaches are first introduced. These models account for both membrane and bending stiffness, allowing predictions of wrinkle onset and morphology. Analytical methods under this framework, although generally limited to idealized conditions, provide fundamental insights into wrinkling mechanics. Depending on loading and boundary conditions, they can be broadly classified into four categories:

(1) Wrinkling induced by tension or shear: this type of wrinkling has received the most attention in both theoretical and experimental studies. Representative studies include the prediction of critical tensile stresses in stretched sheets [7], the derivation of scaling laws for wrinkle wavelength and amplitude [8, 9], the determination of critical buckling stresses [10], and the identification of critical applied strains [11]. [12] further emphasized the importance of geometric nonlinearities in the formation and disappearance of wrinkles, whereas [13] demonstrated within a linear framework that Poisson's effect can trigger wrinkling under tension. In addition, [14] proposed a general analytical model to predict the onset location and characteristic patterns of wrinkles in thin membranes subjected to shear and biaxial tension.

(2) Membranes on a Foundation: [15] analyzed the wrinkle–fold transition in compressed membranes on soft foundations, deriving scaling laws for wavelength and amplitude and explaining localization. Subsequent studies examined the effects of self-weight [16], delamination from the fluid [17], viscous versus elastic response [18], and floating elastica [19], while [20, 21] interpreted the transition as a sequence of bifurcations. For floating membranes under indentation, [22, 23] considered surface tension in very thin sheets, [24] analyzed bending stiffness, and [25] provided unified scaling relations from onset to large indentations. Additional works discussed circular and annular sheets [26, 27] and capillary wrinkling [28, 29].

(3) Pressurized Membranes: [30] derived scaling relations for the wrinkling wavelength and wrinkle number in pressurized spherical membranes, while [31] extended this work with analytical and numerical models to study post-wrinkling behavior, including wrinkle hierarchy and period doubling. Further analytical contributions addressed inflatable structures, with [32–34] focusing on inverse design aspects, [35–37] examining the global mechanics of inflatable tubes and drop-stitch panels, and [38] proposing a bistable inflatable pillow concept.

(4) Growth-Induced Wrinkling: beyond load-driven cases, wrinkling may also arise from growth processes such as swelling or thermal expansion. Analytical approaches include a unified thermodynamic phase diagram for instability patterns [39], a generalized Swift–Hohenberg theory for curved bilayers [40], a dimensionless parameter controlling pattern transitions in core–shell spheres [41], and scaling laws predicting critical wave numbers and strains in aquatic plant leaves [42].

In summary, analytical studies, particularly those by [8] and [15], have elucidated the fundamental mechanism of membrane wrinkling. Because the in-plane stretching stiffness of a membrane scales linearly with thickness, whereas the bending stiffness scales with the cube of thickness, the in-plane stiffness is much larger than the bending stiffness for sufficiently small thickness. Under compression, relying solely on in-plane deformation would lead to a rapid

accumulation of prohibitively large strain energy. By contrast, out-of-plane undulations can release compressive stresses at the expense of comparatively small bending energy, making wrinkling the natural response under compression. In the absence of a foundation, the wrinkle wavelength and amplitude are governed by the competition between compressive strain energy and bending energy: long waves reduce bending costs but release compression inefficiently, whereas short waves release compression more effectively but require higher curvature. The system therefore selects an optimal morphology that minimizes the total energy. When the membrane is supported by a foundation, wrinkling also induces deformation of the substrate. Since long-wave wrinkles create large indentations and significantly increase the foundation energy, the system tends to favor shorter wavelengths, effectively trading additional bending costs for a reduction in foundation energy. Thus, the onset, wavelength, and amplitude of wrinkling emerge as natural outcomes of energy minimization, reflecting an optimal balance among compressive strain energy, bending energy, and (when present) foundation energy. This physical picture not only explains the initiation of wrinkles but also sheds light on their subsequent evolution, including localization, fold formation, and transitions between distinct patterns.

In contrast to these analytical studies, numerical models have also been developed. In particular, the Föppl–von Kármán (FvK) plate model, which is formulated on the basis of linear in-plane strain and linearized curvature, has been widely applied. For example, it has been used to simulate the wrinkling and subsequent re-stabilization phenomena in highly stretched thin films [43], and to investigate the influence of transverse compressive stress distributions on wrinkle formation [44]. The classical FvK formulation, however, relies on the assumption of small in-plane strains, which limits its ability to accurately reproduce responses involving isola-center bifurcations under large deformations. To overcome this shortcoming, the extended FvK (EFvK) model was developed [45]. By incorporating finite in-plane strains, the EFvK framework enhances the representation of geometric nonlinearity and enables predictions of post-buckling behavior. This formulation has subsequently been generalized to account for hyperelastic materials [46, 47], orthotropic materials [48, 49], and anisotropic materials [50]. Moreover, [42] derived growth-modified FvK equations to capture the influence of liquid substrates on the morphogenesis of aquatic plant leaves.

In addition to plate formulations of the FvK type, models based on Kirchhoff–Love (KL) shell theory have also been employed for the simulation of wrinkling and re-stabilization, with good agreement being reported for a variety of thin-film problems [51]. These approaches, nevertheless, still retain the linearized curvature assumption. In contrast, formulations based on Koiter's plate theory [52–54] adopt a more accurate representation of curvature and have been successfully applied to fiber-reinforced systems [55, 56]. Despite this improvement, they continue to rely on a priori kinematic assumptions that constrain their generality. As an alternative to the preceding approaches, a consistent finite-strain plate model using Chebyshev spectral collocation was introduced in [57]. This model preserves asymptotic consistency with the full three-dimensional field equations, thereby avoiding restrictive kinematic assumptions. It has subsequently been generalized to account for anisotropic materials [58], and further extended to a doubly curved shell formulation based on differential geometry [59]. The latter framework has been employed to investigate the influence of curvature on the initiation and re-stabilization of stretched sheets [60], the role of material damage [61], and, more recently,

the wrinkling behavior of tori [62].

However, simulations based on these models typically require fine meshes and are computationally expensive. To reduce computational cost, the Fourier reduced model [63] was proposed to capture wrinkling patterns with few degrees of freedom. However, it is inaccurate near boundaries, and its general applicability remains unproven [64]. Meanwhile, the earlier models still face numerical challenges, including convergence issues near bifurcation points [1], mesh sensitivity [65], and the need to introduce initial imperfections [66]. As a result, continuation strategies such as the arc-length method [45, 67, 68] and the asymptotic numerical method (ANM), which approximates the solution by means of a Taylor series expansion around a known state [69], have become widely employed in wrinkling analysis. In addition, the dynamic relaxation method [70] has also been adopted as an efficient alternative. Even so, as pointed out in [1], the former can trace complex post-buckling paths with bifurcations and hysteresis but often struggles with convergence in highly localized instabilities, while the latter provides a robust alternative using artificial damping and inertia with random imperfections, though it cannot naturally capture subcritical bifurcations or metastable states.

Tension-Field-Theory-Based Approaches

An alternative modeling approach is provided by tension-field theory, first introduced by [71] and later extended by [72] to the torsion of an annular membrane. The theory simplifies the membrane wrinkling problem by neglecting bending stiffness and postulating that the stress state in wrinkled regions satisfies the uniaxial tension condition, that is, the compressive stress component along the wrinkle direction vanishes.

Under this assumption, analytical solutions within the framework of tension-field theory have been obtained for selected membrane configurations subject to simplified boundary conditions, typically under the assumptions of small deformations and linear elasticity. Classic examples include the bending of a rectangular membrane [73] and the torsion of an annular membrane [74], both yielding closed-form expressions for the principal stresses. These analytical solutions are widely used as reference benchmarks for validating numerical models and for providing physical insight into wrinkling phenomena. Subsequent developments extended the applicability of tension-field theory well beyond the original linear framework. [75] formulated a generalized theory capable of describing membranes undergoing arbitrarily large deformations and demonstrated its relevance by modeling surgical procedures on human skin. [76] introduced the concept of energy relaxation into the theory of elastic membranes, replacing the original strain energy density with a suitably relaxed functional and thereby placing tension-field theory on a rigorous variational basis. Building on this foundation, [77] established a comprehensive finite-deformation formulation for isotropic elastic membranes, further consolidating the theoretical underpinnings of the approach. Additional developments of the relaxed-energy approach, addressing both small and large deformations in materials with arbitrary anisotropy, can be found in [78–80].

From a numerical perspective, tension-field-theory-based approaches enable accurate prediction of the stress and average displacement fields even on relatively coarse membrane meshes. They also provide wrinkle orientations and a classification of the membrane domain into taut,

wrinkled, and slack regions. The main drawback of this family of models is that, due to the neglect of bending stiffness, fine-scale wrinkle geometry such as wavelength and amplitude cannot be resolved. Nevertheless, they remain widely used in large-scale simulations of membrane structures [81–83], and in cloth simulations [84, 85], because they offer a favorable compromise between computational efficiency and predictive capability. A comprehensive overview of the literature is provided by [86], while [81] highlights the similarities between different approaches.

Wrinkling models based on tension-field theory can be further classified according to variational consistency. The first category comprises non-variationally consistent models, which rely explicitly on wrinkling criteria to distinguish between taut, wrinkled, and slack states of the membrane. In practice, this means that the numerical implementation contains conditional branching (e.g., if–else statements) based on a chosen criterion, so that the local membrane state is first identified and then assigned a corresponding stiffness expression. Such branching is undesirable both for aesthetic and performance reasons, as emphasized by [87], who noted that reliance on if–else structures is computationally inefficient because the membrane may transition between states; it therefore typically requires many iterations regardless of the numerical method employed. The wrinkling criteria employed in these models can be broadly divided into three types: the principal-stress criterion [88–90], the principal-strain criterion [91, 92], and the mixed criterion [93–95]. Among these, the mixed criterion has been shown to provide the most reliable assessment of the membrane state [96].

Within the non-variational category, two modeling strategies are commonly distinguished. Kinematic modification methods operate by introducing auxiliary parameters into the kinematic description of deformation in order to enforce the vanishing of compressive stress along the wrinkle direction. For example, in the context of finite deformations and isotropic materials, [97, 98] first introduced the concept of a pseudo-deformation tensor, which reflects the in-plane effects of out-of-plane wrinkling and ensures that the stress in the wrinkle direction vanishes. Building on this idea, [99] generalized the approach to anisotropic materials by incorporating the wrinkle direction directly into the deformation gradient tensor and introducing a virtual elongation along that direction to suppress compressive stress. This modeling strategy attracted considerable attention and stimulated further developments [100–103]. Representative works, such as [104], presented explicit formulas for the consistent evaluation of the material (constitutive) stiffness matrix within this framework, thereby enabling robust numerical implementation. Subsequently, [96] demonstrated that the modification of the deformation gradient in the Roddeman model [99] can be reformulated as an equivalent modification of the material (constitutive) tensor, providing a mathematically consistent alternative interpretation. Building on Roddeman's approach, [81] introduced a virtual shear component, providing an alternative modification of the deformation gradient. In contrast, [105] proposed a more direct strategy by modifying the strain components themselves. Both approaches enforce the uniaxial tension condition, under which the normal and shear stresses vanish along the wrinkle direction.

Material modification methods, in contrast, adjust the constitutive relationship to suppress compressive stresses. A representative early approach is the iterative membrane properties (IMP) model [92], which updates the elasticity matrix iteratively based on the strain state

from the previous load step. In addition, several alternative strategies have been developed. Penalization techniques [65, 88, 93, 94, 106] artificially soften selected components of the constitutive tensor in order to reduce compressive stiffness, while projection methods [107–109] achieve the same objective by post-multiplying the constitutive stiffness matrix with a projection operator. Both approaches reduce the material stiffness to zero along the wrinkle orientation, thereby enforcing the uniaxial tension condition in wrinkled regions.

The second category comprises variationally consistent models, which do not rely on explicit wrinkling criteria. These approaches are rooted in the relaxed-energy concept originally proposed by Pipkin [76, 78, 79]. Although Pipkin's method is often classified as a material-modification approach in the literature, it is considered here as the foundation of variationally consistent formulations owing to its variational rigor. This method guarantees that compressive stresses do not appear in the solution. Building on this foundation, [110, 111] first introduced an explicit parameterization of wrinkle strain into a finite element framework, while [112] reformulated the theory as a saddle-point variational system using wrinkling strain and stress as independent variables. [113] demonstrated that, for linear elastic materials, the problem can be expressed as a convex optimization with semidefinite constraints, and [87] extended this framework to hyperelastic membranes and three-dimensional geometries by casting the problem into a conic optimization form solved by interior-point methods. Despite their strong theoretical foundation, these approaches are structurally complex and often rely on nested convex optimization techniques, which makes their implementation mathematically demanding.

Moreover, although the methods discussed above have laid a basic foundation for wrinkling models, their extension to hyperelastic membranes has remained limited. The work of [110] represents an early attempt to incorporate hyperelastic behavior, but the formulation was restricted to the incompressible case and did not address compressible materials. A similar limitation can also be found in [87]. More recently, [64] extended the model of [96] into the hyperelastic regime, including the compressible case. However, this formulation relies on if–else branching based on a wrinkling criterion, which reduces convergence robustness, and requires solving a root-finding problem for the wrinkle direction at each quadrature point, thereby increasing computational cost. These limitations motivate the development of alternative formulations that balance efficiency with variational consistency for hyperelastic materials.

1.3 Objectives and Scope

As outlined in the previous discussion, wrinkling models based on tension-field theory involve a trade-off between structural simplicity and variational rigor. Non-variational formulations employ explicit wrinkling criteria, implemented through if–else branching, which leads to discontinuous updates and limited robustness. In contrast, Pipkin-type relaxed-energy formulations provide a rigorous variational foundation but are structurally complex and rely on nested convex optimization. Moreover, their extension to hyperelastic membranes remains limited, particularly in the treatment of compressible materials.

To address these issues and bridge the gap, this dissertation develops variationally consistent modeling approaches for membrane wrinkling via spectral decomposition.

The proposed approaches are developed and refined through three peer-reviewed studies, each addressing a distinct aspect of the overall methodology.

Paper I [114], published in *Computer Methods in Applied Mechanics and Engineering*, lays the foundation for the proposed variationally consistent modeling approaches. It introduces a strain-based spectral decomposition approach that separates the strain energy into tensile and compressive components. This decomposition enables a single variational energy functional to represent the taut, wrinkled, and slack membrane states in a unified manner. A degradation factor is introduced to modulate the compressive contribution. Depending on its value, the model either eliminates compressive stiffness entirely or retains a small amount to regularize the formulation, improve convergence, and prevent singularities associated with slackening. Both stress and material tensors are derived consistently from the energy functional incorporating the degradation factor. For isotropic materials, the eigenvectors of the strain tensor naturally align with wrinkle orientations. The resulting approach is compact, effective, and readily implementable in standard finite element software.

Paper II [115], published in the *Journal of the Mechanics and Physics of Solids*, investigates alternative ways of separating tensile and compressive behavior within the same variational framework. In addition to the strain-criterion-based formulation introduced in Paper I, a stress-criterion-based model is developed, and based on this model, a mixed-criterion formulation is proposed. The latter modifies the Poisson response to suppress transverse coupling in wrinkled and slack regions. These three formulations are compared across a range of benchmark problems with respect to numerical stability and predictive accuracy.

Paper III, currently under review in *Computer Methods in Applied Mechanics and Engineering*, develops a generalized wrinkling model for hyperelastic materials in the same variationally consistent framework. The formulation supports both compressible and incompressible materials, with the plane-stress condition enforced either analytically or numerically. The resulting model yields a compact stress formulation that depends primarily on the second principal stress. It maintains the clarity and efficiency of the formulations proposed in previous studies while broadening the range of applicable material models.

1.4 Outline

This dissertation is structured into seven chapters.

Chapter 2 establishes the theoretical framework for membranes and shells. The chapter opens with a concise introduction to the differential geometry of surfaces, which provides the geometric background required for the subsequent formulations. Building on this, the general principles of three-dimensional continuum mechanics are summarized, including kinematics, constitutive relations, and variational formulations. These concepts are then systematically specialized to membrane formulations, while the Kirchhoff–Love shell is briefly outlined to provide a reference for comparison in later numerical examples. The discretization

and linearization of the governing equations are also introduced to prepare for subsequent numerical developments. Finally, the material law is extended from linear elasticity to general hyperelasticity, distinguishing between compressible and incompressible cases. This extension prepares the ground for the hyperelastic wrinkling models introduced in Chapter 5.

Chapter 3 introduces the fundamentals of isogeometric analysis. It first outlines the mathematical construction of B-spline and NURBS basis functions, highlighting their advantages that make them suitable for membrane and shell analysis. These basis functions are employed for the discretization in the formulations developed in this dissertation. In addition, the static and dynamic solution methods used in the numerical examples are briefly summarized.

Chapter 4 reviews existing tension-field wrinkling models. The general framework of classical wrinkling algorithms is first outlined, providing the overall structure commonly adopted in the literature. The three possible membrane states (taut, wrinkled, and slack) are then described, together with the three main wrinkling criteria based on principal stresses, principal strains, and their combination. Their respective advantages and limitations are discussed. An important condition within tension-field theory, the uniaxial tension condition, is subsequently introduced as the basis for stress representation in wrinkled regions. Finally, a reference model is presented, which will be employed later in the numerical examples for comparison.

Chapter 5 presents the proposed variationally consistent wrinkling models. The chapter begins with a preliminary explanation of spectral decomposition, which provides the mathematical foundation for the subsequent formulations. The first model is introduced by decomposing the strain energy density into tensile and compressive parts based on the spectral decomposition of the strain tensor, thereby establishing a basic variational framework for handling wrinkling. The model is then theoretically assessed by examining its consistency with the uniaxial tension condition. Building on this, an alternative formulation is developed using the spectral decomposition of the stress tensor. This formulation is subsequently refined into a mixed-criterion-based model that combines the advantages of strain and stress measures to enhance physical consistency. The theoretical properties of these models, in particular regularity and convexity, are analyzed. Finally, the wrinkling model is generalized to hyperelastic materials, enabling its application beyond linear elasticity.

Chapter 6 demonstrates the performance of the proposed wrinkling models through a series of numerical examples. The first part considers seven cases in linear elasticity, including classical benchmark problems and dynamic responses. The second part extends the analysis to hyperelastic membranes, where four representative problems involving inflation, stretching, shear, and twisting are investigated. The results are validated against reference solutions in both linear and hyperelastic cases to assess the accuracy, robustness, and efficiency of the proposed models.

Chapter 7 concludes the dissertation by summarizing the main contributions of the work. An outlook on possible future research directions is also provided.

Appendix A provides further derivations and supplementary material.

Chapter 2

Structural Mechanics of Membranes and Shells

In this chapter, the fundamental concepts required for the structural mechanics of membranes and shells are introduced. The chapter begins with the differential geometry of surfaces, which provides the geometric background, and proceeds with the standard framework of three-dimensional continuum mechanics that are subsequently specialized to membrane and shell formulations. Finally, the material law is extended from linear elasticity to general hyperelasticity, covering both compressible and incompressible cases. The exposition follows standard references [116–118].

2.1 Differential Geometry of Surfaces

This section presents the mathematical framework needed to describe the geometry of curved surfaces in three-dimensional Euclidean space. The aim is to define the essential geometric quantities required for geometrically nonlinear models of thin structures such as membranes and shells. These quantities include tangent vectors, normal vectors, metric tensors, and curvature tensors. In addition, transformation rules for tensor components between different coordinate systems are provided.

Throughout this work, the following notational conventions are adopted. The Einstein summation convention applies. Latin indices take values in {1,2,3} and Greek indices in {1,2}. Bold symbols denote vectors or higher-order tensors, while nonbold symbols denote scalar quantities.

To represent general surfaces of arbitrary shape, curvilinear coordinates are commonly employed. In the associated curvilinear coordinate system, the covariant and contravariant bases, $\mathbf{g}_i$ and $\mathbf{g}^i$, are introduced. A position vector $\mathbf{x}$ on the surface is then expressed by the contravariant coordinates θ^i as:

$$\mathbf{x} = \theta^i \mathbf{g}_i, \tag{2.1}$$

which indicates that the covariant basis vectors are defined as the partial derivatives of the

position vector with respect to the coordinates:

$$\mathbf{g}_i = \frac{\partial \mathbf{x}}{\partial \theta^i} = \mathbf{x}_{,i}. \tag{2.2}$$

The contravariant basis vectors, in turn, are defined as the gradients of the curvilinear coordinates with respect to the spatial position [118]:

$$\mathbf{g}^i = \frac{\partial \theta^i}{\partial \mathbf{x}}. \tag{2.3}$$

By construction, the two bases are mutually dual, satisfying the orthogonality condition

$$\mathbf{g}_i \cdot \mathbf{g}^j = \delta_i^j = \begin{cases} 1, & i = j, \\ 0, & i \neq j, \end{cases} \tag{2.4}$$

where δ_i^j denotes the Kronecker delta.

Since the surface is parametrized by two curvilinear coordinates (θ^1,θ^2), the covariant basis vectors $\mathbf{g}_1$ and $\mathbf{g}_2$ span the tangent plane. These vectors are obtained directly from Equation (2.2). To complete the basis in three-dimensional space, a third covariant basis vector $\mathbf{g}_3$ is introduced. It is defined as the unit normal vector perpendicular to both $\mathbf{g}_1$ and $\mathbf{g}_2$, obtained by normalizing their cross product:

$$\mathbf{g}_3 = \frac{\mathbf{g}_1 \times \mathbf{g}_2}{|\mathbf{g}_1 \times \mathbf{g}_2|}. \tag{2.5}$$

In accordance with Equation (2.4), the third contravariant basis vector $\mathbf{g}^3$ coincides with $\mathbf{g}_3$:

$$\mathbf{g}^3 = \mathbf{g}_3. \tag{2.6}$$

Another fundamental quantity in the differential geometry of surfaces is the metric tensor $\mathbf{g}$. It can be represented in either the covariant or contravariant basis as

$$\mathbf{g} = g^{\alpha\beta}\, \mathbf{g}_\alpha \otimes \mathbf{g}_\beta = g_{\alpha\beta}\, \mathbf{g}^\alpha \otimes \mathbf{g}^\beta, \tag{2.7}$$

where $g_{\alpha\beta}$ and $g^{\alpha\beta}$ denote the covariant and contravariant metric coefficients, respectively.

The covariant metric coefficients are defined by the inner products of the covariant basis vectors:

$$g_{\alpha\beta} = \mathbf{g}_\alpha \cdot \mathbf{g}_\beta. \tag{2.8}$$

This definition gives rise to the so-called first fundamental form of the surface, which encodes the essential geometric properties such as lengths of the base vectors and the angles between them. To obtain the contravariant metric coefficients $g^{\alpha\beta}$, one inverts the matrix composed of the covariant coefficients:

$$\left[g^{\alpha\beta}\right] = \left[g_{\alpha\beta}\right]^{-1}. \tag{2.9}$$

Then, the contravariant basis vectors $\mathbf{g}^\alpha$ can be computed from the covariant ones using the

contravariant metric components $g^{\alpha\beta}$ as follows:

$$\mathbf{g}^{\alpha} = g^{\alpha\beta}\,\mathbf{g}_{\beta}. \tag{2.10}$$

Conversely, the covariant base vectors can be recovered from the contravariant basis via

$$\mathbf{g}_{\alpha} = g_{\alpha\beta}\,\mathbf{g}^{\beta}. \tag{2.11}$$

In addition to the metric description provided by the first fundamental form, the curvature of a surface is characterized by the so-called second fundamental form. The curvature tensor coefficients $b_{\alpha\beta}$ are defined as

$$b_{\alpha\beta} = -\mathbf{g}_{\alpha} \cdot \mathbf{g}_{3,\beta} = -\mathbf{g}_{\beta} \cdot \mathbf{g}_{3,\alpha} = \mathbf{g}_{\alpha,\beta} \cdot \mathbf{g}_{3}, \tag{2.12}$$

where the derivatives $\mathbf{g}_{3,\alpha}$ and $\mathbf{g}_{3,\beta}$ represent changes in the surface normal along the curvilinear coordinates, while $\mathbf{g}_{\alpha,\beta}$ denotes the second derivatives of the position vector with respect to the surface parameters.

Furthermore, the covariant basis vectors $\mathbf{g}_1$ and $\mathbf{g}_2$ can be used to construct a local Cartesian frame. The construction is initiated by choosing the first vector $\mathbf{e}_1$ in the direction of $\mathbf{g}_1$, followed by an orthogonalization to define $\mathbf{e}_2$, and the third vector $\mathbf{e}_3$ is set to coincide with the surface normal $\mathbf{g}_3$, resulting in an orthonormal triad:

$$\mathbf{e}_1 = \frac{\mathbf{g}_1}{\|\mathbf{g}_1\|}, \tag{2.13}$$

$$\mathbf{e}_2 = \frac{\mathbf{g}_2 - (\mathbf{g}_2 \cdot \mathbf{e}_1)\mathbf{e}_1}{\|\mathbf{g}_2 - (\mathbf{g}_2 \cdot \mathbf{e}_1)\mathbf{e}_1\|}, \tag{2.14}$$

$$\mathbf{e}_3 = \mathbf{g}_3. \tag{2.15}$$

In many applications, strain measures are evaluated in curvilinear coordinates, whereas constitutive relations are expressed in a local Cartesian frame. To ensure consistency between these representations, a procedure for transforming tensor components between coordinate systems is provided below.

An arbitrary second-order tensor $\mathbf{z}$ can be expressed in terms of different bases using either its covariant or contravariant components. Specifically, its representation in distinct bases $\mathbf{c}_i, \mathbf{c}^i$ and $\mathbf{d}_i, \mathbf{d}^i$ takes the form

$$\mathbf{z} = c^{ij}\,\mathbf{c}_i \otimes \mathbf{c}_j = c_{ij}\,\mathbf{c}^i \otimes \mathbf{c}^j = d^{ij}\,\mathbf{d}_i \otimes \mathbf{d}_j = d_{ij}\,\mathbf{d}^i \otimes \mathbf{d}^j, \tag{2.16}$$

where c_{ij}, c^{ij} and d_{ij}, d^{ij} denote the tensor components with respect to the corresponding covariant and contravariant bases.

To establish the relationship between components in different bases, one begins with the identity

$$c_{ij}\,\mathbf{c}^i \otimes \mathbf{c}^j = d_{ij}\,\mathbf{d}^i \otimes \mathbf{d}^j. \tag{2.17}$$

Both sides are then multiplied by the covariant basis vectors $\mathbf{d}_k$ and $\mathbf{d}_l$. Applying the orthogonality of dual bases defined in Equation (2.4), i.e., $\mathbf{d}_i \cdot \mathbf{d}^j = \delta_i^j$, the derivation proceeds as follows:

$$\begin{aligned} c_{ij}\, \mathbf{d}_k(\mathbf{c}^i \otimes \mathbf{c}^j)\mathbf{d}_l &= d_{ij}\, \mathbf{d}_k(\mathbf{d}^i \otimes \mathbf{d}^j)\mathbf{d}_l \\ c_{ij}\, (\mathbf{d}_k \cdot \mathbf{c}^i)(\mathbf{c}^j \cdot \mathbf{d}_l) &= d_{ij}\, (\mathbf{d}_k \cdot \mathbf{d}^i)(\mathbf{d}^j \cdot \mathbf{d}_l) \\ &= d_{ij}\, \delta_k^i \delta_l^j \\ &= d_{kl}. \end{aligned} \tag{2.18}$$

Following the same procedure, transformation rules for all relevant forms of tensor components can be derived. The results are summarized as follows:

$$d_{kl} = c_{ij}\, (\mathbf{d}_k \cdot \mathbf{c}^i)(\mathbf{c}^j \cdot \mathbf{d}_l), \tag{2.19}$$

$$d^{kl} = c_{ij}\, (\mathbf{d}^k \cdot \mathbf{c}^i)(\mathbf{c}^j \cdot \mathbf{d}^l), \tag{2.20}$$

$$d_{kl} = c^{ij}\, (\mathbf{d}_k \cdot \mathbf{c}_i)(\mathbf{c}_j \cdot \mathbf{d}_l), \tag{2.21}$$

$$d^{kl} = c^{ij}\, (\mathbf{d}^k \cdot \mathbf{c}_i)(\mathbf{c}_j \cdot \mathbf{d}^l). \tag{2.22}$$

These formulas are fundamental in expressing tensorial quantities consistently when switching between coordinate systems, and will be extensively used in the subsequent developments.

2.2 Fundamentals of Solid Continuum Mechanics

This section provides a formulation of continuum mechanics suitable for modeling structural behavior under finite deformations. All physical quantities are described in a Lagrangian setting, allowing for precise tracking of material points and objective measurement of strain. The theoretical development encompasses the kinematics of deformation, constitutive relations, various stress measures, and the derivation of equilibrium equations via the principle of virtual work.

2.2.1 Kinematics

In the framework of finite deformation theory, the description of a body requires the establishment of a geometric relation between the reference configuration (undeformed state) and the current configuration (deformed state). A material point occupies the position $\mathbf{X}$ in the reference configuration and $\mathbf{x}$ in the current configuration, and the displacement field $\mathbf{u}$ characterizes the transition between the two configurations according to

$$\mathbf{x} = \mathbf{X} + \mathbf{u}. \tag{2.23}$$

Throughout this work, uppercase symbols will denote quantities associated with the reference configuration, while lowercase symbols will refer to the current configuration.

The fundamental quantity describing deformation is the deformation gradient, defined as

$$\mathbf{F} = \frac{\partial \mathbf{x}}{\partial \mathbf{X}}. \tag{2.24}$$

Adopting convective curvilinear coordinates θ^i, such that each material point is identified by the same coordinates in both reference and current configurations, the covariant base vectors in the two configurations follow as

$$\mathbf{g}_i = \frac{\partial \mathbf{x}}{\partial \theta^i}, \qquad \mathbf{G}_i = \frac{\partial \mathbf{X}}{\partial \theta^i}. \tag{2.25}$$

The corresponding contravariant bases $\mathbf{g}^i$ and $\mathbf{G}^i$ are defined as the duals of $\mathbf{g}_i$ and $\mathbf{G}_i$, respectively, and satisfy the standard orthogonality relations with their covariant counterparts. With these definitions, the deformation gradient can be expressed in terms of the curvilinear bases as

$$\mathbf{F} = \frac{\partial \mathbf{x}}{\partial \mathbf{X}} = \frac{\partial \mathbf{x}}{\partial \theta^i} \otimes \frac{\partial \theta^i}{\partial \mathbf{X}} = \mathbf{g}_i \otimes \mathbf{G}^i. \tag{2.26}$$

In an analogous manner, the transpose of the deformation gradient is found as

$$\mathbf{F}^T = \left(\frac{\partial \mathbf{x}}{\partial \mathbf{X}}\right)^T = \frac{\partial \mathbf{X}}{\partial \theta^i} \otimes \frac{\partial \theta^i}{\partial \mathbf{x}} = \mathbf{G}^i \otimes \mathbf{g}_i. \tag{2.27}$$

The inverse deformation gradient is obtained from

$$\mathbf{F}^{-1} = \frac{\partial \mathbf{X}}{\partial \mathbf{x}} = \frac{\partial \mathbf{X}}{\partial \theta^i} \otimes \frac{\partial \theta^i}{\partial \mathbf{x}} = \mathbf{G}_i \otimes \mathbf{g}^i, \tag{2.28}$$

and the inverse transpose follows immediately as

$$\mathbf{F}^{-T} = \mathbf{g}^i \otimes \mathbf{G}_i. \tag{2.29}$$

The transformation between the bases in the two configurations can be illustrated by considering the covariant vector $\mathbf{g}_i$:

$$\mathbf{g}_i = \frac{\partial \mathbf{x}}{\partial \theta^i} = \frac{\partial \mathbf{x}}{\partial \mathbf{X}} \frac{\partial \mathbf{X}}{\partial \theta^i} = \mathbf{F}\mathbf{G}_i. \tag{2.30}$$

Analogous reasoning yields the relations for the remaining bases,

$$\mathbf{g}^i = \mathbf{F}^{-T}\mathbf{G}^i, \qquad \mathbf{G}_i = \mathbf{F}^{-1}\mathbf{g}_i, \qquad \mathbf{G}^i = \mathbf{F}^T\mathbf{g}^i. \tag{2.31}$$

Although $\mathbf{F}$ fully characterizes the local deformation, it does not constitute a suitable strain measure. The main reasons are that $\mathbf{F}$ is in general non-symmetric and that it includes rigid-body rotations. Therefore, objective strain measures are introduced. In this work, the right Cauchy–Green deformation tensor and the Green–Lagrange strain tensor will be employed depending on the specific constitutive model under consideration, and their definitions are

introduced here to provide a unified basis for the subsequent material formulations.

By means of the polar decomposition, the deformation gradient can be expressed as

$$\mathbf{F} = \mathbf{R}\mathbf{U}, \tag{2.32}$$

where $\mathbf{R}$ is a proper orthogonal rotation tensor satisfying $\mathbf{R}^T\mathbf{R} = \mathbf{I}$, $\mathbf{U}$ is the symmetric right stretch tensor, and $\mathbf{I}$ denotes the second-order identity tensor. Based on this decomposition, the right Cauchy–Green tensor $\mathbf{C}$ is obtained as

$$\mathbf{C} = \mathbf{F}^T\mathbf{F} = (\mathbf{R}\mathbf{U})^T(\mathbf{R}\mathbf{U}) = \mathbf{U}^T\mathbf{R}^T\mathbf{R}\mathbf{U} = \mathbf{U}^T\mathbf{U} = \mathbf{U}^2, \tag{2.33}$$

which eliminates the rotational part of the deformation and thus provides an objective measure of strain. Alternatively, with the representations of $\mathbf{F}$ and $\mathbf{F}^T$ given in Equations (2.26) and (2.27), the right Cauchy–Green tensor can be expressed in terms of the curvilinear bases as:

$$\mathbf{C} = \mathbf{F}^T\mathbf{F} = (\mathbf{G}^i \otimes \mathbf{g}_i)(\mathbf{g}_j \otimes \mathbf{G}^j) = (\mathbf{g}_i \cdot \mathbf{g}_j)\,\mathbf{G}^i \otimes \mathbf{G}^j = g_{ij}\,\mathbf{G}^i \otimes \mathbf{G}^j. \tag{2.34}$$

Based on the right Cauchy–Green tensor $\mathbf{C}$, the Green–Lagrange strain tensor $\mathbf{E}$ is defined as

$$\mathbf{E} = \frac{1}{2}(\mathbf{C} - \mathbf{I}), \tag{2.35}$$

where the identity tensor $\mathbf{I}$ in the curvilinear frame of the reference configuration is given by

$$\mathbf{I} = G_{ij}\,\mathbf{G}^i \otimes \mathbf{G}^j. \tag{2.36}$$

Hence, it leads to

$$\mathbf{E} = E_{ij}\mathbf{G}^i \otimes \mathbf{G}^j, \tag{2.37}$$

with the strain components

$$E_{ij} = \frac{1}{2}\,(g_{ij} - G_{ij}). \tag{2.38}$$

The Green–Lagrange strain thus quantifies the change of the metric between the current and reference configurations. Since $\mathbf{E}$ is defined with respect to the reference configuration, it is well-suited for finite strain formulations in a Lagrangian setting, where material points are tracked from their undeformed positions. For this reason, the Green–Lagrange strain is a commonly adopted strain measure in nonlinear continuum mechanics.

2.2.2 Constitutive Equations

In the previous subsection, the Green–Lagrange strain tensor $\mathbf{E}$ has been introduced to characterize the geometric change between the reference and the current configuration. However, the definition of strain alone is not sufficient to describe the mechanical response of a material. In order to establish the relation between strain and stress, constitutive equations are required. They define the evolution of stresses in response to given strains and thus characterize the material behavior.

A standard approach to formulate constitutive equations is based on a strain energy density function ψ. This scalar potential depends on strain measures and provides a unified energy-based framework for the description of material behavior. In this framework, stresses are defined as the first derivative of ψ, while the fourth-order material tensor is obtained from the second derivative. The strain energy function can either be expressed in terms of the Green–Lagrange strain tensor $\mathbf{E}$ or in terms of the right Cauchy–Green tensor $\mathbf{C}$, leading to the equivalent relations

$$\mathbf{S} = \frac{\partial \psi}{\partial \mathbf{E}} = 2\frac{\partial \psi}{\partial \mathbf{C}}, \qquad \mathbb{C} = \frac{\partial^2 \psi}{\partial \mathbf{E}^2} = 4\frac{\partial^2 \psi}{\partial \mathbf{C}^2}. \tag{2.39}$$

Here, $\mathbf{S}$ denotes the second Piola–Kirchhoff stress tensor, which is energetically conjugate to $\mathbf{E}$, and $\mathbb{C}$ denotes the fourth-order material tensor. The representation based on $\mathbf{E}$ is often more natural in strain-based derivations, whereas the representation based on $\mathbf{C}$ is particularly convenient for hyperelastic materials, since most hyperelastic energy functions are directly defined in terms of $\mathbf{C}$.

In terms of the covariant basis of the reference configuration, these tensors can be expanded as

$$\mathbf{S} = S^{ij}\mathbf{G}_i \otimes \mathbf{G}_j, \qquad \mathbb{C} = \mathbb{C}^{ijkl}\mathbf{G}_i \otimes \mathbf{G}_j \otimes \mathbf{G}_k \otimes \mathbf{G}_l. \tag{2.40}$$

It is important to note that different stress measures are used in continuum mechanics. The second Piola–Kirchhoff stress $\mathbf{S}$ is conjugate to $\mathbf{E}$ and is therefore well suited for finite element formulations in the reference configuration. However, it does not directly represent the physically observable stress. The true physical stress is the Cauchy stress tensor $\boldsymbol{\sigma}$, which characterizes the actual stress in the current configuration and corresponds to experimentally measurable quantities. Their relation is given by

$$\boldsymbol{\sigma} = (\det \mathbf{F})^{-1}\mathbf{F}\mathbf{S}\mathbf{F}^T, \tag{2.41}$$

where $\det \mathbf{F}$ is the determinant of the deformation gradient $\mathbf{F}$. Expanding this expression yields

$$\begin{aligned} \boldsymbol{\sigma} &= (\det \mathbf{F})^{-1}\,\mathbf{F}\Big(S^{ij}\,\mathbf{G}_i \otimes \mathbf{G}_j\Big)\mathbf{F}^T = (\det \mathbf{F})^{-1}\,S^{ij}\,(\mathbf{F}\mathbf{G}_i) \otimes (\mathbf{F}\mathbf{G}_j) \\ &= (\det \mathbf{F})^{-1}\,S^{ij}\,\mathbf{g}_i \otimes \mathbf{g}_j = \sigma^{ij}\,\mathbf{g}_i \otimes \mathbf{g}_j, \end{aligned} \tag{2.42}$$

where σ^{ij} are the stress coefficients of Cauchy stress tensor $\boldsymbol{\sigma}$ in the current covariant basis..

In addition, the first Piola–Kirchhoff stress tensor $\mathbf{P}$ can be obtained from $\mathbf{S}$ through the relation

$$\mathbf{P} = \mathbf{F}\mathbf{S} = \left(\mathbf{g}_i \otimes \mathbf{G}^i\right)\left(S^{jk}\,\mathbf{G}_j \otimes \mathbf{G}_k\right) = S^{jk}\,(\mathbf{G}^i \cdot \mathbf{G}_j)\,\mathbf{g}_i \otimes \mathbf{G}_k = S^{ik}\,\mathbf{g}_i \otimes \mathbf{G}_k. \tag{2.43}$$

This expression highlights the two-point character of $\mathbf{P}$, which carries one index in the current configuration ($\mathbf{g}_i$) and one in the reference configuration ($\mathbf{G}_k$). The tensor $\mathbf{P}$ is energetically conjugate to the deformation gradient $\mathbf{F}$. Although it is generally non-symmetric, $\mathbf{P}$ is frequently used in numerical implementations due to its direct dependence on $\mathbf{F}$.

Different choices of the strain energy density function ψ define different material models. As

a representative example and as the basic constitutive framework adopted in this thesis, the St. Venant–Kirchhoff model is considered. It is obtained from a quadratic form in $\mathbf{E}$, and its strain energy density function reads

$$\psi(\mathbf{E}) = \frac{\lambda}{2}\left(\mathrm{tr}\left(\mathbf{E}\right)\right)^2 + \mu \mathrm{tr}\left(\mathbf{E}^2\right), \tag{2.44}$$

where λ and μ are the Lamé constants, related to Young's modulus E and Poisson's ratio ν by

$$\lambda = \frac{E\nu}{(1+\nu)(1-2\nu)}, \qquad \mu = \frac{E}{2(1+\nu)}. \tag{2.45}$$

According to the general relation defined in Equation (2.39), the resulting stress can be expressed as

$$\mathbf{S} = \lambda \mathrm{tr}(\mathbf{E})\mathbf{I} + 2\mu\mathbf{E}. \tag{2.46}$$

Alternatively, this relation can equivalently be expressed through the material tensor $\mathbb{C}$ as

$$\mathbf{S} = \mathbb{C} : \mathbf{E}, \quad S^{ij} = \mathbb{C}^{ijkl} E_{kl}. \tag{2.47}$$

The St. Venant–Kirchhoff model recovers Hooke's law in the small-strain limit and can be viewed as the simplest formal extension of linear elasticity to finite deformations. However, it is known to produce unrealistic results under finite strains, and therefore more general hyperelastic models are required to capture realistic nonlinear material behavior. Such models can be obtained by adopting different forms of the strain energy density function ψ, for example the Neo-Hookean or Mooney–Rivlin models, which will be introduced in Section 2.4.

2.2.3 Equilibrium

In the previous subsections, the Green–Lagrange strain tensor $\mathbf{E}$ and the second Piola–Kirchhoff stress tensor $\mathbf{S}$ have been introduced to describe geometric deformation and material response. However, geometry and constitutive behavior alone are not sufficient to determine the mechanical state of a structure; the solution must also satisfy the equilibrium equations.

In the Lagrangian description, the balance of linear momentum is given by

$$\mathrm{Div}\,\mathbf{P} + \rho_0 \mathbf{B} = \mathbf{0}, \tag{2.48}$$

where $\mathbf{P}$ is the first Piola–Kirchhoff stress tensor, Div denotes the divergence operator, $\mathbf{B}$ is the body force vector, and ρ_0 is the density in the reference configuration. The reference density is assumed to be constant during deformation, and it is denoted by ρ in the following. Together with suitable boundary conditions, this relation defines the strong form of the boundary value problem.

Although the strong form provides a pointwise description of equilibrium, it cannot generally be solved exactly for three-dimensional boundary value problems. Numerical discretization methods such as the finite element method therefore employ a weaker formulation: instead of

enforcing equilibrium pointwise, the equations are required to hold only in an integral sense. This motivates the transformation of the strong form into the weak form.

To derive the weak form, the strong form is multiplied by an admissible virtual displacement field $\delta\mathbf{u}$ and integrated over the reference volume V:

$$\int_V (\operatorname{Div}\mathbf{P} + \rho\mathbf{B}) \cdot \delta\mathbf{u}\,\mathrm{d}V = 0. \tag{2.49}$$

Applying the divergence theorem to the first term yields

$$\int_V (\operatorname{Div}\mathbf{P}) \cdot \delta\mathbf{u}\,\mathrm{d}V = -\int_V \mathbf{P} : \delta\mathbf{F}\,\mathrm{d}V + \int_A \mathbf{T}^{\mathrm{trac}} \cdot \delta\mathbf{u}\,\mathrm{d}A, \tag{2.50}$$

where $\delta\mathbf{F}$ is the variation of the deformation gradient and $\mathbf{T}^{\mathrm{trac}}$ denotes the prescribed traction vector on the boundary A.

Using the work-conjugacy of $\mathbf{P}$ with $\mathbf{F}$ and of $\mathbf{S}$ with $\mathbf{E}$, the first term in Equation (2.50) can be rewritten as

$$\mathbf{P} : \delta\mathbf{F} = \mathbf{S} : \delta\mathbf{E}, \tag{2.51}$$

where $\delta\mathbf{E}$ is the variation of the Green–Lagrange strain tensor. Hence, the weak form of equilibrium is obtained as

$$\int_V \mathbf{S} : \delta\mathbf{E}\,\mathrm{d}V - \int_A \mathbf{T}^{\mathrm{trac}} \cdot \delta\mathbf{u}\,\mathrm{d}A - \int_V \rho\mathbf{B} \cdot \delta\mathbf{u}\,\mathrm{d}V = 0. \tag{2.52}$$

This variational statement is commonly referred to as the principle of virtual work. Introducing the notation

$$\delta W^{\mathrm{int}} = \int_V \mathbf{S} : \delta\mathbf{E}\,\mathrm{d}V, \tag{2.53}$$

$$\delta W^{\mathrm{ext}} = \int_A \mathbf{T}^{\mathrm{trac}} \cdot \delta\mathbf{u}\,\mathrm{d}A + \int_V \rho\mathbf{B} \cdot \delta\mathbf{u}\,\mathrm{d}V, \tag{2.54}$$

the principle of virtual work can be compactly expressed as

$$\delta W = \delta W^{\mathrm{int}} - \delta W^{\mathrm{ext}} = 0. \tag{2.55}$$

This variational formulation provides the basis for finite element discretization, where the virtual displacement field is approximated by interpolation functions and the virtual work equation is transformed into a system of algebraic equations that can be solved numerically.

2.3 Membrane and Shell Formulations

In the previous section, the fundamental theory of finite deformations was introduced within the framework of three-dimensional continuum mechanics. However, for structures whose thickness is much smaller than their characteristic dimensions, the direct application of

a three-dimensional solid model is not only computationally expensive but also involves quantities that are physically negligible. Therefore, in the modeling of membranes and shells, surface theories are commonly employed.

For membrane theory, the structural slenderness justifies the assumption that strains are uniformly distributed through the thickness, such that the midsurface strain can be taken to represent the overall distribution. Consequently, the deformation of a membrane reduces to the change of the first fundamental form of the midsurface, which characterizes the in-plane strain state. This theory is particularly suitable for the analysis of membrane structures, and the wrinkling models proposed in this work are formulated within this framework.

In contrast, shell theory also accounts for bending effects arising from changes in curvature. In this thesis, the Kirchhoff–Love shell theory is employed, in the formulation developed in [119]. This theory assumes that cross sections remain straight during deformation and remain normal to the midsurface. This implies that strains vary linearly through the thickness, while transverse shear strains are neglected. Since the cross sections remain normal to the midsurface, the shell director coincides with the midsurface normal, making the definition of an independent director redundant. As a result, the geometry and mechanical state of the shell can be completely described by its midsurface. The assumption is regarded as accurate for thin shells, and it is generally accepted to hold when the slenderness ratio satisfies $R/t > 20$, where R is the radius of curvature and t is the shell thickness.

It should be noted that, besides the Kirchhoff–Love formulation, there also exist the Reissner–Mindlin theory and other shell models, which are capable of accounting for transverse shear effects or are suitable for relatively thick shells. However, the present work focuses on thin film structures, and shell model is introduced solely as a reference solution for comparison with the proposed membrane wrinkling model. For reasons of simplicity and relevance, the Kirchhoff–Love shell theory is therefore chosen as the sole shell reference.

In the following subsections, the kinematics, constitutive equations, and equilibrium relations of membranes and shells are presented to establish the theoretical foundation for the subsequent derivations and numerical implementations.

2.3.1 Kinematics for Membranes and Shells

The Green–Lagrange strain tensor defined in Equation (2.37) can be decomposed with respect to the three-dimensional reference basis as

$$\mathbf{E} = E_{\alpha\beta}\,\mathbf{G}^{\alpha} \otimes \mathbf{G}^{\beta} + E_{\alpha 3}\,\mathbf{G}^{\alpha} \otimes \mathbf{G}^{3} + E_{33}\,\mathbf{G}^{3} \otimes \mathbf{G}^{3}. \tag{2.56}$$

Here, $E_{\alpha\beta}$ denote the in-plane strain components, $E_{\alpha 3}$ the transverse shear strains, and E_{33} the transverse normal strain. In both membrane and Kirchhoff–Love shell formulations the transverse shear strains vanish, $E_{\alpha 3} = 0$, while the transverse normal strain E_{33} does not vanish a priori. Instead, E_{33} is eliminated by enforcing the plane-stress condition, so that only

the in-plane strains remain. Accordingly, the strain tensor reduces to

$$\mathbf{E} = E_{\alpha\beta}\,\mathbf{G}^{\alpha} \otimes \mathbf{G}^{\beta}, \qquad E_{\alpha\beta} = \frac{1}{2}(g_{\alpha\beta} - G_{\alpha\beta}), \tag{2.57}$$

which provides the common starting point for both membranes and shells.

For membranes, the kinematics are regarded as a specialization of the three-dimensional theory introduced in Section 2.2.1, based on the assumption of a constant strain distribution across the thickness. Under this assumption, the midsurface at $\theta^3 = 0$ fully characterizes the membrane geometry, which is parametrized by the curvilinear coordinates (θ^1,θ^2).

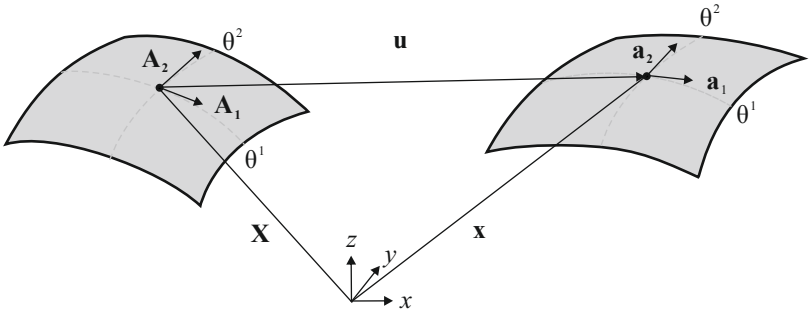

Figure 2.1.: Schematic view of a membrane [114]. The vectors **X** and **x** denote the positions on the midsurface in the reference and deformed configurations, respectively, with **u** as the displacement vector.

The position vector of a material point on the midsurface, as illustrated in Figure 2.1, is expressed as

$$\mathbf{x}(\theta^{\alpha},\theta^3 = 0) = \theta^{\alpha}\mathbf{a}_{\alpha}, \tag{2.58}$$

where $\mathbf{a}_{\alpha}$ are the base vectors of the midsurface. Thus, the covariant base vectors in the reference and current configurations are reduced to

$$\mathbf{G}_{\alpha} = \frac{\partial \mathbf{X}}{\partial \theta^{\alpha}} = \mathbf{A}_{\alpha}, \qquad \mathbf{g}_{\alpha} = \frac{\partial \mathbf{x}}{\partial \theta^{\alpha}} = \mathbf{a}_{\alpha}, \tag{2.59}$$

and the associated contravariant bases $\mathbf{G}^{\alpha}$ and $\mathbf{g}^{\alpha}$ can be determined by the duality relations given in Equation (2.4). According to the definition in Equation (2.8), the corresponding metric coefficients are then obtained as

$$G_{\alpha\beta} = \mathbf{A}_{\alpha} \cdot \mathbf{A}_{\beta} = A_{\alpha\beta}, \qquad g_{\alpha\beta} = \mathbf{a}_{\alpha} \cdot \mathbf{a}_{\beta} = a_{\alpha\beta}, \tag{2.60}$$

which characterize the midsurface geometry in the reference and current configurations, respectively. Consequently, the in-plane strain components defined in Equation (2.57) can be expressed as

$$E_{\alpha\beta} = \frac{1}{2}\left(a_{\alpha\beta} - A_{\alpha\beta}\right). \tag{2.61}$$

This expression shows that the membrane strain is entirely governed by changes in the midsurface metric. As a result, the membrane formulation captures only in-plane extensional

and shear effects, while thickness changes and bending stiffness are neglected.

The shell formulation provides a consistent extension of the membrane description by allowing the strain to vary linearly with the through-thickness coordinate $\theta^3 \in [-t/2, t/2]$, thereby capturing bending effects in addition to in-plane deformation.

For shells, the position vector of an arbitrary material point is written as

$$\mathbf{x}(\theta^\alpha,\theta^3) = \theta^\alpha \mathbf{a}_\alpha + \theta^3 \mathbf{a}_3, \tag{2.62}$$

with $\mathbf{a}_3$ the unit normal to the midsurface of shell. From this parametrization, the covariant base vectors in the current configuration follow as

$$\mathbf{g}_\alpha = \mathbf{a}_\alpha + \theta^3 \mathbf{a}_{3,\alpha}, \qquad \mathbf{g}_3 = \mathbf{a}_3, \tag{2.63}$$

where $\mathbf{g}_\alpha$ represent the base vectors that include the effect of thickness variation, while $\mathbf{g}_3$ remains the surface normal.

The metric coefficients associated with these base vectors can be expanded as

$$g_{\alpha\beta} = (\mathbf{a}_\alpha + \theta^3 \mathbf{a}_{3,\alpha}) \cdot (\mathbf{a}_\beta + \theta^3 \mathbf{a}_{3,\beta}) = a_{\alpha\beta} - 2\theta^3 b_{\alpha\beta} + (\theta^3)^2\, \mathbf{a}_{3,\alpha} \cdot \mathbf{a}_{3,\beta}. \tag{2.64}$$

The first term corresponds to the midsurface metric, while the linear term in θ^3 involves $b_{\alpha\beta}$, the coefficients of the second fundamental form that describe the surface curvature (see Equation (2.12)). The quadratic term proportional to $(\theta^3)^2$ is usually neglected for thin and moderately thick shells [120].

Using these metric expansions, the components of Green–Lagrange strain tensor given in Equation (2.57) becomes

$$E_{\alpha\beta} = \frac{1}{2}\Big((a_{\alpha\beta} - 2\theta^3 b_{\alpha\beta}) - (A_{\alpha\beta} - 2\theta^3 B_{\alpha\beta})\Big). \tag{2.65}$$

This expression contains two contributions: one that is independent of the thickness coordinate and one that varies linearly through the thickness. In compact form, it reads

$$E_{\alpha\beta} = \varepsilon_{\alpha\beta} + \theta^3 \kappa_{\alpha\beta}, \tag{2.66}$$

with

$$\varepsilon_{\alpha\beta} = \frac{1}{2}(a_{\alpha\beta} - A_{\alpha\beta}), \qquad \kappa_{\alpha\beta} = B_{\alpha\beta} - b_{\alpha\beta}. \tag{2.67}$$

Here, the constant term $\varepsilon_{\alpha\beta}$ represents the in-plane membrane strain, describing stretching and shear of the midsurface, while the linear term $\theta^3\kappa_{\alpha\beta}$ accounts for bending strains induced by curvature changes across the thickness. Although defined on the reference configuration, the membrane strains $\varepsilon_{\alpha\beta}$ and curvature changes $\kappa_{\alpha\beta}$ are denoted by lowercase symbols, following the standard convention in shell theory [116].

This formulation unifies membranes and shells within a single representation: the membrane case is obtained by setting $\theta^3 = 0$, whereas the shell case additionally accounts for the bending contribution. Hence, the shell theory can be regarded as a natural extension of the membrane model, preserving the in-plane response and incorporating bending resistance through the

thickness-dependent term.

2.3.2 Stress Resultants and Recovery

Based on the kinematic assumptions introduced before, the strain tensor reduces to the in-plane components $E_{\alpha\beta}$. In addition, the present formulation adopts the plane stress condition $S^{33} = 0$, which modifies the three-dimensional St. Venant–Kirchhoff model of Equation (2.44) into the following form [121]:

$$\psi(\mathbf{E}) = \frac{\lambda}{2}\big(\mathrm{tr}(\mathbf{E})\big)^2 + \mu\,\mathrm{tr}(\mathbf{E}^2) - \frac{\lambda^2}{2(\lambda+2\mu)}\big(\mathrm{tr}(\mathbf{E})\big)^2, \tag{2.68}$$

where the last term directly results from enforcing $S^{33} = 0$. The corresponding stress–strain relation, consistent with Equation (2.47), then reads

$$S^{\alpha\beta} = \mathbb{C}^{\alpha\beta\gamma\delta} E_{\gamma\delta}. \tag{2.69}$$

The strain decomposition has already been introduced in Equation (2.66). A corresponding separation into membrane and bending contributions is also applied to the stresses. The stress resultants are then obtained by integration through the thickness: the normal forces from the membrane part and the bending moments from the curvature part. For linear elastic materials this through-thickness integration can be carried out analytically, yielding the classical expressions for membrane forces and bending moments. For nonlinear constitutive laws, however, the integration must in general be performed numerically.

Explicitly, for linear elasticity one obtains

$$N^{\alpha\beta} = \int_{-t/2}^{t/2} S^{\alpha\beta}\, d\theta^3 = \mathbb{C}^{\alpha\beta\gamma\delta}\, \varepsilon_{\gamma\delta}\, t. \tag{2.70}$$

In the membrane formulation only the in-plane strain contributes, so that stresses are constant through the thickness and no bending moments occur.

In the shell formulation, however, both contributions in Equation (2.66) are present, so that the stress varies linearly through the thickness. Besides the same membrane forces as in the membrane case, the integration produces additional bending moments,

$$M^{\alpha\beta} = \int_{-t/2}^{t/2} S^{\alpha\beta}\, \theta^3\, d\theta^3 = \mathbb{C}^{\alpha\beta\gamma\delta}\, \kappa_{\gamma\delta}\, \frac{t^3}{12}. \tag{2.71}$$

Hence, membranes and shells share the same expression for the membrane forces, while shells extend the formulation by consistently incorporating bending moments due to curvature effects. Thus, the internal virtual work in membrane and shell formulations can be written in the following unified form

$$\delta W^{\mathrm{int}} = \int_V (\mathbf{S} : \delta\mathbf{E})\mathrm{d}V = \int_A (\mathbf{N} : \delta\boldsymbol{\varepsilon} + \mathbf{M} : \delta\boldsymbol{\kappa})\,\mathrm{d}A, \tag{2.72}$$

where dA is the differential area of the midsurface in the reference configuration. In the membrane case, the second term, which represents the bending contribution, vanishes, and only the membrane term remains.

While the preceding relations define the theoretical form of the stress resultants, in numerical analysis these quantities are not obtained directly. Displacement-based methods such as the finite element approach provide only the nodal displacements and the deformed geometry. Other quantities of interest, such as the Cauchy stresses $\boldsymbol{\sigma}$ and the stress resultants, must therefore be evaluated in a postprocessing step, commonly referred to as stress recovery.

Therefore, the following introduces a general procedure for stress recovery, which is of general validity and independent of the discretization method. Since the focus of the present work lies on membrane and shell formulations, the stress recovery procedure is presented here in terms of the Greek indices. Nevertheless, the procedure is equally applicable to solid formulations.

Starting from the deformed geometry, the Green–Lagrange strain coefficients $E_{\alpha\beta}$ can be computed from the metric tensors of the reference and current configurations, see Equation (2.57). Since the material constants are usually given in a local Cartesian system, the strain tensor is subsequently transformed from the curvilinear basis $\mathbf{G}^{\alpha}$ to a local Cartesian basis $\mathbf{E}_{\gamma}$. According to the general transformation rule defined in Equation (2.19), the Cartesian strain components are given by

$$\bar{E}_{\gamma\delta} = E_{\alpha\beta}\,(\mathbf{E}_{\gamma}\cdot\mathbf{G}^{\alpha})\,(\mathbf{G}^{\beta}\cdot\mathbf{E}_{\delta}), \tag{2.73}$$

where the over-bar indicates that the scalar components with respect to the Cartesian basis. On this basis, the second Piola–Kirchhoff stresses follow directly from the constitutive relation,

$$\bar{S}^{\alpha\beta} = \bar{\mathbb{C}}^{\alpha\beta\gamma\delta}\,\bar{E}_{\gamma\delta}, \tag{2.74}$$

with the material tensor expressed in the Cartesian frame. Since the PK2 stresses do not correspond to the actual stresses in the current configuration, they must be related to the Cauchy stress tensor $\boldsymbol{\sigma}$. For this purpose the stress tensor is first transformed back to the curvilinear basis of the reference configuration,

$$S^{\gamma\delta} = \bar{S}^{\alpha\beta}\,(\mathbf{G}^{\gamma}\cdot\mathbf{E}_{\alpha})(\mathbf{E}_{\beta}\cdot\mathbf{G}^{\delta}), \tag{2.75}$$

and then converted into the Cauchy stresses according to

$$\sigma^{\alpha\beta} = \frac{1}{\det\mathbf{F}}\,S^{\alpha\beta}. \tag{2.76}$$

The coefficients $\sigma^{\alpha\beta}$ thus obtained are defined with respect to the current covariant basis $\mathbf{g}_{\alpha}\otimes\mathbf{g}_{\beta}$, which is in general not orthonormal. Therefore, these components cannot directly be interpreted as physical stress values. To obtain stresses in standard normalized units (e.g. $\mathrm{N\,mm^{-2}}$), a final transformation to a local Cartesian basis $\mathbf{e}_{\gamma}\otimes\mathbf{e}_{\delta}$ is required,

$$\bar{\sigma}^{\gamma\delta} = \sigma^{\alpha\beta}\,(\mathbf{e}^{\gamma}\cdot\mathbf{g}_{\alpha})\,(\mathbf{g}_{\beta}\cdot\mathbf{e}^{\delta}). \tag{2.77}$$

The resulting coefficients $\bar{\sigma}^{\gamma\delta}$ then represent the physical stress values in the local Cartesian frame. In addition, the transformation procedure outlined above for stresses can equivalently be applied to the stress resultants in membrane and shell analysis. Accordingly, the membrane forces $N^{\alpha\beta}$ and bending moments $M^{\alpha\beta}$ can be computed from Equations (2.70) and (2.71), and subsequently transformed into the corresponding physical quantities $\bar{N}^{\alpha\beta}$ and $\bar{M}^{\alpha\beta}$. The membrane forces $\bar{N}^{\alpha\beta}$ and bending moments $\bar{M}^{\alpha\beta}$ provide the basis for recovering the in-plane Cauchy stresses $\bar{\sigma}^{\alpha\beta}$ at arbitrary points in the membrane or shell continuum.

2.3.3 Linearization and Discretization

The in-plane strains, together with the membrane forces and bending moments derived in the previous sections, constitute the fundamental quantities that enter the principle of virtual work for membranes and shells. For brevity, the following derivation focuses on the membrane formulation, while the more general shell expression can be found in the literature [119] and is not repeated here.

In the membrane case, two considerations enable a further simplification. First, since the thickness of the membrane is small, the stress is assumed to be constant through the thickness. Second, the wrinkling model developed in this work is likewise formulated at the stress level. Consequently, the membrane forces for membranes reduce to a simple multiplication with the thickness t [64]:

$$N^{\alpha\beta} = \int_{-t/2}^{t/2} S^{\alpha\beta} \, \mathrm{d}\theta^3 \approx S^{\alpha\beta} \, t. \tag{2.78}$$

Moreover, to ensure consistency with the subsequent wrinkling model, the membrane strain was denoted by $\boldsymbol{\varepsilon}$, but since in the membrane case it does not contain bending contributions, it is here denoted by $\mathbf{E}$, as defined in Equation (2.61). Accordingly, in the membrane case, the internal virtual work in Equation (2.72) becomes

$$\delta W^{\mathrm{int}} = \int_A \mathbf{S} : \delta\mathbf{E} \, t \, \mathrm{d}A. \tag{2.79}$$

Hence, the total virtual work of the membrane formulation is obtained by combining the internal and external contributions, leading to

$$\delta W(\mathbf{u}, \delta\mathbf{u}) = \delta W^{\mathrm{int}} - \delta W^{\mathrm{ext}} = \int_A \mathbf{S} : \delta\mathbf{E} \, t \, \mathrm{d}A - \int_A \mathbf{T}^{\mathrm{trac}} \cdot \delta\mathbf{u} \, \mathrm{d}A. \tag{2.80}$$

To numerically solve the variational formulation, both discretization and linearization steps are required. The procedure adopted here largely follows the approach in [114]. The main aspects of the discretization are summarized below. The formulation allows for different types of basis functions, such as standard Lagrange polynomials commonly used in finite element analysis, as well as Non-Uniform Rational B-Splines (NURBS), which are the typical choice in isogeometric analysis (IGA). Because NURBS can represent geometry exactly and provide higher-order continuity, they have been widely adopted in structural mechanics. Their theoretical background and advantages are reviewed in Chapter 3.

The displacement field $\mathbf{u}$ is approximated as a linear combination of basis functions N^a:

$$\mathbf{u} = \sum_{a=1}^{n_{sh}} N^a \mathbf{u}^a, \tag{2.81}$$

where n_{sh} denotes the number of basis functions and $\mathbf{u}^a$ is the vector of nodal displacements. The summation sign is written explicitly since a denotes nodal numbering rather than a tensor index. Each component u_i^a ($i = 1,2,3$) corresponds to the displacement in the global Cartesian directions. Introducing a global degree of freedom index $r = 3(a-1) + i$, the displacement variables can be written as $u_r = u_i^a$. Differentiating the displacement field with respect to the displacement variables u_r gives

$$\frac{\partial \mathbf{u}}{\partial u_r} = N^a \mathbf{e}_i, \tag{2.82}$$

with $\mathbf{e}_i$ denoting the Cartesian basis vectors.

By definition, the residual vector $\mathbf{R}$ is obtained as the derivative of the total virtual work with respect to the displacement variables, i.e.,

$$R_r = \frac{\partial W}{\partial u_r} = \frac{\partial W^{\text{int}}}{\partial u_r} - \frac{\partial W^{\text{ext}}}{\partial u_r} = F_r^{\text{int}} - F_r^{\text{ext}}, \tag{2.83}$$

where $\mathbf{F}^{\text{int}}$ and $\mathbf{F}^{\text{ext}}$ denote the internal and external nodal force vectors, respectively. They are defined as

$$F_r^{\text{int}} = \int_A \mathbf{S} : \frac{\partial \mathbf{E}}{\partial u_r}\, t \, \mathrm{d}A, \quad F_r^{\text{ext}} = \int_A \mathbf{T}^{\text{trac}} \cdot \frac{\partial \mathbf{u}}{\partial u_r} \, \mathrm{d}A. \tag{2.84}$$

The tangent stiffness matrix $\mathbf{K}$ follows by linearization of the residual,

$$K_{rs} = \frac{\partial R_r}{\partial u_s} = \frac{\partial^2 W^{\text{int}}}{\partial u_r \partial u_s} - \frac{\partial^2 W^{\text{ext}}}{\partial u_r \partial u_s} = K_{rs}^{\text{int}} - K_{rs}^{\text{ext}}. \tag{2.85}$$

In expanded form, one obtains

$$K_{rs}^{\text{int}} = \int_A \left(\frac{\partial \mathbf{S}}{\partial u_s} : \frac{\partial \mathbf{E}}{\partial u_r} + \mathbf{S} : \frac{\partial^2 \mathbf{E}}{\partial u_r \partial u_s} \right) t \, \mathrm{d}A, \quad K_{rs}^{\text{ext}} = \int_A \frac{\partial \mathbf{T}^{\text{trac}}}{\partial u_s} \cdot \frac{\partial \mathbf{u}}{\partial u_r} \, \mathrm{d}A. \tag{2.86}$$

Here, the derivative of the second Piola–Kirchhoff stress with respect to u_s is given by

$$\frac{\partial \mathbf{S}}{\partial u_s} = \mathbb{C} : \frac{\partial \mathbf{E}}{\partial u_s}. \tag{2.87}$$

In addition, if the applied traction $\mathbf{T}^{\text{trac}}$ does not depend on the displacement field, the external stiffness contribution $\mathbf{K}^{\text{ext}}$ vanishes. Even in cases where $\mathbf{T}^{\text{trac}} = \mathbf{T}^{\text{trac}}(\mathbf{u})$, this term is often neglected without compromising convergence, provided that the residual $\mathbf{R}$ is evaluated consistently. Furthermore, as can be seen in Equation (2.86), both the first and second derivatives of the strain tensor with respect to the displacement variables are required. Explicit expressions are provided below.

According to the definitions of the position vector $\mathbf{x}$ and the corresponding covariant base

vectors $\mathbf{a}_\alpha$ (see Equation (2.23) and Equation (2.59)), the position vector $\mathbf{x}$ is composed of the reference position vector and the displacement field, while the base vectors follow as the derivatives of the position vector with respect to the surface coordinates. Obviously, all quantities in the reference configuration are invariant to the displacement variables, and therefore their derivatives vanish. It follows that the derivative of the position vector $\mathbf{x}$ with respect to the displacement variables can be expressed as

$$\mathbf{x}_{,r} = \sum_a N^a \, \mathbf{u}^a_{,r}, \tag{2.88}$$

where, for brevity, the notation $(\cdot)_{,r} = \partial(\cdot)/\partial u_r$ is adopted. The derivatives of the covariant base vectors with respect to the displacement variables then read

$$\mathbf{a}_{\alpha,r} = \mathbf{x}_{,\alpha,r} = \sum_a N^a_{,\alpha} \, \mathbf{u}^a_{,r}. \tag{2.89}$$

According to the definition of the metric coefficients, their first derivatives are given by

$$a_{\alpha\beta,r} = (\mathbf{a}_\alpha \cdot \mathbf{a}_\beta)_{,r} = \mathbf{a}_\alpha \cdot \mathbf{a}_{\beta,r} + \mathbf{a}_{\alpha,r} \cdot \mathbf{a}_\beta. \tag{2.90}$$

In the membrane case, the derivatives of the membrane strain with respect to the displacement variables read

$$E_{\alpha\beta,r} = \frac{1}{2} \, (a_{\alpha\beta} - A_{\alpha\beta})_{,r} = \frac{1}{2} \, a_{\alpha\beta,r}. \tag{2.91}$$

Here, the derivative of the reference metric $A_{\alpha\beta}$ vanishes since it is defined in the reference configuration and does not depend on the displacement variables.

The evaluation of the second derivatives proceeds analogously. Because the position vector depends linearly on the displacement variables, all second derivatives with respect to them vanish, i.e.,

$$\mathbf{x}_{,rs} = \sum_a N^a \, \mathbf{u}^a_{,rs} = \mathbf{0}. \tag{2.92}$$

The same argument applies to the covariant base vectors,

$$\mathbf{a}_{\alpha,rs} = \sum_a N^a_{,\alpha} \, \mathbf{u}^a_{,rs} = \mathbf{0}. \tag{2.93}$$

Hence, the second derivatives of the metric coefficients become

$$a_{\alpha\beta,rs} = \mathbf{a}_\alpha \cdot \mathbf{a}_{\beta,rs} + \mathbf{a}_{\alpha,s} \cdot \mathbf{a}_{\beta,r} + \mathbf{a}_{\alpha,rs} \cdot \mathbf{a}_\beta + \mathbf{a}_{\alpha,r} \cdot \mathbf{a}_{\beta,s} = \mathbf{a}_{\alpha,s} \cdot \mathbf{a}_{\beta,r} + \mathbf{a}_{\alpha,r} \cdot \mathbf{a}_{\beta,s}. \tag{2.94}$$

With this result, the second derivatives of the membrane strain components follow as

$$E_{\alpha\beta,rs} = \frac{1}{2} \, a_{\alpha\beta,rs}. \tag{2.95}$$

It is noted that, for the membrane strain, the second derivatives only involve first derivatives of the basis functions (see Equations (2.89) and (2.94)), such that C^0-continuity of the basis functions is sufficient. In contrast, for the shell formulation, the second derivative of the

bending strain, or more precisely the curvature, also enters the expressions, which requires second derivatives of the basis functions and thus C^1-continuity of the basis. The derivation of these terms is considerably more involved. For brevity, the explicit forms are omitted here, and the reader is referred to [122] for further details. This requirement highlights the importance of higher-order continuity provided by NURBS basis functions in isogeometric analysis.

With the explicit forms of the residual vector and the tangent stiffness matrix, the process of linearization and discretization is completed. These quantities provide the essential input for iterative solution strategies of the nonlinear equilibrium equations, which will be addressed in Section 3.5.

2.4 Extension to Hyperelastic Materials

This section extends the membrane and shell formulation to hyperelastic materials. The kinematic assumptions introduced in Section 2.3.1 remain valid in the finite strain regime, and the subsequent procedures of linearization and discretization in Section 2.3.3 are likewise unaffected by the constitutive choice. The essential issue concerns the transverse normal strain E_{33}, which characterizes the thickness stretch. It is directly related to the right Cauchy–Green component C_{33}, but unlike the in-plane strains it is not determined by the midsurface kinematics and must therefore be obtained from the plane stress condition $S^{33} = 0$.

For the St. Venant–Kirchhoff material used in Section 2.3.2, this condition can be satisfied directly, resulting in the additional term in the strain energy function given in Equation (2.68), whereas for general hyperelastic materials such a direct correction is in general difficult to obtain.

For a three-dimensional continuum, according to the definition given in Equation (2.34), the components of the right Cauchy–Green deformation tensor are in general given by $C_{ij} = g_{ij}$. This relation, however, does not hold in the transverse direction for membranes and shells. In the membrane and shell formulations, the covariant basis vector in the thickness direction is $\mathbf{g}_3 = \mathbf{a}_3$. Because $\mathbf{a}_3$ is the unit normal vector of the midsurface, it follows that

$$g_{33} = \mathbf{g}_3 \cdot \mathbf{g}_3 = \mathbf{a}_3 \cdot \mathbf{a}_3 = 1. \tag{2.96}$$

If $C_{33} = g_{33} = 1$ were assumed simply, the plane stress condition would, in general, be violated because

$$S^{33} = 2\,\frac{\partial \psi}{\partial C_{33}} \neq 0. \tag{2.97}$$

Thus, the right Cauchy–Green tensor C_{ij} and its inverse $\check{C}^{ij}$ for membranes and shells take the form

$$C_{ij} = \begin{bmatrix} g_{11} & g_{12} & 0 \\ g_{21} & g_{22} & 0 \\ 0 & 0 & C_{33} \end{bmatrix}, \qquad \check{C}^{ij} = \begin{bmatrix} g^{11} & g^{12} & 0 \\ g^{21} & g^{22} & 0 \\ 0 & 0 & C_{33}^{-1} \end{bmatrix}, \tag{2.98}$$

where the in-plane components $C_{\alpha\beta}$ coincide with the midsurface metric coefficients $g_{\alpha\beta}$, while the transverse component C_{33} represents the actual thickness stretch.

Accordingly, C_{33} must be determined such that the transverse stress component $S^{33} = 0$ is fulfilled. For incompressible materials this can be carried out analytically by imposing the incompressibility constraint, whereas for compressible materials it requires an iterative update procedure. The details of both approaches are presented in the following, based on [122]. Recently, these approaches have been extended to formulations in which the derivatives of the strain energy density function are taken directly with respect to the principal stretches rather than the components of the deformation tensor [123].

Once the plane stress condition is enforced, it can be used to eliminate the transverse normal strain E_{33} by static condensation of the material tensor. In component form, separating the transverse direction, the stress components read

$$S^{33} = \mathbb{C}^{33\gamma\delta} E_{\gamma\delta} + \mathbb{C}^{3333} E_{33}, \qquad S^{\alpha\beta} = \mathbb{C}^{\alpha\beta\gamma\delta} E_{\gamma\delta} + \mathbb{C}^{\alpha\beta 33} E_{33}. \tag{2.99}$$

From the condition $S^{33} = 0$ one obtains

$$E_{33} = -\frac{\mathbb{C}^{33\gamma\delta}}{\mathbb{C}^{3333}} E_{\gamma\delta}. \tag{2.100}$$

Substituting this relation into $S^{\alpha\beta}$ gives

$$S^{\alpha\beta} = \Big(\mathbb{C}^{\alpha\beta\gamma\delta} - \frac{\mathbb{C}^{\alpha\beta 33}\,\mathbb{C}^{33\gamma\delta}}{\mathbb{C}^{3333}}\Big) E_{\gamma\delta}. \tag{2.101}$$

Hence, the constitutive law reduces to purely in-plane components, with the statically condensed material tensor

$$\widehat{\mathbb{C}}^{\alpha\beta\gamma\delta} = \mathbb{C}^{\alpha\beta\gamma\delta} - \frac{\mathbb{C}^{\alpha\beta 33}\,\mathbb{C}^{33\gamma\delta}}{\mathbb{C}^{3333}}. \tag{2.102}$$

For the subsequent derivations it is convenient to summarize a few fundamental operations associated with the right Cauchy–Green deformation tensor $\mathbf{C}$. Both the trace and the determinant of $\mathbf{C}$ will play an important role, and their explicit expressions are given below.

The trace of $\mathbf{C}$ can be written as

$$\operatorname{tr}(\mathbf{C}) = g_{\alpha\beta}\, G^{\alpha\beta} + C_{33}. \tag{2.103}$$

In addition, the determinant of $\mathbf{C}$ can be obtained according to [122] as

$$\det(\mathbf{C}) = \frac{|g_{\alpha\beta}|\, C_{33}}{|G_{\alpha\beta}|} = J_0^2\, C_{33}, \tag{2.104}$$

where J_0 denotes the in-plane Jacobian determinant, defined by

$$J_0 = \sqrt{\frac{|g_{\alpha\beta}|}{|G_{\alpha\beta}|}}. \tag{2.105}$$

This in-plane Jacobian is related to the Jacobian determinant $J = \det(\mathbf{F})$ through

$$J = J_0\sqrt{C_{33}}. \tag{2.106}$$

Besides these measures, it is also useful to recall the three classical invariants of $\mathbf{C}$, which are closely related to the principal stretches $\lambda_1, \lambda_2, \lambda_3$. They are expressed as

$$I_1 = \operatorname{tr}(\mathbf{C}) = \lambda_1^2 + \lambda_2^2 + \lambda_3^2, \tag{2.107}$$

$$I_2 = \frac{1}{2}\Big((\operatorname{tr}\mathbf{C})^2 - \operatorname{tr}(\mathbf{C}^2)\Big) = \lambda_1^2\lambda_2^2 + \lambda_1^2\lambda_3^2 + \lambda_2^2\lambda_3^2, \tag{2.108}$$

$$I_3 = \det(\mathbf{C}) = \lambda_1^2\lambda_2^2\lambda_3^2. \tag{2.109}$$

In the membrane and shell formulation, the third stretch λ_3 represents the thickness stretch and is directly connected to the transverse component of $\mathbf{C}$ as $\lambda_3 = \sqrt{C_{33}}$. In addition, the explicit derivatives of the invariants, as well as those of the inverse of $\mathbf{C}$, are not shown here for brevity; the complete expressions are collected in Appendix A.1.

2.4.1 Incompressible Materials

In order to consistently enforce the incompressibility condition $J = 1$, the elastic strain energy $\psi_{\text{el}}(\mathbf{C})$ is augmented by a Lagrange multiplier p_{LM}, which can be interpreted as the hydrostatic pressure [117]. The resulting potential is expressed as

$$\psi = \psi_{\text{el}}(\mathbf{C}) - p_{\text{LM}}(J - 1). \tag{2.110}$$

In the context of thin structures, the unknown p_{LM} can be eliminated by exploiting the plane stress condition. Before doing so, the three-dimensional stress tensor and the consistent material tangent follow from differentiation of ψ with respect to $\mathbf{C}$, while considering p_{LM} as a function of $\mathbf{C}$:

$$S^{ij} = 2\frac{\partial\psi_{\text{el}}}{\partial C_{ij}} - 2\frac{\partial p_{\text{LM}}}{\partial C_{ij}}(J - 1) - 2p_{\text{LM}}\frac{\partial J}{\partial C_{ij}}, \tag{2.111}$$

$$\begin{aligned}\mathbb{C}^{ijkl} = {} & 4\frac{\partial^2\psi_{\text{el}}}{\partial C_{ij}\partial C_{kl}} - 4\frac{\partial^2 p_{\text{LM}}}{\partial C_{ij}\partial C_{kl}}(J - 1) - 4\frac{\partial p_{\text{LM}}}{\partial C_{ij}}\frac{\partial J}{\partial C_{kl}} \\ & - 4\frac{\partial J}{\partial C_{ij}}\frac{\partial p_{\text{LM}}}{\partial C_{kl}} - 4p_{\text{LM}}\frac{\partial^2 J}{\partial C_{ij}\partial C_{kl}}.\end{aligned} \tag{2.112}$$

The Jacobian determinant admits explicit derivatives with respect to C_{ij},

$$\frac{\partial J}{\partial C_{ij}} = \frac{1}{2}J\check{C}^{ij}, \tag{2.113}$$

$$\frac{\partial^2 J}{\partial C_{ij}\partial C_{kl}} = \frac{1}{4} J \left(\check{C}^{ij}\check{C}^{kl} - \check{C}^{ik}\check{C}^{jl} - \check{C}^{il}\check{C}^{jk} \right). \tag{2.114}$$

By inserting Equation (2.113) into Equation (2.111) and enforcing $J = 1$, one arrives at the plane stress condition, which reads

$$S^{33} = 2\frac{\partial \psi_{\mathrm{el}}}{\partial C_{33}} - p_{\mathrm{LM}} \check{C}^{33} = 0. \tag{2.115}$$

This equation can be solved for p_{LM}, yielding

$$p_{\mathrm{LM}} = 2\frac{\partial \psi_{\mathrm{el}}}{\partial C_{33}} C_{33}. \tag{2.116}$$

Its differentiation with respect to C_{ij} leads to

$$\frac{\partial p_{\mathrm{LM}}}{\partial C_{ij}} = 2\left(\frac{\partial^2 \psi_{\mathrm{el}}}{\partial C_{33}\partial C_{ij}} C_{33} + \frac{\partial \psi_{\mathrm{el}}}{\partial C_{33}} \delta^{i3}\delta^{j3} \right), \tag{2.117}$$

where δ^{ij} is the Kronecker delta.

By inserting the Equations (2.116)–(2.117) together with Equations (2.113)–(2.114) into Equations (2.111)–(2.112), and enforcing the incompressibility condition $J = 1$, the stress and material tensors in the incompressible case reduce to

$$S^{ij} = 2\frac{\partial \psi_{\mathrm{el}}}{\partial C_{ij}} - 2\frac{\partial \psi_{\mathrm{el}}}{\partial C_{33}} C_{33} \check{C}^{ij}, \tag{2.118}$$

$$\begin{aligned} \mathbb{C}^{ijkl} = {} & 4\frac{\partial^2 \psi_{\mathrm{el}}}{\partial C_{ij}\partial C_{kl}} - 2\frac{\partial \psi_{\mathrm{el}}}{\partial C_{33}} C_{33} \left(\check{C}^{ij}\check{C}^{kl} - \check{C}^{ik}\check{C}^{jl} - \check{C}^{il}\check{C}^{jk} \right) \\ & -4\left(\frac{\partial^2 \psi_{\mathrm{el}}}{\partial C_{33}\partial C_{ij}} C_{33} + \frac{\partial \psi_{\mathrm{el}}}{\partial C_{33}} \delta^{i3}\delta^{j3} \right) \check{C}^{kl} - 4\check{C}^{ij} \left(\frac{\partial^2 \psi_{\mathrm{el}}}{\partial C_{33}\partial C_{kl}} C_{33} + \frac{\partial \psi_{\mathrm{el}}}{\partial C_{33}} \delta^{k3}\delta^{l3} \right). \end{aligned} \tag{2.119}$$

For membrane and shell applications, only the in-plane quantities, namely $S^{\alpha\beta}$ and $\widehat{\mathbb{C}}^{\alpha\beta\gamma\delta}$, are considered. The contravariant metric components are taken as $\check{C}^{\alpha\beta} = g^{\alpha\beta}$, while the out-of-plane contribution is represented by $C_{33} = J_0^{-2}$ according to Equation (2.106). The elimination of the transverse strain component is carried out by static condensation, a procedure described in detail in Appendix A.2. Following this step, the stress and material tensors take the form

$$S^{\alpha\beta} = 2\frac{\partial \psi_{\mathrm{el}}}{\partial C_{\alpha\beta}} - 2\frac{\partial \psi_{\mathrm{el}}}{\partial C_{33}} J_0^{-2} g^{\alpha\beta}, \tag{2.120}$$

$$\widehat{\mathbb{C}}^{\alpha\beta\gamma\delta} = 4\frac{\partial^2\psi_{\mathrm{el}}}{\partial C_{\alpha\beta}\partial C_{\gamma\delta}} + 4\frac{\partial^2\psi_{\mathrm{el}}}{\partial C_{33}^2}J_0^{-4}\, g^{\alpha\beta}g^{\gamma\delta} - 4\frac{\partial^2\psi_{\mathrm{el}}}{\partial C_{33}\partial C_{\alpha\beta}}J_0^{-2}\, g^{\gamma\delta}$$
$$- 4\frac{\partial^2\psi_{\mathrm{el}}}{\partial C_{33}\partial C_{\gamma\delta}}J_0^{-2}\, g^{\alpha\beta} + 2\frac{\partial\psi_{\mathrm{el}}}{\partial C_{33}}J_0^{-2}\left(2g^{\alpha\beta}g^{\gamma\delta} + g^{\alpha\gamma}g^{\beta\delta} + g^{\alpha\delta}g^{\beta\gamma}\right). \tag{2.121}$$

When the constitutive quantities are originally expressed in Cartesian coordinates, they can be mapped into a curvilinear coordinate system by means of the base vectors. The transformation rules for the first and second derivatives of the strain energy function are provided in [122].

The preceding discussion established the general framework for incompressible materials. Building on this formulation, a simple illustrative example is provided by the neo-Hookean model, whose strain energy function is given by

$$\psi_{\mathrm{el}} = \frac{1}{2}\mu\,(I_1 - 3), \tag{2.122}$$

where μ denotes the shear modulus. Since the energy function is linear in I_1, its first derivative with respect to C_{ij} is constant, namely $\partial I_1/\partial C_{ij} = G^{ij}$. Consequently, the associated second derivatives vanish, which leads to a significant simplification of the condensed constitutive relations. As a result, the expressions for the in-plane stress and the material tensor reduce to compact forms as

$$S^{\alpha\beta} = \mu\left(G^{\alpha\beta} - J_0^{-2}g^{\alpha\beta}\right), \tag{2.123}$$

$$\widehat{\mathbb{C}}^{\alpha\beta\gamma\delta} = \mu J_0^{-2}\left(2g^{\alpha\beta}g^{\gamma\delta} + g^{\alpha\gamma}g^{\beta\delta} + g^{\alpha\delta}g^{\beta\gamma}\right). \tag{2.124}$$

2.4.2 Compressible Materials

In the compressible case, the plane stress constraint $S^{33} = 0$ is enforced by iteratively updating C_{33} [124, 125]. Applying a Newton linearization to this constraint gives

$$S^{33} + \frac{\partial S^{33}}{\partial C_{33}}\,\Delta C_{33} = S^{33} + \frac{1}{2}\,\mathbb{C}^{3333}\Delta C_{33} = 0. \tag{2.125}$$

From Equation (2.125) the following correction is obtained:

$$\Delta C_{33}^{(I)} = -2\,\frac{S_{(I)}^{33}}{\mathbb{C}_{(I)}^{3333}}, \tag{2.126}$$

with I denoting the iteration index. The updated component then reads

$$C_{33}^{(I+1)} = C_{33}^{(I)} + \Delta C_{33}^{(I)}. \tag{2.127}$$

After each update of $\mathbf{C}$, recompute $\mathbf{S}(\mathbf{C})$ and $\mathbb{C}(\mathbf{C})$ accordingly.

To illustrate the procedure, adopt the compressible neo-Hookean strain energy:

$$\psi = \frac{1}{2}\,\mu\left(J^{-2/3}\,\mathrm{tr}(\mathbf{C}) - 3\right) + \frac{1}{4}K\left(J^2 - 1 - 2\ln J\right), \tag{2.128}$$

where μ and K are the shear and bulk moduli. Using the relations in Equation (2.39) yields the three-dimensional stress and material tensors:

$$S^{ij} = \mu J^{-2/3}\left(G^{ij} - \frac{1}{3}\,\mathrm{tr}(\mathbf{C})\,\check{C}^{ij}\right) + \frac{1}{2}K\left(J^2 - 1\right)\check{C}^{ij}, \tag{2.129}$$

$$\begin{aligned}\mathbb{C}^{ijkl} = \frac{1}{9}\,\mu J^{-2/3}\,&\left(\mathrm{tr}(\mathbf{C})\left(2\check{C}^{ij}\check{C}^{kl} + 3\check{C}^{ik}\check{C}^{jl} + 3\check{C}^{il}\check{C}^{jk}\right) - 6\left(G^{ij}\check{C}^{kl} + \check{C}^{ij}G^{kl}\right)\right)\\ &+ K\left(J^2\check{C}^{ij}\check{C}^{kl} - \frac{1}{2}(J^2-1)\left(\check{C}^{ik}\check{C}^{jl} + \check{C}^{il}\check{C}^{jk}\right)\right).\end{aligned} \tag{2.130}$$

The iteration is initialized with

$$C^{(0)}_{ij} = g_{ij}: \qquad C^{(0)}_{ij} = \begin{bmatrix} g_{11} & g_{12} & 0\\ g_{21} & g_{22} & 0\\ 0 & 0 & 1\end{bmatrix}, \tag{2.131}$$

so that the in-plane entries remain fixed, $C_{\alpha\beta} \equiv g_{\alpha\beta}$, while only $C^{(I)}_{33}$ is updated.

After computing $C^{(I+1)}_{33}$ from Equations (2.126)–(2.127), update $\mathrm{tr}(\mathbf{C})^{(I+1)}$ and $J^{(I+1)}$, then evaluate the new tensors $S^{ij}_{(I+1)}$ and $\mathbb{C}^{ijkl}_{(I+1)}$. The loop proceeds until the plane-stress residual meets a prescribed tolerance. Finally, form the statically condensed tensor $\widehat{\mathbb{C}}$ via Equation (2.102), and retain only the in-plane components $S^{\alpha\beta}$ and $\widehat{\mathbb{C}}^{\alpha\beta\gamma\delta}$ for the membrane or shell formulation. As in the incompressible setting, any 3D material law may be employed for $\mathbf{S}$ and $\widehat{\mathbb{C}}$.

Chapter 3

Isogeometric Analysis

3.1 Introduction

Accurate geometric representation is a fundamental prerequisite for reliable analysis in computational mechanics, particularly when structural performance is sensitive to curvature and slenderness. In classical finite element analysis, the computational domain is usually discretized with low-order Lagrange elements, whereas Computer-Aided Design (CAD) models employ smooth spline descriptions such as B-splines and NURBS. This mismatch necessitates a CAD-to-mesh conversion that can introduce geometric errors, especially in curved or thin-walled structures. Moreover, mesh generation is often manual and time-consuming, becoming a bottleneck in high-fidelity analyses or optimization-driven studies with frequently changing geometries.

Isogeometric analysis (IGA) [126] addresses this gap by employing the same spline function spaces that define the CAD geometry (B-splines or NURBS) to approximate the solution fields. Aligning geometry and analysis in this way largely removes the need for CAD-to-mesh conversion and its geometric errors, while also providing practical numerical advantages. Higher interelement continuity improves the smoothness and accuracy of the approximation. The exact geometric representation provided by NURBS has been shown to significantly enhance the accuracy and reliability of pre-buckling analyses of shell structures [127]. In structural dynamics and stability analyses, the spectral properties of IGA lead to smoother and more reliable eigenmodes and critical loads [128, 129]. In addition, the native compatibility with CAD supports seamless design-to-analysis workflows and facilitates automated shape and topology optimization, thereby reducing preprocessing effort and enhancing overall efficiency. These advantages make IGA a robust and suitable framework for the membrane wrinkling analyses developed in this thesis. The subsequent review follows the standard exposition in [116, 126], to which the reader is referred for further details.

3.2 B-Spline Basis

Geometries in CAD as well as solutions in isogeometric analysis are commonly represented by splines, which are piecewise polynomial functions characterised by their smoothness. Among

them, B-splines form the fundamental building blocks; their rational extension, NURBS, will be presented in the next section.

The B-spline basis is defined recursively by the Cox-De Boor formula from a given knot vector. For a given polynomial degree p and number of basis functions n, the knot vector is

$$\Xi = \{\xi_1, \xi_2, \ldots, \xi_{n+p+1}\}, \qquad \xi_i \leq \xi_{i+1}, \tag{3.1}$$

where Ξ is a non-decreasing sequence of parametric coordinates that partitions the domain into knot spans. The length of the knot vector is therefore $n + p + 1$, consistent with the number of basis functions.

The smoothness of B-spline basis functions depends on the polynomial degree p and the multiplicity k of the knots. Inside each knot span (interval) the basis is C^∞ continuous, while across a simple knot ($k = 1$) the continuity reduces to C^{p-1}. If a knot value is repeated k times, the continuity at that location becomes C^{p-k}. For example, in the cubic case ($p = 3$), a simple knot yields C^2 continuity, whereas a triple knot ($k = 3$) leaves only C^0 continuity. This ability to systematically control smoothness across the domain makes B-splines particularly well-suited for structural formulations involving higher-order derivatives, such as Kirchhoff–Love shells. Compared to conventional finite elements based on C^0-continuous Lagrange polynomials, B-splines therefore provide superior approximation quality and enable more accurate representation of curvature-driven responses such as buckling and wrinkling.

In practice, the most common form is the open knot vector, in which the first and last knots are repeated $p + 1$ times. This construction enforces interpolation of the first and last points and provides well-defined tangents at both ends of the curve. Since these properties are typically required in geometric modeling, open knot vectors constitute the standard choice in CAD and, consequently, in isogeometric analysis.

As for basis functions, they are piecewise constants for $p = 0$,

$$N_{i,0}(\xi) = \begin{cases} 1, & \xi_i \leq \xi < \xi_{i+1} \\ 0, & \text{otherwise} \end{cases}, \tag{3.2}$$

and for $p > 0$ they satisfy

$$N_{i,p}(\xi) = \frac{\xi - \xi_i}{\xi_{i+p} - \xi_i} N_{i,p-1}(\xi) + \frac{\xi_{i+p+1} - \xi}{\xi_{i+p+1} - \xi_{i+1}} N_{i+1,p-1}(\xi). \tag{3.3}$$

The recursive definition of B-spline basis functions leads to several fundamental mathematical properties:

- Local support: each basis function is non-zero within the knot span $[\xi_i, \xi_{i+p+1}]$ and vanishes elsewhere.
- Non-negativity: the basis functions satisfy $N_{i,p}(\xi) \geq 0$ for all ξ.
- Partition of unity: $\sum_{i=1}^{n} N_{i,p}(\xi) = 1$ for all ξ.
- Linear independence: $\sum_{i=1}^{n} \alpha_i N_{i,p}(\xi) = 0 \quad \Leftrightarrow \quad \alpha_i = 0,\ i = 1, 2, \ldots, n.$

Beyond their mathematical properties, B-spline basis functions acquire geometric meaning

when combined with a set of control points. A B-spline curve of degree p is defined as

$$\mathbf{C}(\xi) = \sum_{i=1}^{n} N_{i,p}(\xi)\,\mathbf{P}_i, \tag{3.4}$$

where $\mathbf{P}_i \in \mathbb{R}^d$ are the control points in physical space. A B-spline curve lies within the convex hull of its control points; for an open knot vector it interpolates the first and last point, and its overall shape is guided by the control polygon connecting the control points, which provides an intuitive link between the mathematical definition of B-splines and their geometric representation.

B-spline curves exhibit several additional geometric properties that are essential in CAD and isogeometric analysis. In general, the control points are not interpolated, which provides flexibility in shaping the curve. Each control point influences at most $p + 1$ knot spans, ensuring local control of the geometry. The curve is C^∞ continuous within knot spans and reduces to C^{p-k} continuity at a knot of multiplicity k. Moreover, affine transformations of the curve can be performed directly by applying the same transformation to its control points. These properties, together with local support, non-negativity, and partition of unity, establish the strong geometric fidelity and numerical robustness.

3.3 NURBS Basis and Geometry

While B-spline basis functions are highly versatile in representing smooth curves and surfaces, they are inherently limited to polynomial geometry. For example, even simple conic sections such as circles and ellipses cannot be exactly represented using polynomial B-splines. To overcome this limitation, rational basis functions are introduced. By extending B-splines to include a set of weights associated with each control point, one obtains Non-Uniform Rational B-splines (NURBS), which significantly enhances geometric modeling capabilities without sacrificing the favorable properties of the underlying B-spline framework.

A NURBS basis function is defined as a weighted rational form of a B-spline basis:

$$R_{i,p}(\xi) = \frac{N_{i,p}(\xi) w_i}{\sum_{i=1}^{n} N_{i,p}(\xi) w_i}. \tag{3.5}$$

Here, $N_{i,p}(\xi)$ is the standard B-spline basis of degree p, and w_i is the weight associated with the i-th control point. When all weights are equal, the NURBS basis reduces to the standard B-spline basis.

Using these rational functions, a NURBS curve is constructed as:

$$\mathbf{C}(\xi) = \sum_{i=1}^{n} R_{i,p}(\xi)\,\mathbf{P}_i. \tag{3.6}$$

This rational formulation enables the exact representation of geometries that B-splines can only approximate, including circular arcs, ellipses, parabolas, and other conic sections.

In the case of surfaces, a NURBS surface is constructed by tensor product of NURBS basis functions in two parametric directions ξ and η:

$$R_{i,j}^{p,q}(\xi,\eta) = \frac{N_{i,p}(\xi)M_{j,q}(\eta)w_{i,j}}{\sum_{i=1}^{n}\sum_{j=1}^{m} N_{i,p}(\xi)M_{j,q}(\eta)w_{i,j}}. \tag{3.7}$$

Here, $N_{i,p}(\xi)$ and $M_{j,q}(\eta)$ denote the univariate B-spline basis functions of degrees p and q in the ξ- and η-directions, respectively.

The corresponding surface geometry is therefore given by

$$\mathbf{S}(\xi,\eta) = \sum_{i=1}^{n}\sum_{j=1}^{m} R_{i,j}^{p,q}(\xi,\eta)\,\mathbf{P}_{i,j}. \tag{3.8}$$

This construction generalizes further to three parametric directions (ξ,η,ζ), yielding NURBS solids, which provide exact descriptions of standard CAD primitives such as spheres, cylinders, and swept volumes. For brevity, the explicit expressions of the corresponding basis functions and solid geometry are omitted here, the reader is referred to [126].

From the perspective of numerical analysis, NURBS retain key properties of B-spline functions, such as local support, non-negativity, and partition of unity. However, unlike B-splines, NURBS basis functions are rational, and their derivatives involve both numerator and denominator terms, which require additional care in integration and differentiation. Despite this, the benefits offered by geometric exactness justify the increased computational complexity in many engineering applications.

In isogeometric analysis, the use of NURBS not only ensures that the computational geometry coincides exactly with the CAD model, but also provides high-regularity basis functions that are essential in curvature-dependent formulations such as thin shell analysis. This dual role of preserving both geometry and analysis smoothness makes NURBS indispensable in practical IGA implementations.

3.4 Refinement Strategies in Isogeometric Analysis

Refinement is a fundamental tool in numerical analysis for improving solution accuracy and controlling approximation error. In classical finite element methods, refinement typically involves either increasing the number of elements (h-refinement) or raising the polynomial degree of the basis functions (p-refinement). Isogeometric analysis not only inherits these two refinement modes but also introduces a third one, known as k-refinement.

In h-refinement, the knot vector is augmented by inserting additional knot values. This increases the number of basis functions and control points, thereby enhancing the resolution of

the function space. Importantly, the geometry defined by the NURBS representation remains exact under h-refinement due to the affine invariance and partition of unity properties of the basis functions. Since this operation does not alter the polynomial degree, the continuity across element interfaces remains at C^{p-1}; only repeated knots reduce it further according to their multiplicity.

By contrast, in p-refinement, the polynomial degree of the basis functions is elevated, increasing the number of basis functions and control points but preserving the number of elements. This is particularly advantageous in structural applications where derivative information, such as curvature, plays a critical role.

A defining feature of isogeometric analysis is the ability to perform k-refinement, which combines degree elevation with knot insertion. The order in which these two operations are applied is critical for the resulting continuity. For instance, if degree elevation is performed first, from $p = 2$ to $p = 3$, then inserting a new knot yields $C^{p-k} = C^{3-1} = C^2$ continuity at this knot. By contrast, if the knot is inserted first while the basis is still quadratic ($p = 2$), the resulting continuity is $C^{p-k} = C^{2-1} = C^1$ at this knot. Subsequent degree elevation does not increase this continuity, as the process preserves all existing continuity levels. This illustrates that k-refinement corresponds to performing degree elevation prior to knot insertion [130], ensuring that the resulting function spaces achieve the highest possible continuity for a given polynomial degree and mesh resolution. Such enhanced smoothness is particularly advantageous in applications involving thin shells or beams, where curvature information is essential for accurately capturing bending behavior.

Although the aforementioned refinement strategies provide strong global approximation capabilities, they do not inherently offer local adaptivity. In many structural problems such as those involving localized loading, contact, or crack propagation, it is desirable to refine the mesh only in regions of interest. Standard tensor-product B-spline and NURBS constructions are inherently global: inserting a knot in one part of the domain generally affects the entire mesh, which can lead to unnecessary computational cost.

To address this limitation, locally refined splines (LR-splines) have been developed as a generalization of tensor-product B-splines. In LR-spline spaces, refinement is carried out by introducing new line segments into the parametric mesh, effectively subdividing selected knot spans while leaving the rest of the domain unchanged. This allows for localized mesh densification without sacrificing linear independence or continuity. Importantly, LR-splines preserve many of the desirable features of B-splines, including local support, affine invariance, and partition of unity, while providing the flexibility needed for adaptive refinement strategies.

In the context of isogeometric analysis, refinement strategies are important in balancing accuracy, efficiency, and geometric fidelity. Global techniques such as k-refinement provide smooth and robust discretizations for problems governed by curvature-dependent energies, whereas local methods like LR-splines enable focused resolution enhancement in areas where solution features demand higher accuracy. The availability of both global and local refinement tools within the isogeometric framework allows for adaptive and efficient modeling of complex structural behavior.

3.5 Static and Dynamic Solution Methods

This section summarizes the numerical procedures employed in this work. Static analyses are solved using the Newton–Raphson iterative scheme, whereas dynamic analyses are performed with the generalized-α time integration method. The following subsections present the derivations and formulations of these methods with the expressions in Section 2.3.3.

3.5.1 Newton–Raphson Iteration Method

The Newton–Raphson method is widely used in nonlinear analysis due to its fast quadratic convergence properties. It represents the standard iterative scheme for nonlinear equilibrium problems and is therefore employed in this work.

After discretization of the weak form, as introduced in Section 2.3.3, the equilibrium equations can be expressed in terms of the internal and external nodal force vectors. To facilitate incremental loading, the external load is represented by a constant reference vector $\mathbf{F}^{\text{ext}}$, which specifies the final load distribution to be applied. A scalar load factor λ^{load} is introduced to control its magnitude, such that

$$\mathbf{F}^{\text{ext}}(\lambda^{\text{load}}) = \lambda^{\text{load}}\,\mathbf{F}^{\text{ext}}. \tag{3.9}$$

At the beginning of the analysis, $\lambda^{\text{load}} = 0$ corresponds to the unloaded state, and $\lambda^{\text{load}} = 1$ corresponds to the full reference load. The load is thus applied gradually by increasing λ^{load} step by step. In addition, it is assumed that $\mathbf{F}^{\text{ext}}$ is independent of the displacement vector $\mathbf{u}$, meaning that the load distribution remains fixed during the analysis. Under this assumption, the nonlinear algebraic system takes the form

$$\mathbf{R}(\mathbf{u}, \lambda^{\text{load}}) = \mathbf{F}^{\text{int}}(\mathbf{u}) - \lambda^{\text{load}}\,\mathbf{F}^{\text{ext}} = \mathbf{0}, \tag{3.10}$$

where $\mathbf{R}$ is the residual vector that measures the imbalance between internal and external forces.

Since the internal force vector depends nonlinearly on the displacement field, the residual cannot be solved directly and requires an iterative procedure. Expanding the residual in a first-order Taylor series about the current iterate $\mathbf{u}_n$ yields

$$\mathbf{R}(\mathbf{u}_n + \Delta\mathbf{u}_n) \approx \mathbf{R}(\mathbf{u}_n) + \mathbf{K}(\mathbf{u}_n)\,\Delta\mathbf{u}_n, \tag{3.11}$$

with the tangent stiffness matrix $\mathbf{K}(\mathbf{u})$ defined as the derivative of the residual. Since the external force vector is independent of the displacement, no contribution arises from the external part. The Newton update equation then follows as

$$\mathbf{K}(\mathbf{u}_n)\,\Delta\mathbf{u}_n = -\mathbf{R}(\mathbf{u}_n, \lambda^{\text{load}}), \tag{3.12}$$

and the displacement vector is updated according to

$$\mathbf{u}_{n+1} = \mathbf{u}_n + \Delta\mathbf{u}_n. \tag{3.13}$$

The iterations are repeated until convergence is achieved. A typical convergence criterion requires that the residual norm becomes sufficiently small relative to the applied load,

$$\frac{\|\mathbf{R}(\mathbf{u}_n, \lambda^{\text{load}})\|}{\|\lambda^{\text{load}}\,\mathbf{F}^{\text{ext}}\|} < \varepsilon_{\text{tol}}, \tag{3.14}$$

where ε_{tol} is a prescribed tolerance. By consistently evaluating the tangent stiffness matrix, the Newton–Raphson method achieves quadratic convergence in the vicinity of the solution, making it an efficient and robust tool for nonlinear analysis. Besides standard load control

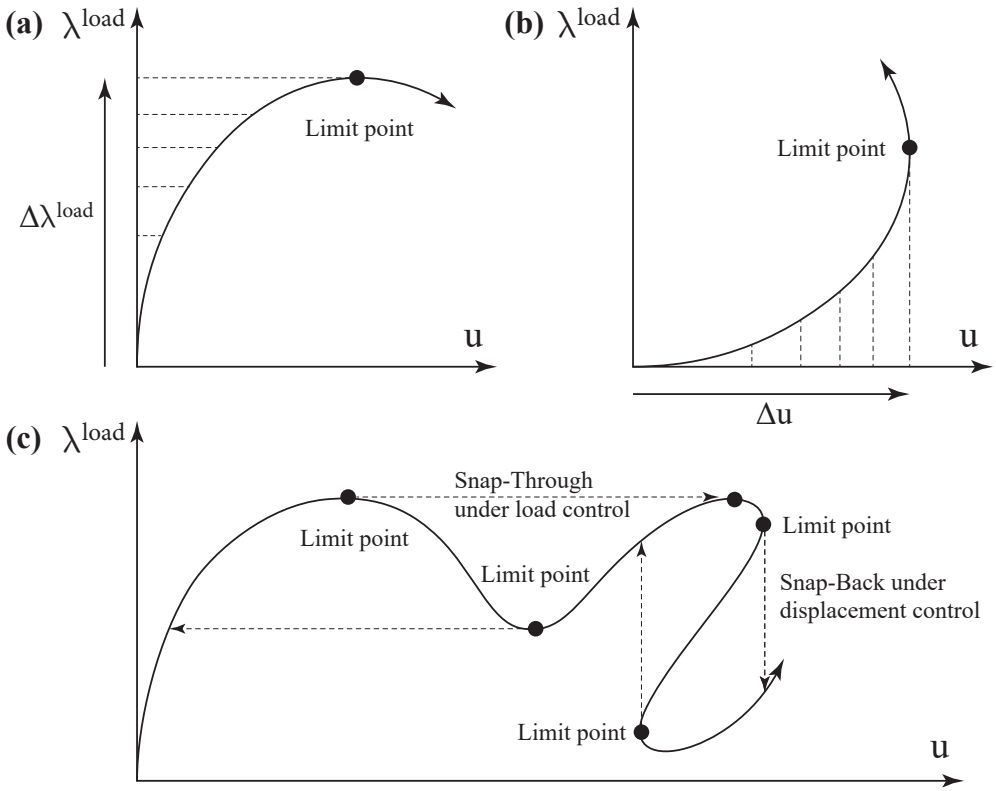

Figure 3.1.: Instabilities in Newton's method [131]: (a) a system unstable under load control (snap–through), (b) a system unstable under displacement control (snap–back), (c) a system unstable under both load and displacement control.

introduced above, displacement control is also frequently adopted, in which a specific displacement component is prescribed incrementally and the associated reactions are obtained from the solution.

Despite its efficiency, the Newton iteration method may fail to follow the true equilibrium path once the tangent stiffness approaches zero. This shortcoming stems from its formulation: the load parameter is enforced to vary monotonically from one increment to the next, reflecting

the usual practice in structural analysis that external loads are increased monotonically. Consequently, when the equilibrium path contains a limit point, the algorithm cannot remain on the equilibrium curve.

Such difficulties become pronounced in problems governed by instability or material softening. Classical examples include buckling analyses and nonlinear materials that exhibit work softening; similar effects may also arise from strong geometric nonlinearities in finite deformation problems. In these cases, Newton's method typically loses the equilibrium path once the structure passes a limit point.

Under load control this phenomenon appears as a snap–through instability, while under displacement control it may appear as a snap–back instability, and in some cases both occur simultaneously, as illustrated in Figure 3.1. These issues underline that, although Newton's method is highly effective up to the critical point, it cannot capture the post-critical response. Path-following strategies, such as the arc-length method, are therefore required. The reader is referred to standard references [132].

3.5.2 Generalized-α Method

For the dynamic analysis, the generalized-α method is adopted. This implicit time integration scheme provides second-order accuracy together with controlled numerical dissipation, making it particularly suitable for nonlinear structural dynamics.

The semi-discrete residual form of the governing equation is:

$$\mathbf{R} = \mathbf{M}_d\ddot{\mathbf{u}} + \mathbf{C}_d\dot{\mathbf{u}} + \mathbf{F}^{\text{int}} - \mathbf{F}^{\text{ext}} = \mathbf{0}, \tag{3.15}$$

where $\dot{\mathbf{u}}$ and $\ddot{\mathbf{u}}$ are the first and second time derivatives (velocity and acceleration) of the displacement vector $\mathbf{u}$, and $\mathbf{M}_d$ is the consistent mass matrix, defined by:

$$M_{rs}^d = \rho t \int_A \frac{\partial \mathbf{u}}{\partial u_r} \cdot \frac{\partial \mathbf{u}}{\partial u_s} \, \mathrm{d}A, \tag{3.16}$$

with ρ denoting the material density and t the thickness parameter. Here, $\mathbf{C}_d$ represents the damping matrix.

In the generalized-α method, the primary variables are not evaluated directly at the discrete time levels τ_n and τ_{n+1}. Instead, they are interpolated at an intermediate stage indexed by α, using the weighting parameters α_f and α_m. This leads to the following relations:

$$\mathbf{u}_\alpha = \alpha_f \mathbf{u}_{n+1} + (1 - \alpha_f)\mathbf{u}_n, \tag{3.17}$$

$$\dot{\mathbf{u}}_\alpha = \alpha_f \dot{\mathbf{u}}_{n+1} + (1 - \alpha_f)\dot{\mathbf{u}}_n, \tag{3.18}$$

$$\ddot{\mathbf{u}}_\alpha = \alpha_m \ddot{\mathbf{u}}_{n+1} + (1 - \alpha_m)\ddot{\mathbf{u}}_n. \tag{3.19}$$

The displacement and velocity at time step τ_{n+1} are updated according to the Newmark scheme, which gives

$$\mathbf{u}_{n+1} = \mathbf{u}_n + \Delta\tau\, \dot{\mathbf{u}}_n + \frac{1}{2}(\Delta\tau)^2 \left((1-2\beta)\ddot{\mathbf{u}}_n + 2\beta\ddot{\mathbf{u}}_{n+1}\right), \tag{3.20}$$

$$\dot{\mathbf{u}}_{n+1} = \dot{\mathbf{u}}_n + \Delta\tau \left((1-\gamma)\ddot{\mathbf{u}}_n + \gamma\ddot{\mathbf{u}}_{n+1}\right). \tag{3.21}$$

Here, $\Delta\tau = \tau_{n+1} - \tau_n$ denotes the time increment, and β and γ are the standard Newmark parameters. With these definitions, the internal and external force vectors are consistently evaluated at the interpolated configuration:

$$\mathbf{F}^{\text{int}}_{\alpha} = \mathbf{F}^{\text{int}}(\mathbf{u}_{\alpha}), \tag{3.22}$$

$$\mathbf{F}^{\text{ext}}_{\alpha} = \mathbf{F}^{\text{ext}}(\mathbf{u}_{\alpha}). \tag{3.23}$$

For the special case of external loads that are independent of displacement, the interpolation reduces to a linear combination of the values at the discrete time levels:

$$\mathbf{F}^{\text{ext}}_{\alpha} = \alpha_f \mathbf{F}^{\text{ext}}_{n+1} + (1-\alpha_f)\mathbf{F}^{\text{ext}}_{n}. \tag{3.24}$$

Linearization of the residual at the intermediate stage yields the incremental relation

$$\frac{\mathrm{d}\mathbf{R}_{\alpha}}{\mathrm{d}\ddot{\mathbf{u}}_{n+1}}\,\Delta\ddot{\mathbf{u}}_{n+1} = -\mathbf{R}_{\alpha}, \tag{3.25}$$

which serves as the basis for the iterative solution procedure.

In the presence of viscous damping and assuming a constant damping matrix, the above expression takes the form

$$\left(\alpha_m\mathbf{M}_d + \alpha_f\gamma\Delta\tau\,\mathbf{C}_d + \alpha_f\beta(\Delta\tau)^2\mathbf{K}(\mathbf{u}_{\alpha})\right)\Delta\ddot{\mathbf{u}}_{n+1} = -\mathbf{M}_d\ddot{\mathbf{u}}_{\alpha} - \mathbf{C}_d\dot{\mathbf{u}}_{\alpha} - \mathbf{F}^{\text{int}}_{\alpha} + \mathbf{F}^{\text{ext}}_{\alpha}, \tag{3.26}$$

where $\mathbf{K}(\mathbf{u}_{\alpha})$ denotes the tangent stiffness matrix evaluated at the interpolated configuration.

Alternatively, the residual may also be linearized directly with respect to the displacement vector, leading to

$$\frac{\mathrm{d}\mathbf{R}_{\alpha}}{\mathrm{d}\mathbf{u}_{n+1}}\,\Delta\mathbf{u}_{n+1} = -\mathbf{R}_{\alpha}. \tag{3.27}$$

Once the displacement increment is known, the corresponding acceleration and velocity at time step τ_{n+1} can be updated through the following expressions:

$$\ddot{\mathbf{u}}_{n+1} = \frac{1}{\beta(\Delta\tau)^2}\left(\mathbf{u}_{n+1} - \mathbf{u}_n\right) - \frac{1}{\beta\Delta\tau}\,\dot{\mathbf{u}}_n - \left(\frac{1}{2\beta} - 1\right)\ddot{\mathbf{u}}_n, \tag{3.28}$$

$$\dot{\mathbf{u}}_{n+1} = \frac{\gamma}{\beta\Delta\tau}(\mathbf{u}_{n+1} - \mathbf{u}_n) + \left(1 - \frac{\gamma}{\beta}\right)\dot{\mathbf{u}}_n + \left(1 - \frac{\gamma}{2\beta}\right)\Delta\tau\,\ddot{\mathbf{u}}_n. \tag{3.29}$$

If the damping matrix is again assumed constant, the linearized system based on displacement

increments becomes

$$\left(\alpha_m \frac{\mathbf{M}_d}{\beta(\Delta\tau)^2} + \alpha_f \frac{\gamma}{\beta\Delta\tau}\mathbf{C}_d + \alpha_f \mathbf{K}(\mathbf{u}_\alpha)\right)\Delta\mathbf{u}_{n+1} = -\mathbf{M}_d\ddot{\mathbf{u}}_\alpha - \mathbf{C}_d\dot{\mathbf{u}}_\alpha - \mathbf{F}_\alpha^{\text{int}} + \mathbf{F}_\alpha^{\text{ext}}. \tag{3.30}$$

The parameters of the generalized-α method are expressed in terms of the numerical dissipation parameter $\rho_\infty \in [0,1]$, which governs the numerical dissipation of the high-frequency response. They are given by

$$\alpha_m = \frac{2-\rho_\infty}{1+\rho_\infty}, \qquad \alpha_f = \frac{1}{1+\rho_\infty}, \qquad \beta = \frac{(1-\alpha_f+\alpha_m)^2}{4}, \qquad \gamma = \frac{1}{2} - \alpha_f + \alpha_m. \tag{3.31}$$

In the present work, a value of $\rho_\infty = 0.5$ is adopted, corresponding to a moderate level of high-frequency dissipation while retaining second-order accuracy. To clarify the role of ρ_∞, it is instructive to examine the limiting cases of the scheme. For $\rho_\infty = 1$, the method yields $\alpha_m = \alpha_f = 0.5$, which removes numerical dissipation entirely and reduces the formulation to the classical average acceleration scheme of the Newmark family. In this case, the integration is non-dissipative and energy-conserving, making it suitable when preservation of the full dynamic response is required. In the opposite limit $\rho_\infty = 0$, the parameters become $\alpha_m = 2$ and $\alpha_f = 1$, which produces the maximally dissipative variant of the scheme. This configuration suppresses all high-frequency components and is closely related to the Hilber–Hughes–Taylor-α method (HHT), which was originally proposed as a dissipative extension of the Newmark scheme. The generalized-α method can therefore be viewed as a unifying framework that interpolates between these two extremes, ranging from a non-dissipative average acceleration scheme to a strongly dissipative HHT-type scheme. In practical terms, the numerical dissipation parameter ρ_∞ (spectral radius) serves as a user-defined control parameter that balances accuracy and robustness in nonlinear dynamic simulations.

Chapter 4

Fundamentals of Tension-Field Wrinkling Models

This chapter outlines the theoretical foundation of wrinkling models formulated within the framework of tension-field theory. Despite differences in specific formulations, most existing approaches follow a common modeling structure consisting of three key components: (1) the classification of the membrane state using a wrinkling criterion; (2) the enforcement of the uniaxial tension condition; and (3) the determination of the wrinkle direction, which is subsequently incorporated into the formulation to modify the stress and material response.

The structure of this chapter is as follows. Section 4.1 summarizes the general procedure commonly adopted in wrinkling models. The three modeling components are then addressed individually in Section 4.2, which reviews established wrinkling criteria and compares their respective merits; Section 4.3, which discusses the uniaxial tension condition and its role in wrinkling formulations; and Section 4.4, which presents a reference model from the literature, used both as an illustrative example for wrinkle direction determination and as a benchmark in the numerical studies.

4.1 General Procedure of Wrinkling Models

The overall procedure is illustrated in Algorithm 1, which summarizes the Gauss-point-level implementation of the wrinkling model within each iteration step of a nonlinear analysis.

In this procedure, the strain tensor $\mathbf{E}$ is obtained from the deformation field computed in the previous iteration. Together with the original material tensor $\mathbb{C}$, this strain is used to evaluate the second Piola–Kirchhoff stress tensor $\mathbf{S}$. The membrane state is then identified as either taut, wrinkled, or slack, according to a prescribed wrinkling criterion involving the principal stresses $S_{1/2}$ and principal strains $E_{1/2}$, under the ordering assumption $S_1 \geq S_2$, and $E_1 \geq E_2$.

Upon determination of the membrane state, the constitutive response is adjusted accordingly. Here, $\mathbf{S}'$ and $\mathbb{C}'$ denote the stress and material tensors computed specifically for the wrinkled state, based on a wrinkling formulation. In contrast, $\mathbf{S}_{\text{eff}}$ and $\mathbb{C}_{\text{eff}}$ represent the state-dependent response used in the numerical procedure. The symbol $\mathbb{O}$ denotes a fourth-order zero tensor, whose components are all zeros.

Algorithm 1: Wrinkling model algorithm at Gauss-point level

Input : Strain tensor $\mathbf{E}$; original material tensor $\mathbb{C}$
Output The effective stress tensor $\mathbf{S}_{\text{eff}}$ and material tensor $\mathbb{C}_{\text{eff}}$
:
Compute the stress tensor $\mathbf{S}$ from $\mathbf{E}$ and $\mathbb{C}$;
Extract principal stresses S_1, S_2 and principal strains E_1, E_2;
Determine the membrane state using a wrinkling criterion;
if *taut* **then**
  $\mathbf{S}_{\text{eff}} = \mathbf{S}, \quad \mathbb{C}_{\text{eff}} = \mathbb{C};$
else if *slack* **then**
  $\mathbf{S}_{\text{eff}} = \mathbf{0}, \quad \mathbb{C}_{\text{eff}} = \mathbb{O};$
else if *wrinkled* **then**
  Determine the wrinkle direction θ;
  $\mathbf{S}_{\text{eff}} = \mathbf{S}'(\theta), \quad \mathbb{C}_{\text{eff}} = \mathbb{C}'(\theta);$
return $\mathbf{S}_{\text{eff}}, \mathbb{C}_{\text{eff}}$

In the taut state, the stress and material tensors are directly computed from the standard membrane theory without modification. In the wrinkled state, compressive stress components are removed to ensure the physical admissibility of the solution. This is typically achieved through modified constitutive laws or kinematics, as briefly discussed in Chapter 1.

In the slack state, both tensors are set to zero. However, in practical finite element implementations, assigning strictly null values may cause numerical issues such as stiffness matrix singularity or poor convergence. To address this, small regularizations could be introduced. Alternatively, several dedicated formulations have been proposed for slack-state behavior; see [65, 81, 108] for representative examples.

4.2 Membrane States and Wrinkling Criteria

In wrinkling models constructed within the framework of tension-field theory, a fundamental step is to classify the membrane state. The membrane is typically considered to be in one of three possible states: taut, wrinkled, slack. These membrane states are illustrated in Figure 4.1. In the literature, three types of wrinkling criteria have been proposed to distinguish between these states. To the best of the author's knowledge, the earliest criterion was proposed by [73], based on the principal stress. Later, [92] introduced a criterion based on principal strain. Subsequently, a mixed criterion was developed by [99], which incorporates both stress and strain. Among these, the mixed criterion is the most widely used, as it offers a more comprehensive and physically accurate judgment of the membrane state.

A summary of the corresponding classification rules is provided in Table 4.1. For an isotropic St. Venant–Kirchhoff material under the plane stress condition, the relationship between

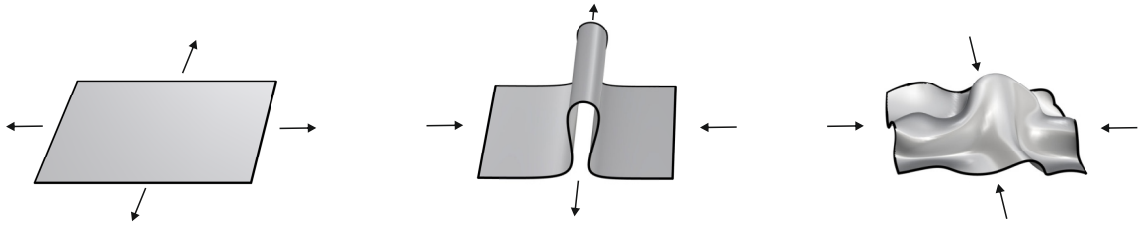

(a) Taut **(b)** Wrinkled **(c)** Slack

Figure 4.1.: Illustration of membrane states [115]: (a) taut, (b) wrinkled, and (c) slack.

principal stresses and principal strains is given by

$$S_1 = \frac{E}{1-\nu^2}(E_1 + \nu E_2), \quad S_2 = \frac{E}{1-\nu^2}(E_2 + \nu E_1). \tag{4.1}$$

Table 4.1.: Overview of wrinkling criteria for different membrane states.

Membrane state	Principal stress criterion	Principal strain criterion	Mixed criterion
Taut	$S_2 > 0$	$E_2 > 0$	$S_2 > 0$
Wrinkled	$S_2 \leq 0$ and $S_1 > 0$	$E_2 \leq 0$ and $E_1 > 0$	$S_2 \leq 0$ and $E_1 > 0$
Slack	$S_1 \leq 0$	$E_1 \leq 0$	$E_1 \leq 0$

Because these criteria differ in formulation, they can lead to inconsistent classifications in complex deformation scenarios, as observed by [93, 94]. Figure 4.2 visualizes these differences by mapping representative membrane states into the principal stress–strain space.

A typical misclassification of the principal stress criterion occurs when the principal strains satisfy

$$E_1 > 0, \quad E_2 < 0, \quad E_1 + \nu E_2 < 0. \tag{4.2}$$

This combination corresponds to a region on the left side of the line with slope $-\frac{1}{\nu}$ in Figure 4.2(a). According to Equation (4.1), the condition $E_1 + \nu E_2 < 0$ leads to $S_1 < 0$, and, under the ordering assumption $S_1 \geq S_2$, it follows that $S_2 < 0$ as well. The stress criterion therefore classifies the membrane as slack. However, the strain state reveals that $E_1 > 0$. As noted by [99], if one of the principal values of the strain tensor is positive, there exist directions in which the material is stretched, and consequently, the stress tensor must contain positive components. Therefore, this configuration should not be simply categorized as slack, but rather identified as wrinkled.

By contrast, the principal strain criterion exhibits limitations in identifying taut configurations, particularly in cases where the Poisson effect leads to compressive strain in one direction, despite the membrane remaining under tension, as in the region above the line with slope $-\nu$ in Figure 4.2(b). In such cases, when

$$E_1 > 0, \quad E_2 < 0, \quad E_2 + \nu E_1 > 0, \tag{4.3}$$

the strain criterion identifies the configuration as wrinkled. However, the corresponding stress

state is

$$S_1 > 0, \quad S_2 > 0, \tag{4.4}$$

indicating that the membrane is subject to tensile stress in both principal directions and should therefore be regarded as taut.

The mixed criterion aims to improve upon the aforementioned issues by incorporating both principal stress and strain. As depicted in Figure 4.2(c), it performs well in the transitional cases. However, as pointed out in [95], the classification of membrane states cannot rely solely on current strain or stress, and must account for their evolution; based on this observation, nine different states were proposed to distinguish wrinkling more accurately. Despite this, the mixed criterion remains the most widely adopted method in the literature, owing to its conceptual simplicity and reasonable performance across a broad range of applications.

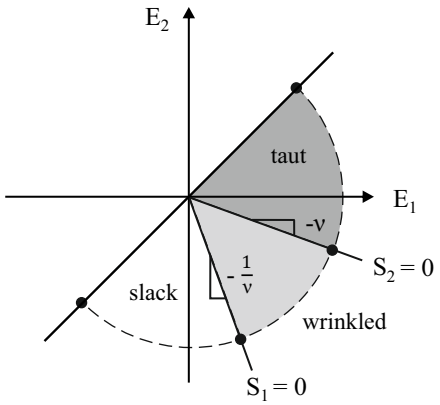

(a) Principal stress criterion

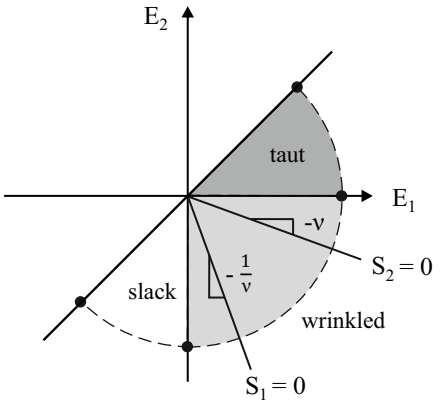

(b) Principal strain criterion

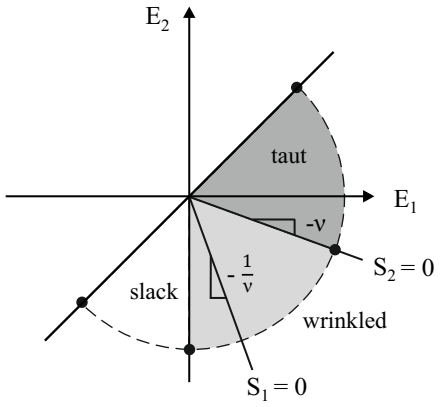

(c) Mixed criterion

Figure 4.2.: Classification of membrane states in the principal strain space based on different wrinkling criteria.

4.3 Uniaxial Tension Condition

Most existing wrinkling models for membranes are formulated based on the uniaxial tension condition, which originates from classical tension-field theory. This theory postulates that, in wrinkled regions, the stress component along the wrinkle direction is completely released, while tension is sustained only in the direction perpendicular to the wrinkles. The present section revisits this fundamental assumption and establishes its mathematical formulation.

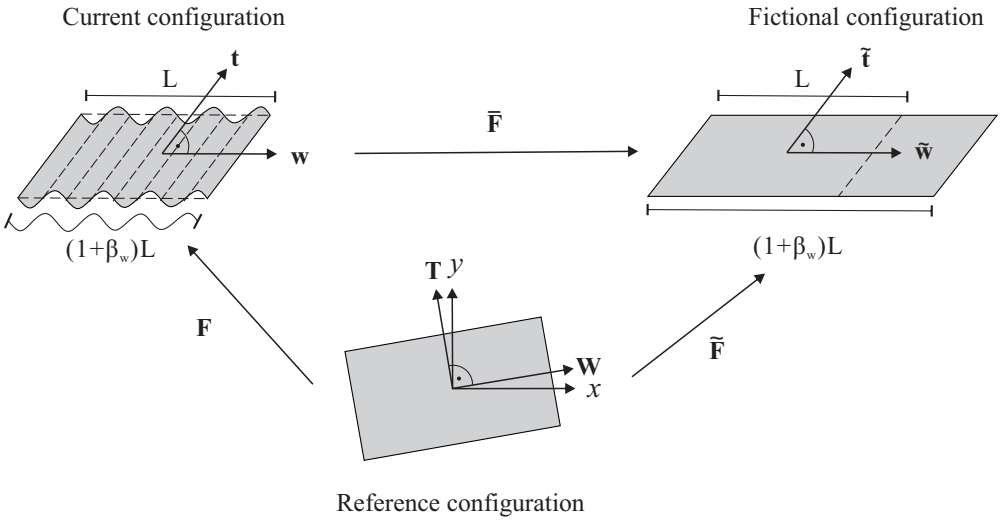

Figure 4.3.: Transformations among the various configurations of a membrane.

As illustrated in Figure 4.3, the modeling framework involves three distinct configurations: the reference configuration, the current configuration representing the actual wrinkled surface, and a fictitious configuration in which the membrane is artificially flattened by introducing an in-plane virtual extension. The actual deformation from the reference configuration to the current configuration is described by the standard deformation gradient $\mathbf{F}$. To represent the wrinkled region as a locally planar surface, a modified deformation gradient $\tilde{\mathbf{F}}$ is introduced by composing an artificial stretch tensor $\bar{\mathbf{F}}$ with $\mathbf{F}$, such that

$$\tilde{\mathbf{F}} = \bar{\mathbf{F}}\,\mathbf{F} = (\mathbf{I} + \beta_w\,\mathbf{w} \otimes \mathbf{w})\,\mathbf{F}, \tag{4.5}$$

where $\mathbf{I}$ is the second-order identity tensor, β_w is a scalar parameter that characterizes the fictitious extension in the wrinkle direction, and $\mathbf{w}$ is a unit vector aligned with the wrinkle direction in the current configuration. This formulation was originally proposed by [99] as a means to describe wrinkled membranes through a fictitious in-plane stretch. Owing to its simplicity and physical interpretability, this construction has attracted widespread attention and has been employed in a broad range of wrinkling models to enforce uniaxial tension conditions in a geometrically consistent manner.

The wrinkle direction in each configuration is denoted by $\mathbf{w}$, $\tilde{\mathbf{w}}$, and $\mathbf{W}$, corresponding to the current, fictitious, and reference configurations, respectively. These vectors satisfy the

pull-back relation

$$\mathbf{W} = \mathbf{F}^{\mathrm{T}}\mathbf{w} = \tilde{\mathbf{F}}^{\mathrm{T}}\tilde{\mathbf{w}}, \tag{4.6}$$

ensuring consistent mapping across configurations. The vector $\mathbf{W}$ can be expressed in terms of the contravariant basis vectors $\mathbf{G}^{\alpha}$ of the reference configuration as

$$\mathbf{W} = W_{\alpha}\,\mathbf{G}^{\alpha}, \quad \text{with} \quad W_1 = -W\sin\theta, \quad W_2 = W\cos\theta, \tag{4.7}$$

where θ denotes the angle of the wrinkle direction. The coefficient W is defined such that the corresponding spatial vector $\mathbf{w}$ has unit length.

To construct a local orthonormal basis, a second vector $\mathbf{T}$ is introduced such that $\mathbf{T}\cdot\mathbf{W} = 0$. It is written similarly as

$$\mathbf{T} = T_{\alpha}\,\mathbf{G}^{\alpha}, \quad \text{with} \quad T_1 = T\cos\theta, \quad T_2 = T\sin\theta, \tag{4.8}$$

and the coefficient T is chosen such that the corresponding spatial vector $\mathbf{t}$ is a unit vector. The vector $\mathbf{T}$ is related to its spatial counterparts via

$$\mathbf{T} = \mathbf{F}^{\mathrm{T}}\mathbf{t} = \tilde{\mathbf{F}}^{\mathrm{T}}\tilde{\mathbf{t}}, \tag{4.9}$$

where $\mathbf{t}$ and $\tilde{\mathbf{t}}$ are unit vectors orthogonal to $\mathbf{w}$ and $\tilde{\mathbf{w}}$, respectively, in the current and fictitious configurations. The pair $(\mathbf{W}, \mathbf{T})$ thus defines a local orthonormal basis in the reference configuration, providing a consistent framework for projecting stress components in the wrinkling formulation.

According to the classical tension-field theory, a wrinkled membrane is assumed to be in a uniaxial tension state in which stress is entirely released along the wrinkle direction. In the present formulation, this assumption is imposed in the fictitious configuration by requiring that the modified Cauchy stress tensor $\tilde{\boldsymbol{\sigma}}$ satisfies

$$\tilde{\boldsymbol{\sigma}}\,\tilde{\mathbf{w}} = \mathbf{0}, \tag{4.10}$$

indicating that there is no stress component in the direction $\tilde{\mathbf{w}}$. This condition can be expressed equivalently in scalar form as

$$\tilde{\mathbf{w}}\cdot\tilde{\boldsymbol{\sigma}}\,\tilde{\mathbf{w}} = 0, \qquad \tilde{\mathbf{t}}\cdot\tilde{\boldsymbol{\sigma}}\,\tilde{\mathbf{w}} = 0. \tag{4.11}$$

To reformulate this condition in the reference configuration, the modified Cauchy stress $\tilde{\boldsymbol{\sigma}}$ is expressed in terms of the modified second Piola–Kirchhoff stress $\mathbf{S}'$ by means of the standard push-forward relation

$$\tilde{\boldsymbol{\sigma}} = \frac{1}{\det\tilde{\mathbf{F}}}\,\tilde{\mathbf{F}}\,\mathbf{S}'\,\tilde{\mathbf{F}}^{\mathrm{T}}. \tag{4.12}$$

Substituting this expression, together with Equations (4.6) and (4.9), into Equation (4.11),

yields

$$\tilde{\mathbf{w}} \cdot \tilde{\boldsymbol{\sigma}}\, \tilde{\mathbf{w}} = \frac{1}{\det \tilde{\mathbf{F}}} \left(\tilde{\mathbf{F}}^{\mathrm{T}} \tilde{\mathbf{w}}\right) \cdot \mathbf{S}' \left(\tilde{\mathbf{F}}^{\mathrm{T}} \tilde{\mathbf{w}}\right) = \frac{1}{\det \tilde{\mathbf{F}}}\, \mathbf{W} \cdot \mathbf{S}'\, \mathbf{W}, \tag{4.13}$$

$$\tilde{\mathbf{t}} \cdot \tilde{\boldsymbol{\sigma}}\, \tilde{\mathbf{w}} = \frac{1}{\det \tilde{\mathbf{F}}} \left(\tilde{\mathbf{F}}^{\mathrm{T}} \tilde{\mathbf{t}}\right) \cdot \mathbf{S}' \left(\tilde{\mathbf{F}}^{\mathrm{T}} \tilde{\mathbf{w}}\right) = \frac{1}{\det \tilde{\mathbf{F}}}\, \mathbf{T} \cdot \mathbf{S}'\, \mathbf{W}. \tag{4.14}$$

It follows that the uniaxial tension condition in the fictitious configuration is equivalently expressed in the reference configuration as

$$\mathbf{W} \cdot \mathbf{S}'\, \mathbf{W} = 0, \qquad \mathbf{T} \cdot \mathbf{S}'\, \mathbf{W} = 0. \tag{4.15}$$

Using the explicit expressions of $\mathbf{W}$ and $\mathbf{T}$, the conditions in Equation (4.15) can be expressed in component form as

$$\mathbf{W} \cdot \mathbf{S}'\, \mathbf{W} = W_\alpha\, S'^{\alpha\beta}\, W_\beta, \tag{4.16}$$

$$\mathbf{T} \cdot \mathbf{S}'\, \mathbf{W} = T_\alpha\, S'^{\alpha\beta}\, W_\beta, \tag{4.17}$$

and expended as

$$W_\alpha\, S'^{\alpha\beta}\, W_\beta = W^2(\sin^2\theta\, S'^{11} + \cos^2\theta\, S'^{22} - 2\sin\theta\cos\theta\, S'^{12}), \tag{4.18}$$

$$T_\alpha\, S'^{\alpha\beta}\, W_\beta = TW(-\cos\theta\sin\theta\, S'^{11} + \cos\theta\sin\theta\, S'^{22} + (\cos^2\theta - \sin^2\theta)\, S'^{12}). \tag{4.19}$$

These expressions can be reorganized in vector form using the Voigt notation. Let

$$\{\mathbf{S}'\} = [S'^{11}\ S'^{22}\ S'^{12}]^T, \tag{4.20}$$

and define the following direction-dependent projection vectors:

$$\mathbf{U}_2 = [\sin^2\theta\ \ \cos^2\theta\ \ -2\cos\theta\sin\theta]^T, \tag{4.21}$$

$$\mathbf{U}_3 = [-\cos\theta\sin\theta\ \ \cos\theta\sin\theta\ \ \cos^2\theta - \sin^2\theta]^T. \tag{4.22}$$

Then the uniaxial tension condition can be expressed as the vanishing of the corresponding linear projections:

$$\mathbf{U}_2 \cdot \{\mathbf{S}'\} = 0, \qquad \mathbf{U}_3 \cdot \{\mathbf{S}'\} = 0. \tag{4.23}$$

Together with the vector

$$\mathbf{U}_1 = [\cos^2\theta\ \ \sin^2\theta\ 2\cos\theta\sin\theta]^T, \tag{4.24}$$

these vectors form the columns of a rotation matrix. The matrix and its transpose are given by

$$\mathbf{Q} = \begin{bmatrix} c^2 & s^2 & 2cs \\ s^2 & c^2 & -2cs \\ -cs & cs & c^2 - s^2 \end{bmatrix}, \qquad \mathbf{Q}^{\mathrm{T}} = [\mathbf{U}_1\ \mathbf{U}_2\ \mathbf{U}_3] = \begin{bmatrix} c^2 & s^2 & -cs \\ s^2 & c^2 & cs \\ 2cs & -2cs & c^2 - s^2 \end{bmatrix}, \tag{4.25}$$

where $c = \cos\theta$ and $s = \sin\theta$. Accordingly, the rotated stress vector in the wrinkle-aligned

coordinate frame is given by

$$\{\hat{\mathbf{S}}'\} = \mathbf{Q}\{\mathbf{S}'\}, \tag{4.26}$$

where $\{\hat{\mathbf{S}}'\} = [\hat{S}'^{11}\ \hat{S}'^{22}\ \hat{S}'^{12}]^T$ represents the components of the stress tensor in a rotated orthonormal frame aligned with the wrinkle direction. In this frame, $\hat{S}'^{22}$ corresponds to the normal stress along the wrinkle direction, and $\hat{S}'^{12}$ represents the shear stress component. The uniaxial tension condition is therefore imposed by requiring both of these stress components to vanish.

4.4 Reference Model for Numerical Comparison

In this section, the wrinkling model originally proposed by [96] is briefly reviewed. This model is employed in the numerical examples as a reference solution for comparison with the formulation developed in this work. The original version was formulated within the finite element framework and was later extended to isogeometric analysis by [70]. More recently, it has also been generalized to hyperelastic materials [64]. The following presentation is intended to provide a concise overview of the formulation; for detailed derivations and implementation aspects, the reader is referred to the original literature.

4.4.1 Kinematic Equation

To incorporate wrinkling effects into standard membrane formulations, [96] adopted a kinematic modification originally introduced by [99], using the modified deformation gradient $\tilde{\mathbf{F}} = (\mathbf{I} + \beta_w\, \mathbf{w} \otimes \mathbf{w})\mathbf{F}$ as defined in Equation (4.5). This modified deformation gradient is specifically defined for the wrinkled state, from which the corresponding Green–Lagrange strain tensor is obtained as

$$\mathbf{E}' = \frac{1}{2}\left(\tilde{\mathbf{F}}^{\mathrm{T}}\tilde{\mathbf{F}} - \mathbf{I}\right). \tag{4.27}$$

Substitution of the expression for $\tilde{\mathbf{F}}$ yields

$$\tilde{\mathbf{F}}^{\mathrm{T}}\tilde{\mathbf{F}} = \mathbf{F}^{\mathrm{T}}(\mathbf{I} + \beta_w\, \mathbf{w} \otimes \mathbf{w})^{\mathrm{T}}(\mathbf{I} + \beta_w\, \mathbf{w} \otimes \mathbf{w})\mathbf{F}. \tag{4.28}$$

Using the identity $(\mathbf{w} \otimes \mathbf{w})^{\mathrm{T}} = \mathbf{w} \otimes \mathbf{w}$ and noting that $\mathbf{w}^{\mathrm{T}}\mathbf{w} = 1$, the middle term simplifies to

$$(\mathbf{I} + \beta_w\, \mathbf{w} \otimes \mathbf{w})^{\mathrm{T}}(\mathbf{I} + \beta_w\, \mathbf{w} \otimes \mathbf{w}) = \mathbf{I} + 2\beta_w\, \mathbf{w} \otimes \mathbf{w} + \beta_w^2\, \mathbf{w} \otimes \mathbf{w} = \mathbf{I} + \beta_w(\beta_w + 2)\, \mathbf{w} \otimes \mathbf{w}. \tag{4.29}$$

Hence, the modified right Cauchy–Green deformation tensor is obtained as

$$\tilde{\mathbf{F}}^{\mathrm{T}}\tilde{\mathbf{F}} = \mathbf{F}^{\mathrm{T}}\mathbf{F} + \beta_w(\beta_w + 2)\, \mathbf{F}^{\mathrm{T}}(\mathbf{w} \otimes \mathbf{w})\mathbf{F}. \tag{4.30}$$

The modified strain tensor $\mathbf{E}'$ can then be written in the form

$$\mathbf{E}' = \frac{1}{2}\left(\mathbf{F}^{\mathrm{T}}\mathbf{F} - \mathbf{I}\right) + \frac{1}{2}\beta_w(\beta_w + 2)\, \mathbf{F}^{\mathrm{T}}(\mathbf{w} \otimes \mathbf{w})\mathbf{F}. \tag{4.31}$$

The first term corresponds to the standard Green–Lagrange strain tensor $\mathbf{E} = \frac{1}{2}(\mathbf{F}^{\mathrm{T}}\mathbf{F} - \mathbf{I})$, while the second term defines the additional strain associated with the wrinkling modification, commonly referred to in the literature as the wrinkle strain. The modified strain is thus expressed as

$$\mathbf{E}' = \mathbf{E} + \mathbf{E}_w, \quad \text{with} \quad \mathbf{E}_w = \frac{1}{2}\beta_w(\beta_w + 2)\,\mathbf{W} \otimes \mathbf{W}, \tag{4.32}$$

where $\mathbf{W} = \mathbf{F}^{\mathrm{T}}\mathbf{w}$ denotes the pull-back of the wrinkle direction to the reference configuration. When expressed in contravariant components relative to the material basis $\mathbf{G}_\alpha$, the modified Green–Lagrange strain tensor takes the form

$$E'_{\alpha\beta} = E_{\alpha\beta} + \frac{1}{2}\beta_w(\beta_w + 2)\,W_\alpha W_\beta, \tag{4.33}$$

where $E_{\alpha\beta}$ are the components of the standard strain tensor $\mathbf{E}$, and W_α are the components of the wrinkle direction vector $\mathbf{W}$ in the reference configuration. To simplify this expression by using the Equation (4.7), the wrinkle direction vector is decomposed into a unit direction and a scalar magnitude as

$$W_\alpha = W R_\alpha, \qquad \text{with} \quad R_\alpha = \{-\sin\theta,\ \cos\theta\}\,. \tag{4.34}$$

Substituting this into the strain expression yields

$$E'_{\alpha\beta} = E_{\alpha\beta} + \frac{1}{2}\beta_w(\beta_w + 2)\,W^2\,R_\alpha R_\beta. \tag{4.35}$$

Introducing the wrinkle strain amplitude

$$\gamma_w = \frac{1}{2}\beta_w(\beta_w + 2)\,W^2, \tag{4.36}$$

the strain tensor can be compactly written as

$$E'_{\alpha\beta} = E_{\alpha\beta} + \gamma_w\,R_\alpha R_\beta. \tag{4.37}$$

In this form, both the wrinkle direction angle θ and the wrinkle strain amplitude γ_w remain undetermined and will be computed by enforcing the uniaxial tension condition, as described in the following subsection.

4.4.2 Determination of Wrinkle Direction

In the presence of wrinkling, the strain tensor $\mathbf{E}$ is modified to include an additional directional stretch component, as defined in Equation (4.37), the modified second Piola–Kirchhoff stress tensor corresponding to the modified strain is given by the linear elastic constitutive relation

$$S'^{\alpha\beta} = S^{\alpha\beta} + \gamma_w\,\mathbb{C}^{\alpha\beta\gamma\delta}R_\gamma R_\delta, \tag{4.38}$$

with $S^{\alpha\beta} = \mathbb{C}^{\alpha\beta\gamma\delta}E_{\gamma\delta}$ denoting the original stress in the absence of wrinkling.

To determine the wrinkle direction angle θ and the corresponding strain amplitude γ_w, the uniaxial tension condition is imposed. By projecting the modified stress along R_α and its orthogonal complement $R_\alpha^\perp = \{\cos\theta, \sin\theta\}$, two scalar constraints are obtained:

$$S'^{\alpha\beta} R_\alpha R_\beta = 0, \qquad S'^{\alpha\beta} R_\alpha^\perp R_\beta = 0. \tag{4.39}$$

Substituting the expression for $S'_{\alpha\beta}$ into these equations yields

$$S^{\alpha\beta} R_\alpha R_\beta + \gamma_w \, \mathbb{C}^{\alpha\beta\gamma\delta} R_\alpha R_\beta R_\gamma R_\delta = 0, \tag{4.40}$$

$$S^{\alpha\beta} R_\alpha^\perp R_\beta + \gamma_w \, \mathbb{C}^{\alpha\beta\gamma\delta} R_\alpha^\perp R_\beta R_\gamma R_\delta = 0. \tag{4.41}$$

From Equation (4.40), the wrinkle strain amplitude γ_w can be solved explicitly as

$$\gamma_w = -\frac{S^{\alpha\beta} R_\alpha R_\beta}{\mathbb{C}^{\alpha\beta\gamma\delta} R_\alpha R_\beta R_\gamma R_\delta}. \tag{4.42}$$

Substituting this expression into Equation (4.41) leads to a nonlinear equation in θ:

$$f(\theta) = S^{\alpha\beta} R_\alpha^\perp R_\beta + \gamma_w \mathbb{C}^{\alpha\beta\gamma\delta} R_\alpha^\perp R_\beta R_\gamma R_\delta = 0. \tag{4.43}$$

The only unknown in this equation is the angle θ, which can be computed using a root-finding algorithm. The range of θ in which a solution may exist can be restricted in advance by applying the conditions $\beta_w > 0$ and $S'_{\alpha\beta} R_\alpha^\perp R_\beta^\perp > 0$ [104]. Once the wrinkle direction angle θ is determined, the associated wrinkle strain amplitude γ_w, the modified strain $\mathbf{E}'$, and the corresponding stress $\mathbf{S}'$ can be computed.

Remark 4.1. Furthermore, this equation also reveals the relation between the wrinkle direction and the principal directions of stress or strain, which is discussed in detail in A.3.

4.4.3 Variational Formulation

In the weak form, the variations of the strain tensor $\mathbf{E}$ and stress tensor $\mathbf{S}$, denoted by $\delta\mathbf{E}$ and $\delta\mathbf{S}$, respectively, must be considered. For regions under taut conditions, these variations follow the standard elastic formulation. In the slack regions, the stress vanishes, hence no internal virtual work is generated. However, in the wrinkled domain, the modified strain $\mathbf{E}'$ and stress $\mathbf{S}'$ require special treatment.

The virtual internal work for the wrinkled state is expressed as

$$\delta W^{\text{int}} = \int_A \mathbf{S}' : (\delta\mathbf{E} + \delta\mathbf{E}_w) \, t \, dA. \tag{4.44}$$

As pointed out by [96], the variation of the wrinkle-induced strain does not contribute to the virtual work. This is because the stress vanishes in the wrinkle direction. Physically, the wrinkle strain corresponds to a deformation that stretches the membrane in a direction with

zero stress, and therefore does not alter the strain energy. Hence,

$$\mathbf{S}' : \delta\mathbf{E}_w = 0. \tag{4.45}$$

The virtual work expression thus simplifies to

$$\delta W^{\text{int}} = \int_A \mathbf{S}' : \delta\mathbf{E}\, t\, dA. \tag{4.46}$$

To compute the consistent tangent stiffness matrix, the virtual internal work expression is linearized [64]. This yields

$$\delta^2 W^{\text{int}} = \int_A \delta\mathbf{S}' : \delta\mathbf{E}\, t\, dA + \int_A \mathbf{S}' : \delta^2\mathbf{E}\, t\, dA, \tag{4.47}$$

where $\delta\mathbf{S}'$ denotes the variation of the stress tensor and $\delta^2\mathbf{E}$ is the second variation of the strain tensor. The variation of stress is assumed to be directly related to the variation of strain through the material tensor for the wrinkled state:

$$\delta\mathbf{S}' = \frac{\mathrm{d}\mathbf{S}'}{\mathrm{d}\mathbf{E}} : \delta\mathbf{E} = \mathbb{C}' : \delta\mathbf{E}, \tag{4.48}$$

where $\mathbb{C}'$ denotes the fourth-order modified material tensor that accounts for the wrinkled configuration. Substituting this relation into the expression above leads to the linearized virtual work:

$$\delta^2 W^{\text{int}} = \int_A (\mathbb{C}' : \delta\mathbf{E}) : \delta\mathbf{E}\, t\, dA + \int_A \mathbf{S}' : \delta^2\mathbf{E}\, t\, dA. \tag{4.49}$$

4.4.4 Derivation of the Modified Material Tensor

To construct the modified material tensor in the wrinkled configuration, the variation of the modified second Piola–Kirchhoff stress tensor with respect to the strain tensor must be computed. The Equation (4.48) can be extended as

$$\delta S'^{\alpha\beta} = \frac{\mathrm{d}S'^{\alpha\beta}}{\mathrm{d}E_{\sigma\tau}}\,\delta E_{\sigma\tau} = \left(\frac{\partial S^{\alpha\beta}}{\partial E_{\sigma\tau}} + \frac{\mathrm{d}\gamma_w}{\mathrm{d}E_{\sigma\tau}}\,\mathbb{C}^{\alpha\beta\gamma\delta} R_\gamma R_\delta + \gamma_w \mathbb{C}^{\alpha\beta\gamma\delta}\frac{\mathrm{d}(R_\gamma R_\delta)}{\mathrm{d}E_{\sigma\tau}}\right)\delta E_{\sigma\tau}. \tag{4.50}$$

From this expression, it is clear that two additional terms are required: the derivatives of $R_\gamma R_\delta$ and γ_w with respect to $E_{\sigma\tau}$, respectively.

The derivative of $R_\gamma R_\delta$ is computed via the chain rule. Using the definitions of $R_\alpha = \{-\sin\theta, \cos\theta\}$ and its orthogonal complement $R_\alpha^\perp = \{\cos\theta, \sin\theta\}$, one obtains

$$\frac{\mathrm{d}(R_\gamma R_\delta)}{\mathrm{d}E_{\sigma\tau}} = \frac{\partial(R_\gamma R_\delta)}{\partial\theta}\frac{\partial\theta}{\partial E_{\sigma\tau}} = (R_\gamma^\perp R_\delta + R_\gamma R_\delta^\perp)\,\frac{\partial\theta}{\partial E_{\sigma\tau}}. \tag{4.51}$$

The full derivative of γ_w is decomposed into two parts:

$$\frac{\mathrm{d}\gamma_w}{\mathrm{d}E_{\sigma\tau}} = \frac{\partial\gamma_w}{\partial E_{\sigma\tau}} + \frac{\partial\gamma_w}{\partial\theta}\frac{\partial\theta}{\partial E_{\sigma\tau}}. \tag{4.52}$$

The first partial derivative $\partial\gamma_w/\partial E_{\sigma\tau}$ is expressed as

$$\frac{\partial\gamma_w}{\partial E_{\sigma\tau}} = -\frac{\mathbb{C}^{\alpha\beta\sigma\tau}R_\alpha R_\beta}{\mathbb{C}^{\alpha\beta\gamma\delta}R_\alpha R_\beta R_\gamma R_\delta}. \tag{4.53}$$

The second partial derivative is computed from the definition of γ_w, leading to

$$\begin{aligned}\frac{\partial\gamma_w}{\partial\theta} =& -\frac{\left(\mathbb{C}^{\alpha\beta\gamma\delta}R_\alpha R_\beta R_\gamma R_\delta\right)\left(S^{\alpha\beta}\frac{\partial(R_\alpha R_\beta)}{\partial\theta}\right)}{\left(\mathbb{C}^{\alpha\beta\gamma\delta}R_\alpha R_\beta R_\gamma R_\delta\right)^2} \\ &+ \frac{\left(S^{\alpha\beta}R_\alpha R_\beta\right)\left(\mathbb{C}^{\alpha\beta\gamma\delta}\left(\frac{\partial(R_\alpha R_\beta)}{\partial\theta}R_\gamma R_\delta + R_\alpha R_\beta\frac{\partial(R_\gamma R_\delta)}{\partial\theta}\right)\right)}{\left(\mathbb{C}^{\alpha\beta\gamma\delta}R_\alpha R_\beta R_\gamma R_\delta\right)^2} \\ =& -\frac{\gamma_w\,\mathbb{C}^{\alpha\beta\gamma\delta}R_\alpha R_\beta\frac{\partial(R_\gamma R_\delta)}{\partial\theta}}{\mathbb{C}^{\alpha\beta\gamma\delta}R_\alpha R_\beta R_\gamma R_\delta}.\end{aligned} \tag{4.54}$$

To evaluate $\partial\theta/\partial E_{\sigma\tau}$, the root condition from the uniaxial tension constraint is considered. Differentiating the scalar equation $f(\theta) = 0$ with respect to strain yields

$$\frac{\partial f}{\partial E_{\sigma\tau}} + \frac{\partial f}{\partial\theta}\frac{\partial\theta}{\partial E_{\sigma\tau}} = 0. \tag{4.55}$$

Solving for $\partial\theta/\partial E_{\sigma\tau}$ gives

$$\frac{\partial\theta}{\partial E_{\sigma\tau}} = -\frac{\partial f}{\partial E_{\sigma\tau}}\left(\frac{\partial f}{\partial\theta}\right)^{-1}. \tag{4.56}$$

The individual terms are evaluated as follows. The derivative of f with respect to strain reads

$$\frac{\partial f}{\partial E_{\sigma\tau}} = \mathbb{C}^{\alpha\beta\sigma\tau}R^\perp_\alpha R_\beta - \frac{\partial\gamma_w}{\partial E_{\sigma\tau}}\mathbb{C}^{\alpha\beta\gamma\delta}R^\perp_\alpha R_\beta R_\gamma R_\delta. \tag{4.57}$$

The derivative of f with respect to θ includes multiple directional terms:

$$\begin{aligned}\frac{\partial f}{\partial\theta} =& S^{\alpha\beta}\frac{\partial(R^\perp_\alpha R_\beta)}{\partial\theta} + \frac{\partial\gamma_w}{\partial\theta}\,\mathbb{C}^{\alpha\beta\gamma\delta}R^\perp_\alpha R_\beta R_\gamma R_\delta \\ &+ \gamma_w\,\mathbb{C}^{\alpha\beta\gamma\delta}\left(\frac{\partial(R^\perp_\alpha R_\beta)}{\partial\theta}R_\gamma R_\delta + R^\perp_\alpha R_\beta\frac{\partial(R_\gamma R_\delta)}{\partial\theta}\right).\end{aligned} \tag{4.58}$$

The directional derivatives used above are given by

$$\frac{\partial(R^\perp_\alpha R_\beta)}{\partial\theta} = -R_\alpha R_\beta + R^\perp_\alpha R^\perp_\beta. \tag{4.59}$$

By substituting Equations (4.54)–(4.59) into Equation (4.50), the variation of the modified stress tensor $\delta\mathbf{S}'$ is obtained, from which the modified material tensor $\mathbb{C}'$ can also be derived.

In the hyperelastic case, the derivation proceeds similarly, but the modified material tensor $\mathbb{C}'(\mathbf{E})$ becomes a nonlinear function of strain or deformation tensor. As a result, the variation of stress includes an additional sixth-order tensor term arising from the derivative $\partial\mathbb{C}^{\alpha\beta\gamma\delta}/\partial E_{\sigma\tau}$. Moreover, the wrinkle direction function $f(\theta, \mathbf{E})$ depends on both θ and $\mathbf{E}$, and its derivative with respect to strain includes additional contributions, see [64] for more details.

Chapter 5

Variationally Consistent Wrinkling Models

This chapter introduces various variationally consistent modeling approaches for membrane wrinkling. The formulation is based on spectral decomposition, which enables a unified treatment of taut, wrinkled, and slack regimes without the use of explicit wrinkling criteria. Section 5.1 introduces the spectral decomposition framework and its associated tensorial derivatives, which provide the basis for subsequent model construction. Section 5.2 presents the strain-criterion-based model as the initial formulation. Section 5.3 provides a detailed assessment of this model and develops alternative formulations. Finally, Section 5.4 extends the modeling framework to hyperelastic membranes.

5.1 Spectral Decomposition Framework

Spectral decomposition provides a general means of representing symmetric second-order tensors through their principal values and directions, and it serves as a fundamental tool in the modeling framework developed in this dissertation.

Let $\mathbf{A} \in \mathbb{R}^{3\times3}$ be a symmetric second-order tensor. Owing to symmetry, its three distinct eigenvalues A_i are real and the corresponding eigenvectors $\mathbf{N}_i$ form an orthonormal basis. The spectral decomposition of $\mathbf{A}$ reads

$$\mathbf{A} = A_i \, \mathbf{M}_i, \quad \text{with} \quad \mathbf{M}_i = \mathbf{N}_i \otimes \mathbf{N}_i, \tag{5.1}$$

where $\mathbf{M}_i$ denotes the symmetric second-order projection tensor onto the principal direction $\mathbf{N}_i$. In the context of nonlinear finite element formulations, the material tensor is obtained by differentiating the stress tensor with respect to the strain. Thus, the derivatives of the eigenvalues and the corresponding projection tensors must be evaluated.

The derivative of each eigenvalue with respect to $\mathbf{A}$ is straightforward and given by

$$\frac{\partial A_i}{\partial \mathbf{A}} = \mathbf{M}_i, \tag{5.2}$$

while the derivative of the eigenvectors is expressed as

$$\frac{\partial \mathbf{N}_i}{\partial \mathbf{A}} = \frac{1}{A_i - A_j} \mathbf{N}_j \otimes \left(\mathbf{N}_i \otimes \mathbf{N}_j + \mathbf{N}_j \otimes \mathbf{N}_i \right), \quad i \neq j. \tag{5.3}$$

Using the product rule, the derivative of the projection tensor $\mathbf{M}_i$ follows as

$$\mathbb{M}_i = \frac{\partial \mathbf{M}_i}{\partial \mathbf{A}} = \frac{1}{2(A_i - A_j)} \left(\mathbb{G}_{ij} + \mathbb{G}_{ji} \right), \quad i \neq j, \tag{5.4}$$

where the fourth-order tensor $\mathbb{G}_{ij}$ is defined componentwise by

$$\mathbb{G}_{ij}^{klmn} = M_i^{km} M_j^{ln} + M_i^{kn} M_j^{lm}. \tag{5.5}$$

Additionally, the tensor product between projection tensors is defined by

$$\mathbb{Q}_{ij} = \mathbf{M}_i \otimes \mathbf{M}_j, \quad \mathbb{Q}_{ij}^{klmn} = M_i^{kl} M_j^{mn}, \tag{5.6}$$

which frequently appears in the construction of fourth-order material tensors. By definition, a fourth-order tensor $\mathbb{A}$ is said to be major symmetric if

$$\mathbb{A}^{ijkl} = \mathbb{A}^{klij}. \tag{5.7}$$

Both $\mathbb{Q}_{ii}$ and $\mathbb{M}_i$ satisfy this property. In contrast, the off-diagonal tensor $\mathbb{Q}_{ij}$ with $i \neq j$ is only minor symmetric, satisfying

$$\mathbb{Q}_{ij}^{klmn} = \mathbb{Q}_{ij}^{lkmn} = \mathbb{Q}_{ij}^{klnm}. \tag{5.8}$$

Nevertheless, the symmetrized combination $\mathbb{Q}_{ij} + \mathbb{Q}_{ji}$ restores major symmetry. This observation is particularly relevant when analyzing the symmetry properties of material tensors constructed from principal directions.

In the case of repeated eigenvalues, the above expressions involving inverse differences $(A_i - A_j)^{-1}$ become singular and must be evaluated through appropriate limiting procedures. The specific limit forms adopted in this work follow the treatment proposed by [133]. This procedure ensures that all derivatives remain well defined and numerically stable. Alternatively, projection tensors can be reformulated using eigenprojections, which remain well defined in the presence of eigenvalue multiplicity. For further details, the reader is referred to the original formulation in [134].

Although the membrane models are defined in three spatial dimensions, the enforcement of the plane stress condition reduces the stress and strain tensors to two-dimensional forms. Consequently, only two principal values contribute to the spectral representation. The general three-dimensional formulation presented here allows for a unified spectral treatment and is reduced accordingly in plane stress applications.

5.2 Strain-Criterion-Based Wrinkling Model

This section presents a novel, variationally consistent wrinkling formulation based on a strain energy decomposition approach. The decomposition strategy was originally introduced by [133] in the context of phase-field fracture, where only tensile stress contributes to crack propagation. In that framework, the tensile part of the strain energy is subject to degradation, while the compressive part remains unaffected to avoid unphysical crack growth under compression. The method was subsequently extended to plane-stress problems by [121].

In contrast, membranes exhibit the opposite mechanical response: they are unable to sustain compressive stress. This motivates the exclusion of compressive energy contributions in membrane formulations. Although the physical mechanisms differ from those in fracture, the same spectral decomposition technique can be adapted to describe the mechanical behavior of membranes in different states such as taut, wrinkled, or slack, without requiring an explicit wrinkling criterion. The corresponding mathematical formulation is detailed below.

The key idea is to decompose the strain tensor $\mathbf{E}$ into its tensile and compressive components by evaluating its principal strains and directions. Specifically, the strain tensor is expressed as

$$\mathbf{E} = E_\alpha \, \mathbf{N}_\alpha \otimes \mathbf{N}_\alpha, \tag{5.9}$$

where E_α are the eigenvalues (principal strains) and $\mathbf{N}_\alpha$ the corresponding orthonormal eigenvectors of the strain tensor. The tensile and compressive parts of the strain tensor, denoted by $\mathbf{E}^+$ and $\mathbf{E}^-$, are constructed by selectively retaining the positive and negative principal strain components using Heaviside functions $H^\pm(x)$:

$$\mathbf{E}^\pm = H^\pm(E_\alpha) \, E_\alpha \, \mathbf{N}_\alpha \otimes \mathbf{N}_\alpha, \tag{5.10}$$

where the functions $H^+(x)$ and $H^-(x)$ are defined as

$$H^+(x) = \begin{cases} 1, & x > 0 \\ 0, & x \leq 0 \end{cases}, \qquad H^-(x) = \begin{cases} 1, & x < 0 \\ 0, & x \geq 0 \end{cases}, \tag{5.11}$$

such that

$$H^\pm(x) \, x = \langle x \rangle^\pm = \frac{1}{2}(x \pm |x|), \tag{5.12}$$

where $\langle \cdot \rangle^\pm$ denotes the Macaulay bracket (or ramp function). For convenience, the strain decomposition is equivalently written as

$$\mathbf{E}^\pm = \langle E_\alpha \rangle^\pm \, \mathbf{N}_\alpha \otimes \mathbf{N}_\alpha. \tag{5.13}$$

Following this decomposition, the energy functional associated with the St. Venant material model, as defined in Equation (2.68), can be split into tensile and compressive contributions as

$$\psi \, (\mathbf{E}) = \psi^+ \, (\mathbf{E}) + \psi^- \, (\mathbf{E}) \, , \tag{5.14}$$

where the positive and negative parts are defined by

$$\psi^{\pm}(\mathbf{E}) = \frac{\lambda}{2}\left(\langle \mathrm{tr}(\mathbf{E})\rangle^{\pm}\right)^2 + \mu\,\mathrm{tr}\left(\left(\mathbf{E}^{\pm}\right)^2\right) - \frac{\lambda^2}{2(\lambda+2\mu)}\left(\langle \mathrm{tr}(\mathbf{E})\rangle^{\pm}\right)^2. \tag{5.15}$$

Based on the energy decomposition, the second Piola–Kirchhoff stress tensor inherits an additive form, which is obtained in a variationally consistent manner by taking the derivative of the energy functional with respect to the Green–Lagrange strain tensor:

$$\mathbf{S} = \frac{\partial \psi(\mathbf{E})}{\partial \mathbf{E}} = \frac{\partial \psi^{+}(\mathbf{E})}{\partial \mathbf{E}} + \frac{\partial \psi^{-}(\mathbf{E})}{\partial \mathbf{E}} = \mathbf{S}^{+} + \mathbf{S}^{-}, \tag{5.16}$$

where the positive and negative stress tensors $\mathbf{S}^{\pm}$ are defined as:

$$\mathbf{S}^{\pm} = \left(\frac{\lambda}{2} - \frac{\lambda^2}{2(\lambda+2\mu)}\right)\frac{\partial\left(\langle \mathrm{tr}(\mathbf{E})\rangle^{\pm}\right)^2}{\partial \mathbf{E}} + \mu\frac{\partial\,\mathrm{tr}\left((\mathbf{E}^{\pm})^2\right)}{\partial \mathbf{E}}. \tag{5.17}$$

The derivative of the trace operator with respect to the strain tensor is given by

$$\frac{\partial\,\mathrm{tr}(\mathbf{E})}{\partial \mathbf{E}} = \mathbf{I}. \tag{5.18}$$

Using the chain rule for the first term, and noting that the Heaviside function merely extracts the positive or negative part of its argument, the following identity is obtained:

$$\frac{\partial\left(\langle \mathrm{tr}(\mathbf{E})\rangle^{\pm}\right)^2}{\partial \mathbf{E}} = \frac{\partial\left(H^{\pm}(\mathrm{tr}(\mathbf{E}))\,\mathrm{tr}(\mathbf{E})\right)^2}{\partial \mathbf{E}} = 2H^{\pm}(\mathrm{tr}(\mathbf{E}))\,\mathrm{tr}(\mathbf{E})\mathbf{I} = 2\langle \mathrm{tr}(\mathbf{E})\rangle^{\pm}\mathbf{I}. \tag{5.19}$$

The second term, involving the double contraction $\mathbf{E}^{\pm} : \mathbf{E}^{\pm}$, is evaluated as:

$$\frac{\partial\,\mathrm{tr}\left((\mathbf{E}^{\pm})^2\right)}{\partial \mathbf{E}} = \frac{\partial\left(\mathbf{E}^{\pm} : \mathbf{E}^{\pm}\right)}{\partial \mathbf{E}} = 2\mathbf{E}^{\pm}. \tag{5.20}$$

Substituting Equations (5.19) and (5.20) into Equation (5.17) yields the final expression of the additively decomposed stress tensor:

$$\mathbf{S}^{\pm} = \left(\lambda - \frac{\lambda^2}{\lambda+2\mu}\right)\langle \mathrm{tr}(\mathbf{E})\rangle^{\pm}\,\mathbf{I} + 2\mu\,\mathbf{E}^{\pm}. \tag{5.21}$$

Then, the material tensor can be obtained by deriving the stress tensor with respect to the strain tensor:

$$\mathbb{C} = \frac{\partial \mathbf{S}}{\partial \mathbf{E}} = \frac{\partial \mathbf{S}^{+}}{\partial \mathbf{E}} + \frac{\partial \mathbf{S}^{-}}{\partial \mathbf{E}} = \mathbb{C}^{+} + \mathbb{C}^{-}, \tag{5.22}$$

where the positive and negative parts are given by:

$$\mathbb{C}^{\pm} = \left(\lambda - \frac{\lambda^2}{\lambda+2\mu}\right)\frac{\partial\left(\langle \mathrm{tr}(\mathbf{E})\rangle^{\pm}\,\mathbf{I}\right)}{\partial \mathbf{E}} + 2\mu\,\frac{\partial \mathbf{E}^{\pm}}{\partial \mathbf{E}}. \tag{5.23}$$

The first term involves the derivative of the trace operator. Introducing the fourth-order identity tensor $\mathbb{J}$, defined by

$$\mathbb{J}_{\alpha\beta\gamma\delta} = \frac{\partial \left(\mathrm{tr}(\mathbf{E})\mathbf{I}\right)_{\alpha\beta}}{\partial E_{\gamma\delta}} = \begin{cases} 1, & \text{if } \alpha = \beta \text{ and } \gamma = \delta, \\ 0, & \text{otherwise,} \end{cases} \tag{5.24}$$

the first term becomes

$$\frac{\partial \left(\langle \mathrm{tr}(\mathbf{E}) \rangle^{\pm} \mathbf{I}\right)}{\partial \mathbf{E}} = H^{\pm}(\mathrm{tr}(\mathbf{E}))\, \mathbb{J}. \tag{5.25}$$

The second term corresponds to the derivative of the positive and negative strain tensors $\mathbf{E}^{\pm}$ with respect to the strain tensor, and is expressed as

$$\frac{\partial \mathbf{E}^{\pm}}{\partial \mathbf{E}} = \frac{\partial \left(H^{\pm}(E_\alpha) E_\alpha \mathbf{M}_\alpha\right)}{\partial \mathbf{E}} = H^{\pm}(E_\alpha) \left(\frac{\partial E_\alpha}{\partial \mathbf{E}} \otimes \mathbf{M}_\alpha + E_\alpha \frac{\partial \mathbf{M}_\alpha}{\partial \mathbf{E}} \right), \tag{5.26}$$

where the derivatives of eigenvalues and projection tensors with respect to strain tensor give rise to the fourth-order tensors $\mathbb{Q}_{\alpha\alpha}$ and $\mathbb{G}_{\alpha\beta}$, as defined in Equations (5.6) and (5.5). Then, the derivative of $\mathbf{E}^{\pm}$ is rewritten as:

$$\frac{\partial \mathbf{E}^{\pm}}{\partial \mathbf{E}} = H^{\pm}(E_\alpha) \ \left(\mathbb{Q}_{\alpha\alpha} + E_\alpha \, \mathbb{M}_\alpha\right), \tag{5.27}$$

Substituting into the expression for $\mathbb{C}^{\pm}$, its final form becomes

$$\mathbb{C}^{\pm} = \left(\lambda - \frac{\lambda^2}{\lambda + 2\mu}\right) H^{\pm}\left(\mathrm{tr}(\mathbf{E})\right) \mathbb{J} + 2\mu \left(H^{\pm}(E_\alpha) \ \left(\mathbb{Q}_{\alpha\alpha} + E_\alpha \, \mathbb{M}_\alpha\right)\right). \tag{5.28}$$

Within this spectral-decomposition-based framework in Equations (5.14)–(5.28), the tensile and compressive components of the energy, stress, and material tensors emerge naturally from the eigenstructure of the strain tensor. In this setting, positive terms are associated with tension, while negative terms correspond to compression. By retaining only the positive parts in Equations (5.14), (5.16), and (5.22), a membrane wrinkling formulation is obtained:

$$\psi_{\text{eff}} = \psi^{+}, \quad \mathbf{S}_{\text{eff}} = \mathbf{S}^{+}, \quad \mathbb{C}_{\text{eff}} = \mathbb{C}^{+}, \tag{5.29}$$

which reflects the physical assumption that the membrane cannot sustain compression and compressive stress components are therefore suppressed.

The proposed formulation can be seamlessly integrated into standard finite element or isogeometric frameworks, as detailed in Section 2.3. No explicit wrinkling criterion or case-wise logic is required during analysis; instead, the membrane state is implicitly identified through the principal strains, consistent with the principal strain criterion. The classification is given by

$$\begin{aligned} & & E_2 > 0: \quad & \text{taut}, \\ E_1 > 0, \quad & E_2 \leq 0: \quad & \text{wrinkled}, \\ & E_1 \leq 0: \quad & \text{slack}. \end{aligned} \tag{5.30}$$

In a taut region, where both principal strains are positive, the effective energy, stress, and material tensors in Equation (5.29) coincide with those of classical membrane theory, and the full in-plane stiffness is preserved. When the membrane enters a wrinkled state, the compressive components are excluded automatically, and only the tensile parts contribute to the response. The formulation, despite avoiding any explicit switching logic, is still capable of providing complete information regarding both the membrane states and the directions of wrinkling, comparable to conventional wrinkling models. In this regime, the wrinkle direction corresponds to the second principal strain direction $\mathbf{N}_2$, along which compressive stresses vanish and wrinkles develop, while the perpendicular direction $\mathbf{N}_1$, associated with the first principal strain, carries the tensile load. In the slack regime, where both principal strains are non-positive, no tensile components are present; as a result, the effective energy, stress, and stiffness tensors reduce to zero, and the membrane is unable to sustain any load. In this way, taut, wrinkled, and slack responses are unified within a single variationally consistent formulation.

Despite these advantages, the formulation in Equation (5.29) eliminates compressive stiffness entirely, and therefore represents slack regions as completely stress-free. In a corresponding finite element formulation, however, even a modest amount of compression can lead to element interpenetration, and slack regions may cause the global stiffness matrix to become ill conditioned or singular.

A practical solution is to introduce residual compressive stiffness by augmenting the positive energy, stress, and material tensors with a scaled contribution from their negative parts:

$$\psi_{\text{eff}} = \psi^+ + \eta\,\psi^-, \qquad \mathbf{S}_{\text{eff}} = \mathbf{S}^+ + \eta\,\mathbf{S}^-, \qquad \mathbb{C}_{\text{eff}} = \mathbb{C}^+ + \eta\,\mathbb{C}^-, \tag{5.31}$$

where $0 \leq \eta \ll 1$ governs the remaining stiffness in compression. The inclusion of residual compressive stiffness provides a unified and robust extension of the original model (see Equation (5.29)), maintaining variational consistency while improving numerical stability.

Although η could, in principle, be selected based on the buckling resistance of the membrane, it is employed here purely as a numerical stabilisation parameter. Its role is to suppress element interpenetration, avoid singularities in the global stiffness matrix, and enhance the convergence behaviour of iterative solvers. Comparable strategies are reported in the literature, where η is interpreted as a penalty factor [65, 93], an allowable compressive stress [108], or a residual compressive stiffness [81]. The present work adopts the last interpretation, with η acting as a degradation factor that governs the residual energy, stress, and stiffness under compression. The influence of different η values is examined in Section 6.1.8; in cases where slackening and element interpenetration are not critical, the choice $\eta = 0$ is generally sufficient.

While the strain-criterion-based model captures the essential features of wrinkled membranes in a variationally consistent manner, numerical experiments presented in Sections 6.1.2 and 6.1.3 have shown that this strain-based decomposition may exhibit certain limitations in shear-dominated problems. In order to investigate the source of these limitations and to explore potential improvements, a detailed evaluation is conducted in the following section.

5.3 Model Assessment and Development

This section presents a assessment of the strain-, stress-, and mixed-criterion-based models. The evaluation is carried out in three steps: first, the strain-criterion-based model is examined with respect to the uniaxial tension condition (Section 5.3.1); second, an alternative stress-based decomposition and its mixed extension are introduced (Section 5.3.2); and finally, the regularity and convexity properties of the resulting energy functions are analyzed (Section 5.3.3).

5.3.1 Evaluation via Uniaxial Tension Condition

Following the strain-based decomposition approach presented in Section 5.2, the strain energy density is split into positive and negative parts through the spectral decomposition of the strain tensor. By differentiating these energy contributions with respect to strain, one obtains the corresponding positive and negative stress components. For convenience of reference in the subsequent analysis, the expression for the positive and negative components of the stress tensor is restated here:

$$\mathbf{S}_{\text{eff}} = \mathbf{S}^{+} + \eta\, \mathbf{S}^{-}, \tag{5.32}$$

$$\mathbf{S}^{\pm} = \left(\lambda - \frac{\lambda^2}{\lambda + 2\mu}\right) \langle \operatorname{tr}(\mathbf{E}) \rangle^{\pm}\, \mathbf{I} + 2\mu \mathbf{E}^{\pm}, \tag{5.33}$$

where these material parameters (Lamé constants) can be equivalently expressed in terms of the Young's modulus E and Poisson's ratio ν as

$$\lambda = \frac{E\nu}{(1+\nu)(1-2\nu)}, \qquad \mu = \frac{E}{2(1+\nu)}. \tag{5.34}$$

Substituting these relations into the stress expression leads to the following form of the positive and negative stress tensors, in which the Heaviside functions are explicitly represented:

$$\mathbf{S}^{\pm} = \frac{E}{1-\nu^2} \left(\nu H^{\pm}(\operatorname{tr}(\mathbf{E}))\, \operatorname{tr}(\mathbf{E})\mathbf{I} + (1-\nu) H^{\pm}(E_\alpha) E_\alpha \mathbf{M}_\alpha \right). \tag{5.35}$$

Given the symmetry of $\mathbf{E} = E_1\mathbf{M}_1 + E_2\mathbf{M}_2$, spectral decomposition applies and the trace can be computed as

$$\operatorname{tr}(\mathbf{E}) = \mathbf{E} : \mathbf{I} = E_1(\mathbf{M}_1 : \mathbf{I}) + E_2(\mathbf{M}_2 : \mathbf{I}). \tag{5.36}$$

Using $\mathbf{I} = \mathbf{M}_1 + \mathbf{M}_2$ and the orthogonality relation

$$\mathbf{M}_\alpha : \mathbf{M}_\beta = \delta_{\alpha\beta}, \tag{5.37}$$

where $\delta_{\alpha\beta}$ is the Kronecker delta, equal to 1 if $\alpha = \beta$ and 0 otherwise, it follows that

$$\operatorname{tr}(\mathbf{E}) = E_1 + E_2, \qquad \operatorname{tr}(\mathbf{E})\mathbf{I} = (E_1 + E_2)(\mathbf{M}_1 + \mathbf{M}_2). \tag{5.38}$$

Substituting this identity into the stress expression leads to the reformulated form:

$$\mathbf{S}^{\pm} = \frac{E}{1-\nu^2}\left(H^{\pm}(E_\alpha)(1-\nu)E_\alpha\mathbf{M}_\alpha + H^{\pm}(\mathrm{tr}(\mathbf{E}))\,\nu\left(E_\alpha\mathbf{M}_\alpha + E_\alpha\mathbf{M}_\beta\right)\right), \quad \alpha \neq \beta. \tag{5.39}$$

Consequently, the corresponding positive and negative material tensors based on this split are rewritten as:

$$\begin{aligned}\mathbb{C}^{\pm} = \frac{E}{1-\nu^2}\Big(&H^{\pm}(E_\alpha)\,(1-\nu)(\mathbb{Q}_{\alpha\alpha} + E_\alpha\mathbb{M}_\alpha) + \\ &H^{\pm}(\mathrm{tr}(\mathbf{E}))\,\nu(\mathbb{Q}_{\alpha\alpha} + E_\alpha\mathbb{M}_\alpha + E_\alpha\mathbb{M}_\beta + \mathbb{Q}_{\alpha\beta})\Big), \quad \alpha \neq \beta.\end{aligned} \tag{5.40}$$

An assessment of the strain-criterion-based model is presented below. This formulation exhibits two fundamental limitations.

First, since the classification of membrane states is determined by the signs of the principal strains, the model inherits the shortcomings of the principal strain criterion. This issue has been discussed in Section 4.2, where it was shown that the principal strain criterion may misclassify the transition between taut and wrinkled states, especially when compared to the mixed criterion. Consequently, this may lead to underestimation of stress in certain taut configurations.

Second, the model may yield inaccurate stress predictions in wrinkled regions that show slight discrepancies compared to conventional tension field theory.

To evaluate this behavior, the uniaxial tension condition in Equation (4.15) is applied to the stress expression. For isotropic materials, the wrinkling directions aligns with the principal directions of stress or strain, i.e., $\mathbf{W} = \mathbf{N}_2$. Accordingly, the expression becomes:

$$\mathbf{W}\cdot\mathbf{S}_{\mathrm{eff}}\,\mathbf{W} = \mathbf{S}_{\mathrm{eff}} : \mathbf{W}\otimes\mathbf{W} = \mathbf{S}_{\mathrm{eff}} : \mathbf{M}_2. \tag{5.41}$$

For the wrinkled state, where $E_1 > 0$ and $E_2 \leq 0$, the assessment is carried out with $\eta = 0$ for convenience, since a very small degradation factor already renders the compressive contributions negligible. Then, the effective stress takes the form

$$\mathbf{S}_{\mathrm{eff}} = \frac{E}{1-\nu^2}\Big((1-\nu)E_1\mathbf{M}_1 + H^{+}(\mathrm{tr}(\mathbf{E}))\,\nu\big(E_1\mathbf{M}_1 + E_1\mathbf{M}_2 + E_2\mathbf{M}_1 + E_2\mathbf{M}_2\big)\Big). \tag{5.42}$$

Projecting this expression onto the wrinkling direction $\mathbf{M}_2$ yields

$$\mathbf{S}_{\mathrm{eff}} : \mathbf{M}_2 = \frac{E}{1-\nu^2}\left(H^{+}(\mathrm{tr}(\mathbf{E}))\,\nu\,(E_1 + E_2)\right) = \frac{E}{1-\nu^2}\left(H^{+}(\mathrm{tr}(\mathbf{E}))\,\nu\,\mathrm{tr}(\mathbf{E})\right). \tag{5.43}$$

To evaluate whether this expression satisfies the uniaxial tension condition $\mathbf{S}_{\mathrm{eff}} : \mathbf{M}_2 = 0$, it is necessary to examine the sign of $\mathrm{tr}(\mathbf{E})$. As shown in Equation (5.43), this condition is satisfied if and only if $\mathrm{tr}(\mathbf{E}) \leq 0$. When $\mathrm{tr}(\mathbf{E}) > 0$, the trace-dependent term remains strictly positive, resulting in a nonzero tensile stress in the wrinkle direction. This indicates that the strain-criterion-based model does not strictly enforce the uniaxial tension condition and may produce overstiff responses in wrinkled regions. Nevertheless, these deviations are typically small in numerical applications and can often be regarded as negligible.

5.3.2 Stress- and Mixed-Criterion-Based Wrinkling Models

Following the same framework introduced in Equation (5.31), an alternative tension–compression split is considered based on the spectral decomposition of the stress tensor $\mathbf{S}$, which naturally aligns with a principal stress-based wrinkling criterion. This formulation is subsequently modified to obtain a wrinkling model governed by a mixed criterion.

A stress-based decomposition of the energy density ψ was initially proposed in [135] in the context of phase-field fracture, and is given by

$$\psi^{\pm} = \frac{1}{2}(\mathbf{S}^{\pm} : \mathbf{E}). \tag{5.44}$$

The corresponding positive and negative components of the stress tensor are defined through the spectral decomposition:

$$\mathbf{S}^{\pm} = H^{\pm}(S_\alpha)\, S_\alpha\, \mathbf{N}^{\mathbf{S}}_\alpha \otimes \mathbf{N}^{\mathbf{S}}_\alpha = H^{\pm}(S_\alpha)\, S_\alpha\, \mathbf{M}^{\mathbf{S}}_\alpha, \tag{5.45}$$

where S_α are the principal stresses and $\mathbf{N}^{\mathbf{S}}_\alpha$ the corresponding eigenvectors of the stress tensor. The tensor $\mathbf{M}^{\mathbf{S}}_\alpha$ denotes the spectral projection onto the α-th stress eigendirection. Similarly, $\mathbf{M}^{\mathbf{E}}_\alpha$ represent the projection associated with the α-th strain eigenvector $\mathbf{N}^{\mathbf{E}}_\alpha$. For isotropic materials, the principal directions of stress and strain coincide, and hence the projection tensors satisfy

$$\mathbf{M}_\alpha = \mathbf{M}^{\mathbf{E}}_\alpha = \mathbf{M}^{\mathbf{S}}_\alpha. \tag{5.46}$$

In the case of a St. Venant–Kirchhoff material, the principal stresses can be written explicitly in terms of the principal strains. Substituting these expressions into the stress decomposition leads to the relation

$$\mathbf{S}^{\pm} = \frac{E}{1-\nu^2}\, H^{\pm}(E_\alpha + \nu E_\beta)\, (E_\alpha + \nu E_\beta)\, \mathbf{M}_\alpha, \quad \alpha \neq \beta. \tag{5.47}$$

Substituting the positive and negative stresses into Equation (5.31), the effective stress tensor $\mathbf{S}_{\text{eff}}$ is obtained and its behavior under different membrane states is summarized as follows. In the taut state, where both principal stresses are positive, the full stress is retained. In the slack state, where both principal stresses are non-positive, the effective stress vanishes when $\eta = 0$, while for $\eta \ll 1$ it remains close to zero, as only a very small residual compressive contribution persists. In the wrinkled state, characterized by $S_1 > 0$ and $S_2 \leq 0$, the negative component $\mathbf{S}^-$ is completely suppressed when $\eta = 0$, so that $\mathbf{S}_{\text{eff}} = \mathbf{S}^+ = S_1\mathbf{M}_1$. Consequently, the stress tensor contains no component along the second eigendirection, and the uniaxial tension condition $\mathbf{S}_{\text{eff}} : \mathbf{M}_2 = 0$ is automatically satisfied in the wrinkled region.

The positive and negative material tensors $\mathbb{C}^{\pm}$ are obtained by differentiating the corresponding stresses with respect to strain and are given by

$$\mathbb{C}^{\pm} = \frac{E}{1-\nu^2}\left(H^{\pm}(E_\alpha + \nu E_\beta)\Big((\mathbf{M}_\alpha + \nu \mathbf{M}_\beta) \otimes \mathbf{M}_\alpha + (E_\alpha + \nu E_\beta)\frac{\partial \mathbf{M}_\alpha}{\partial \mathbf{E}} \Big), \quad \alpha \neq \beta. \right. \tag{5.48}$$

This can be rewritten as

$$\mathbb{C}^{\pm} = \frac{E}{1-\nu^2} H^{\pm}(E_\alpha + \nu E_\beta)\Big(\mathbb{Q}_{\alpha\alpha} + \nu\mathbb{Q}_{\alpha\beta} + (E_\alpha + \nu E_\beta)\mathbb{M}_\alpha\Big), \quad \alpha \neq \beta. \tag{5.49}$$

Although the principal stress-based decomposition naturally satisfies the uniaxial tension condition, it presents several limitations that warrant attention.

First, this decomposition inherits the drawbacks of the principal stress-based wrinkling criterion, which may misclassify the transition between wrinkled and slack states. Specifically, when both principal stresses are non-positive, i.e., $S_1 \leq 0$ and $S_2 \leq 0$, while the first principal strain remains tensile, i.e., $E_1 > 0$, the criterion incorrectly identifies the configuration as slack, whereas the mixed criterion correctly classifies it as wrinkled. As a result, the model underestimates the effective stiffness, leading to an overly compliant response. Interestingly, when the Poisson's ratio ν is set to zero, the stress-based criterion implicitly reduces to one governed by principal strain. Under the same conditions $S_1 \leq 0$, $S_2 \leq 0$, the classification then depends solely on the sign of E_1, correcting the misclassification and restoring appropriate stiffness in such ambiguous cases.

Second, the material tensor constructed from this decomposition does not retain major symmetry in all membrane states. As discussed in Section 5.1, the fourth-order tensors $\mathbb{Q}_{\alpha\alpha}$ and $\mathbb{M}_\alpha$ are major symmetric, while $\mathbb{Q}_{\alpha\beta}$ for $\alpha \neq \beta$ is only minor symmetric. However, the sum $\mathbb{Q}_{12} + \mathbb{Q}_{21}$ is major symmetric. As a consequence, the resulting material tensor $\mathbb{C}_{\text{eff}}$ is major symmetric in taut and slack states, where $\mathbb{Q}_{12}$ and $\mathbb{Q}_{21}$ in the positive part either appear or vanish simultaneously. In contrast, this property is lost in the wrinkled state, where the second principal stresses S_2 is negative, and the material tensor contains only a single off-diagonal term, such as $\mathbb{Q}_{12}$, thereby reducing to a minor symmetric form. Notably, the major symmetry is recovered when the Poisson's ratio ν is set to zero, indicating that the symmetry structure is affected by the Poisson effect. In contrast, the strain-based decomposition maintains major symmetry of the material tensor across all membrane states. As shown in Equation (5.40), the off-diagonal components $\mathbb{Q}_{12}$ and $\mathbb{Q}_{21}$ are either both included or both excluded depending on the sign of $\text{tr}(\mathbf{E})$, and their combined contribution remains major symmetric.

Third, the stress decomposition is applied solely at the level of the stress tensor, by artificially suppressing the second principal stress in wrinkled regions, without introducing a corresponding modification in the strain field. This creates a fundamental inconsistency between the stress and strain representations. To illustrate this inconsistency, consider the linear isotropic constitutive relation. Enforcing zero stress in the second principal direction yields

$$S_2 = \frac{E}{1-\nu^2}(E_2 + \nu E_1) = 0, \tag{5.50}$$

which implies the following relation between the principal strains:

$$E_2 = -\nu E_1. \tag{5.51}$$

Substituting this into the expression for the first principal stress gives

$$S_1 = \frac{E}{1-\nu^2}\left(E_1 + \nu E_2\right) = \frac{E}{1-\nu^2}\left(E_1 - \nu^2 E_1\right) = E E_1. \tag{5.52}$$

This result shows that enforcing $S_2 = 0$ implicitly constrains the strain field through the relation $E_2 = -\nu E_1$. Substituting this condition into the constitutive law eliminates the influence of Poisson's ratio, leading to an effective response $S_1 = E E_1$ that coincides with a uniaxial tension state as if $\nu = 0$. However, in the stress-criterion-based model, the constitutive relation itself remains $S_1 = \frac{E}{1-\nu^2}\left(E_1 + \nu E_2\right)$, without any explicit constraint on E_2. This discrepancy reveals an inherent inconsistency between the stress and strain representations in the stress-based decomposition, since modifying the stress tensor alone implicitly alters the admissible strain field that the original constitutive law does not account for.

Based on the preceding analysis, a unified modification is introduced to preserve the key advantage of the stress-based decomposition, namely the inherent satisfaction of the uniaxial tension condition, while converting the purely stress-based wrinkling criterion into a mixed form. This is accomplished by adjusting the Poisson's ratio through the following expression:

$$\nu^* = H^+(E_2 + \nu E_1)\,\nu. \tag{5.53}$$

This formulation eliminates the effect of Poisson coupling in the wrinkled and slack states, where such transverse interaction is no longer physically relevant, and retains the classical Poisson behavior only in the taut state. In the slack state, where both principal strains are negative, only a small residual stress remains due to the degradation factor $\eta \ll 1$. Accordingly, any influence of Poisson coupling is insignificant and can be neglected. In the literature [81], this regime is sometimes referred to as secondary wrinkling and can be interpreted as a decoupled state, similar in nature to the wrinkled state.

Inserting Equation (5.53) into the stress expression in Equation (5.47) leads to the following form:

$$\mathbf{S}^{\pm} = \frac{E}{(1-\nu^{*2})} H^{\pm}(E_\alpha + \nu^* E_\beta)(E_\alpha + \nu^* E_\beta)\mathbf{M}_\alpha, \quad \alpha \neq \beta. \tag{5.54}$$

In turn, the material tangent tensor given in Equation (5.49) becomes

$$\mathbb{C}^{\pm} = \frac{E}{1-\nu^{*2}} H^{\pm}\left(E_\alpha + \nu^* E_\beta\right)\left(\mathbb{Q}_{\alpha\alpha} + \nu^* \mathbb{Q}_{\alpha\beta} + (E_\alpha + \nu^* E_\beta)\mathbb{M}_\alpha\right), \quad \alpha \neq \beta. \tag{5.55}$$

The associated strain energy density then takes the form

$$\psi^{\pm} = \frac{E}{2(1-\nu^{*2})} H^{\pm}\left(E_\alpha + \nu^* E_\beta\right)\left(E_\alpha + \nu^* E_\beta\right) E_\alpha, \quad \alpha \neq \beta. \tag{5.56}$$

As evident from Equation (5.55), this modification effectively combines the advantages of both stress- and strain-based decompositions and leads to two primary improvements. First, it eliminates the asymmetry introduced by the original stress-criterion-based model. In wrinkled regions, setting $\nu^* = 0$ removes the contribution from $\mathbb{Q}_{\alpha\beta}$, thereby restoring major symmetry in the material tensor, see Equation (5.55). Second, the approach guarantees consistency with

the uniaxial tension condition while aligning the classification of wrinkled states with the mixed criterion, enhancing the physical fidelity of the formulation.

5.3.3 Regularity and Convexity Analysis

The mathematical properties of strain energy functions in membrane wrinkling models plays a key role in ensuring both physical consistency and numerical stability. In particular, convexity, as characterized by the positive semi-definiteness of the Hessian matrix, guarantees the well-posedness of the variational problem and the uniqueness of minimizers, thereby facilitating robust convergence of numerical solvers. Meanwhile, the gradient of the energy function corresponds to the stress state, and its continuity is essential for reliable linearization. Non-smooth or discontinuous derivatives may lead to inaccurate residual predictions, causing Newton-type algorithms to oscillate or diverge. Therefore, analyzing convexity and derivative continuity is essential for validating the mathematical soundness and computational reliability of the proposed models.

The expressions for $\psi^{\pm}$ in the three proposed models are presented below in terms of principal strains. These correspond to the strain-criterion-based model:

$$\psi^{\pm} = \frac{E}{2(1-\nu^2)}\left(\nu H^{\pm}\left(E_\alpha + E_\beta\right)\left(E_\alpha + E_\beta\right)^2 + (1-\nu)\left(H^{\pm}\left(E_\alpha\right)E_\alpha^2\right)\right), \quad \alpha \neq \beta. \tag{5.57}$$

the stress-criterion-based model:

$$\psi^{\pm} = \frac{E}{2(1-\nu^2)} H^{\pm}(E_\alpha + \nu E_\beta)(E_\alpha + \nu E_\beta)E_\alpha, \quad \alpha \neq \beta. \tag{5.58}$$

and the mixed-criterion-based model:

$$\psi^{\pm} = \frac{E}{2(1-\nu^{*2})} H^{\pm}(E_\alpha + \nu^* E_\beta)(E_\alpha + \nu^* E_\beta)E_\alpha, \quad \alpha \neq \beta. \tag{5.59}$$

The effective energy is computed as $\psi_{\text{eff}} = \psi^+ + \eta\psi^-$, as defined in Equation (5.31).

To analyze the mathematical behavior of the energy functions, a uniform grid with resolution $n = 500$ is generated over the principal strain domain $[-0.1, 0.1]^2$, restricted to the physically admissible region $E_1 \geq E_2$. The material parameters are set as $E = 1$ and $\nu = 0.3$. The degradation factor η is tested with two values, $\eta = 0$ and $\eta = 10^{-4}$.

The first-order derivatives of the modified energy density $\psi_{\text{eff}}(E_1, E_2)$ are evaluated using central differences:

$$\frac{\partial \psi_{\text{eff}}}{\partial E_\alpha} \approx \frac{\psi_{\text{eff}}(E_\alpha + h) - \psi_{\text{eff}}(E_\alpha - h)}{2h}, \quad h = 10^{-6}. \tag{5.60}$$

At each grid point, the gradient magnitude is computed as

$$\|\nabla \psi_{\text{eff}}\| = \sqrt{\left(\frac{\partial \psi_{\text{eff}}}{\partial E_1}\right)^2 + \left(\frac{\partial \psi_{\text{eff}}}{\partial E_2}\right)^2}, \tag{5.61}$$

which reflects the rate of energy variation and highlights regions of rapid stress change.

To assess convexity and numerical stability, the second-order derivatives are approximated by finite differences to construct the Hessian matrix:

$$\mathbf{H} = \begin{bmatrix} \dfrac{\partial^2 \psi_{\text{eff}}}{\partial E_1^2} & \dfrac{\partial^2 \psi_{\text{eff}}}{\partial E_1 \partial E_2} \\ \dfrac{\partial^2 \psi_{\text{eff}}}{\partial E_2 \partial E_1} & \dfrac{\partial^2 \psi_{\text{eff}}}{\partial E_2^2} \end{bmatrix}. \tag{5.62}$$

The smallest eigenvalue $\lambda_{\min}$ of $\mathbf{H}$ is extracted at each point as an indicator of local convexity; non-negative $\lambda_{\min}$ implies positive semi-definiteness of the Hessian, and therefore ψ_{eff} is convex in that region.

Contour plots of $\lambda_{\min}(E_1, E_2)$ are generated to visualize convex and non-convex regions of the energy landscape. The contour $\lambda_{\min} = 0$ is highlighted with dashed lines to delineate the convexity boundary. In parallel, the gradient magnitude $\|\nabla \psi_{\text{eff}}\|$ is plotted to evaluate stress smoothness. In addition, the plots are partitioned into taut, wrinkled, and slack regions based on the mixed criterion, which is widely recognized as the most reliable classification of membrane states. These regions are annotated in all plots and separated by dashed curves to aid the interpretation of membrane behavior.

Figure 5.1 compares the regularity and convexity characteristics of the three proposed models with $\eta = 0$. Figures 5.1(a) and (b) correspond to the mixed-criterion-based model. In Figure 5.1(a), the distribution of $\|\nabla \psi_{\text{eff}}\|$ is continuous, indicating that the effective energy function $\psi_{\text{eff}}(E_1, E_2)$ is continuously differentiable over its domain and belongs to the class C^1. Figure 5.1(b) shows the minimum eigenvalue $\lambda_{\min}(\mathbf{H})$ of the Hessian matrix. Within each region (taut, wrinkled, slack), this eigenvalue remains constant and non-negative, implying that the Hessian is constant and positive semi-definite, and the energy function is convex in each region. However, $\lambda_{\min}$ exhibits discontinuities across region boundaries, and the function is therefore not globally C^2. Since these discontinuities are restricted to switching lines in the principal strain space, the lack of C^2 regularity has only limited effect on numerical behavior, and in practice, floating-point perturbations prevent iterates from remaining on switching lines, further mitigating any adverse effects.

Figures 5.1(c) and (d) illustrate the results for the strain-criterion-based model. The structure is comparable to that of the mixed-criterion-based model: the distribution of $\|\nabla \psi_{\text{eff}}\|$ is continuous, and $\lambda_{\min}$ remains non-negative and constant within each region but exhibits jumps across interfaces. The strain-criterion-based model also possesses C^1 regularity, piecewise convexity, and second-order discontinuities that are confined to boundary curves. Its numerical performance is therefore similarly stable.

In contrast, the stress-criterion-based model exhibits a different regularity structure. As shown in Figure 5.1(e), the gradient $\nabla \psi_{\text{eff}}$ is discontinuous across the interface between the slack and wrinkled regions, which implies that the function is not C^1. Moreover, Figure 5.1(f) indicates that $\lambda_{\min}(\mathbf{H})$ becomes negative within the wrinkled region, indicating a loss of local convexity. The combination of gradient discontinuity and loss of convexity may lead to numerical instabilities in variational formulations, such as abrupt changes in descent directions

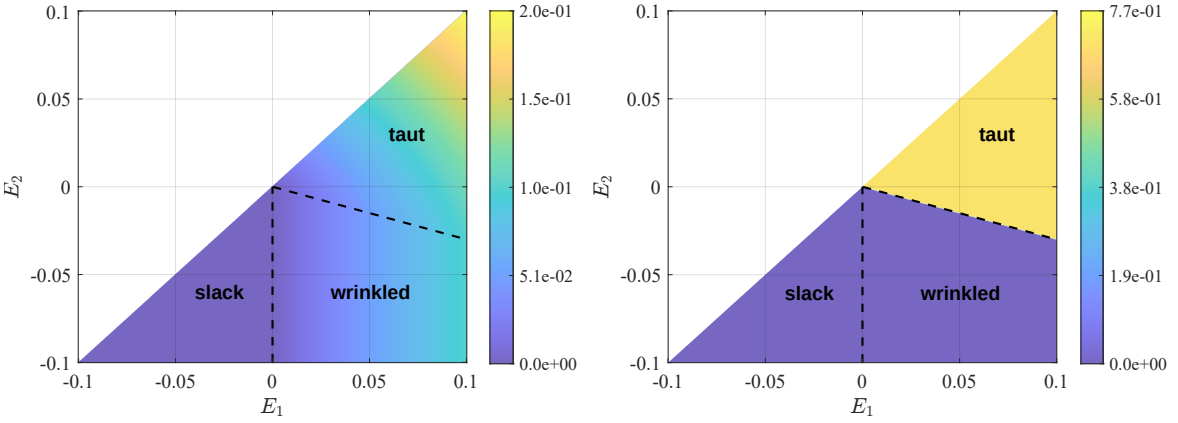

(a) $\|\nabla\psi_{\text{eff}}\|$ (mixed-criterion-based model)

(b) $\lambda_{\min}(\mathbf{H})$ (mixed-criterion-based model)

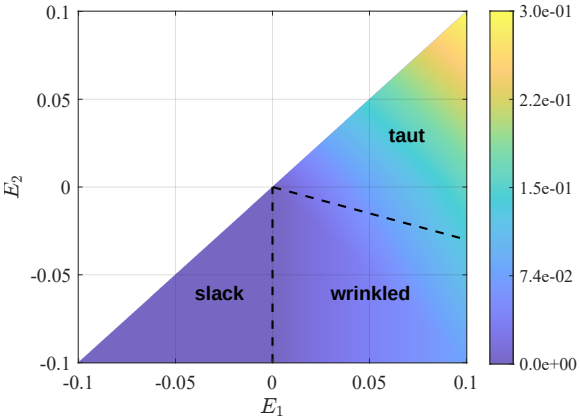

(c) $\|\nabla\psi_{\text{eff}}\|$ (strain-criterion-based model)

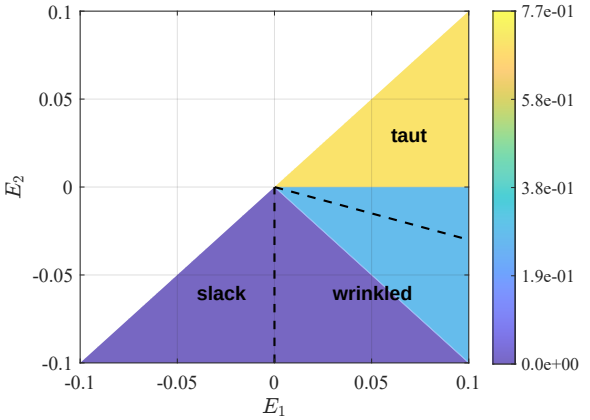

(d) $\lambda_{\min}(\mathbf{H})$ (strain-criterion-based model)

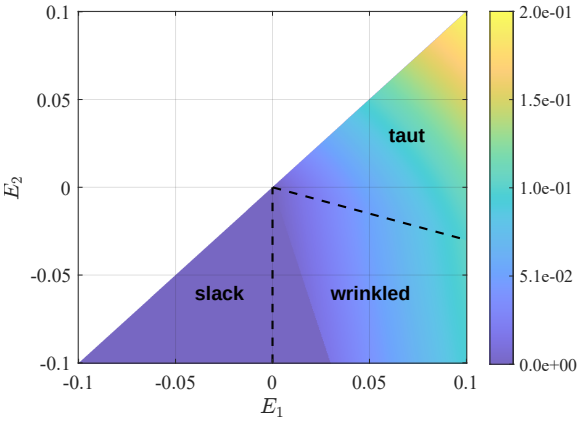

(e) $\|\nabla\psi_{\text{eff}}\|$ (stress-criterion-based model)

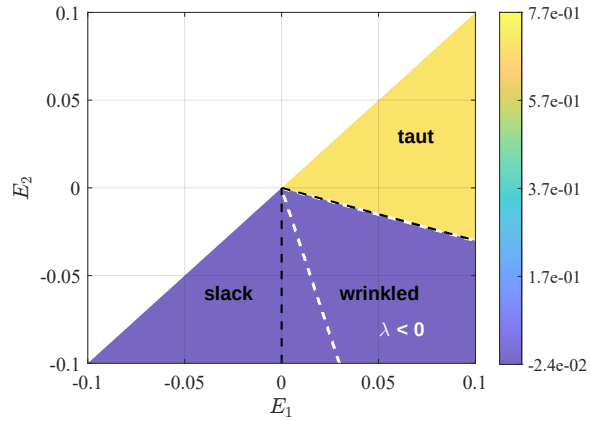

(f) $\lambda_{\min}(\mathbf{H})$ (stress-criterion-based model)

Figure 5.1.: Gradient magnitude $\|\nabla\psi_{\text{eff}}\|$ and minimum Hessian eigenvalue $\lambda_{\min}(\mathbf{H})$ of the effective energy function $\psi_{\text{eff}}(E_1, E_2)$ with $\eta = 0$ for three wrinkling models.

and oscillatory convergence. Although the stress-criterion-based model is physically intuitive and straightforward to construct, its limited regularity in the wrinkled region may pose risks in practical applications.

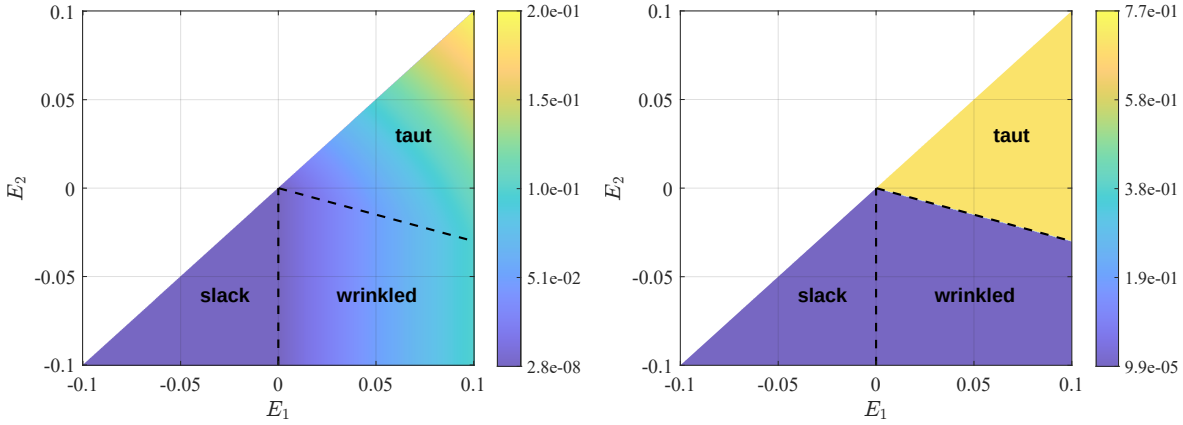

(a) $\|\nabla\psi_{\text{eff}}\|$ **(b)** $\lambda_{\min}(\mathbf{H})$

Figure 5.2.: Gradient magnitude $\|\nabla\psi_{\text{eff}}\|$ and minimum Hessian eigenvalue $\lambda_{\min}(\mathbf{H})$ of the effective energy function $\psi_{\text{eff}}(E_1, E_2)$ with $\eta = 10^{-4}$ for mixed- criterion-based model.

In addition, the case with $\eta = 10^{-4}$ is analyzed to evaluate the effect of penalization of compressive energy. The results for the mixed-criterion-based model are presented in Figure 5.2. Due to the similarity, only the mixed case is shown, while the results of the strain- and stress-criterion-based models are omitted for brevity. Compared to the case with $\eta = 0$, the minimum eigenvalue of the Hessian, $\lambda_{\min}(\mathbf{H})$, in the wrinkled and slack regions is no longer zero but raised to strictly positive values, indicating that the Hessian is positive definite within each of these regions and that the energy function is strictly convex there. Meanwhile, the gradient magnitude $\|\nabla\psi_{\text{eff}}\|$ remains continuous, and the energy function retains C^1 regularity. Nevertheless, discontinuities in the second derivatives persist across the interfaces between regions, and therefore the function remains piecewise C^2 rather than globally C^2. This lack of C^2 regularity originates from the non-smooth nature of the Heaviside function employed in the model, which could theoretically be alleviated by adopting smoother approximations.

5.4 Generalization to Hyperelastic Membranes

This section aims to extend the wrinkling model to hyperelastic membranes by adopting the same underlying strategy as in the linear elastic case: the stress and material tensors are decomposed into positive and negative components, enabling the taut, wrinkled, and slack states to be represented within a single expression. However, within this framework, the proper decomposition of stress becomes particularly crucial due to the nonlinear nature of hyperelasticity and the requirement to satisfy the uniaxial tension condition. To this end, a modified deformation gradient is introduced following the approach proposed by [99].

The modified deformation gradient $\tilde{\mathbf{F}}$ introduces a virtual extension along the wrinkle direction, as defined in Equation (4.5). For isotropic materials, the wrinkle direction coincides with the second principal direction of stress or strain, owing to the coaxiality of the stress and strain tensors, which share the same principal directions. See A.3 for a proof. Accordingly, the

modified strain tensor $\mathbf{E}'$ for the wrinkled state, as defined in Equation (4.32), takes the form

$$\mathbf{E}' = \mathbf{E} + \gamma_w \mathbf{M}_2, \tag{5.63}$$

where γ denotes the amplitude of strain in the wrinkling direction and the additional term is the so-called wrinkled strain $\mathbf{E}_w = \gamma_w \mathbf{M}_2$. The modified stress in the wrinkled state for hyperelastic materials, expressed as $\mathbf{S}' = \mathbf{S}(\mathbf{E}')$, is obtained by linearizing the stress tensor about the Green–Lagrange strain $\mathbf{E}$, i.e.,

$$\mathbf{S}' = \mathbf{S}(\mathbf{E}') = \mathbf{S}(\mathbf{E}) + \frac{\partial \mathbf{S}}{\partial \mathbf{E}} : \mathbf{E}_w + O(\mathbf{E}_w^2) \approx \mathbf{S}(\mathbf{E}) + \mathbb{C}(\mathbf{E}) : \mathbf{E}_w. \tag{5.64}$$

Substituting the expression of wrinkled strain into the constitutive relation yields the corresponding stress tensor:

$$\mathbf{S}' = \mathbb{C} : \mathbf{E}' = \mathbb{C} : (\mathbf{E} + \gamma_w \mathbf{M}_2) = \mathbf{S} + \gamma_w \mathbb{C} : \mathbf{M}_2. \tag{5.65}$$

The unknown scalar γ is determined by enforcing the uniaxial tension condition $\mathbf{S}' : \mathbf{M}_2 = 0$, which leads to

$$\gamma_w = -\frac{\mathbf{M}_2 : \mathbf{S}}{\mathbf{M}_2 : \mathbb{C} : \mathbf{M}_2}. \tag{5.66}$$

Since $\mathbf{M}_2$ is defined in the principal coordinate system, a transformation from the curvilinear coordinate frame is necessary. The full transformation procedure can be found in [51]. Substituting the expression for γ into Equation (5.65) yields a purely projection-based form for the stress:

$$\mathbf{S}' = \left(\mathbb{I} - \frac{1}{\mathbf{M}_2 : \mathbb{C} : \mathbf{M}_2} \, (\mathbb{C} : \mathbf{M}_2) \otimes \mathbf{M}_2 \right) : \mathbf{S} = \mathbb{B} : \mathbf{S}, \tag{5.67}$$

where $\mathbb{I}$ is the fourth-order identity tensor and $\mathbb{B}$ is a projection operator.

Using the spectral form $\mathbf{S} = S_1\mathbf{M}_1 + S_2\mathbf{M}_2 + S_3\mathbf{M}_3$, the modified stress becomes:

$$\mathbf{S}' = \left(\mathbb{I} - \frac{1}{\mathbf{M}_2 : \mathbb{C} : \mathbf{M}_2} \, (\mathbb{C} : \mathbf{M}_2) \otimes \mathbf{M}_2 \right) : (S_1\mathbf{M}_1 + S_2\mathbf{M}_2 + S_3\mathbf{M}_3) \, . \tag{5.68}$$

Given the orthogonality condition $\mathbf{M}_i : \mathbf{M}_j = \delta_{ij}$, the projection simplifies, resulting in:

$$\mathbf{S}' = S_1\mathbf{M}_1 + S_2\mathbf{M}_2 + S_3\mathbf{M}_3 - \frac{S_2}{\mathbf{M}_2 : \mathbb{C} : \mathbf{M}_2} \, \mathbb{C} : \mathbf{M}_2. \tag{5.69}$$

In this expression, the first three terms reconstruct the original stress tensor, while the last term provides a correction aligned with the wrinkling direction. To capture all possible membrane states (taut, wrinkled, and slack) within a unified variationally consistent formulation, the stress tensor in Equation (5.69) is decomposed into positive and negative parts according to the mixed wrinkling criterion proposed in [115]:

$$\mathbf{S}^{\pm} = H^{\pm}(E_1) \, \mathbf{S} \pm H^{-}(S_2) H^{+}(E_1) \, \frac{-S_2}{\mathbf{M}_2 : \mathbb{C} : \mathbf{M}_2} \, \mathbb{C} : \mathbf{M}_2, \tag{5.70}$$

where $E_1 = \lambda_1^2 - 1$, with λ_1 denoting the first principal stretch in hyperelastic materials.

The corresponding material tensors are derived by differentiating $\mathbf{S}^{\pm}$ with respect to the Cauchy–Green deformation tensor $\mathbf{C}$:

$$\begin{aligned}\mathbb{C}^{\pm} = 2\frac{\partial \mathbf{S}^{\pm}}{\partial \mathbf{C}} = H^{\pm}(E_1)\,\mathbb{C} \pm H^{-}(S_2)H^{+}(E_1)\Bigg(2\frac{\partial S_2}{\partial \mathbf{C}} \otimes \left(\frac{-1}{\mathbf{M}_2 : \mathbb{C} : \mathbf{M}_2}\,\mathbb{C} : \mathbf{M}_2\right) \\ + 2S_2\frac{\partial}{\partial \mathbf{C}}\left(\frac{-1}{\mathbf{M}_2 : \mathbb{C} : \mathbf{M}_2}\,\mathbb{C} : \mathbf{M}_2\right)\Bigg).\end{aligned} \tag{5.71}$$

The derivative of the second term in Equation (5.71) can be written as:

$$\begin{aligned}\frac{\partial}{\partial \mathbf{C}}\left(\frac{-1}{\mathbf{M}_2 : \mathbb{C} : \mathbf{M}_2}\,\mathbb{C} : \mathbf{M}_2\right) = -\Bigg(\frac{\partial}{\partial \mathbf{C}}\left(\frac{1}{\mathbf{M}_2 : \mathbb{C} : \mathbf{M}_2}\right) \otimes (\mathbb{C} : \mathbf{M}_2) \\ + \frac{1}{\mathbf{M}_2 : \mathbb{C} : \mathbf{M}_2}\left(\frac{\partial \mathbb{C}}{\partial \mathbf{C}} : \mathbf{M}_2 + \mathbb{C} : \frac{\partial \mathbf{M}_2}{\partial \mathbf{C}}\right)\Bigg).\end{aligned} \tag{5.72}$$

For the scalar prefactor, the derivative is given by:

$$\frac{\partial}{\partial \mathbf{C}}\left(\frac{1}{\mathbf{M}_2 : \mathbb{C} : \mathbf{M}_2}\right) = -\frac{\frac{\partial \mathbf{M}_2}{\partial \mathbf{C}} : \mathbb{C} : \mathbf{M}_2 + \mathbf{M}_2 : \frac{\partial \mathbb{C}}{\partial \mathbf{C}} : \mathbf{M}_2 + \mathbf{M}_2 : \mathbb{C} : \frac{\partial \mathbf{M}_2}{\partial \mathbf{C}}}{(\mathbf{M}_2 : \mathbb{C} : \mathbf{M}_2)^2}. \tag{5.73}$$

As evident from these expressions, full evaluation of $\mathbb{C}^{\pm}$ requires the derivatives $\partial S_2/\partial \mathbf{C}$, $\partial \mathbf{M}_2/\partial \mathbf{C}$, and $\partial \mathbb{C}/\partial \mathbf{C}$.

The derivative $\partial S_2/\partial \mathbf{C}$ can be computed via the chain rule using the principal stretches λ_i:

$$\frac{\partial S_2}{\partial \mathbf{C}} = \frac{\partial S_2}{\partial \lambda_i^2}\frac{\partial \lambda_i^2}{\partial \mathbf{C}} = \frac{1}{2\lambda_i}\frac{\partial S_2}{\partial \lambda_i}\,\mathbf{M}_i. \tag{5.74}$$

The specific form of $\partial S_2/\partial \lambda_i$ depends on the form of the hyperelastic strain energy density ψ. For compressible materials, $\partial S_2/\partial \lambda_i$ can be directly computed from the second derivatives of the strain energy function expressed in terms of the principal stretches. For incompressible materials, the expression is more involved owing to the incompressibility constraint and follows the formulation given in [51]:

$$\begin{aligned}\frac{\partial S_\alpha}{\partial \lambda_\beta} = \frac{1}{\lambda_\alpha}\Bigg(\frac{\partial^2 \psi}{\partial \lambda_\alpha \partial \lambda_\beta} - \frac{1}{\lambda_\beta}\left(\lambda_3 \frac{\partial^2 \psi}{\partial \lambda_3 \partial \lambda_\alpha} + \delta^3_\alpha \frac{\partial \psi}{\partial \lambda_3}\right) \\ - \frac{1}{\lambda_\alpha}\left(\lambda_3 \frac{\partial^2 \psi}{\partial \lambda_3 \partial \lambda_\beta} + \delta^3_\beta \frac{\partial \psi}{\partial \lambda_3}\right) - \lambda_3 \frac{\partial \psi}{\partial \lambda_3}\frac{1-\delta^\beta_\alpha}{\lambda_\alpha \lambda_\beta} \\ - \delta^\beta_\alpha \frac{1}{\lambda_\alpha}\left(\frac{\partial \psi}{\partial \lambda_\alpha} - \frac{1}{\lambda_\alpha}\lambda_3 \frac{\partial \psi}{\partial \lambda_3}\right)\Bigg).\end{aligned} \tag{5.75}$$

The derivative of $\mathbf{M}_2$ is obtained via the spectral projector formula given in Equation (5.4), and the sixth-order tensor $\mathbb{D} = \partial\mathbb{C}/\partial\mathbf{C}$ can be evaluated either analytically or via finite differences [136]. To simplify computation, the term involving $\mathbb{D}$ may be disregarded; however, as a consequence, the Newton–Raphson method may no longer exhibit its standard quadratic convergence behavior.

Following the framework defined in Equation (5.31), the stress and material tensors are modified as $\mathbf{S}_{\text{eff}} = \mathbf{S}^+ + \eta\,\mathbf{S}^-$ and $\mathbb{C}_{\text{eff}} = \mathbb{C}^+ + \eta\,\mathbb{C}^-$, where $\eta \ll 1$ allows controlled retention or suppression of compressive components, thus enabling a hyperelastic wrinkling model applicable across all membrane states.

Remark 5.1. Equation (5.69) can be simplified in the case of linear elasticity under plane stress conditions. Specifically, the term involving $\mathbf{M}_2$ reduces to

$$S_2\mathbf{M}_2 + \frac{-S_2}{\mathbf{M}_2 : \mathbb{C} : \mathbf{M}_2}\mathbb{C} : \mathbf{M}_2 = -\nu S_2\mathbf{M}_1, \tag{5.76}$$

as a result of the following identities in isotropic plane stress elasticity.

The constitutive tensor is given by

$$\mathbb{C} = \left(\lambda - \frac{\lambda^2}{\lambda + 2\mu}\right)\mathbf{I}\otimes\mathbf{I} + 2\mu\mathbb{I} = \frac{E}{1-\nu^2}\left(\nu\,\mathbf{I}\otimes\mathbf{I} + (1-\nu)\,\mathbb{I}\right), \tag{5.77}$$

where all quantities follow their standard definitions in isotropic plane stress elasticity, as introduced previously. Using the spectral decomposition $\mathbf{I} = \mathbf{M}_1 + \mathbf{M}_2$ and the orthogonality relation

$$\mathbf{I} : \mathbf{M}_2 = (\mathbf{M}_1 + \mathbf{M}_2) : \mathbf{M}_2 = 1, \tag{5.78}$$

the following contractions can be evaluated:

$$\mathbb{C} : \mathbf{M}_2 = \frac{E}{1-\nu^2}\left(\nu\,\mathbf{I} + (1-\nu)\,\mathbf{M}_2\right), \quad \mathbf{M}_2 : \mathbb{C} : \mathbf{M}_2 = \frac{E}{1-\nu^2}, \tag{5.79}$$

which leads directly to the identity

$$\mathbf{M}_2 + \left(-\frac{1}{\mathbf{M}_2 : \mathbb{C} : \mathbf{M}_2}\right)\mathbb{C} : \mathbf{M}_2 = -\nu\,\mathbf{M}_1. \tag{5.80}$$

Substituting into Equation (5.69), the modified stress tensor under plane stress simplifies to

$$\mathbf{S}' = S_1\mathbf{M}_1 - \nu S_2\mathbf{M}_1, \tag{5.81}$$

where the principal stresses S_1 and S_2 are related to the principal strains through the standard plane stress relations: $S_1 = \frac{E}{1-\nu^2}(E_1 + \nu E_2)$, and $S_2 = \frac{E}{1-\nu^2}(E_2 + \nu E_1)$. Inserting these expressions into Equation (5.81) yields the compact result

$$\mathbf{S}' = EE_1\mathbf{M}_1, \tag{5.82}$$

which coincides with the wrinkled-state stress representation given in Equation (5.54).

Chapter 6

Numerical Examples

This chapter presents a series of numerical examples designed to evaluate the performance of the proposed wrinkling formulations. The test cases cover a broad spectrum of loading and boundary conditions for membrane structures, including in-plane bending, torsion, shear, biaxial stretching, inflation, free fall, and dynamic response problems. The aim is to demonstrate the accuracy, robustness, and convergence behavior of the proposed approach in both static and dynamic regimes, ranging from fundamental benchmarks with available reference solutions to more complex configurations representative of engineering applications.

In the elastic setting (Section 6.1), three different wrinkling models are developed and compared in this thesis: the strain-criterion-based model, the stress-criterion-based model, and the mixed-criterion-based model. These comparisons provide a comprehensive assessment of alternative decomposition strategies. In the hyperelastic setting (Section 6.2), the focus is placed on validating the applicability of the proprosed model to nonlinear material behavior. Due to the inherent complexity of hyperelastic constitutive responses, only a limited number of benchmark examples are available in the literature. Therefore, the proposed results are further compared against those obtained with Kirchhoff–Love shell elements, which serve as a high-fidelity reference.

In addition, unless otherwise specified, all numerical examples are conducted with the degradation factor set to $\eta = 0$.

6.1 Wrinkling in Elastic Membranes

6.1.1 In-Plane Bending of a Rectangular Membrane

In the first numerical example, the predictive performance of the proposed wrinkling models is evaluated using a classical benchmark problem involving the in-plane bending of a pre-stretched rectangular membrane. This test case, originally formulated by [73], has been widely adopted for the validation of wrinkling models, as demonstrated in [82, 91, 104, 108, 137–139].

The membrane is rectangular in shape, with geometric dimensions denoted by length L, height H, and thickness t. It is modeled as an isotropic, linear elastic material characterized by

Young's modulus E and Poisson's ratio ν. These quantities are defined to provide physical meaning to the analytical and numerical formulations, although their specific values are not required in the derivation of the analytical solution.

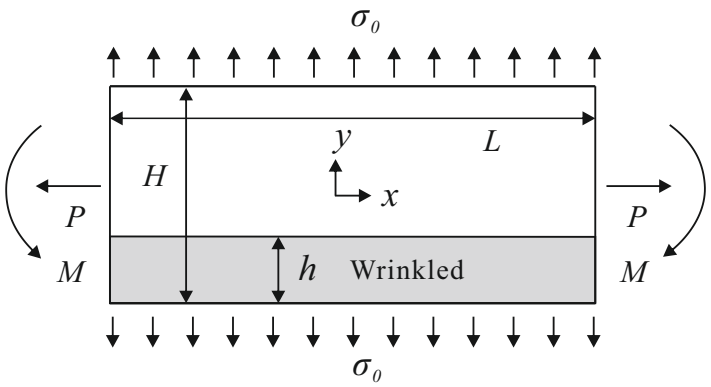

Figure 6.1.: In-plane pure bending of a pre-tensioned rectangular membrane [115].

As illustrated in Figure 6.1, the membrane is subjected to a uniform pre-stretching stress σ_0 along the y-direction. Axial forces $P = \sigma_0 tH$ and bending moments M are applied on the lateral boundaries. As the bending moment increases, a wrinkling band of height h forms near the lower edge of the membrane, indicated by the shaded region. The analytical expression describing the onset and growth of the wrinkling band is given by [73] as:

$$\frac{h}{H} = \begin{cases} 0 & M/PH < 1/6 \\ 3M/PH - 1/2 & 1/6 \leq M/PH < 1/2 \end{cases}. \tag{6.1}$$

Within the wrinkled region, the axial stress σ_x vanishes entirely, while the membrane remains taut in the unwrinkled upper region. The corresponding distribution of axial stress along the vertical coordinate is:

$$\frac{\sigma_x}{\sigma_0} = \begin{cases} \frac{2(y/H - h/H)}{(1-h/H)^2} & h/H < y/H \leq 1 \\ 0 & 0 \leq y/H \leq h/H \end{cases}, \tag{6.2}$$

where y/H is the normalized vertical position within the membrane.

Additionally, the moment–curvature relation describing the bending response of the membrane is given by:

$$\frac{2M}{PH} = \begin{cases} \frac{EH^2 t\kappa}{6P} & \frac{EH^2 t\kappa}{2P} \leq 1 \\ 1 - \frac{2}{3}\sqrt{\frac{2P}{EH^2 t\kappa}} & \frac{EH^2 t\kappa}{2P} > 1 \end{cases}, \tag{6.3}$$

where κ denotes the curvature of the deformed configuration.

In the numerical simulations, symmetry is exploited by modeling only the right half of the membrane, as shown in Figure 6.2. The simulations adopt $L = 2$, $H = 1$, $t = 0.01$, $E = 100$, and $\sigma_0 = 5 \times 10^{-4}$ as fixed parameters. The Poisson's ratio ν is varied and specified in each respective test case. The membrane is discretized using an 11×5 bi-quadratic isogeometric mesh, following the method described in [96]. Symmetry conditions are enforced

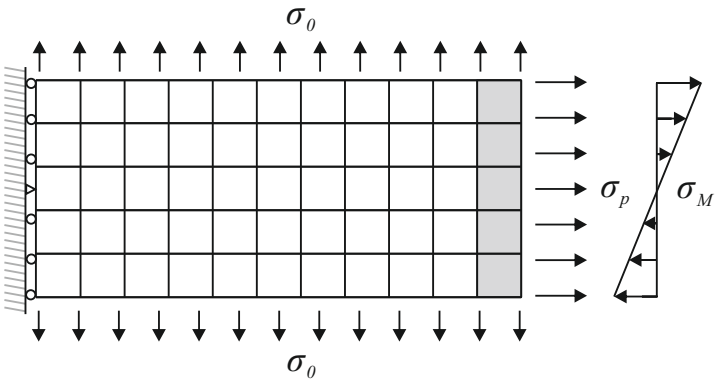

Figure 6.2.: Numerical simulation settings for the right half of the rectangular membrane under in-plane bending [115].

by constraining horizontal displacement along the entire left boundary and fixing the vertical displacement at its midpoint. Equivalent stress distributions are applied to represent the axial load and bending moment, given by $\sigma_p = P/tH$ and $\sigma_M = 6M/tH^2(2y/H - 1)$, respectively. The bending moment is increased incrementally over a range of moment-load ratios $2M/PH$, from 0.4 to 0.825. In order to maintain uniform bending, the membrane elements located at the far right edge are assumed to remain taut and are modeled without incorporating wrinkling modifications.

To evaluate the predictive performance of the proposed wrinkling models, a comparison is made between the normal stress component σ_x predicted by each model and the corresponding analytical solution. The stress distributions are examined under varying moment–load ratios

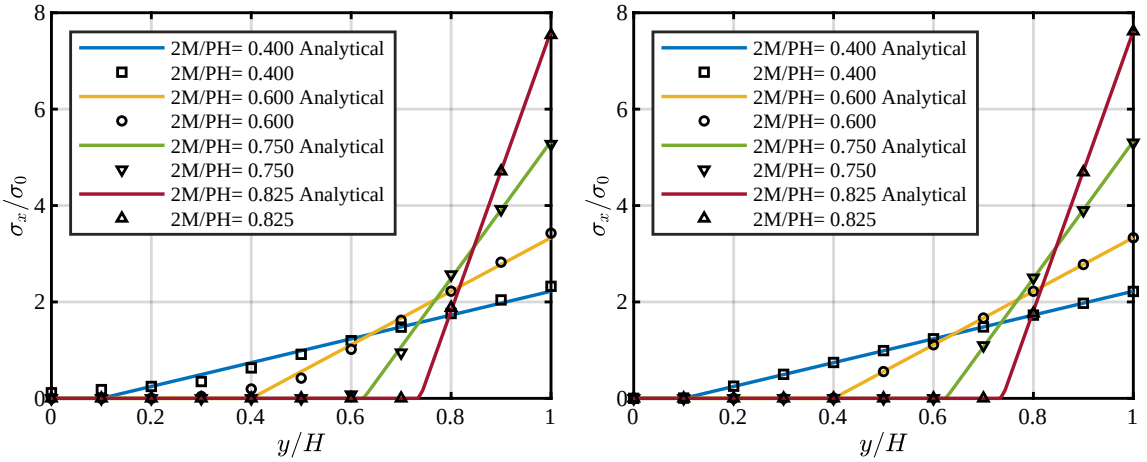

(a) Poisson's ratio $\nu = 0.3$ **(b)** Poisson's ratio $\nu = 0$

Figure 6.3.: Normal stress σ_x predicted by the strain-criterion-based model and compared with the analytical solution for various $2M/PH$ values: (a) $\nu = 0.3$, (b) $\nu = 0$ [114].

$2M/PH$, with the normalized vertical coordinate y/H used as the horizontal axis to ensure consistency across all cases.

For the strain-criterion-based model, the predicted stress distributions are shown in Figure 6.3.

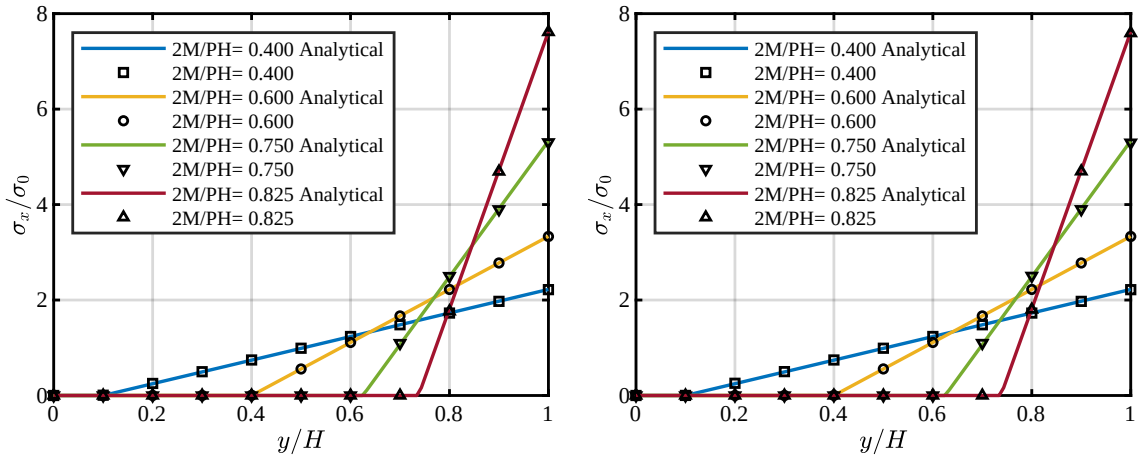

(a) Stress-criterion-based model **(b)** Mixed-criterion-based model

Figure 6.4.: Normal stress σ_x predicted by (a) the stress-criterion-based model and (b) the mixed-criterion-based model, compared with the analytical solution for various $2M/PH$ values at Poisson's ratio $\nu = 0.3$ [115].

When Poisson's ratio is set to $\nu = 0$, the numerical results coincide exactly with the analytical profile, as shown in Figure 6.3(b). In contrast, a slight deviation is observed for $\nu = 0.3$, particularly at $2M/PH = 0.4$ and 0.6, as illustrated in Figure 6.3(a).

This discrepancy can be attributed to two fundamental differences between the two approaches. First, the analytical solution determines the wrinkled region based on a principal stress criterion, explicitly enforcing the second principal stress to vanish within the wrinkled zone. The strain-criterion-based model, however, does not inherently satisfy this condition, and may thus allow nonzero second principal stress in regions identified as wrinkled. Second, as discussed in Section 5.3.1, the strain-criterion-based model additionally relies on tr($\mathbf{E}$), the trace of the Green–Lagrange strain tensor. As shown in Equation (5.39), the uniaxial tension

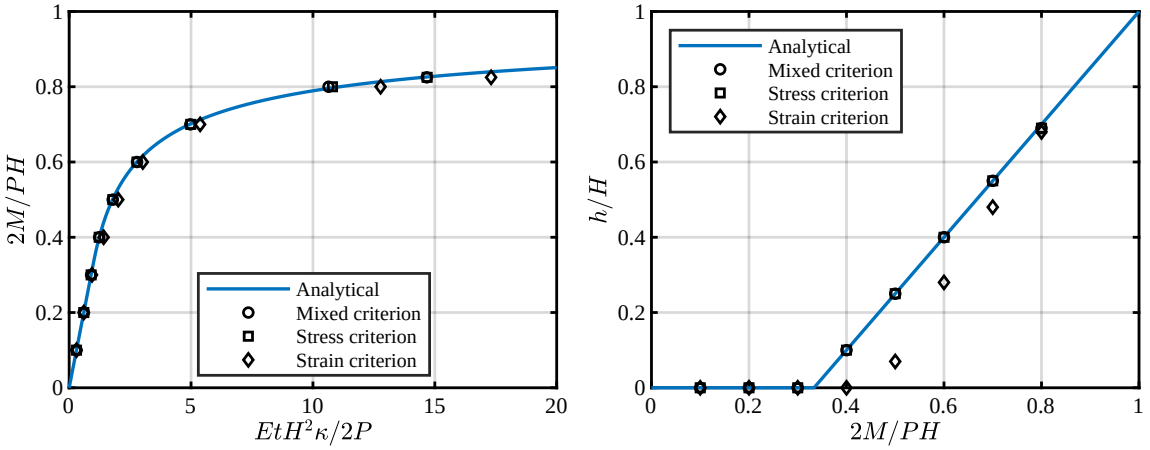

(a) Moment–curvature relation **(b)** Moment–wrinkling height relation

Figure 6.5.: Comparison of model predictions with the analytical solution [115]: (a) moment–curvature relation, and (b) moment–wrinkling height relation.

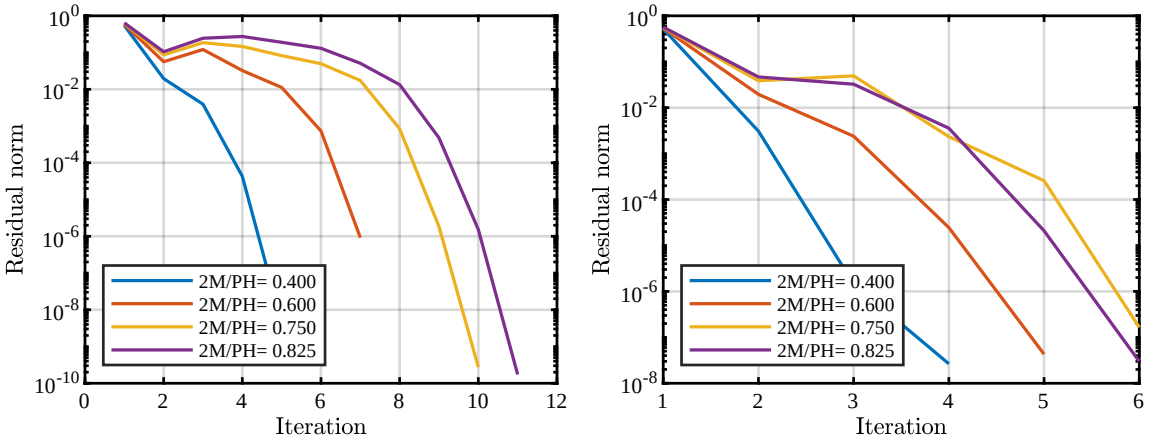

(a) Strain-criterion-based model

(b) Stress-criterion-based model

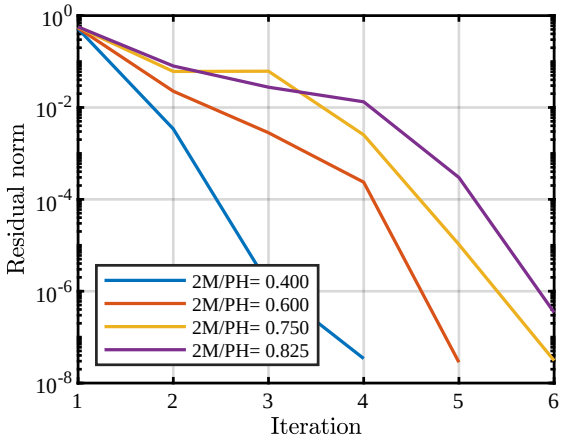

(c) Mixed-criterion-based model

Figure 6.6.: Convergence behavior of the proposed models [115]: number of iterations required during the second load step to reach the residual tolerance for (a) strain-, (b) stress-, and (c) mixed-criterion-based models.

condition is satisfied only when $\mathrm{tr}(\mathbf{E}) \leq 0$. When Poisson's ratio is set to zero, the lateral strain vanishes and the trace term becomes zero, allowing the condition to hold throughout the wrinkled region and yielding full consistency with the analytical solution. Despite the deviations observed at lower moments, the difference remains small and is negligible for practical purposes, as further supported by the subsequent examples.

By contrast, the mixed-criterion-based model produce results that are in complete agreement with the analytical solution across all loading stages, as illustrated in Figures 6.4(a) and 6.4(b). For the stress-criterion-based model, although it has been discussed in the corresponding section that it merely eliminates the stress artificially without making a corresponding adjustment to the strain, its impact in this example may be negligible. This suggests that, within the wrinkled region, the condition $E_2 = -\nu E_1$ may be satisfied, thereby yielding results consistent with the analytical solution. However, it is highly likely that this occurs only under such specific boundary conditions.

To further evaluate model performance, Figure 6.5(a) compares the predicted moment–

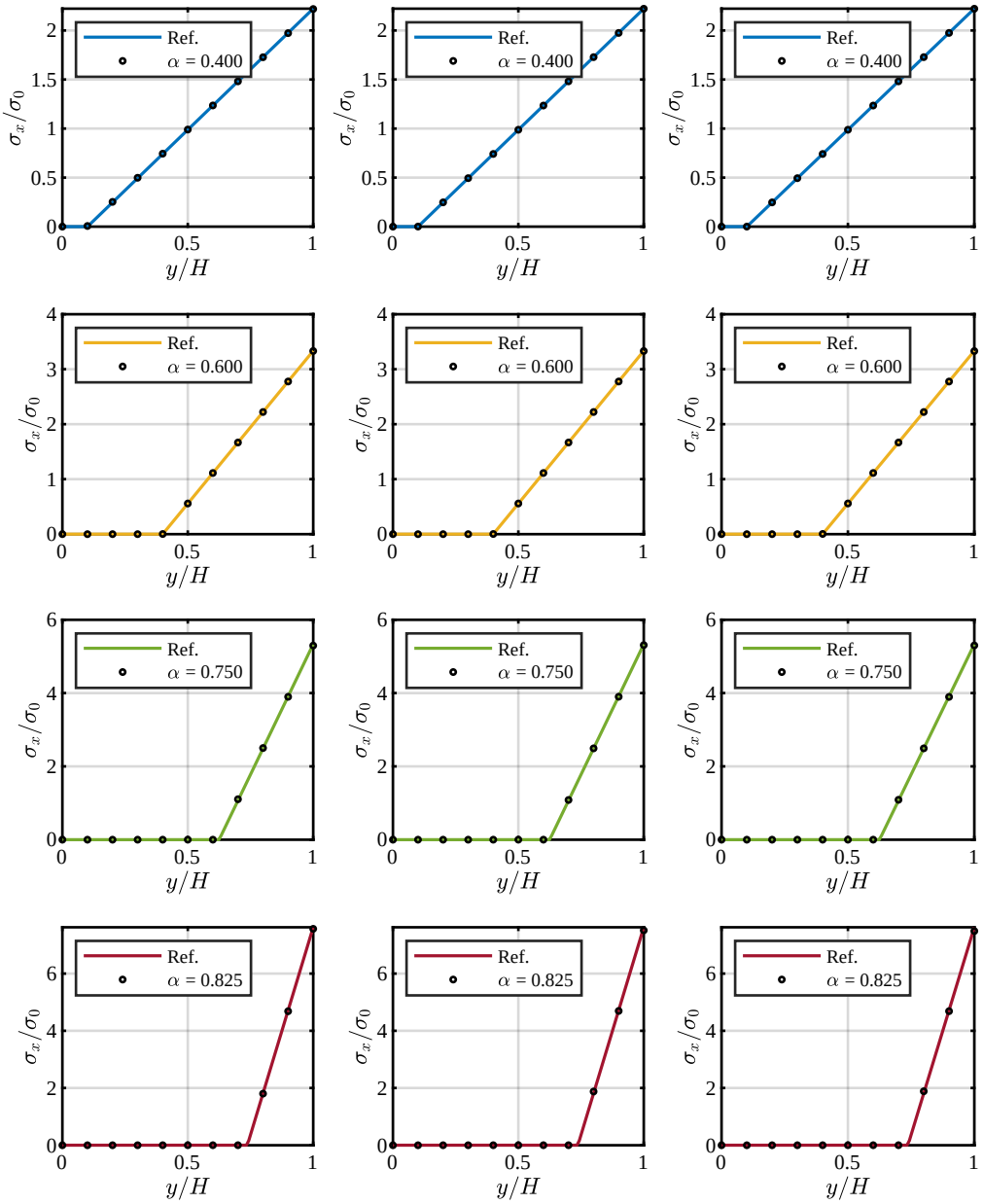

Figure 6.7.: Mesh convergence study of the proposed wrinkling model (mixed-criterion-based, $p = 2$, $\nu = 0.3$): distribution of normalized normal stress σ_x/σ_0 along the membrane height y/H under different moment-load ratio $\alpha = 2M/PH$. From left to right, results are shown for meshes with 11×5, 23×11, and 43×21 elements. The analytical solution (Ref.) is shown as a solid line.

curvature response, while Figure 6.5(b) presents the corresponding evolution of the wrinkled band height. Both the mixed-criterion-based and stress-criterion-based models demonstrate excellent agreement with the analytical solution over the full range of moment-load ratios, accurately capturing the global curvature and the extent of the wrinkled region.

By contrast, the strain-criterion-based model exhibits noticeable deviations in the predicted wrinkle height, particularly at lower moment levels (see Figure 6.5(b)). This discrepancy

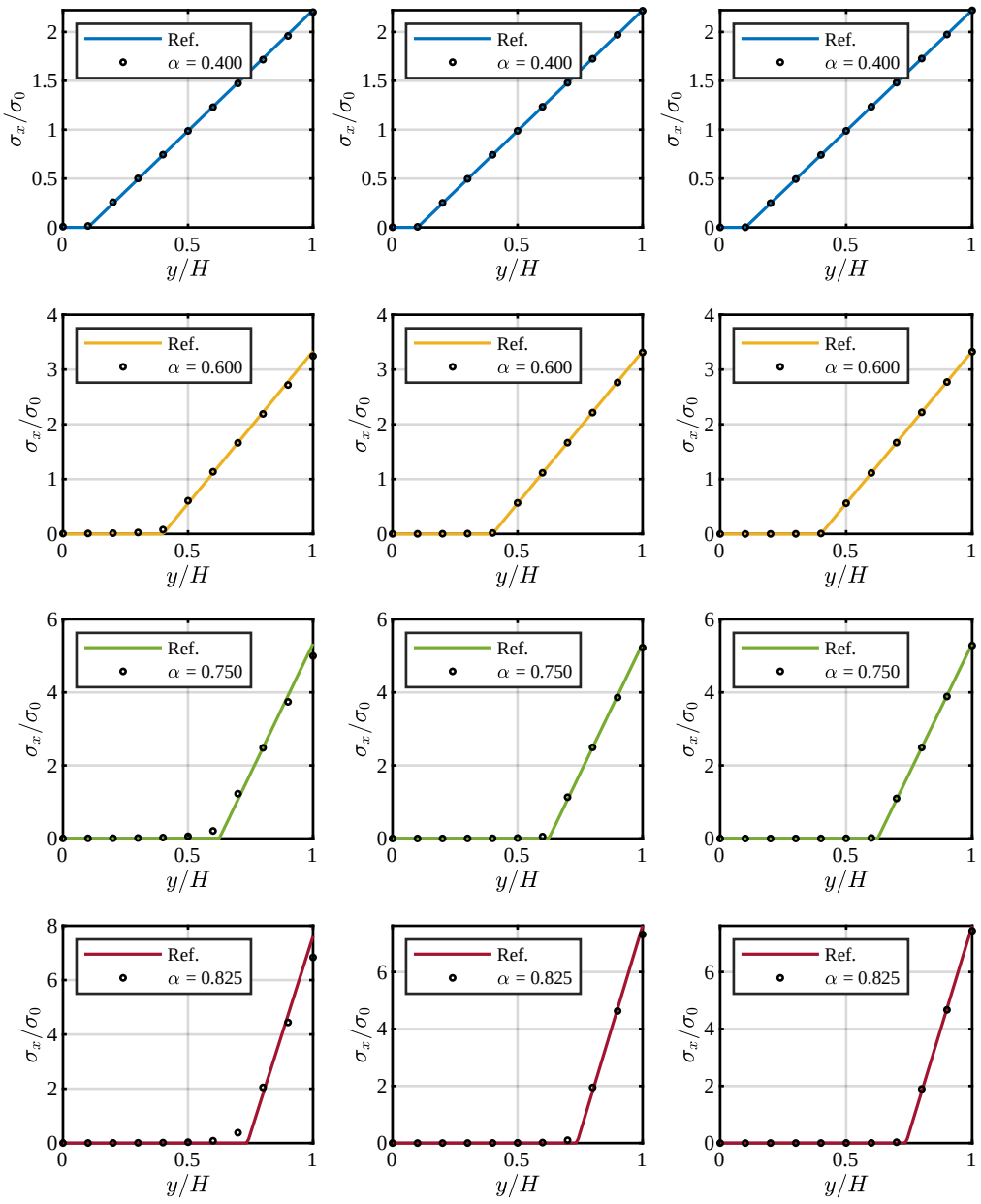

Figure 6.8.: Mesh convergence study of the proposed wrinkling model (mixed-criterion-based, $p = 1$, $\nu = 0.3$): distribution of normalized normal stress σ_x/σ_0 along the membrane height y/H under different load parameters $\alpha = 2M/PH$. From left to right, results are shown for meshes with 11×5, 23×11, and 43×21 elements. The analytical solution (Ref.) is shown as a solid line.

diminishes gradually as the bending moment increases. The underlying cause has been previously explained in the context of stress prediction and is not repeated here.

In addition to predictive accuracy, the convergence behavior of the three wrinkling models is compared in Figure 6.6, which shows the residual norm versus iteration count for the second load step, identified as the most computationally intensive step in the simulation. Among

the three, the mixed- and the stress-criterion-based models exhibit comparable convergence performance, both requiring the fewest iterations to meet the prescribed tolerance. In contrast, the strain-criterion-based model shows slightly slower convergence, especially at higher bending moment levels, where up to 10 or more iterations are needed. These results highlight the computational advantage of the mixed-criterion-based model, which remain robust and efficient across different loading conditions.

Based on the results discussed above, the mixed-criterion-based model can be regarded as the most reliable among the three formulations in terms of predictive accuracy and convergence behavior. To further demonstrate its robustness, a mesh convergence study is conducted and presented in Figure 6.7, which shows the distribution of the normal stress component σ_x along the membrane height H for various values of the moment load ratio (denoted by $\alpha = 2M/PH$ for convenience), using different mesh densities with polynomial degree $p = 2$. The results confirm that the model maintains consistent accuracy under mesh refinement. Similar convergence behavior is also observed for the strain- and stress-criterion-based models in this benchmark problem and is therefore omitted here to avoid redundancy.

To demonstrate compatibility with standard finite element discretizations, the corresponding results with $p = 1$ are provided in Figure 6.8, indicating that the formulation remains effective with lower-order elements.

6.1.2 Torsion of a Annual Membrane

In the second numerical example, an annular membrane undergoing wrinkling due to the rotation of a rigid central hub is examined. This problem was first investigated by [73], and was subsequently extended by [74] to incorporate different connection types between the central hub and the membrane. It has since become a widely used benchmark for validating wrinkling models [82, 91, 96, 104, 137, 138]. The geometric configuration of the membrane is illustrated in Figure 6.9, characterized by an inner radius of a, an outer radius of b, and a thickness of t.

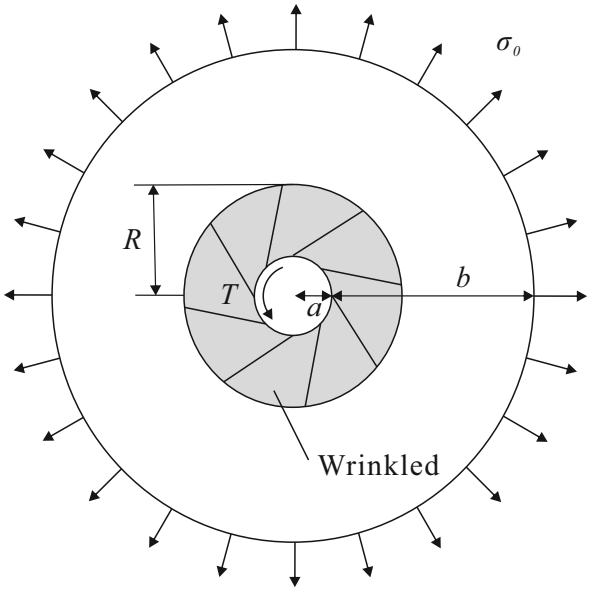

Figure 6.9.: Wrinkle formation in the annular membrane under torsion.

The inner boundary of the membrane is rigidly fixed to the central hub, ensuring no relative displacement, while the outer boundary is subjected to a uniform radial pre-stress σ_0, creating an initial tension state throughout the membrane. Additionally, a torque T is applied at the inner boundary, resulting in the rotation of the central hub by an angle ϕ. As the hub rotates, a wrinkled zone emerges in the region adjacent to the inner edge of the membrane, extending outward to a radius of R. With increasing applied torque T, the extent of the wrinkled region also grows progressively. An analytical formulation relating the wrinkle band radius R to the applied torsion T was derived in [74]. This relation is determined by solving the following equations:

$$\frac{1}{A} + \frac{1}{B} - \ln\left(\frac{B}{A}\right) - \frac{2}{3} = 0, \tag{6.4}$$

$$\bar{C}_1^2 - \left(1 + 2\bar{C}_1\left(\frac{a}{b}\right)^2\right)^2 \bar{R}^4 + \bar{T}^2 = 0, \tag{6.5}$$

$$\bar{C}_2 = \left(\bar{R} + \left(\frac{1}{\bar{R}} + 2\bar{R}\left(\frac{a}{b}\right)^2 \bar{C}_1\right)\right)^2 + \left(\frac{\bar{T}}{\bar{R}}\right)^2, \tag{6.6}$$

with

$$\bar{T} = \frac{T}{2\pi a^2 \sigma_0 t}, \quad \bar{R} = \frac{R}{a}, \quad A = \frac{\bar{C}_2}{\bar{T}^2} - 1, \quad B = \frac{\bar{R}^2 \bar{C}_2}{\bar{T}^2} - 1. \tag{6.7}$$

These expressions are based on the assumption that the Poisson's ratio ν of the membrane is $\frac{1}{3}$. Once $\bar{C}_1$, $\bar{C}_2$, and $\bar{T}$ are obtained, the nondimensionalized first and second principal stresses can be calculated as:

$$\frac{\sigma_1}{\sigma_0} = \begin{cases} \frac{\bar{C}_2/\bar{r}}{\sqrt{\bar{C}_2 - \bar{T}^2/\bar{r}^2}} & \bar{r} < \bar{R} \\ 2\bar{C}_1 \left(\frac{a}{b}\right)^2 + 1 + \frac{\sqrt{\bar{C}_1^2 + \bar{T}^2}}{\bar{r}^2} & \bar{r} \geq \bar{R} \end{cases}, \tag{6.8}$$

$$\frac{\sigma_2}{\sigma_0} = \begin{cases} 0 & \bar{r} < \bar{R} \\ 2\bar{C}_1 \left(\frac{a}{b}\right)^2 + 1 - \frac{\sqrt{\bar{C}_1^2 + \bar{T}^2}}{\bar{r}^2} & \bar{r} \geq \bar{R} \end{cases}, \tag{6.9}$$

where $\bar{r} = r/a$, with r denoting the radial distance from the hub center to the location of stress evaluation.

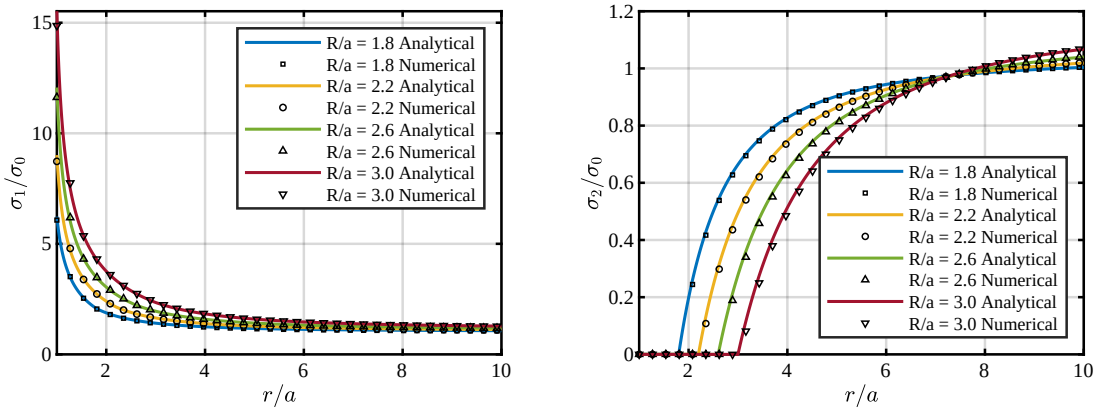

(a) First principal stress distribution

(b) Second principal stress distribution

Figure 6.10.: Comparison of the first (a) and second (b) principal stresses obtained from the mixed-criterion-based model with analytical solutions for various R/a ratios.

In the numerical simulation, the membrane has an inner radius of $a = 0.2\,\text{m}$, an outer radius of $b = 2\,\text{m}$, and a uniform thickness of $t = 1\,\text{mm}$. The material is modeled as linear elastic and isotropic, with Young's modulus $E = 1 \times 10^9\,\text{Pa}$ and Poisson's ratio $\nu = \frac{1}{3}$. A uniform radial stress $\sigma_0 = 1 \times 10^6\,\text{Pa}$ is prescribed as a prestress in the membrane. Since a surface element formulation is used, the actual quantity applied at the outer boundary is a line load of magnitude $\sigma_0 t$, where t denotes the membrane thickness. This ensures that the resulting in-plane stress state corresponds to the intended pre-tensioned condition. The domain is discretized using a 32×32 mesh of bi-quadratic elements. In the simulation, a series of wrinkle radii R/a ranging from 1.8 to 3.0 are prescribed. For each prescribed radius, the corresponding twisting angle ϕ is computed via Equations (6.4)–(6.6) and translated into nodal displacements applied along the inner boundary. The outer boundary remains fixed

during this process, ensuring that the deformation response captures the effect of imposed torsion.

The results of the numerical simulation using the mixed-criterion-based model are presented in Figure 6.10, together with the corresponding analytical results. Figure 6.10(a) and Figure 6.10(b) show the comparisons of the first and second principal stress distributions, respectively, under various prescribed R/a ratios. As shown in Figure 6.10(b), the mixed-criterion-based model accurately captures the transition between the wrinkled and taut regions, as well as the associated stress variations. In the wrinkled region, the stress decreases sharply to zero, whereas in the taut region, it gradually increases, in excellent agreement with the analytical trend. These results demonstrate the effectiveness of the mixed-criterion-based wrinkling model.

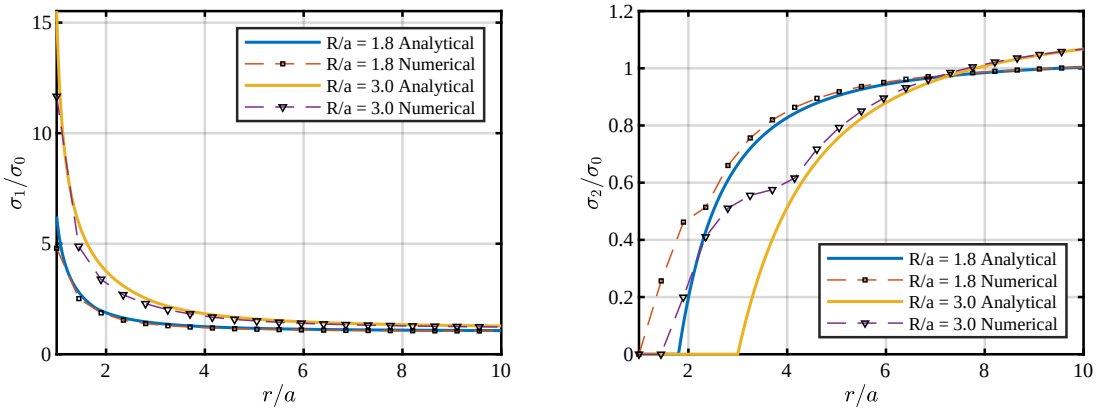

(a) First principal stress distribution **(b)** Second principal stress distribution

Figure 6.11.: Comparison of the first (a) and second (b) principal stresses obtained from the strain-criterion-based model with analytical solutions for various R/a ratios.

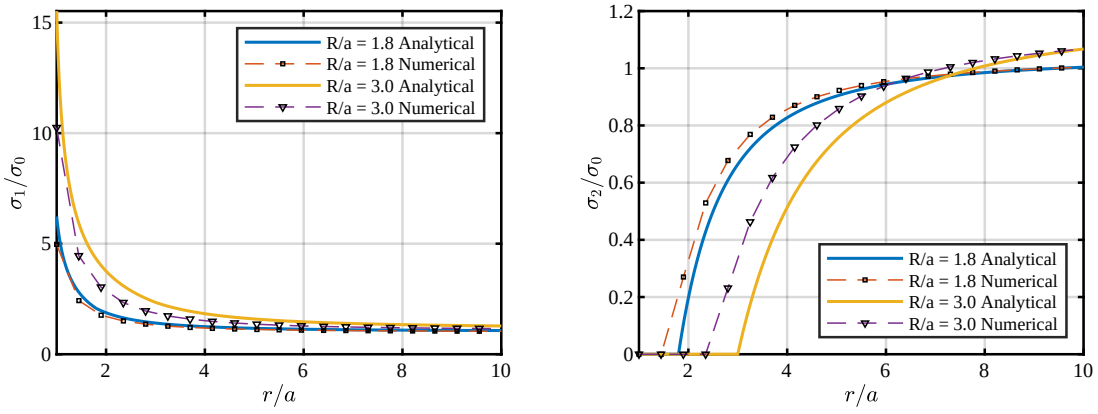

(a) First principal stress distribution **(b)** Second principal stress distribution

Figure 6.12.: Comparison of the first (a) and second (b) principal stresses obtained from the stress-criterion-based model with analytical solutions for various R/a ratios.

In contrast, the strain-, and stress-criterion-based models exhibit noticeable discrepancies

from the analytical solution in this torsion-dominated test case. The corresponding results are shown in Figure 6.11 and Figure 6.12, respectively. To highlight the differences more clearly, only two representative cases, $R/a = 1.8$ and $R/a = 3.0$, are presented, corresponding to the minimum and maximum wrinkle radii considered.

As discussed in the last bending example, the strain-criterion-based model determines the wrinkled region based on the sign of the trace of the strain tensor, $\mathrm{tr}(\mathbf{E})$. In torsion-dominated problems, the limitations of this criterion tend to manifest more clearly, leading to relatively larger deviations from the analytical stress distribution.

For the stress-criterion-based model, the wrinkling criterion is also based on the principal stress, consistent with the analytical solution. Since the first principal stress S_1 remains strictly positive throughout the membrane in this case, no slack state occurs. Consequently, the principal stress wrinkling criterion and the mixed wrinkling criterion yield identical predictions of the wrinkled domains. Nevertheless, the formulation of S_1 used in the stress-criterion-based model (see Equation (5.47)) does not incorporate any correction of the second principal strain E_2 within the wrinkled region. In contrast, the mixed-criterion-based model applies a regularized treatment of E_2 that reflects the underlying geometric constraints, resulting in improved agreement with the analytical stress field. The discrepancies observed in the stress-criterion-based model therefore originate from the absence of such strain correction in its formulation. This finding further supports the robustness of the mixed-criterion-based model in capturing torsion- or shear-dominated wrinkling behavior.

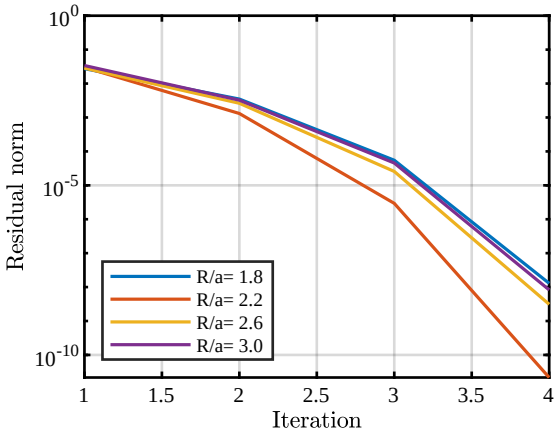

Figure 6.13.: Representative convergence behavior of the mixed-criterion-based model for various wrinkle radii R/a in the wrinkling simulation.

As a final remark for this example, Figure 6.13 illustrates the convergence behavior of the mixed-criterion-based model. Since all three models exhibit similar iterative performance, and the stress-, and strain-criterion-based models produce inaccurate stress predictions, only the mixed-criterion-based model is shown here as a representative case. The results indicate rapid convergence within a few iterations across all prescribed wrinkle radii, further confirming the numerical robustness of the proposed approach.

6.1.3 Simple Shear of a Rectangular Membrane

In this example, the wrinkling response of a rectangular membrane under in-plane shear deformation is investigated to assess the performance of the proposed wrinkling models in a shear-dominated stress state. The membrane, illustrated in Figure 6.14, has a width of 380 mm, a height of 128 mm, and a thickness of 0.025 mm. It is made of Kapton®, a polyimide film characterized by a Young's modulus of $E = 3500\,\mathrm{N\,mm^{-2}}$ and a Poisson's ratio of $\nu = 0.31$.

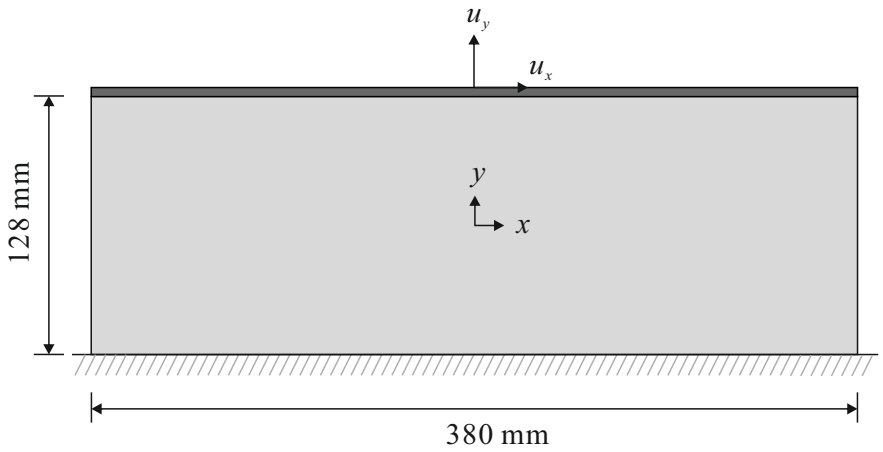

Figure 6.14.: Geometry and boundary conditions of the rectangular membrane under simple shear [115].

This benchmark problem has been widely adopted in the study of shear-induced wrinkling instabilities, following the reference work in [68], where both physical experiments (see Figure 6.15) and nonlinear shell simulations using ABAQUS were conducted. In that study, the membrane was discretized using a highly refined mesh consisting of over 13,000 S4R5 shell elements, allowing accurate resolution of individual wrinkle wavelengths and amplitudes. Subsequent studies in [95, 108] introduced tension-field-based wrinkling models for the same configuration, enabling efficient computation without resolving the fine-scale geometry of wrinkles. The present numerical setup adopts the modeling assumptions proposed in [95, 108], and the boundary conditions are defined accordingly.

Specifically, the membrane is discretized by a 40×10 mesh and fully constrained in the out-of-plane (z-) direction. The bottom edge is clamped in both the x- and y-directions. A two-step loading sequence is applied to the top edge: an initial vertical displacement of 0.05 mm introduces a small pre-stretch, followed by incremental horizontal displacements $u_x = 1.6\,\mathrm{mm}$ and $u_x = 3.0\,\mathrm{mm}$ while the vertical position remains fixed. The lateral edges are traction-free.

To evaluate the predictive capability of the wrinkling formulations, the principal stresses along the horizontal midline of the membrane (denoted as section A–A in Figure 6.15) are shown in Figure 6.16. The results from three different models are compared against the shell reference solution presented in [68], which serves as the benchmark. Although the shell solution is treated as a reference in this study, it should be noted that it constitutes a

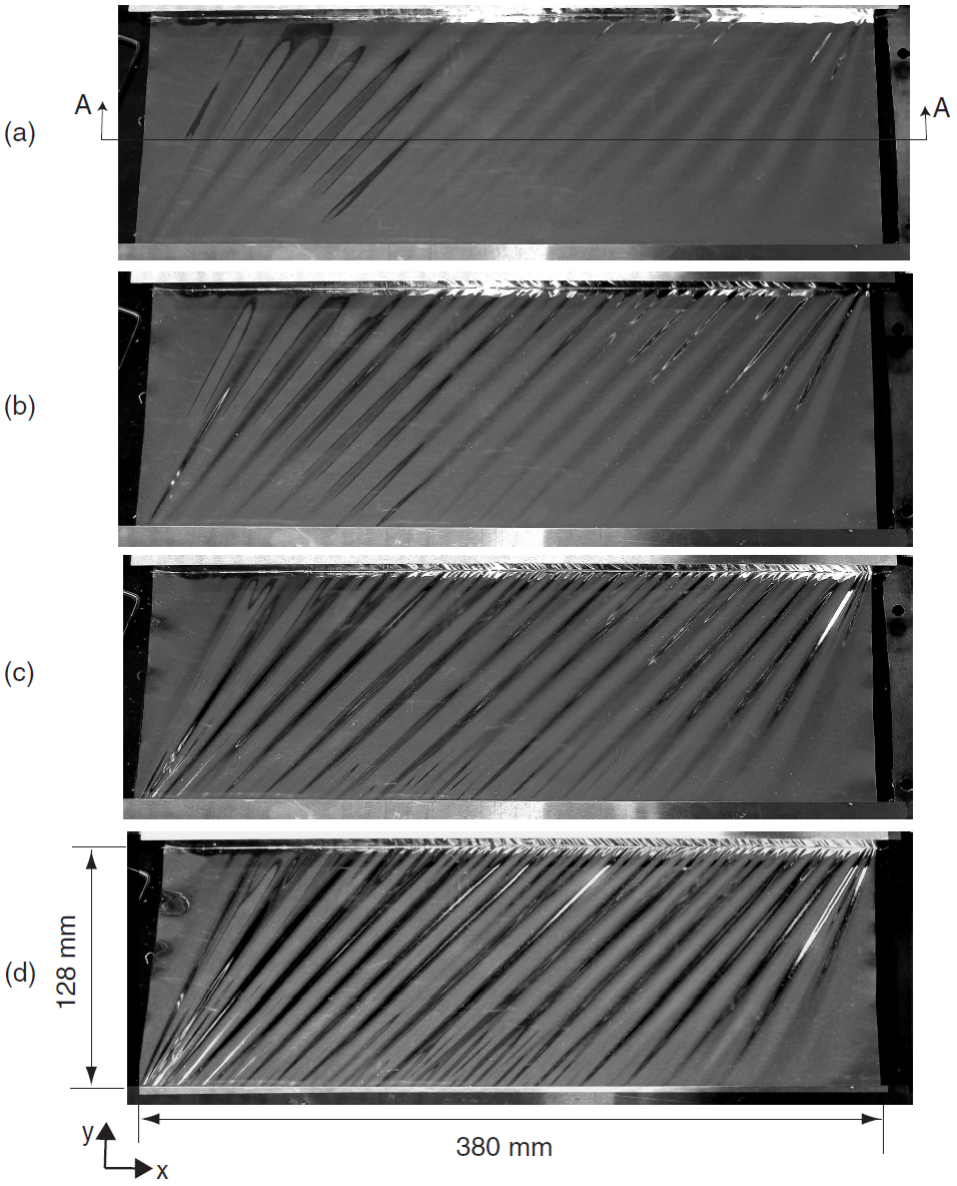

Figure 6.15.: Wrinkling patterns observed in a Kapton® membrane under different levels of shear displacement [68]: (a) $u_x = 0.5\,\text{mm}$, (b) $u_x = 1.0\,\text{mm}$, (c) $u_x = 2.0\,\text{mm}$, and (d) $u_x = 3.0\,\text{mm}$.

numerical approximation based on fine discretization and imperfection seeding, rather than an experimentally measured ground truth.

Among the three wrinkling models, the mixed-criterion-based model shows excellent agreement with the shell reference, reproducing peak first principal stress values of approximately 23 MPa and 43 MPa for $u_x = 1.6\,\text{mm}$ and $u_x = 3.0\,\text{mm}$, respectively. In contrast, the strain-criterion-based model underestimates the first principal stresses, with values around 18 MPa and 33 MPa. This discrepancy is likely due to the limited capability of the strain-based spectral decomposition to capture shear-dominated states, a limitation also reported in fracture simulations [140]. The stress-criterion-based model fails to converge due to the numerical

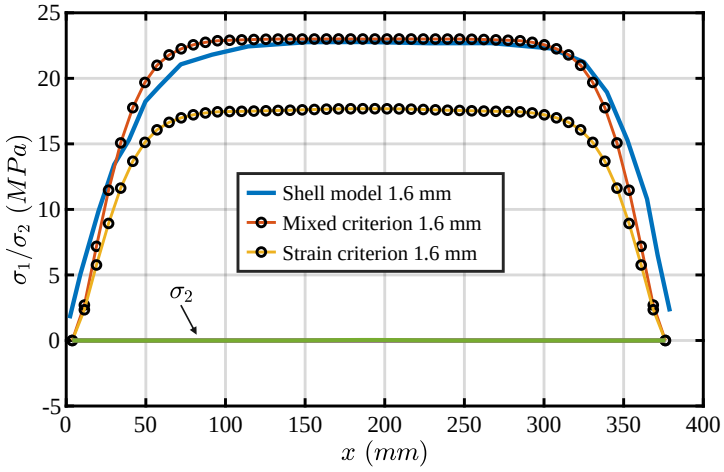

(a) $u_x = 1.6\,\text{mm}$

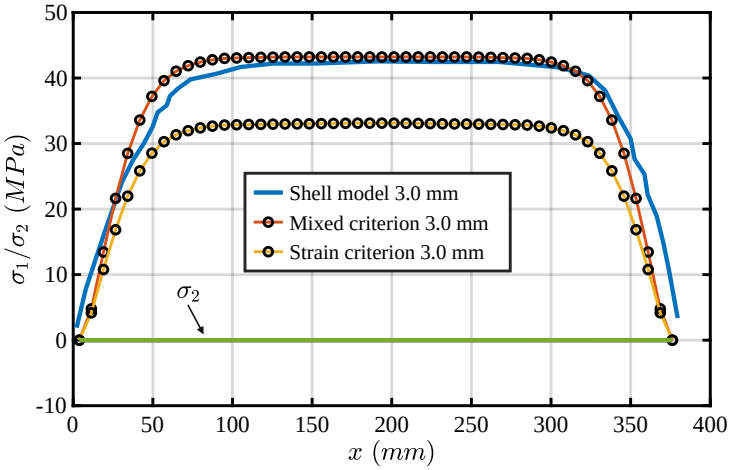

(b) $u_x = 3.0\,\text{mm}$

Figure 6.16.: Distribution of principal stresses along the horizontal midline (section A–A) of the membrane under different shear displacements [115].

issues discussed in Section 5.3.3 and is therefore excluded from the comparison. In all wrinkling models, the second principal stress σ_2 remains close to zero throughout the domain, consistent with the shell reference and the expected behavior in wrinkled regions.

The global shear response is further examined in Figure 6.17. The shell model captures an initial linear regime followed by a notable reduction in stiffness as the reaction force reaches approximately 10 N, signaling the onset of wrinkling. The mixed-criterion-based model replicates this trend closely. The strain-criterion-based model underestimates the reaction force, especially at larger displacements. In contrast, the standard membrane model lacks any mechanism to deactivate compressive stress and thus retains higher in-plane stiffness in wrinkled regions. As a result, it substantially overpredicts the reaction forces under shear loading.

These comparisons underscore the necessity of incorporating wrinkling effects to obtain physically realistic predictions. Notably, the mixed-criterion-based model achieves this level

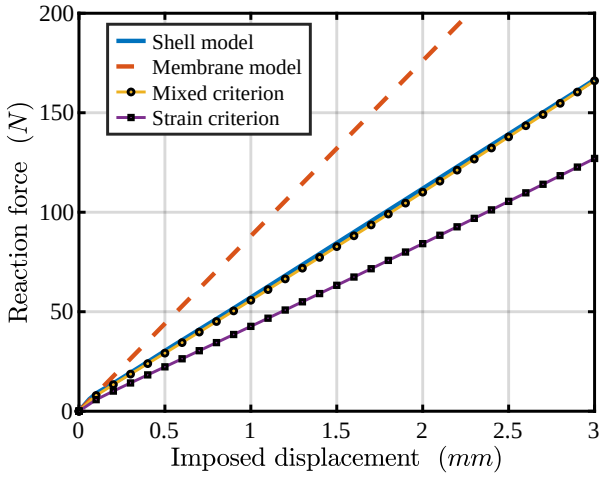

Figure 6.17.: Reaction force versus displacement response of the rectangular membrane under in-plane shear loading [115].

of accuracy using a significantly coarser mesh than the shell reference, demonstrating its computational efficiency without requiring fine discretization.

Furthermore, Figure 6.18 shows the convergence history of the mixed-criterion-based model for the simple shear test at two prescribed displacement levels, $u_x = 1.6$ mm and $u_x = 3.0$ mm. Compared to $u_x = 1.6$ mm, the case with $u_x = 3.0$ mm requires more iterations to reach the prescribed tolerance. Nevertheless, both cases converge rapidly, achieving convergence within approximately 20–40 iterations, and exhibit nearly identical initial convergence rates. The convergence histories for the strain-, and stress-criterion-based models are not shown here for brevity.

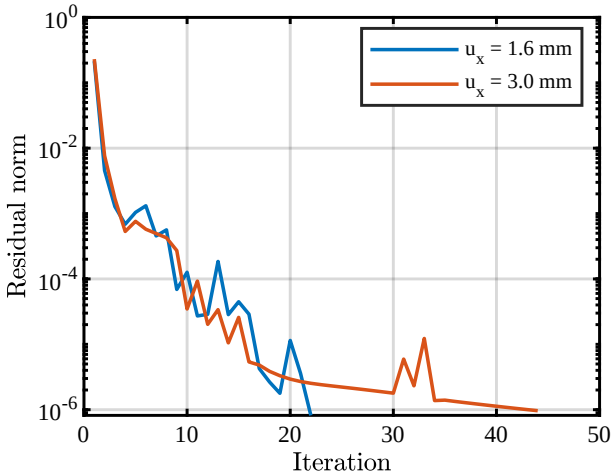

Figure 6.18.: Convergence behavior of the mixed-criterion-based model at prescribed displacements $u_x = 1.6$ mm and 3.0 mm in the simple shear test.

Figure 6.19 visualizes the wrinkling intensity and trajectories of the membrane subjected to simple shear, as predicted by the mixed-criterion-based model. Only the wrinkled regions are

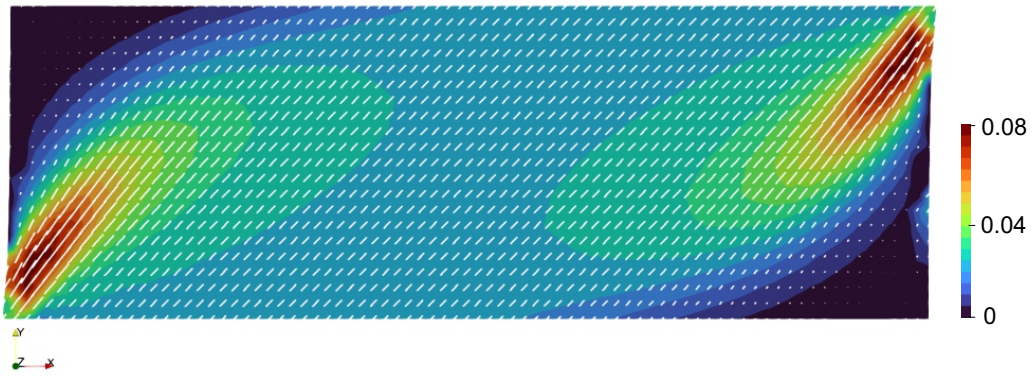

Figure 6.19.: Visualization of wrinkling intensity and trajectories in the membrane under simple shear, computed using the mixed-criterion-based model.

shown; elements identified as taut or slack have their wrinkling intensity and trajectory set to zero and are therefore excluded from the visualization.

In the wrinkled regions, the trajectories indicate the orientation of the first principal strain, while the length of each segment is scaled proportionally to the second principal strain. The wrinkling intensity is computed as the normalized magnitude of the first eigenvector of strain. The dominant wrinkling orientation observed in Figure 6.19 aligns closely with an angle of approximately 45°, which is in excellent agreement with the experimental observations illustrated in Figure 6.15.

6.1.4 Biaxial Corner Stretching of a Flat Membrane

In this example, the proposed wrinkling models are assessed through a benchmark problem involving a square membrane subjected to diagonal corner forces T_1 and T_2. This test setup originates from the experimental study in [141], and was later investigated numerically using refined shell meshes in their follow-up work [68]. Since then, these results have served as a qualitative reference for evaluating and comparing the behavior of different wrinkling models [95, 108].

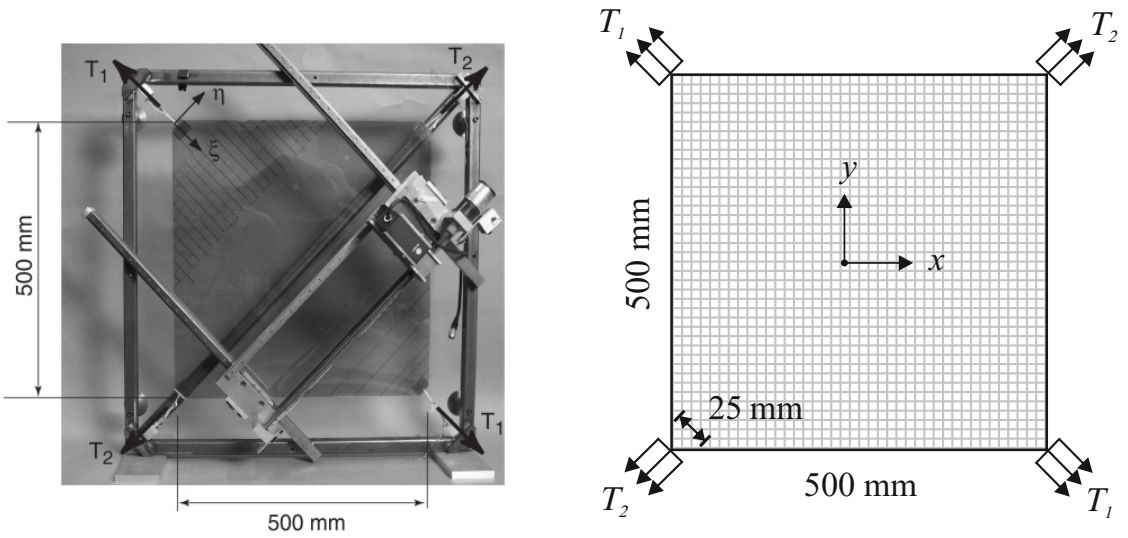

(a) Square membrane experimental setup mounted vertically, adapted from [141].

(b) Numerical configuration for the diagonal loading case [114].

Figure 6.20.: Experimental and numerical configurations for analyzing the wrinkling behavior of a square membrane under diagonal corner loads.

The geometry, illustrated in Figure 6.20, consists of a flat membrane with side length 500 mm and thickness 25 µm. Fabricated from Kapton®, the membrane exhibits a Young's modulus of $E = 3500\,\text{MPa}$ and a Poisson's ratio of $\nu = 0.31$. Tensile forces T_1 and T_2 are applied diagonally at the four corners over a width of 25 mm, generating a biaxial stretching configuration. As reported in the experiment, T_1 is gradually increased from 5 N to 20 N while keeping T_2 constant at 5 N, corresponding to load ratios from 1 to 4. Under equal loads, wrinkles first appear near the corners, and as T_1 increases, they progressively evolve along the T_1-direction diagonal.

To numerically reproduce this behavior, a 40×40 mesh of bi-cubic membrane elements was employed. Boundary constraints follow the approach of [108]: the center of the membrane is fixed to eliminate rigid body modes, lateral movement at the midpoint of the top edge is blocked in the x-direction to suppress rotation, and out-of-plane (z-direction) motion is restricted for all control points. For comparison, the reference shell solution from [68] was generated in ABAQUS using a refined finite element model composed of S4R5 shell elements. The mesh resolution was chosen to sufficiently resolve individual wrinkle waves, and a mesh density sensitivity study was conducted to ensure convergence of the wrinkling patterns. The

simulation procedure consisted of three steps: (1) a light uniform prestress was applied to stabilize the flat configuration and suppress localized modes; (2) an eigenvalue buckling analysis was carried out to extract a set of global wrinkling modes, which were then superposed and introduced as initial imperfections; (3) a geometrically nonlinear analysis was performed with automatic stabilization and fine load increments to track the formation and evolution of wrinkles.

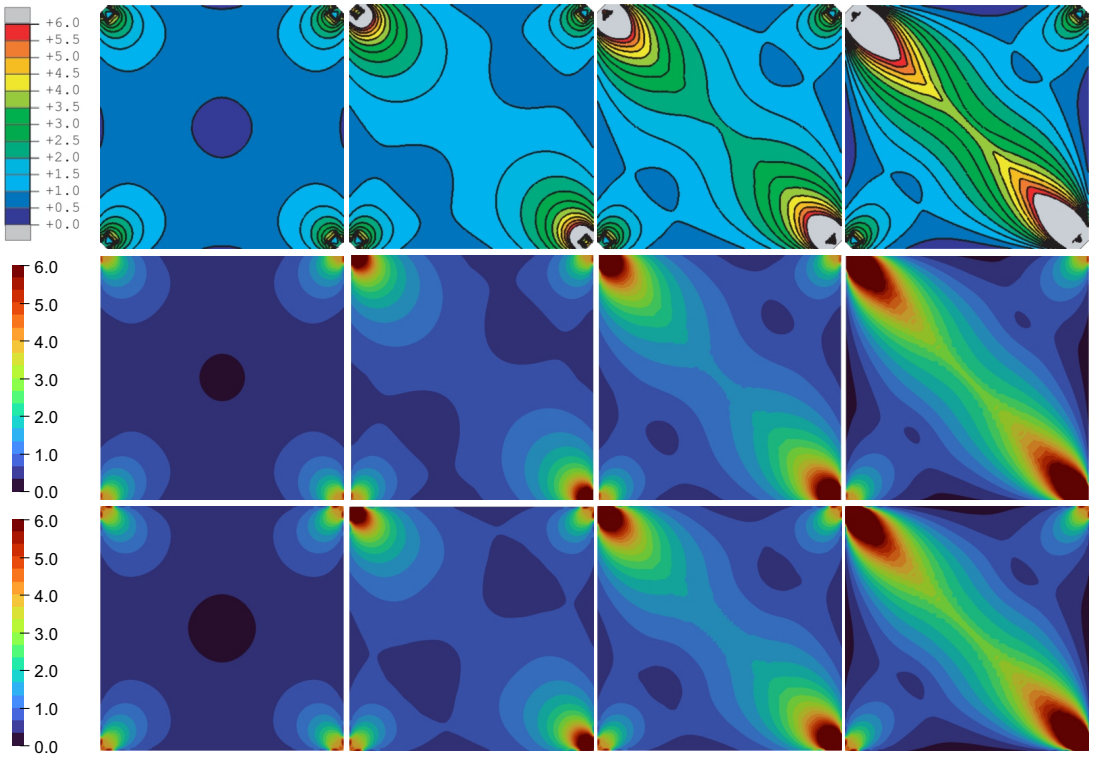

(**a**) $T_1/T_2 = 1$ (**b**) $T_1/T_2 = 2$ (**c**) $T_1/T_2 = 3$ (**d**) $T_1/T_2 = 4$

Figure 6.21.: Comparison of the first principal stress distributions (in MPa) predicted by different models under load ratios $T_1/T_2 = 1$–4. The top row shows the reference solution obtained from a shell model reported in [68]; the middle row displays the results from the mixed-criterion-based model [115]; and the bottom row corresponds to the strain-criterion-based model [114].

Figure 6.21 compares the distributions of the first principal stress under varying load ratios $T_1/T_2 = 1$–4. The top row shows the reference results obtained from a thin shell model [68], while the middle and bottom rows correspond to the predictions of the mixed-criterion-based model and the strain-criterion-based model, respectively. The stress-criterion-based model failed to converge for higher T_1/T_2 ratios and is therefore not shown here. Overall, the mixed- and strain-criterion-based models reproduce stress distributions very similar to those of the thin shell model, but their predictions differ in detail depending on the load ratio.

At $T_1/T_2 = 1$, all models predict stress concentrations at the four corners. A central low-stress circular region is clearly visible in the reference solution, which is well captured by the strain-criterion-based model, while the mixed-criterion-based model predicts a similar region but with reduced extent. At $T_1/T_2 = 2$, the onset of diagonal stress amplification appears. The

mixed-criterion-based model preserves the shape and separation of low-stress zones more accurately, while the strain-criterion-based model shows slightly merged. At $T_1/T_2 = 3$, a well-defined diagonal stress band emerges. The mixed-criterion-based model yields a sharper, more localized pattern, whereas the strain-criterion-based model shows a broader, smoother transition. At $T_1/T_2 = 4$, the diagonal dominates the stress field. The strain-criterion-based model better reproduces the elliptical low-stress regions near the membrane boundaries, while the mixed-criterion-based model exhibits more focused but less extended contours.

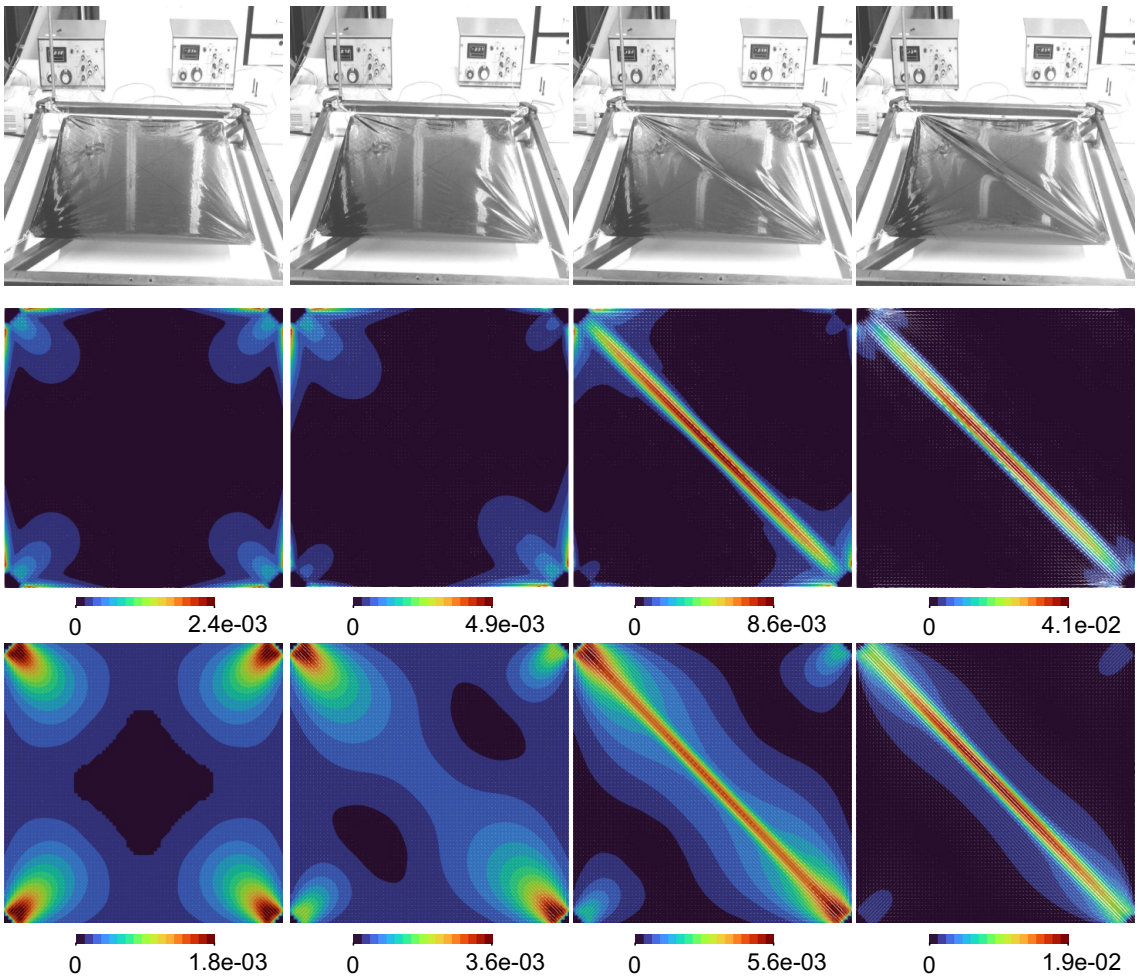

Figure 6.22.: Comparison of the wrinkling intensity and trajectories predicted by different models under load ratios $T_1/T_2 = 1$–4. The top row presents the experimental observations reported in [141]; the middle row displays the results from the mixed-criterion-based model; and the bottom row corresponds to the strain-criterion-based model [114].

Figure 6.22 provides a complementary view by comparing the wrinkling intensity and trajectories. The experimental observations reveal a transition from symmetric corner wrinkles to a dominant diagonal band. Both models capture this evolution, yet with different visual characteristics. At $T_1/T_2 = 1$, the strain-criterion-based model reproduces the symmetric

wrinkle patterns near the corners more comprehensively, while the mixed-criterion-based model underrepresents the affected area. As the load ratio increases to 2 and 3, diagonal wrinkles begin to dominate. The mixed-criterion-based model shows sharper and more concentrated wrinkle paths, whereas the strain-criterion-based model produces wider, more diffuse distributions. At $T_1/T_2 = 4$, the diagonal wrinkles becomes more pronounced in both models, but the strain-criterion-based model better reflects the observed lateral spreading. It is worth noting that the wrinkling intensity predicted by the mixed-criterion-based model tends to be stronger. As a result, only highly wrinkled regions are visibly emphasized, making milder wrinkles less apparent. This contributes to its more localized appearance compared to the broader coverage in the strain-based plots.

In summary, the strain-criterion-based model more accurately captures the initial symmetric patterns and the full spatial extent of wrinkles at low and high load ratios, while the mixed-criterion-based model provides better localization and sharpness during the transitional stages. These respective strengths are consistently reflected in both the stress distributions and wrinkling intensity, indicating the differences between the predictions of the two models.

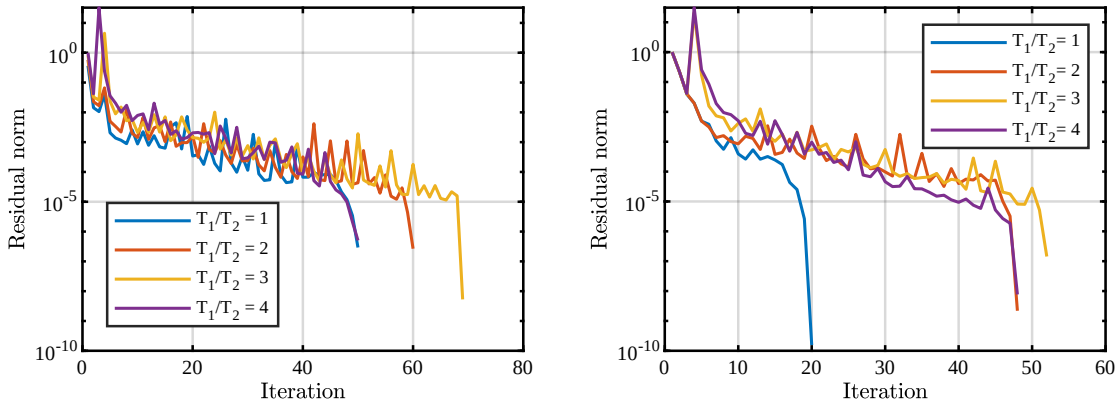

(a) Mixed-criterion-based model **(b)** Strain-criterion-based model [114]

Figure 6.23.: Convergence behavior of the mixed-, and strain-criterion-based models in the biaxial corner stretching test.

Finally, Figure 6.23 shows the convergence histories of the mixed-criterion-based model (a) and the strain-criterion-based model (b) in the biaxial corner stretching test for different load ratios T_1/T_2. For the mixed-criterion-based model, all cases exhibit similar convergence rates and require approximately 45–70 iterations to reach the prescribed tolerance. The strain-criterion-based model generally converges in fewer iterations, typically within the range of 20–55. In both models, higher load ratios generally lead to slightly longer convergence histories. Overall, both models demonstrate robust convergence behavior across the tested loading conditions.

6.1.5 Inflation of a Square Airbag

This numerical example considers a square isotropic membrane subjected to uniform inflation pressure, representing a fully three-dimensional deformation case distinct from the previous in-plane test scenarios. The benchmark was originally proposed in [142] and has since been widely used for validating membrane wrinkling formulations [65, 67, 86, 88, 108, 114, 143–146].

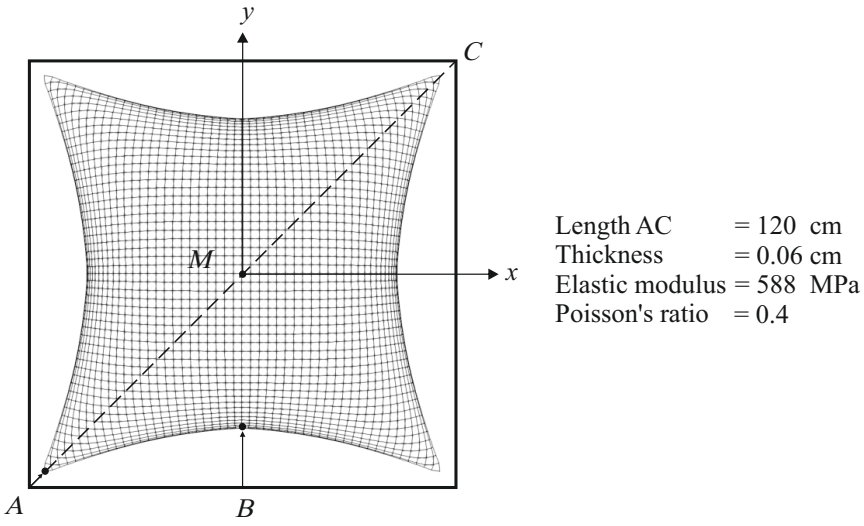

Figure 6.24.: Geometric and material properties of the square membrane used for inflation simulations [114].

As shown in Figure 6.42, the square membrane has a diagonal length of $AC = 120\,\text{cm}$ and a thickness of $t = 0.06\,\text{cm}$. The material is modeled as a linear isotropic material with Young's modulus $E = 588\,\text{MPa}$ and Poisson's ratio $\nu = 0.4$. Exploiting symmetry, only one-quarter of the structure is simulated. Symmetric boundary conditions are applied along the inner edges, while vertical displacement is constrained along the outer edges. A pressure load P, acting normal to the deformed membrane surface, is gradually increased up to 5000 Pa.

As discussed in [67], the inflation of a square membrane structure presents a numerical challenge due to the stiffness singularity that arises when pressure is applied to an initially undeformed surface. One approach to address this issue is dynamic relaxation (DR), which approximates a static equilibrium solution via pseudo-dynamic transient analysis [70]. A more straightforward alternative, also proposed in [67, 144], is to apply small in-plane dead loads along the x- and y-directions at the two outer edges. These dead loads are gradually released as the pressure P increases and are fully removed once the pressure reaches its final value. This method effectively avoids the initial singularity and enables accurate simulation of the airbag inflation process.

To assess the mesh sensitivity and facilitate comparison with prior studies, the membrane is discretized using bilinear membrane elements with mesh resolutions of 4×4, 5×5, 8×8, and 10×10. For each case, the following quantities are extracted: the vertical displacement at point M (u_z^M), the radial displacement at point A (r_A), the y-component of displacement at point B (u_y^B), and the first principal stress at point M (σ_1^M). The results are presented in Tables 6.1 and 6.2.

Table 6.1.: Comparison of results from literature and present work for mesh refinements 4×4 and 5×5.

No. elements	4×4							5×5						
	[88]	[143]	[108]	[96]	strain	stress	mixed	[88]	[143]	[108]	[96]	strain	stress	mixed
u_z^M (m)	0.2090	0.2150	0.2149	0.2145	0.2152	0.2159	0.2145	0.2170	0.2160	0.2159	0.2156	0.2163	0.2169	0.2156
r_A (m)	0.0570	0.0608	0.0972	0.0971	0.0947	0.0478	0.0971	0.0630	0.0594	0.0882	0.0881	0.0864	0.0479	0.0881
u_y^B (m)	0.1018	0.1170	0.1202	0.1201	0.1199	0.1056	0.1201	0.1103	0.1170	0.1215	0.1213	0.1209	0.1067	0.1213
σ_1^M (MPa)	3.4	-	3.2	3.3	3.3	3.5	3.3	3.5	-	3.6	3.6	3.6	3.9	3.6

Table 6.2.: Comparison of results from literature and present work for mesh refinements 8×8 and 10×10.

No. elements	8×8							10×10				
	[88]	[143]	[108]	[96]	strain	stress	mixed	[108]	[96]	strain	stress	mixed
u_z^M (m)	0.2050	0.2140	0.2166	0.2162	0.2166	-	0.2162	0.2167	0.2163	0.2167	-	0.2163
r_A (m)	0.0470	0.0580	0.0738	0.0737	0.0731	-	0.0737	0.0692	0.0691	0.0683	-	0.0691
u_y^B (m)	0.1301	0.1190	0.1227	0.1225	0.1219	-	0.1225	0.1237	0.1235	0.1228	-	0.1235
σ_1^M (MPa)	3.5	-	3.8	3.8	3.8	-	3.8	3.8	3.8	3.8	-	3.8

As shown in the tables, the strain-, and mixed-criterion-based models demonstrate good agreement with results reported in the literature across a range of mesh resolutions. In contrast, the stress-criterion-based model tends to overestimate displacements and often encounters convergence issues, particularly for finer meshes. Additionally, the reference model [96] presented in Section 4.4 has also been implemented; its results are identical to those of the mixed-criterion-based model, whereas the convergence behavior is markedly different. As shown in Figure 6.25, which reports the iteration histories for the 10×10 mesh at the final load step, the mixed-, and strain-criterion-based models reach the prescribed tolerance within roughly 10–20 iterations, while the reference model requires several hundred iterations. The strong convergence of the proposed formulations is attributed to variational consistency: both the stress and the material tensor are derived from a single expression consistently.

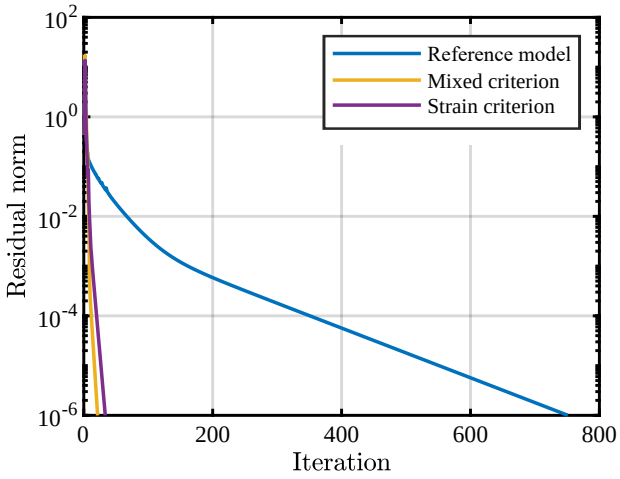

Figure 6.25.: Comparison of the convergence behavior of different models with mesh 10×10 during the final step.

Furthermore, Figure 6.26 presents the mesh convergence analysis of the vertical displacement

at point M, where Figure 6.26(a) shows the predicted displacement values, and Figure 6.26(b) displays the corresponding relative errors with respect to normalized mesh size h/h_{max}. Here, h represents the characteristic element size of a given mesh, and $h_{\max}$ refers to that of the coarsest mesh, so that $h/h_{\max} = 1$ corresponds to the coarsest discretization (4 elements), while for 10 elements one obtains $h/h_{\max} = 4/10 = 0.4$. For brevity, the reference model [96] is omitted, as its predictions are nearly identical to those of the mixed-criterion-based model. All three wrinkling models provide comparable predictions across different mesh resolutions. The strain-criterion-based model yields values that closely follow the reference solution from [108], especially for intermediate mesh sizes. As pointed out in [108], their wrinkling formulation achieves a convergence rate of $O(h^2)$ under uniform mesh refinement, meaning that halving the element size reduces the error to roughly one quarter of its previous value. In this study, the proposed mixed-criterion-based model exhibits a nearly identical convergence trend. The relative error in u_z^M decreases consistently with mesh refinement and closely parallels the behavior reported in [108], demonstrating the effectiveness and robustness of the mixed-criterion-based model. By contrast, the stress-criterion-based model fails to converge for this case and is therefore excluded from the figure.

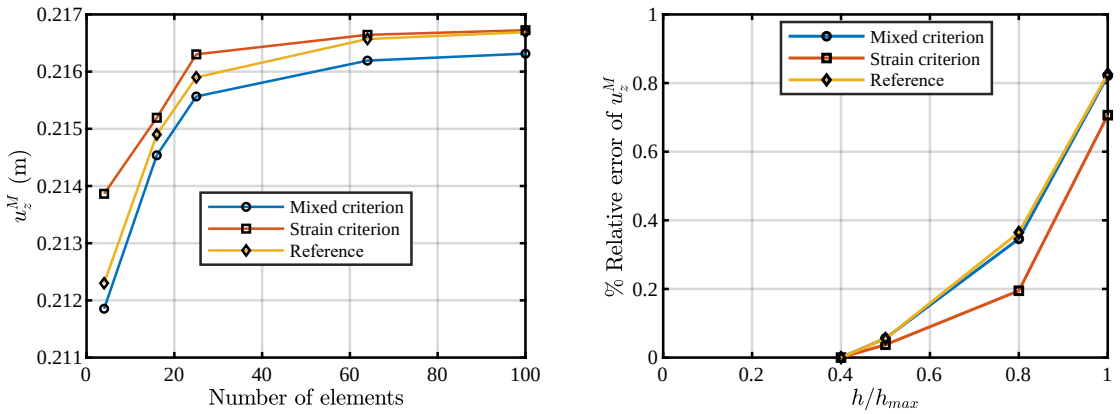

(a) **(b)**

Figure 6.26.: Mesh convergence analysis of the vertical displacement at point M: (a) predicted displacement under different mesh resolutions; (b) relative error with respect to normalized mesh size.

In addition, [70] recently reported the occurrence of local self-penetration in membrane inflation simulations when the mesh is sufficiently refined. While the phenomenon was clearly observed, its underlying cause was not thoroughly analyzed and remains an open question in the literature.

In the present work, similar penetration effects have been identified in both the strain- and the mixed-criterion-based models. In both cases, when using fine meshes and applying the inflation loading described previously, abrupt and unphysical deformations were observed near the center and boundary regions of the membrane. To illustrate this phenomenon, only the results obtained using the strain-criterion-based model are presented here. Since both models yield qualitatively similar penetration behavior under identical simulation conditions, the strain-criterion-based model is considered sufficiently representative.

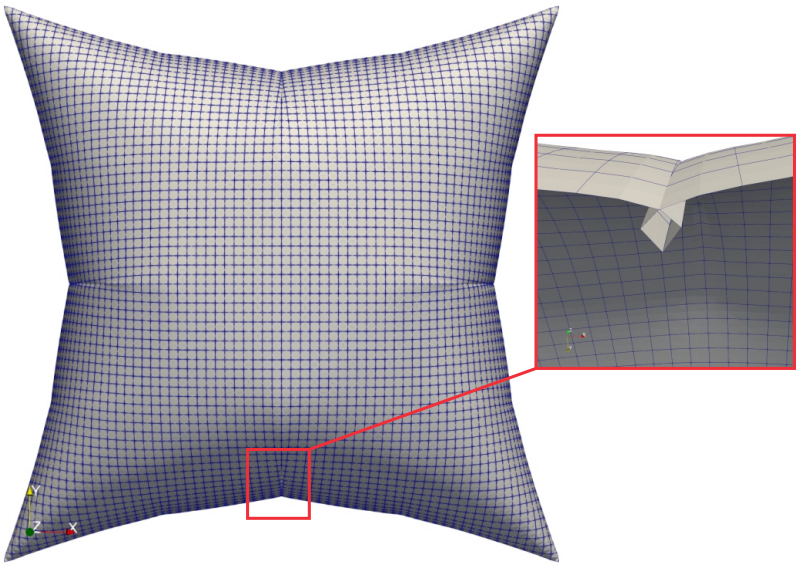

Figure 6.27.: Self-penetration at point B of the airbag with a 32×32 mesh ($\eta = 0$) [114].

As shown in Figure 6.27, refining the mesh to 32×32 elements leads to a sudden increase in the vertical displacement at point M and a local contraction at point B. These irregularities are indicative of self-penetration and suggest the presence of nonphysical responses in the numerical solution.

A plausible explanation for this behavior is the complete loss of compressive stiffness in wrinkled membrane regions. Without any residual compressive resistance, small perturbations or geometric irregularities may cause inward-folding or overlapping of membrane patches. This hypothesis is consistent with the findings in [65, 66, 81, 108], who argued that membranes in wrinkled states should retain a very small compressive stiffness in order to prevent numerical instabilities and preserve physical realism.

In the present framework, this concept is incorporated through the parameter η, which introduces a small artificial compressive stiffness in the energy functional, as defined in Equation (5.31). To investigate its influence on the penetration behavior, a parametric study is conducted for the values $\eta = 10^{-8}, 10^{-6}, 10^{-5}, 10^{-4}$.

Figure 6.28 presents the displacements u_z^M and u_y^B under different values of η and varying mesh densities. For η ranging from 10^{-8} to 10^{-5}, no convergence is achieved with respect to mesh refinement. By contrast, stable and convergent results are observed for $\eta = 10^{-4}$.

Further insights can be drawn from Figure 6.29, which displays the local deformation at point B for the 32×32 mesh with different η values. Clear signs of self-penetration are present for $\eta = 10^{-8}, 10^{-6}, 10^{-5}$ (Figures 6.29(a)–(c)). These artifacts vanish only for $\eta = 10^{-4}$ (Figure 6.29(d)).

These results indicate that the inclusion of a small compressive stiffness, regulated by the degradation factor η, effectively mitigates self-penetration and enhances the robustness of the numerical solution. However, the choice of η must be carefully balanced. If chosen too small, its regularizing effect is insufficient; if too large, it introduces unrealistic membrane behavior

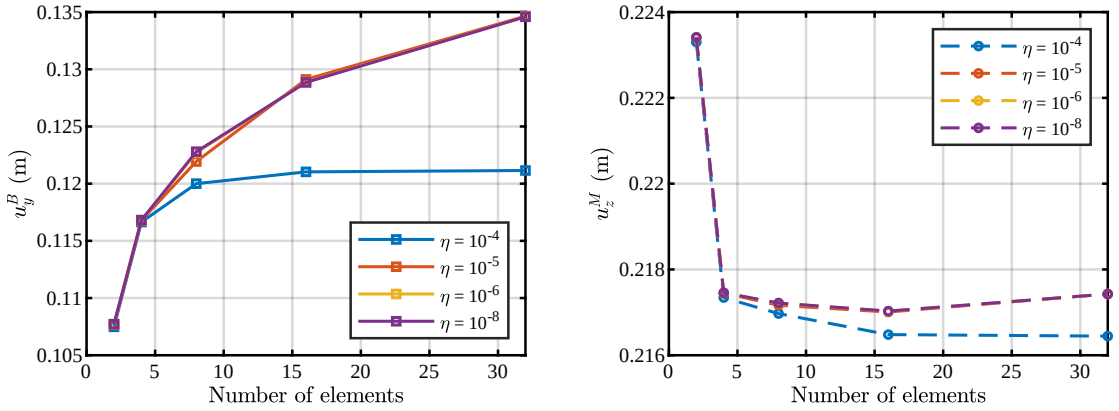

(a) **(b)**

Figure 6.28.: Displacements at points M and B under different values of η [114].

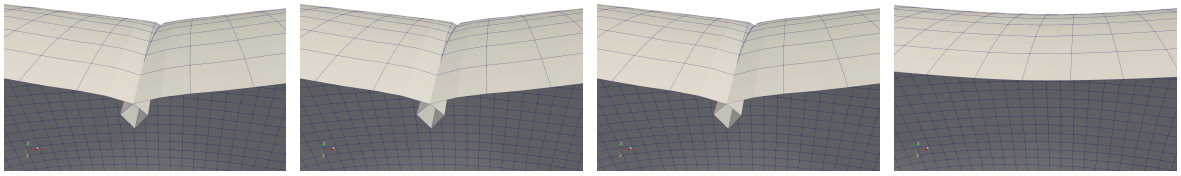

(a) $\eta = 10^{-8}$ **(b)** $\eta = 10^{-6}$ **(c)** $\eta = 10^{-5}$ **(d)** $\eta = 10^{-4}$

Figure 6.29.: Deformation near point B for the 32×32 mesh with various values of η [114].

by enforcing excessive compressive resistance.

Furthermore, Figure 6.28 shows that the influence of η is mesh-dependent. For coarse meshes (e.g., 2×2 or 4×4 elements), the results are largely insensitive to η. In contrast, finer meshes (starting from 8×8 elements) exhibit significant sensitivity to this parameter. In conclusion, this study suggests that the appropriate value of η varies with the problem and the mesh size, and is usually established on an empirical basis. Lastly, it is worth emphasizing that even with $\eta = 0$, the global response of the membrane remains in good agreement with reference data from the literature. Local quantities such as displacements and stress distributions may show deviations, but the overall mechanical behavior is still reasonably well captured.

6.1.6 Free Fall of a Square Blanket

In this example, a loose membrane subjected solely to self-weight is analyzed, representing a hanging blanket supported at its corners, as illustrated in Figure 6.30. The blanket has a side length of $L = 1\,\text{m}$ and a thickness of $t = 1.77\,\text{mm}$. The material parameters are: Young's modulus $E = 30\,000\,\text{Pa}$, Poisson's ratio $\nu = 0.3$, and surface density $\rho = 0.144\,\text{kg}\,\text{mm}^{-2}$, which accounts for the gravitational loading.

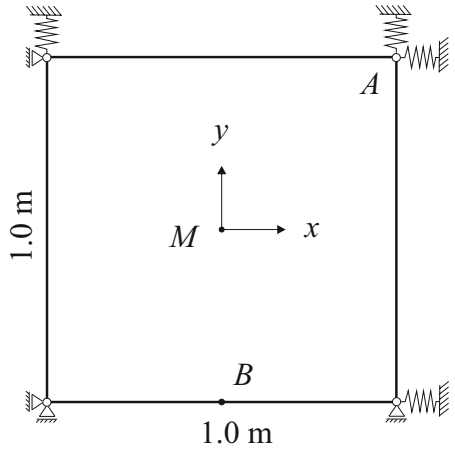

Figure 6.30.: Hanging blanket under self-weight [115].

The four corners are rigidly constrained in the z-direction, while in-plane displacements are elastically supported, enabling substantial deformations under gravity. These elastic supports are modeled using a penalty formulation based on the method proposed in [147], with a penalty parameter $\alpha = 10^{-2}$, corresponding to an equivalent spring stiffness of $K_{\text{spring}} = 22.95\,\text{kN}\,\text{m}^{-1}$. To resolve the wrinkling behavior, the membrane is discretized using a 25×25 mesh of bi-quadratic elements.

To assess the proposed models, simulations are also performed using the wrinkling model proposed by [96] under identical conditions. This model is regarded as the reference solution. Table 6.3 presents a comparison of several key quantities at representative points: the vertical displacement at the center of the membrane (u_z^M), the horizontal displacement in the x-direction at the top-right corner (u_x^A), the horizontal displacement in the x-direction at the midpoint of the bottom edge (u_x^B), and the first principal stress at the membrane center (σ_1^M).

Table 6.3.: Comparison of the displacements and first principal stress with $\nu = 0.3$.

Mesh (25×25)	u_z^M (m)	u_x^A (m)	u_x^B (m)	σ_1^M (Pa)
Reference [96]	−0.2833	−0.03406	−0.01703	642.66
Mixed criterion	−0.2833	−0.03406	−0.01703	623.95
Strain criterion	−0.2956	−0.03290	−0.01645	586.14
Stress criterion	−0.2887	−0.03365	−0.01683	621.34

The mixed-criterion-based model exhibits excellent agreement with the reference across all evaluated quantities. At the reported precision, the displacement values coincide to the fourth decimal place, while the first principal stress (σ_1) shows only minor differences

that are negligible. The strain-criterion-based model predicts slightly larger displacements, particularly in the vertical direction at point M, whereas the stress-criterion-based model also shows some deviation but remains closer to the mixed criterion. Regarding stress prediction, the strain-criterion-based model underestimates the first principal stress σ_1^M, while the stress-criterion-based model provides a more accurate approximation.

Figure 6.31 compares the convergence behavior of all models. The stress-criterion-based model converges most rapidly, reaching the numerical tolerance in only five iterations. The strain-, and mixed-criterion-based models follow closely, both converging within approximately fifteen iterations. In contrast, the reference model requires over 100 iterations to achieve convergence.

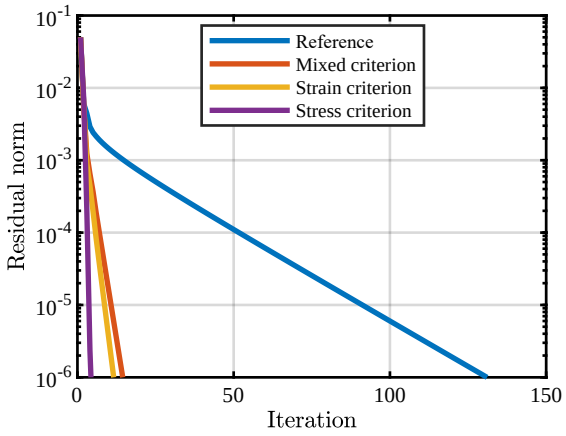

Figure 6.31.: Comparison of the convergence behavior of different models during the final step with various Poisson's ratios [115].

These results demonstrate that the series of models formulated within the spectral decomposition framework exhibit excellent convergence behavior, requiring significantly fewer iterations to reach the prescribed tolerance. This reduction in iteration count leads to improved computational efficiency and shorter overall solution time compared to the reference method.

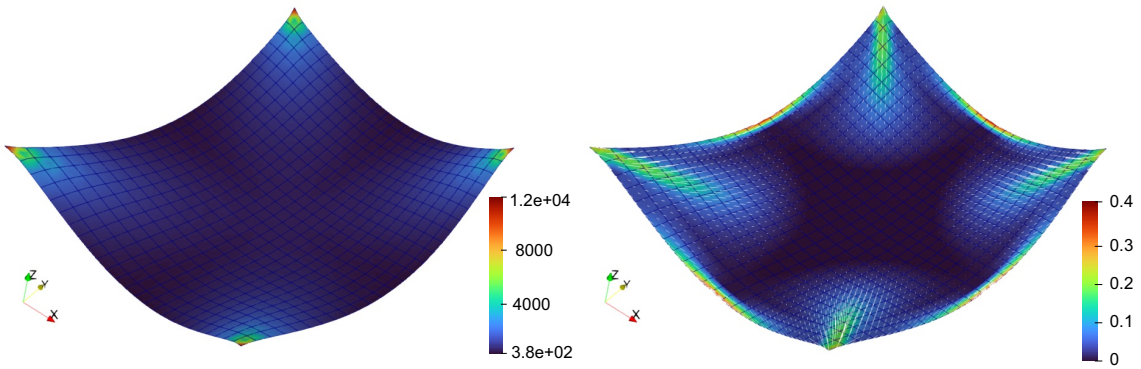

(a) First principal stress **(b)** Wrinkling intensity and trajectories

Figure 6.32.: Predictions by the mixed-criterion-based model.

Furthermore, the first principal stress distribution and the corresponding wrinkling intensity

are shown in Figure 6.32. As the blanket sags, wrinkles initiate near the corners and develop along the edges, consistent with physical expectations.

6.1.7 Dynamic Response of a Lice Skirt under Steady Towing

This example investigates the dynamic deformation response of a sea-lice skirt subjected to constant-speed towing. Sea-lice skirts are flexible vertical membranes commonly used in aquaculture to block parasites from entering surface waters.

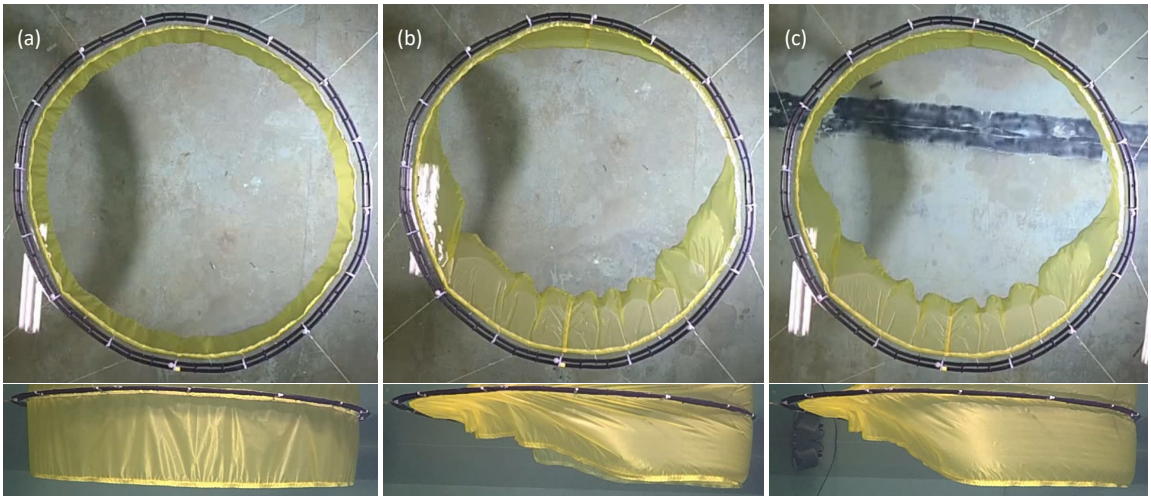

Figure 6.33.: Observed skirt deformation in the towing tank test: (a) initial submerged configuration, (b) intermediate stage during towing, and (c) steady-state deformation. The upstream face collapses inward, while the rear surface shows slight outward bulging.

The analysis is based on experimental observations from a physical model test campaign conducted by SINTEF Ocean in 2019. In these experiments, a flexible skirt was suspended from a rigid frame and towed at constant velocities through still water. A lead line was integrated into the lower edge of the skirt to provide vertical tension, ensuring that the membrane remained submerged and extended during towing. The deformation of the skirt was recorded using an underwater stereo camera system in combination with digital image correlation (DIC). Different towing speeds were tested, producing distinct deformation modes. For illustration, Figure 6.33 shows one representative sequence of skirt shapes: the initial configuration just after submersion, an intermediate towing stage, and a steady-state deformation. In this case, the upstream side of the skirt collapses inward due to hydrodynamic compression, while the rear surface exhibits mild outward bulging. In addition to deformation measurements, the towing forces were monitored throughout the experiments, providing quantitative data for comparison with numerical simulations. The present simulation aims to reproduce the characteristic deformation behavior observed in the experiments.

The modeling setup, including the structural and material parameters, as well as the loading conditions and boundary constraints, was adopted from earlier work by collaborators. As illustrated in Figure 6.34, the cylindrical membrane has a radius of 0.75 m, a height of 0.3003 m, and a uniform thickness of 0.3 mm. It is initially flat and free of prestress. A linear elastic material model is employed, characterized by a Young's modulus $E = 1 \times 10^8$ Pa, Poisson's ratio $\nu = 0.2$, and a surface density of $3\,\mathrm{kg\,mm^{-2}}$.

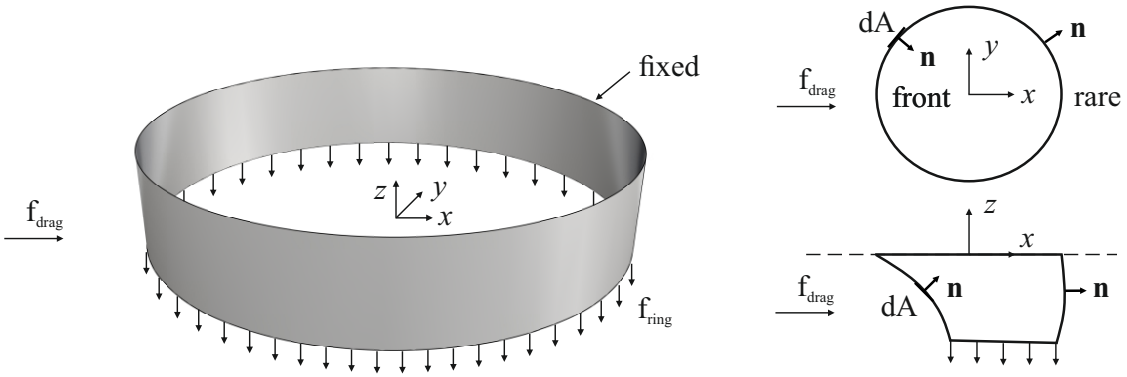

Figure 6.34.: Schematic of the simulation setup: Boundary conditions and applied loads (left) and illustration of the directional surface load $\mathbf{f}_{\text{drag}}$ (right).

The top edge of the membrane is fully fixed in the numerical model, while a downward dead load $f_{\text{ring}} = 0.21\,\text{N}\,\text{m}^{-1}$ is applied at the bottom to maintain vertical extension. To approximate the hydrodynamic pressure acting on the membrane during underwater towing, a projected surface load denoted by f_{drag} is introduced. The load acts in the direction of the local surface normal $\mathbf{n}$ and is weighted by its x-component, such that regions facing the towing direction experience higher loading. To ensure this behavior, all normal vectors are reoriented in advance so that their x-components are non-negative. This construction introduces directional sensitivity and provides a simplified approximation of flow-facing pressure without requiring a full fluid simulation. The load amplitude f_{drag} increases linearly from zero at the beginning of the simulation and reaches a maximum value of 8 Pa, which is then held constant.

The dynamic analysis covers a total simulation time of 10 seconds, discretized into 1000 uniform time steps of 0.01 seconds each. Time integration is performed using the generalized-α method, as described in Section 3.5.2. The numerical dissipation parameter used in this simulation is $\rho_\infty = 0.5$. The mass matrix is constructed using a consistent formulation. The damping matrix is taken as proportional to the mass matrix, with a constant scaling coefficient $\xi = 2.0$, which introduces moderate viscous damping. In this example, the cylindrical membrane is discretized into four patches, each represented by a 64×8 mesh.

Figures 6.35 and 6.36 present the side and top views of the dynamic deformation patterns obtained with the shell element, the membrane element, and the mixed-criterion-based model with a degradation factor $\eta = 10^{-3}$ proposed in this thesis at 0.5, 1.0, 2.0, 6.0, and 10.0 seconds. The evolution can be divided into four stages roughly. Initial stage (0–0.5 s): as the drag load is applied, fine-scale wrinkles appear on the upstream face, with the fewest wrinkles observed in the shell model, a larger number in the membrane model, and the most pronounced wrinkling in the wrinkling model. Frontal stabilization stage (0.5–2.0 s): in the shell and membrane models the frontal region progressively stabilizes. The overall geometry remains approximately symmetric with respect to the towing axis, although not perfectly so. In contrast, the wrinkling model develops more visible asymmetric wrinkles during this stage, but the overall geometry still remains broadly symmetric. At the same time, small but visible shape adjustments can already be observed along the sides and the rear face. Lateral–rear evolution

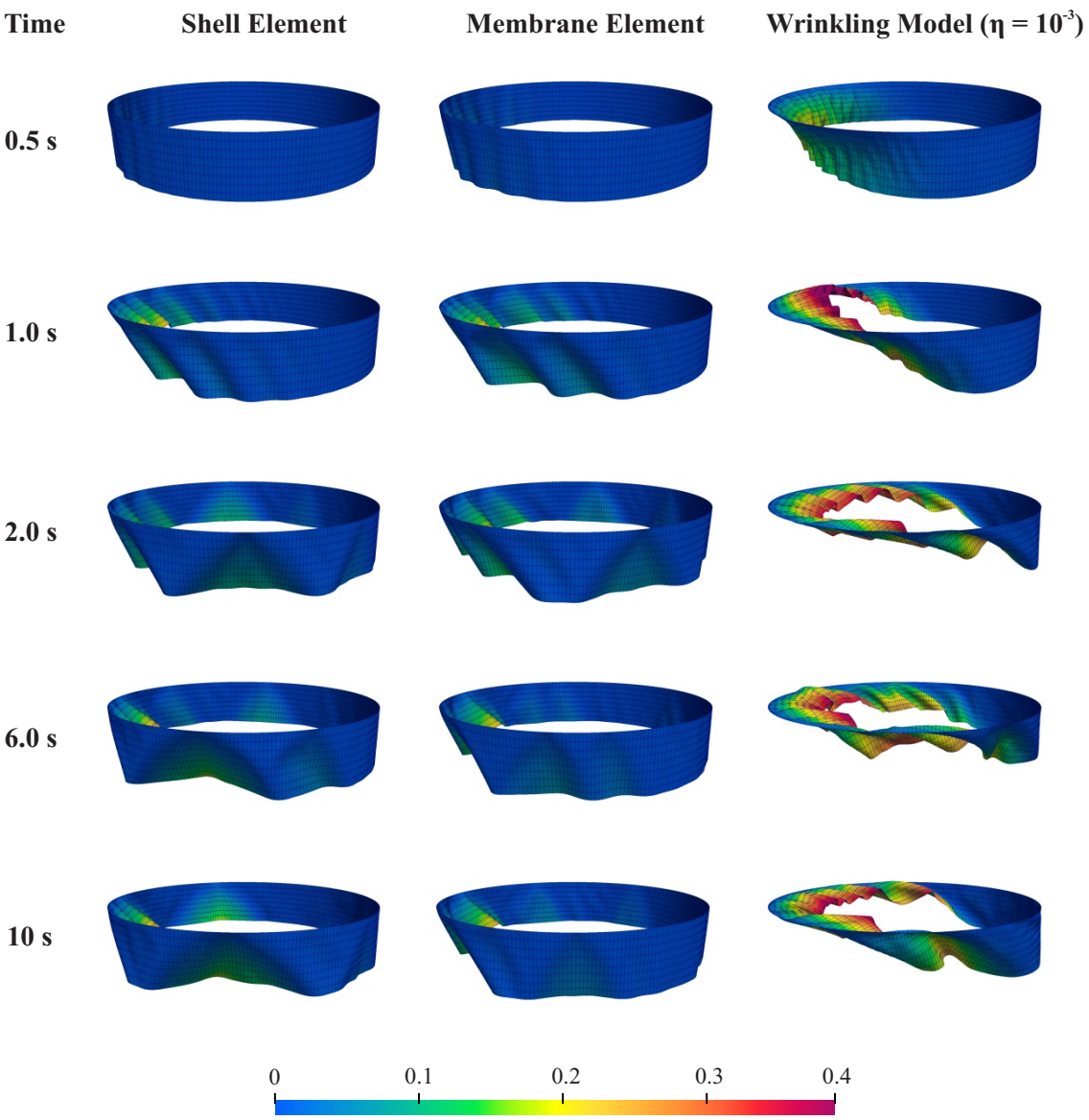

Figure 6.35.: Time evolution of the skirt deformation in side view obtained with different models.

stage (2.0–6.0 s): the frontal region in the shell and membrane models remains essentially unchanged, while the sides and the rear continue to undergo gradual shape modifications. In the top view, small-scale opening and closing along the edges can be identified. In comparison, the wrinkling model shows further growth in wrinkle amplitude and coverage, with wrinkles extending from the upstream face toward the lateral and rear regions, thereby enhancing the overall non-uniformity of the deformation. Late stage (6.0–10.0 s): the shell and membrane models remain essentially stable without significant further changes, whereas the wrinkling model exhibits more pronounced non-uniform features in both side and top views. Wrinkles in the lateral and rear regions continue to evolve slowly, indicating a sustained process of local

instability.

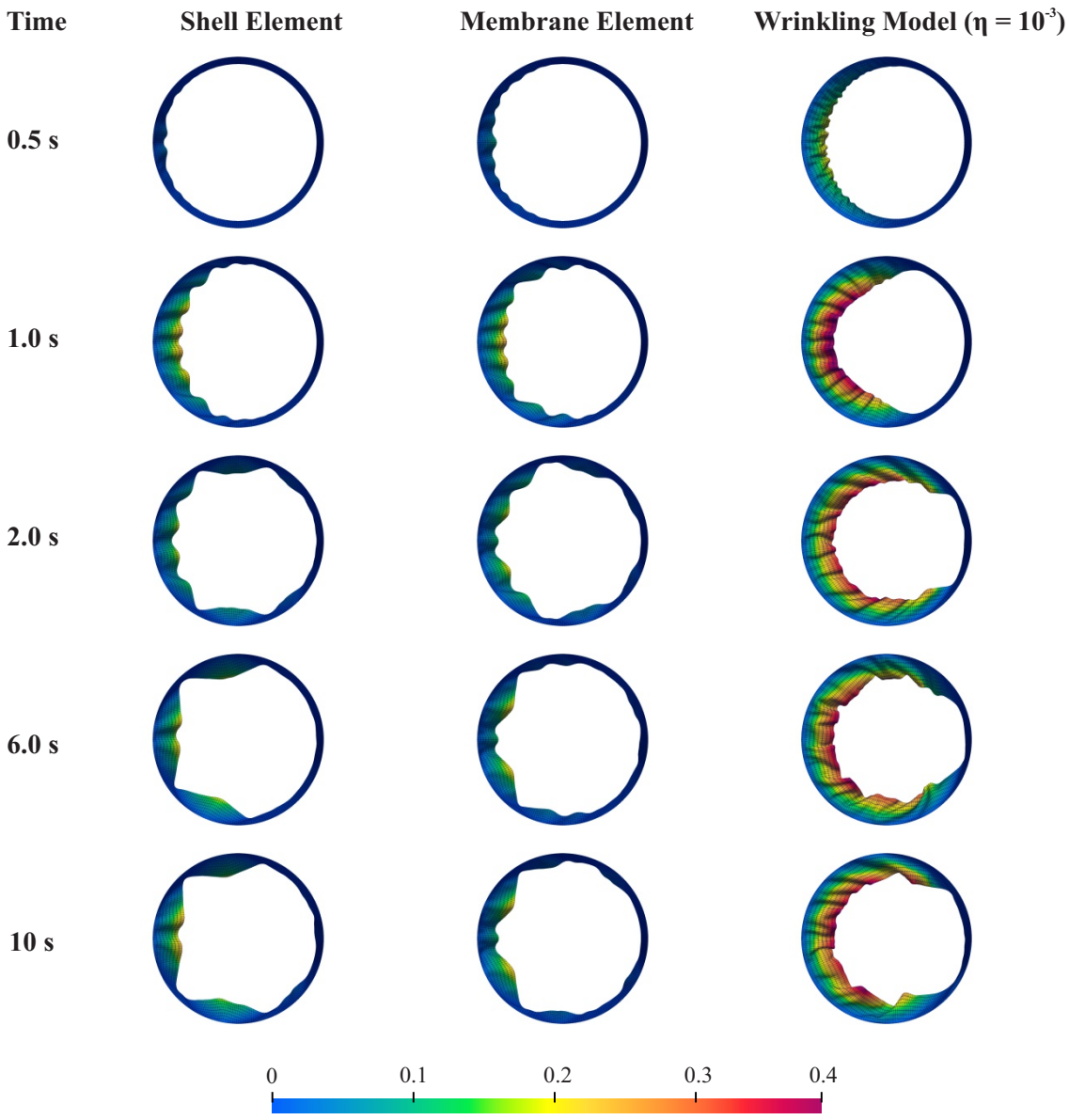

Figure 6.36.: Time evolution of the skirt deformation in top view obtained with different models.

In the shell simulations, most wrinkles appear as long-wavelength modes, suggesting that the current mesh resolution may not be sufficient to resolve finer-scale wrinkling structures. A higher mesh density would likely capture additional details. In the wrinkling model simulations, it is likely that the softening mechanism introduced in the wrinkling model, i.e., the significant reduction of compressive stiffness, makes the system more susceptible to small perturbations and drives it toward asymmetric wrinkling. In addition, the accumulation of numerical errors during time integration may further amplify these deviations. Furthermore, the choice of the degradation factor is also critical. When the degradation factor is set

identically to zero or 10^{-4}, the membrane becomes excessively slackened in this configuration. As a result, unphysical distortions arise at the lower edge during the initial stage, including abnormal element deformations and even interpenetration between elements. Since these outcomes deviate substantially from the experimental observations, such results are not presented here.

The corresponding reaction forces at the top edge are reported in Figure 6.37. These forces represent the numerical counterpart of the monitored forces in the experiments. However, the simulated results still deviate significantly from the experimental measurements, and therefore no direct quantitative comparison is attempted here.

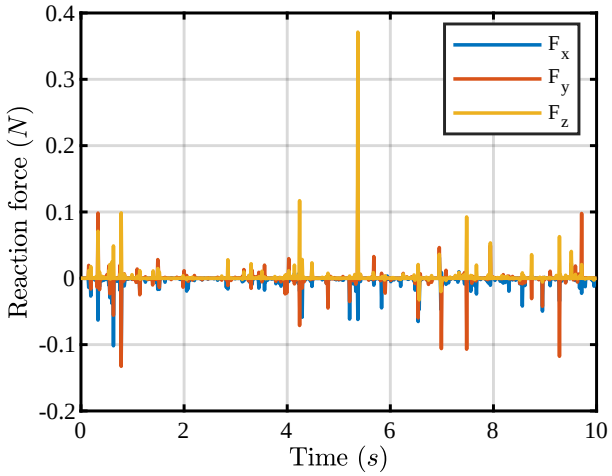

Figure 6.37.: Time histories of the reaction forces extracted at the top edge.

It should be emphasized that the present modeling strategy remains an approximation. The drag load formulation, damping assumptions, and material parameters are largely based on empirical choices rather than precisely measured values. In the experiments, the skirt is towed at a prescribed velocity (m/s), whereas in the present simulations the drag is imposed as a surface load, and the conversion between the two is not straightforward. The damping coefficient in particular has been selected heuristically, and its actual magnitude is not known. Moreover, additional physical factors have not yet been incorporated into the present modeling, including turbulence effects, three-dimensional flow–structure interaction, skirt permeability and porosity, buoyancy forces, added-mass contributions, and many other influences of similar importance. The simulation is further complicated by the strong slackening of the membrane, which makes the numerical analysis highly challenging. Despite these limitations, the results demonstrate that the mixed-criterion-based wrinkling model developed in this thesis can be successfully incorporated into large-scale dynamic simulations. The model shows good potential for capturing asymmetric wrinkling phenomena in flow-induced membrane instabilities, even though further developments are required for quantitative agreement with experimental observations.

6.1.8 Influence of the Degradation Factor η

This study examines the role of the degradation factor η and its influence on the numerical results. The factor appears in Equation (5.31), where a very small positive value η is introduced into the negative components of the strain energy density, stress, and material tensor. This procedure serves to remove or reduce the negative contributions, thereby preventing the emergence of compressive stress. Mathematically, this approach effectively imposes a lower bound on quantities that may degrade to zero or become negative, thus maintaining the numerical controllability of the tangent stiffness in the Newton–Raphson iteration. In principle, η can be set to zero; in fact, the vast majority of numerical examples in the literature, as well as most cases in this study, adopt $\eta = 0$. However, in the airbag inflation example, an initial investigation into different values of η was conducted, and it was found that a moderate increase in η can prevent self-penetration. The present subsection therefore carries out a broader evaluation on multiple representative cases with the mixed-criterion-based model: simple shear test (Section 6.1.3), biaxial corner stretching test (Section 6.1.4), airbag inflation (Section 6.1.5), and free fall of blanket (Section 6.1.6) to assess the sensitivity of the results to η and to analyze its potential impact on the iterative process in different scenarios.

In each case, four values of η were assigned: 0, 10^{-8}, 10^{-6}, and 10^{-4}. This range was chosen because η must satisfy $\eta \ll 1$ to ensure that it acts only as a minor correction without altering the material response. Besides, even though the precise definition and implementation of η vary across different works, values on the order of 10^{-4} are commonly adopted [65, 81, 108]. The present choice from 0 to 10^{-4} therefore broadly covers the range encountered in previous studies.

Depending on the loading mode (force-controlled or displacement-controlled), the results present either the reaction force or the displacement at a specific observation point. Accuracy

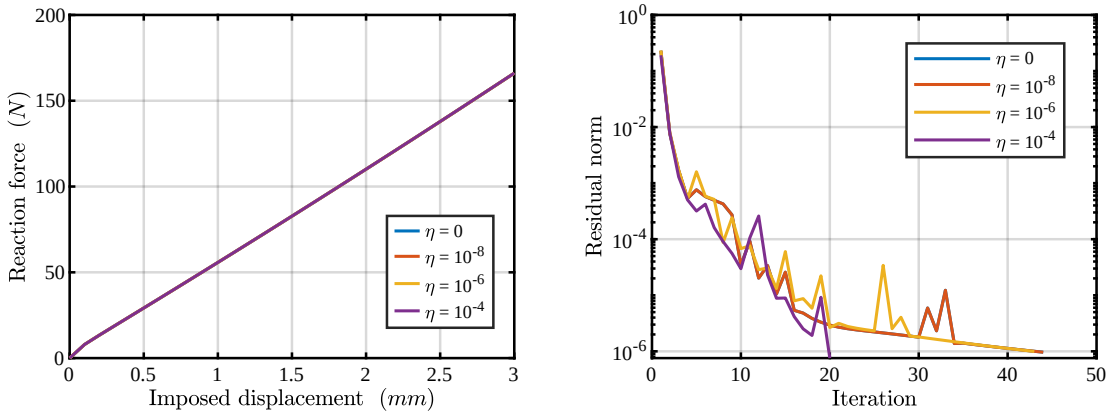

(a) **(b)**

Figure 6.38.: Influence of η in the simple shear test (Section 6.1.3): (a) reaction force–displacement; (b) residual norm history.

is assessed by comparison with the $\eta = 0$ case, and convergence performance is measured by the number of iterations required to meet an identical residual tolerance. All examples employ

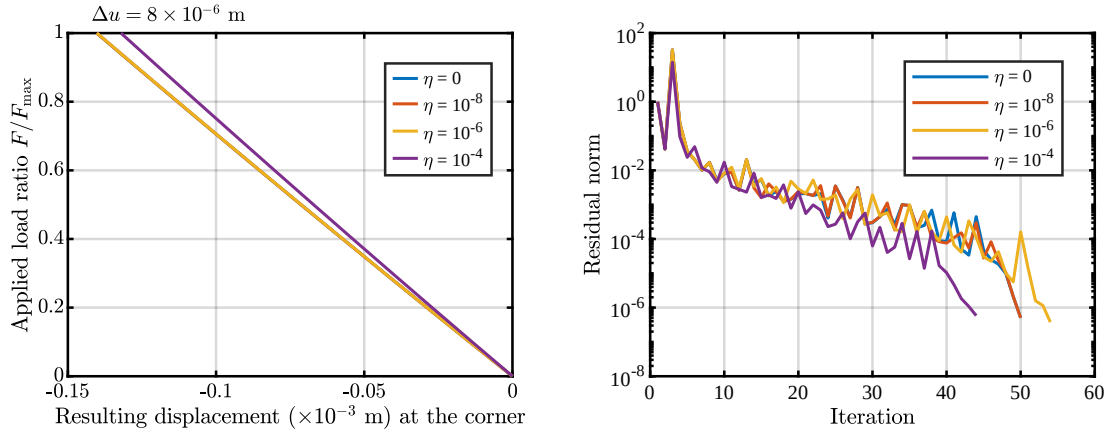

(a) **(b)**

Figure 6.39.: Influence of η in the biaxial corner stretching test (Section 6.1.4): (a) displacement at upper-left corner; (b) residual norm history.

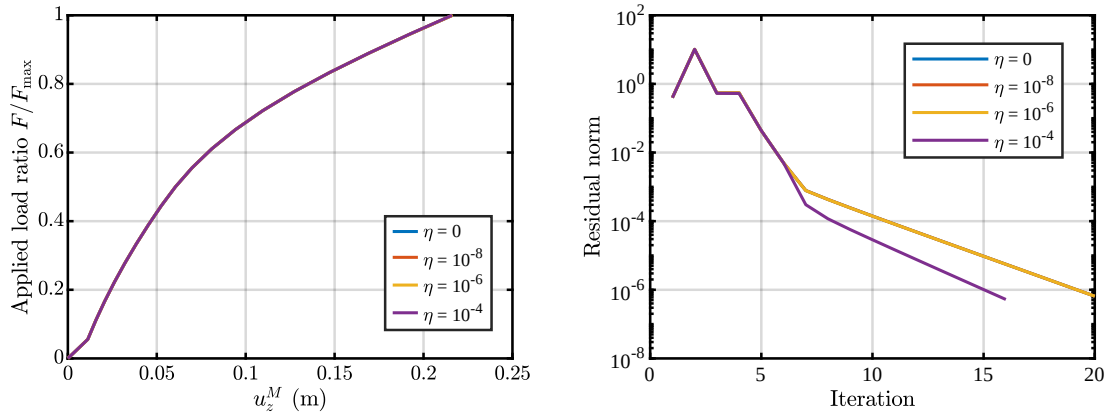

(a) **(b)**

Figure 6.40.: Influence of η in the airbag inflation test (Section 6.1.5): (a) center displacement; (b) residual norm history.

the finest mesh resolution used in their respective studies. In particular, the airbag inflation model is discretized with a 10×10 mesh.

The results are shown in Figures 6.38–6.41. Increasing η from 0 to 10^{-4} produces negligible changes in the physical response for most cases; the only exception is the biaxial corner stretching test, where the displacement at a specific observation point differs by approximately 8×10^{-6} m, which is insignificant in magnitude. This discrepancy may be attributed to the loading configuration, in which forces are applied at the corner nodes, causing stronger stress concentrations and amplifying the influence of the minor correction introduced by η. If the observation point were located in the central region of the membrane or in an area with a gentler stress gradient, the effect would likely be as negligible as in the other examples.

In terms of convergence, $\eta = 10^{-4}$ leads to a substantial reduction in the number of iterations compared with smaller values ($\eta = 0, 10^{-8}, 10^{-6}$): approximately 55.6% in the simple shear test, 16.2% in the biaxial corner stretching test, 20% in the airbag inflation, and 43.3% in

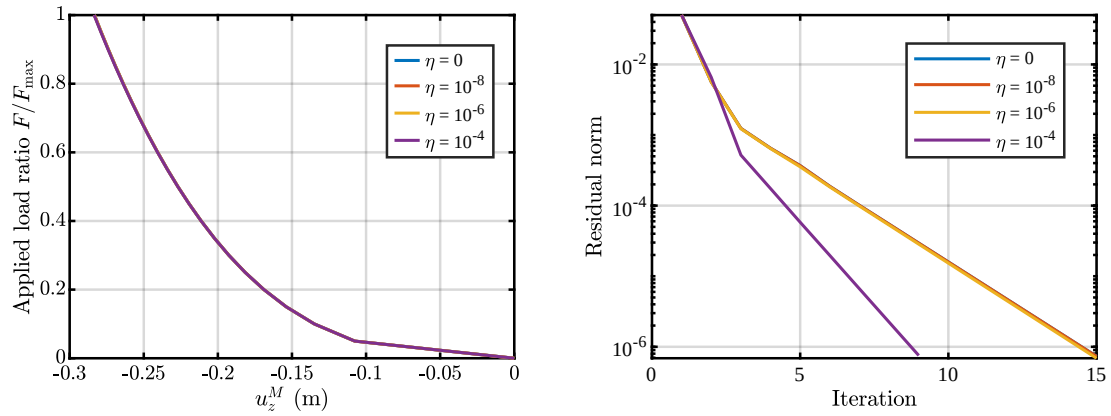

(a) **(b)**

Figure 6.41.: Influence of η in the free fall of blanket (Section 6.1.6): (a) center displacement; (b) residual norm history.

the free fall of blanket, with an overall average reduction of about 34% (range 16%–56%). This improvement arises because a non-zero η introduces a lower-bound stiffness in the components associated with wrinkled/slack states. Unlike the case of $\eta = 0$, where the slack region carries no stiffness, a small positive η imparts a "soft support" that stabilizes the system and accelerates convergence without significantly altering the physical response. A moderate choice of η can thus improve convergence while maintaining accuracy. However, its optimal magnitude depends on problem-specific factors such as loading, material behavior, and mesh resolution. Although values on the order of 10^{-4} have been reported in the literature, no universal standard exists, and empirical calibration is often required. The development of a systematic procedure for selecting η therefore remains an open topic.

6.2 Wrinkling in Hyperelastic Membranes

6.2.1 Inflation of a Hyperelastic Airbag

The first benchmark concerns the pressurization of a square isotropic membrane, which serves to assess the predictive capability of the proposed formulation for hyperelastic materials.

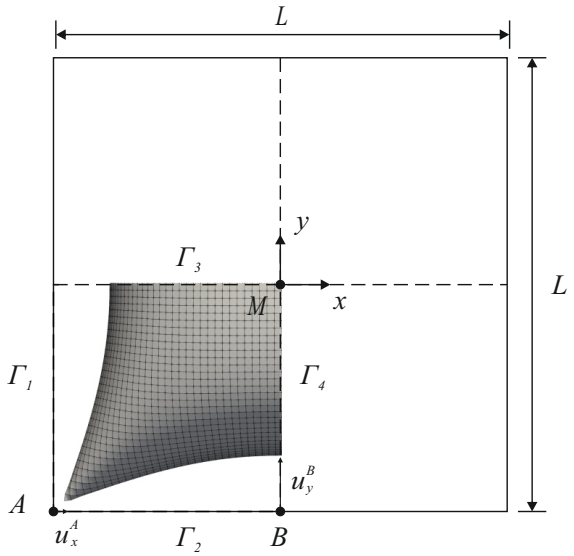

Figure 6.42.: Geometry and boundary conditions of an airbag subjected to inflation pressure.

Originally suggested by [142] for linear elastic materials and later generalized to hyperelastic systems in [64, 67], this problem has become a standard reference in the literature. The configuration is depicted in Figure 6.42: a square membrane with length $L = \sqrt{1.2^2/2}$ m and thickness $t = 0.1$ mm. The constitutive response is modeled by a compressible Neo-Hookean material, whose strain energy density reads

$$\psi(\mathbf{C}) = \frac{\mu}{2}\left(J^{-2/3}\,\mathrm{tr}\,(\mathbf{C}) - 3\right) + \frac{K}{4}\left(J^2 - 1 - 2\ln J\right), \tag{6.10}$$

with shear modulus $\mu = \frac{E}{2(1+\nu)}$ and bulk modulus $K = \frac{E}{3(1-2\nu)}$, determined from Young's modulus $E = 588$ MPa and Poisson's ratio $\nu = 0.4$. Owing to symmetry, only one quarter of the structure is represented. On the edges Γ_3 and Γ_4, symmetry conditions are enforced, while the outer boundaries Γ_1 and Γ_2 are constrained against out-of-plane displacements. The surface is loaded by a pressure P acting normal to the membrane, gradually increased up to 5000 Pa. As pointed out in earlier studies, applying pressure directly to an initially flat membrane may result in a singular stiffness matrix at the beginning of the computation, which renders the problem numerically delicate. To avoid this difficulty, auxiliary dead loads are first introduced in the x- and y-directions along edges Γ_1 and Γ_2 in order to prestretch the membrane. These auxiliary loads are progressively reduced and finally removed once the prescribed pressure reaches its maximum value.

For consistency with previous investigations, the discretization relies on bi-linear membrane elements with mesh densities from 8×8 up to 32×32. In addition, a degradation factor of $\eta = 1 \times 10^{-3}$ is employed. Table 6.4 collects the main quantities of interest obtained from the simulations: the central out-of-plane displacement u_z^M, the in-plane displacements at corner points A and B (u_x^A, u_y^B), and the first principal stress at the membrane center (σ_1^M).

Table 6.4.: Comparison of results from literature and current model (CM).

No. elements	5x5	25x25	8x8		16x16		32x32		16x16	32x32	64x64	128x128
	[67]		[64]	CM	[64]	CM	[64]	CM	KL-shell			
u_z^M (m)	0.2144	0.2245	0.2153	0.2246	0.2181	0.2245	0.2188	0.2244	0.2215	0.2229	0.2235	0.2244
u_x^A (m)	0.0265	0.0307	0.0357	0.0345	0.0333	0.0330	0.0315	0.0319	0.0283	0.0295	0.0303	0.0306
u_y^B (m)	0.1207	0.1158	-	0.1137	-	0.1141	-	0.1141	0.1096	0.1093	0.1116	0.1214
σ_1^M (MPa)	-	-	-	17.3	-	17.3	-	17.3	17.8	17.6	17.4	17.2

The comparison in Table 6.4 highlights the very good agreement between the current model, the KL-shell solution, and the values reported by [64, 67]. Although the KL-shell solution is not yet fully converged, the discrepancy between the 64×64 and 128×128 discretizations is merely 0.366 ‰, which supports the reliability of the finest mesh as a reference. Remarkably, even the coarsest 8×8 mesh yields a central displacement u_z^M close to the reference obtained from a 128×128 bi-cubic KL-shell computation. As the mesh is refined, the predictions of the proposed wrinkling model progressively approach the KL-shell solution. Accurate results are therefore obtained already on relatively coarse meshes, leading to a substantial reduction in computational cost compared with high-order shell formulations. This aspect is of practical relevance for large-scale membrane problems, where fine meshes are often computationally prohibitive. Overall, these observations confirm both the efficiency and reliability of the wrinkling model under pressurized membrane conditions.

6.2.2 Stretching of a Hyperelastic Rectangular Membrane

In the second benchmark, the wrinkling behavior of a rectangular membrane under uniaxial tension is investigated. This configuration has been widely studied in the literature [45–47, 51, 57, 148, 149], as it exhibits the characteristic sequence of wrinkle initiation at small strains followed by restabilization at finite strain. The geometry is illustrated in Figure 6.43, where the dimensions of the membrane are $L = 0.28\,\mathrm{m}$, $W = 0.14\,\mathrm{m}$, and $t = 0.14\,\mathrm{mm}$, corresponding to aspect ratios $L/W = 2$ and $t/W = 10^{-3}$.

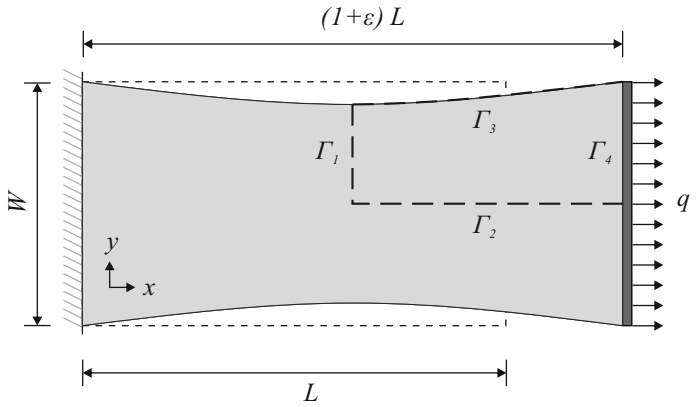

Figure 6.43.: Geometry and boundary conditions of a rectangular membrane under stretching.

In the simulation, a uniform displacement is prescribed along the right boundary, producing an axial strain ε in the x-direction, while the opposite edge is fixed to prevent rigid body motion. Exploiting symmetry, only one quarter of the domain is discretized. The boundary conditions are specified as follows: along Γ_1, symmetry is enforced by constraining $u_x = 0$; along Γ_2, anti-symmetry is imposed by restricting displacements in the y- and z-directions. The edge Γ_3 remains traction-free, whereas along Γ_4 displacements in y- and z-directions are fixed, and the displacement in the x-direction is constrained to remain uniform.

In line with the comparison carried out in [51], the membrane is modeled as an incompressible Mooney–Rivlin material, which was demonstrated to reproduce experimental data most accurately among the models considered. The strain energy density function is given by

$$\psi_{\mathrm{el}}(\mathbf{C}) = \frac{c_1}{2}\,(I_1 - 3) + \frac{c_2}{2}\,(I_2 - 3)\,, \tag{6.11}$$

where the material parameters are $c_1 = 3.16\times10^5\,\mathrm{Pa}$ and $c_2 = 1.24\times10^5\,\mathrm{Pa}$. Following [150], the domain is discretized with a 32×32 bi-cubic Kirchhoff–Love shell mesh to resolve the onset and development of wrinkling, and the nonlinear response is traced by means of Crisfield's spherical arc-length method [132]. The KL-shell simulation reproduces the experimental wrinkling behavior with respect to both amplitude and critical strain, and therefore serves as a reliable reference for the assessment of the proposed model.

The global structural response is depicted in Figure 6.44, which shows the reaction force against the applied strain. Up to $\varepsilon \approx 0.3$, the force–strain curves obtained from the KL-shell and the current formulation (based on an 16×8 bilinear mesh) are virtually indistinguishable, indicating

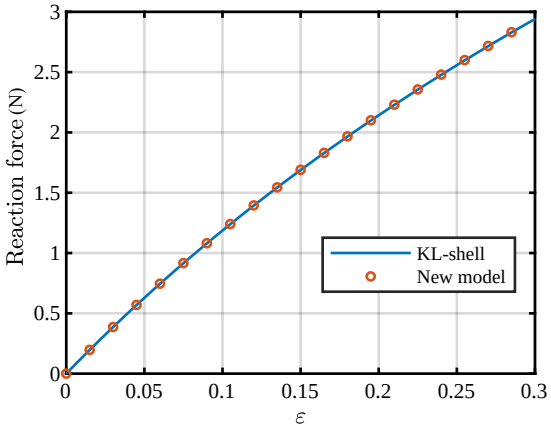

Figure 6.44.: Comparison of reaction forces between the KL-shell model and the current model under varying strain.

excellent agreement in both the pre-buckling regime and the early post-buckling range. Since the KL-shell approach is capable of describing the entire wrinkling evolution, including the eventual disappearance of wrinkles at larger strains, whereas a tension-field–based formulation does not capture this restabilization, the comparison is limited to $0 \leq \varepsilon \leq 0.3$, i.e., the strain interval in which wrinkles actively develop and both models remain applicable.

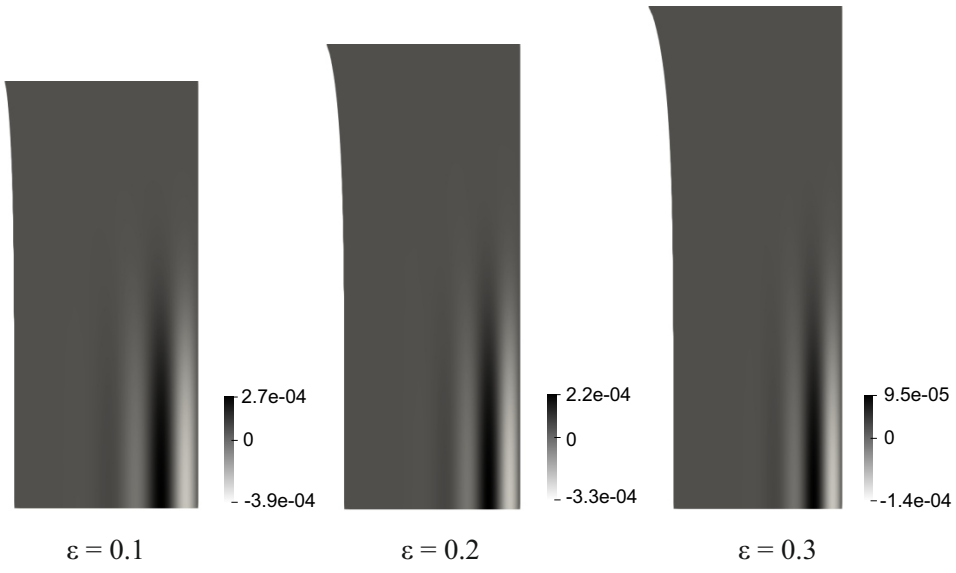

Figure 6.45.: Wrinkle amplitude evolution under increasing strain predicted by the KL-shell model (in m).

Figure. 6.45 presents the wrinkling patterns predicted by the KL-shell model at three representative strain levels. With increasing strain, the KL-shell results display a progressive reduction in wrinkling wavelength (see Figure 6.46), indicating that the wrinkled zone becomes more localized, while the wrinkle amplitude decreases simultaneously.

The evolution of the wrinkled region width predicted by the two models is compared in

Figure. 6.46. According to the KL-shell model, the wrinkling width is zero at the beginning,

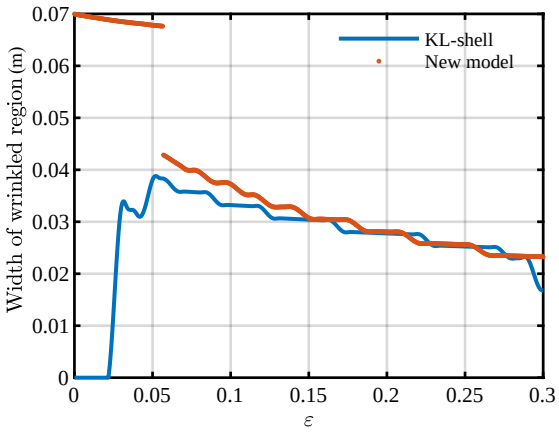

Figure 6.46.: Comparison of the width of the wrinkled region under increasing strain between the KL-shell model and the new model. The wrinkling width is measured along the boundary Γ_1 of the membrane.

starts to increase at approximately $\varepsilon \approx 0.025$, and reaches a maximum of about 0.04 m at $\varepsilon \approx 0.05$. As the stretching continues, the width gradually diminishes, and when the strain approaches $\varepsilon \approx 0.3$, the wrinkles start to disappear rapidly due to overstretching. This trend successfully reproduces the entire sequence from wrinkle initiation to re-stabilization. The new model, by contrast, does not reproduce these transition phases due to the inherent characteristics of tension field theory: wrinkling is already predicted at the onset of loading as a result of compressive stresses near the edges, and the membrane is still considered wrinkled even when the strain exceeds $\varepsilon \approx 0.3$. It is important to highlight, however, that the new model exhibits a pronounced jump in the predicted wrinkling width around $\varepsilon \approx 0.05$. Beyond this point, the predictions of both models become highly consistent, starting at about 0.04 m and gradually decreasing to nearly 0.023 m. This demonstrates that the new model provides accurate and reliable results within the principal wrinkling regime, despite the limitations inherited from tension field theory at the onset and termination of wrinkling.

6.2.3 Shear Loading of a Hyperelastic Membrane

In the third benchmark, the focus is placed on a rectangular membrane subjected to shear-dominated loading. The specimen has dimensions of 200 mm in length, 100 mm in width, and 0.2 mm in thickness, as depicted in Figure 6.47. The hyperelastic response is described by the formulation proposed in [110], where the plane-stress strain energy potential is expressed as

$$\psi(\mathbf{C}) = \frac{1}{2}\mu\left(\operatorname{tr}(\mathbf{C}) - 2\right) - \frac{\lambda + 2\mu}{4}\left(2\log J + \log\left(\lambda + 2\mu\right) - \log\left(\lambda J^2 + 2\mu\right)\right), \tag{6.12}$$

with the material constants given by $\lambda = 1852.07\,\mathrm{N\,mm^{-2}}$ and $\mu = 207.90\,\mathrm{N\,mm^{-2}}$.

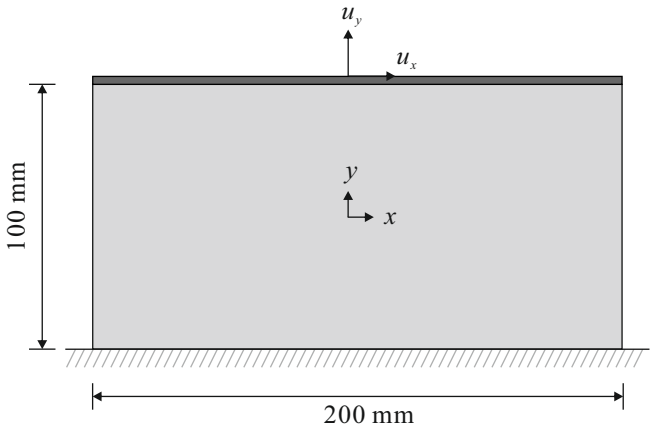

Figure 6.47.: Geometry and boundary conditions of a rectangular membrane under shear deformation.

The loading sequence follows the procedure outlined in [110]. At the beginning of the loading process, a small vertical displacement of $u_y = 1\,\mathrm{mm}$ is applied along the upper edge while keeping $u_x = 0\,\mathrm{mm}$ fixed, thereby introducing a slight tensile stretch. In the subsequent stage, the horizontal displacement u_x is gradually increased up to 10 mm, while the vertical displacement u_y is maintained at 1 mm, resulting in a predominantly shear-induced deformation state.

The shear force–displacement response obtained with a 32×16 mesh of bi-linear membrane elements is shown in Figure 6.48. During the initial loading stage, all models exhibit an almost linear relation between reaction force and displacement. At $u_x \approx 2\,\mathrm{mm}$, both the proposed formulation and the reference solution of [110] show a distinct reduction in slope, reflecting a loss of stiffness due to the onset of wrinkling. The subsequent response is characterized by a softened but still increasing force, consistent with the progressive development of wrinkling under shear. By contrast, the classical membrane formulation fails to reproduce this behavior: its response curve remains nearly linear with a constant slope, leading to an overestimation of stiffness in the wrinkling regime. This discrepancy clearly highlights the limitations of neglecting wrinkling effects in shear-dominated deformation.

Overall, the comparison demonstrates that the proposed formulation reproduces the essential features of the shear-induced wrinkling response with high fidelity. In particular, the accurate

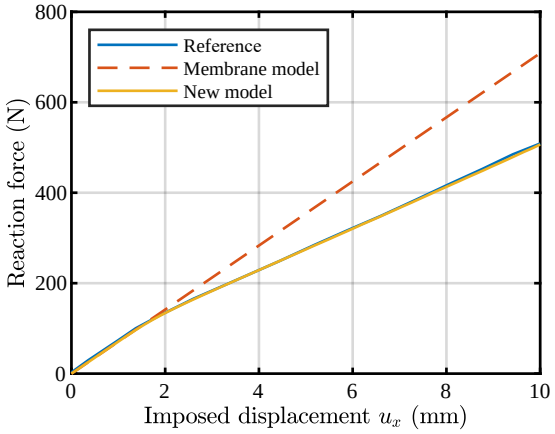

Figure 6.48.: Shear force–displacement response.

prediction of the stiffness reduction and the close agreement with the reference solution confirm the robustness of the approach beyond pure tension cases. These results provide further evidence that the formulation is capable of capturing wrinkling phenomena in a broad range of loading conditions, including shear-dominated deformation states where classical membrane models are inadequate.

6.2.4 Twisting of a Prestretched Membrane

In the final benchmark, a membrane subjected to combined stretching and twisting is examined. The geometry is shown in Figure 6.49: the initial configuration is trapezoidal, with a top width of 100 mm, a bottom width of 50 mm, and a height of 100 mm. The membrane thickness is negligible compared with the in-plane dimensions and is set to 5×10^{-3} mm.

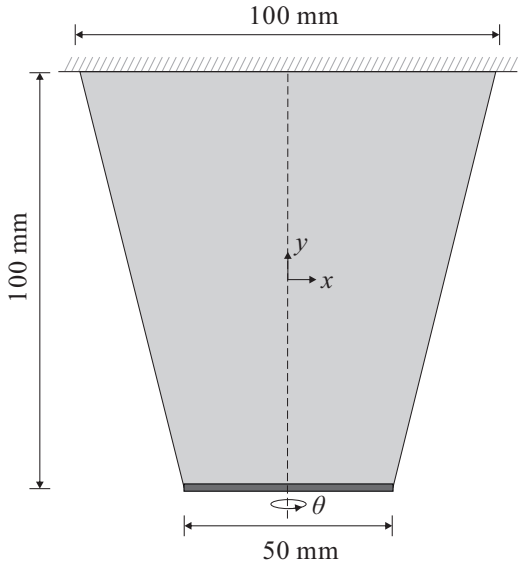

Figure 6.49.: Geometry and boundary conditions of a trapezoidal membrane subjected to stretching and twisting.

The hyperelastic material response is modeled with an incompressible Neo-Hookean law, defined as

$$\psi_{\mathrm{el}}(\mathbf{C}) = \frac{\mu}{2}\,(I_1 - 3)\,, \tag{6.13}$$

where the shear modulus μ is determined from Young's modulus $E = 1 \times 10^3$ MPa and Poisson's ratio $\nu = 0.5$.

The loading is applied in two stages. The top boundary is fully clamped, preventing all translations. In the first stage, the bottom edge is displaced downward by 50 mm, inducing a finite tensile strain. In the second stage, the bottom edge undergoes a prescribed rotational displacement around the vertical axis, thereby twisting the membrane. This combined loading condition activates wrinkling, which evolves with increasing rotation, as illustrated in Figure 6.51.

To establish a reference solution, the problem is discretized using bi-cubic KL-shell elements with meshes of 16×16, 32×32, and 64×64. The torque is computed by integrating the nodal reaction forces multiplied by the corresponding rotational displacements along the loaded edge. Figure 6.50 shows the torque–rotation response. The torque grows nonlinearly with increasing rotation, and the incremental stiffness gradually decreases. The convergence of the results with mesh refinement confirms that the 64×64 KL-shell discretization provides a reliable reference.

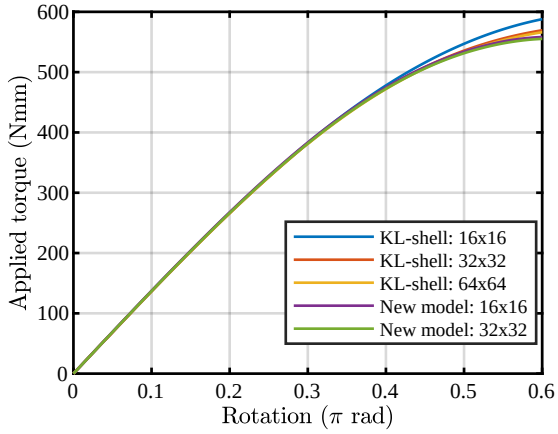

Figure 6.50.: Torque–rotation response.

The predictions of the proposed wrinkling model, discretized with bi-quadratic membrane elements, are compared against the KL-shell reference. Even on the coarse 16×16 mesh, the global response agrees closely with the reference across the full rotation range, with only minor deviations at the largest rotations. This agreement highlights the efficiency of the proposed model, which achieves accurate results at a fraction of the computational cost of shell formulations.

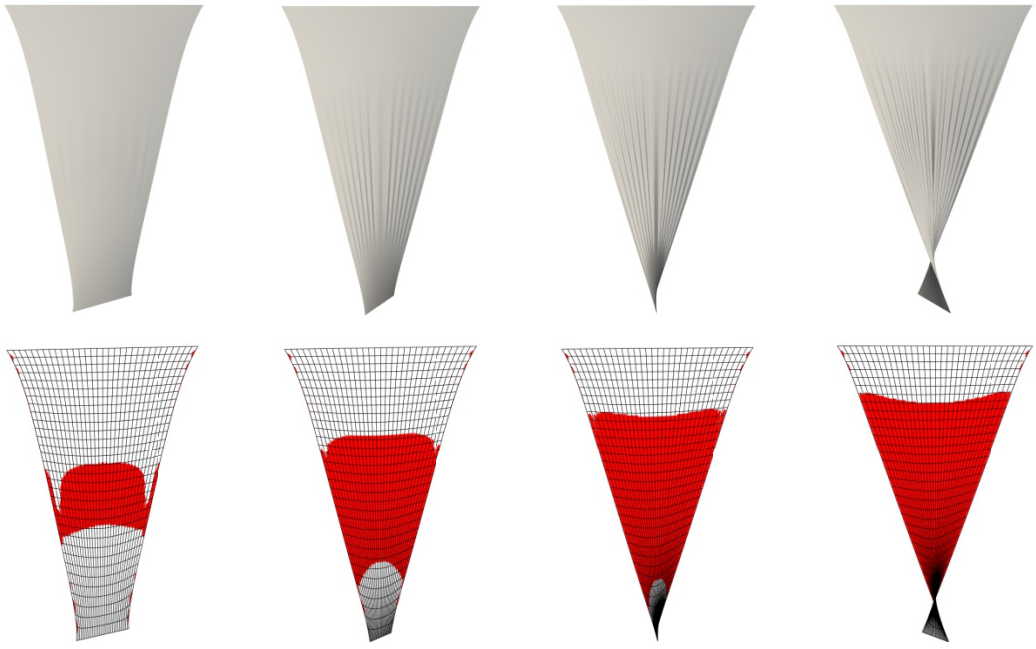

Figure 6.51.: Comparison of wrinkling evolution under increasing rotation: KL-shell results (top) and proposed model (bottom). Red indicates wrinkled regions; white indicates taut or slack zones.

In addition to global quantities, the model also provides detailed predictions of wrinkling

patterns. Figure 6.51 compares the wrinkling regions from the KL-shell solution with those identified by the proposed formulation. Red areas denote wrinkled zones, while white indicates taut or slack regions. At $\theta = 0.3\pi$ (Figure 6.51(a)), a narrow wrinkled band emerges along the central axis, whereas the upper and lower ends remain taut. At $\theta = 0.4\pi$ (Figure 6.51(b)), the wrinkles extend further toward the clamped and loaded edges. At $\theta = 0.5\pi$ (Figure 6.51(c)), the wrinkles become more pronounced and occupy most of the mid-region. Finally, at $\theta = 0.6\pi$ (Figure 6.51(d)), the wrinkled band spans nearly the entire height of the membrane, leaving only narrow taut strips near the boundaries. The close match between the two sets of predictions confirms that the proposed formulation can accurately reproduce both the global torsional response and the local wrinkling evolution.

Chapter 7

Conclusions and Outlook

This dissertation develops various variationally consistent approaches for the numerical modeling of membrane wrinkling. These approaches are formulated within a unified framework that enables the consistent treatment of the taut, wrinkled, and slack states in a single expression. By construction, the framework avoids both nested-optimization relaxations and the if–else state switching that are characteristic of existing tension-field models. The central idea is to separate the strain energy density into tensile and compressive parts through spectral decomposition of strain and stress tensors. Since a membrane cannot resist compression, a degradation factor is introduced for the compressive part of the energy. The compressive contribution may either be removed in accordance with tension-field theory to enforce zero compressive stiffness, or retained with a very small degradation factor to enhance robustness, allow slack states, prevent element interpenetration, and avoid singular stiffness matrices. As a result, the three states emerge naturally without case-specific branching, and stress as well as material constitutive tensors are consistently derived from the modified strain energy, ensuring both physical consistency and numerical stability. Under isotropy, the eigenvectors obtained from the spectral decomposition of the strain tensor directly provide the wrinkle orientations, eliminating the need for additional identification procedures and thereby improving interpretability and simplifying postprocessing. These approaches are readily implementable, compatible with standard finite element methods and isogeometric analysis, and can be directly integrated into commercial finite element environments.

Within this framework, three alternative approaches of the tensile–compressive split are introduced and compared for the St. Venant–Kirchhoff material, each corresponding to a different wrinkling criterion: the principal strain criterion, the principal stress criterion, and the mixed criterion. Among these, the strain-criterion-based model performs reliably for many loading paths; however, it may lose accuracy in shear-dominated scenarios. The stress-criterion-based model is non-convex in the wrinkled regime and is therefore more sensitive to iterative solvers and numerical noise, with reduced regularity at wrinkled state. The mixed-criterion-based model is obtained as a modification of the stress-criterion-based formulation by setting the Poisson ratio to zero in the wrinkled and slack states, thereby eliminating transverse coupling that is no longer physically relevant. This simple adjustment yields a model that is both compact and effective: it satisfies the uniaxial-tension requirement of tension-field theory and provides higher accuracy than the strain-, or stress-criterion-based models, since the latter either lose accuracy under shear-dominated loading or lack the

corresponding strain correction.

The wrinkling model is then extended to hyperelastic materials. Following the projection strategy, a modified deformation gradient is introduced that excludes compressive contributions along the wrinkle direction. On this basis, the tensile–compressive split is applied in a reformulated form that accounts for nonlinear constitutive behavior while also satisfying the uniaxial-tension condition. Combined with the mixed wrinkling criterion, this construction leads to a compact stress formulation, depending mainly on the second principal stress. The resulting formulation reduces implementation effort and computational cost, providing a natural and efficient generalization from linear elasticity to hyperelasticity.

The proposed wrinkling models are examined through a broad set of numerical studies in both linear elastic and hyperelastic regimes. The examples cover diverse loading and boundary conditions, ranging from fundamental benchmarks such as bending, torsion, shear, biaxial stretching, and inflation to dynamic and hyperelastic cases of practical relevance. Results are systematically compared against analytical solutions, fine-mesh Kirchhoff–Love shell models, experimental data, and established wrinkling formulations reported in the literature, showing good agreement in both linear elastic and hyperelastic regimes. The results demonstrate that among the three criteria, the mixed formulation provides the best overall balance of accuracy, robustness, and numerical stability across loading types. The influence of the degradation factor is also examined: very small values leave the mechanical response essentially unaffected; however, they can accelerate convergence by reducing the number of iterations required. Overall, these models provide a solid theoretical and computational foundation for the numerical modeling of complex membrane wrinkling problems and establish a reliable basis for their analysis in engineering applications.

However, the present work remains limited to isotropic hyperelastic membranes. A natural next step is to extend the formulation to plasticity and subsequently to anisotropic materials. In anisotropic membranes, wrinkle orientations do not coincide with principal strain directions; they can be approximated by principal stress directions as pointed out in [81], but this approximation still requires systematic validation. The current formulation is primarily based on projection operators of the strain tensor, and future work will therefore focus on developing a stress-based variant in which the split is constructed along principal stress directions, in order to achieve a more accurate representation of wrinkling in anisotropic settings.

In addition, the present framework is formulated in a purely mechanical setting. An important direction for future research is to explore couplings with other physical fields, such as thermal, electrical, or fracture phenomena. Since the tensile–compressive split originates from phase-field models for fracture, a close conceptual link exists: wrinkling models suppress compressive stresses, whereas phase field fracture models suppress tensile stresses. This complementarity provides a natural basis for a unified formulation that can describe the interaction between wrinkling and crack initiation or propagation in a more straightforward manner.

Furthermore, although the membrane element embedded with a wrinkling model is effective in representing the macroscopic response, accurately predicting the stress field with coarse meshes and significantly lower computational cost compared to shell elements, it can only provide the average displacement field and cannot resolve wrinkle details such as wavelength

and amplitude due to the absence of bending stiffness. A promising direction for future research is to develop approaches that can recover these fine-scale features while maintaining relatively low computational cost, thereby improving the predictive capability of the method with respect to the actual morphology of wrinkles.

Finally, and most significantly, another limitation concerns the scope of tension-field theory (TFT) itself. TFT is strictly valid only for very thin membranes, and it was shown in [66] that while conventional plate theory treats a structure as a membrane when the slenderness ratio exceeds about 100, TFT requires the slenderness ratio to be greater than roughly 1000 for its predictions to become reasonable. Even then, post-buckling analyses reveal that wrinkled regions still sustain finite compressive stresses, which are completely excluded by TFT. Moreover, nearly all existing wrinkling formulations remain rooted in TFT and, despite differences in detail, are fundamentally aimed at enforcing the uniaxial tension condition. This paradigm has constrained the development of alternative approaches. Future work should therefore not only characterize the magnitude and influence of compressive stresses in wrinkled or slack regions, but also explore alternative theories in which different admissibility conditions may emerge. Such a shift would mark a significant step forward, opening new directions beyond the traditional tension-field paradigm.

Appendix

A.1 Tensor Derivatives of Invariants

For hyperelastic materials, it is necessary to compute the derivatives of the invariants of the right Cauchy–Green deformation tensor $\mathbf{C}$, as well as the derivatives of its inverse. This appendix provides explicit expressions for these derivatives in tensorial form, Cartesian index notation, and curvilinear index notation.

The derivative of the inverse tensor $\mathbf{C}^{-1}$ with respect to $\mathbf{C}$ is given by

$$\frac{\partial \mathbf{C}^{-1}}{\partial \mathbf{C}} = -\mathbf{C}^{-1} \odot \mathbf{C}^{-1}, \quad \left(\frac{\partial \mathbf{C}^{-1}}{\partial \mathbf{C}}\right)_{ijkl} = -\frac{1}{2}\left(C^{-1}_{ik} C^{-1}_{jl} + C^{-1}_{il} C^{-1}_{jk}\right). \tag{A.1}$$

The derivatives of the trace of $\mathbf{C}$, its square, and cube are

$$\frac{\partial \mathrm{tr}(\mathbf{C})}{\partial \mathbf{C}} = \mathbf{I}, \quad \frac{\partial \mathrm{tr}(\mathbf{C}^2)}{\partial \mathbf{C}} = 2\mathbf{C}, \quad \frac{\partial \mathrm{tr}(\mathbf{C}^3)}{\partial \mathbf{C}} = 3\mathbf{C}^2, \tag{A.2}$$

where $\mathbf{I}$ is the identity tensor. The derivative of the determinant of $\mathbf{C}$ is

$$\frac{\partial \det(\mathbf{C})}{\partial \mathbf{C}} = \det(\mathbf{C})\, \mathbf{C}^{-1}. \tag{A.3}$$

Applying the chain rule to Equation (A.3), the second derivative of $\det(\mathbf{C})$ becomes

$$\frac{\partial^2 \det(\mathbf{C})}{\partial \mathbf{C}\, \partial \mathbf{C}} = \det(\mathbf{C}) \left(\mathbf{C}^{-1} \otimes \mathbf{C}^{-1} - \mathbf{C}^{-1} \odot \mathbf{C}^{-1}\right). \tag{A.4}$$

With these preliminary results, the derivatives of the invariants of $\mathbf{C}$ can be computed. For convenience, the invariants are defined as

$$I_1 = \mathrm{tr}(\mathbf{C}), \quad I_2 = \tfrac{1}{2}\big((\mathrm{tr}(\mathbf{C}))^2 - \mathrm{tr}(\mathbf{C}^2)\big), \quad I_3 = \det(\mathbf{C}). \tag{A.5}$$

In tensorial and Cartesian index notation, their first and second derivatives are

$$\frac{\partial I_1}{\partial \mathbf{C}} = \mathbf{I}, \quad \frac{\partial I_1}{\partial C_{ij}} = \delta_{ij}, \quad \frac{\partial^2 I_1}{\partial \mathbf{C}\, \partial \mathbf{C}} = \mathbf{0}, \quad \frac{\partial^2 I_1}{\partial C_{ij} \partial C_{kl}} = 0, \tag{A.6}$$

$$\frac{\partial I_2}{\partial \mathbf{C}} = \mathrm{tr}(\mathbf{C})\mathbf{I} - \mathbf{C}, \quad \frac{\partial^2 I_2}{\partial \mathbf{C}\,\partial \mathbf{C}} = \mathbf{I} \otimes \mathbf{I} - \mathbb{I}, \tag{A.7}$$

where $\mathbb{I}$ denotes the symmetric fourth-order identity tensor. In Cartesian notation, these derivatives are

$$\frac{\partial I_2}{\partial C_{ij}} = \mathrm{tr}(\mathbf{C})\delta_{ij} - C_{ij}, \quad \frac{\partial^2 I_2}{\partial C_{ij}\partial C_{kl}} = \delta_{ij}\delta_{kl} - \tfrac{1}{2}(\delta_{ik}\delta_{jl} + \delta_{il}\delta_{jk}). \tag{A.8}$$

Since I_3 coincides with $\det(\mathbf{C})$, its derivatives follow directly from Equations (A.3) and (A.4). For completeness, they are listed as

$$\frac{\partial I_3}{\partial \mathbf{C}} = \det(\mathbf{C})\,\mathbf{C}^{-1}, \quad \frac{\partial^2 I_3}{\partial \mathbf{C}\,\partial \mathbf{C}} = \det(\mathbf{C})\left(\mathbf{C}^{-1} \otimes \mathbf{C}^{-1} - \mathbf{C}^{-1} \odot \mathbf{C}^{-1}\right), \tag{A.9}$$

and in Cartesian index form,

$$\frac{\partial I_3}{\partial C_{ij}} = \det(\mathbf{C})\,C^{-1}_{ij}, \quad \frac{\partial^2 I_3}{\partial C_{ij}\partial C_{kl}} = \det(\mathbf{C})\left(C^{-1}_{ij}C^{-1}_{kl} - \tfrac{1}{2}(C^{-1}_{ik}C^{-1}_{jl} + C^{-1}_{il}C^{-1}_{jk})\right). \tag{A.10}$$

In curvilinear coordinates, the covariant coefficients C_{ij} are obtained from the kinematic relations. Since these quantities are used to construct the material tensor in the covariant basis, the contravariant components are preferred and given as $C^{ij} = C_{mn}G^{mi}G^{nj}$. The inverse tensor is expressed as $\mathbf{C}^{-1} = \check{C}^{ij}\mathbf{G}_i \otimes \mathbf{G}_j$, with $[\check{C}^{ij}] = [C_{ij}]^{-1}$.

In curvilinear notation, the derivatives are written as

$$\frac{\partial I_1}{\partial C_{ij}} = G^{ij}, \quad \frac{\partial^2 I_1}{\partial C_{ij}\partial C_{kl}} = 0, \tag{A.11}$$

$$\frac{\partial I_2}{\partial C_{ij}} = \mathrm{tr}(\mathbf{C})G^{ij} - C_{mn}G^{mi}G^{nj}, \quad \frac{\partial^2 I_2}{\partial C_{ij}\partial C_{kl}} = G^{ij}G^{kl} - \tfrac{1}{2}(G^{ik}G^{jl} + G^{il}G^{jk}), \tag{A.12}$$

$$\frac{\partial I_3}{\partial C_{ij}} = \det(\mathbf{C})\,\check{C}^{ij}, \quad \frac{\partial^2 I_3}{\partial C_{ij}\partial C_{kl}} = \det(\mathbf{C})\left(\check{C}^{ij}\check{C}^{kl} - \tfrac{1}{2}(\check{C}^{ik}\check{C}^{jl} + \check{C}^{il}\check{C}^{jk})\right). \tag{A.13}$$

A.2 Static Condensation of E_{33} for Incompressible Materials

In the context of incompressible hyperelastic membranes and shells, the transverse strain component E_{33} does not represent an independent degree of freedom. Instead, the constraint $S^{33} = 0$ must be imposed, which effectively eliminates E_{33} from the constitutive description. This appendix summarizes the analytical procedure required for the static condensation of the thickness strain, so that only the in-plane material response remains.

The condensed in-plane material tensor $\widehat{\mathbb{C}}^{\alpha\beta\gamma\delta}$ is derived from the full fourth-order tensor $\mathbb{C}^{ijkl}$ by applying the plane stress condition. Its general definition is given as

$$\widehat{\mathbb{C}}^{\alpha\beta\gamma\delta} = \mathbb{C}^{\alpha\beta\gamma\delta} - \frac{\mathbb{C}^{\alpha\beta 33}\,\mathbb{C}^{33\gamma\delta}}{\mathbb{C}^{3333}}. \tag{A.14}$$

To perform the condensation explicitly, the full material tensor $\mathbb{C}^{ijkl}$ is recalled. Taking into account incompressibility and the contribution of the Lagrange multiplier, it reads

$$\begin{aligned}\mathbb{C}^{ijkl} = {} & 4\frac{\partial^2\psi_{\mathrm{el}}}{\partial C_{ij}\partial C_{kl}} - 2\frac{\partial\psi_{\mathrm{el}}}{\partial C_{33}}C_{33}\left(\check{C}^{ij}\check{C}^{kl} - \check{C}^{ik}\check{C}^{jl} - \check{C}^{il}\check{C}^{jk}\right) \\ & -4\left(\frac{\partial^2\psi_{\mathrm{el}}}{\partial C_{33}\partial C_{ij}}C_{33} + \frac{\partial\psi_{\mathrm{el}}}{\partial C_{33}}\delta^{i3}\delta^{j3}\right)\check{C}^{kl} - 4\check{C}^{ij}\left(\frac{\partial^2\psi_{\mathrm{el}}}{\partial C_{33}\partial C_{kl}}C_{33} + \frac{\partial\psi_{\mathrm{el}}}{\partial C_{33}}\delta^{k3}\delta^{l3}\right).\end{aligned} \tag{A.15}$$

The next step is to identify the relevant tensor components. The in-plane block is expressed as

$$\begin{aligned}\mathbb{C}^{\alpha\beta\gamma\delta} = {} & 4\frac{\partial^2\psi_{\mathrm{el}}}{\partial C_{\alpha\beta}\partial C_{\gamma\delta}} - 2\frac{\partial\psi_{\mathrm{el}}}{\partial C_{33}}C_{33}\left(\check{C}^{\alpha\beta}\check{C}^{\gamma\delta} - \check{C}^{\alpha\gamma}\check{C}^{\beta\delta} - \check{C}^{\alpha\delta}\check{C}^{\beta\gamma}\right) \\ & - 4\frac{\partial^2\psi_{\mathrm{el}}}{\partial C_{33}\partial C_{\alpha\beta}}C_{33}\check{C}^{\gamma\delta} - 4\check{C}^{\alpha\beta}\frac{\partial^2\psi_{\mathrm{el}}}{\partial C_{33}\partial C_{\gamma\delta}}C_{33},\end{aligned} \tag{A.16}$$

while the coupling block takes the form

$$\begin{aligned}\mathbb{C}^{\alpha\beta 33} = {} & 4\frac{\partial^2\psi_{\mathrm{el}}}{\partial C_{\alpha\beta}\partial C_{33}} - 2\frac{\partial\psi_{\mathrm{el}}}{\partial C_{33}}C_{33}\left(\check{C}^{\alpha\beta}\check{C}^{33}\right) - 4\left(\frac{\partial^2\psi_{\mathrm{el}}}{\partial C_{33}\partial C_{\alpha\beta}}C_{33}\right)\check{C}^{33} \\ & - 4\check{C}^{\alpha\beta}\left(\frac{\partial^2\psi_{\mathrm{el}}}{\partial C_{33}^2}C_{33} + \frac{\partial\psi_{\mathrm{el}}}{\partial C_{33}}\right) \\ = {} & -\check{C}^{\alpha\beta}\left(6\frac{\partial\psi_{\mathrm{el}}}{\partial C_{33}} + 4\frac{\partial^2\psi_{\mathrm{el}}}{\partial C_{33}^2}C_{33}\right),\end{aligned} \tag{A.17}$$

and, by symmetry, the corresponding expression for the block with indices $(33\gamma\delta)$ is

$$\mathbb{C}^{33\gamma\delta} = -\check{C}^{\gamma\delta}\left(6\frac{\partial\psi_{\mathrm{el}}}{\partial C_{33}} + 4\frac{\partial^2\psi_{\mathrm{el}}}{\partial C_{33}^2}C_{33}\right). \tag{A.18}$$

The purely transverse part is obtained as

$$\begin{aligned}\mathbb{C}^{3333} =& 4\frac{\partial^2\psi_{\mathrm{el}}}{\partial C_{33}^2} + 2\frac{\partial\psi_{\mathrm{el}}}{\partial C_{33}} C_{33}\left(\check{C}^{33}\right)^2 \\ &- 4\left(\frac{\partial^2\psi_{\mathrm{el}}}{\partial C_{33}^2} C_{33} + \frac{\partial\psi_{\mathrm{el}}}{\partial C_{33}}\right)\check{C}^{33} - 4\check{C}^{33}\left(\frac{\partial^2\psi_{\mathrm{el}}}{\partial C_{33}^2} C_{33} + \frac{\partial\psi_{\mathrm{el}}}{\partial C_{33}}\right) \\ =& -\check{C}^{33}\left(6\frac{\partial\psi_{\mathrm{el}}}{\partial C_{33}} + 4\frac{\partial^2\psi_{\mathrm{el}}}{\partial C_{33}^2} C_{33}\right),\end{aligned} \tag{A.19}$$

From these relations, the product term in Equation (A.14) evaluates to

$$\frac{\mathbb{C}^{\alpha\beta 33}\,\mathbb{C}^{33\gamma\delta}}{\mathbb{C}^{3333}} = -\check{C}^{\alpha\beta}\check{C}^{\gamma\delta}\left(6\frac{\partial\psi_{\mathrm{el}}}{\partial C_{33}} C_{33} + 4\frac{\partial^2\psi_{\mathrm{el}}}{\partial C_{33}^2} C_{33}^2\right). \tag{A.20}$$

Substituting these expressions back into Equation (A.14) yields the condensed material tensor:

$$\begin{aligned}\widehat{C}^{\alpha\beta\gamma\delta} =& 4\frac{\partial^2\psi_{\mathrm{el}}}{\partial C_{\alpha\beta}\partial C_{\gamma\delta}} + 4\frac{\partial^2\psi_{\mathrm{el}}}{\partial C_{33}^2} C_{33}^2\check{C}^{\alpha\beta}\check{C}^{\gamma\delta} - 4\frac{\partial^2\psi_{\mathrm{el}}}{\partial C_{33}\partial C_{\alpha\beta}} C_{33}\check{C}^{\gamma\delta} \\ &- 4\check{C}^{\alpha\beta}\frac{\partial^2\psi_{\mathrm{el}}}{\partial C_{33}\partial C_{\gamma\delta}} C_{33} + 2\frac{\partial\psi_{\mathrm{el}}}{\partial C_{33}} C_{33}\left(2\check{C}^{\alpha\beta}\check{C}^{\gamma\delta} + \check{C}^{\alpha\gamma}\check{C}^{\beta\delta} + \check{C}^{\alpha\delta}\check{C}^{\beta\gamma}\right).\end{aligned} \tag{A.21}$$

Finally, for computational purposes one may substitute $\check{C}^{\alpha\beta} = g^{\alpha\beta}$ and $C_{33} = J_0^{-2}$, which provides the compact representation

$$\begin{aligned}\widehat{C}^{\alpha\beta\gamma\delta} =& 4\frac{\partial^2\psi_{\mathrm{el}}}{\partial C_{\alpha\beta}\partial C_{\gamma\delta}} + 4\frac{\partial^2\psi_{\mathrm{el}}}{\partial C_{33}^2} J_o^{-4} g^{\alpha\beta} g^{\gamma\delta} - 4\frac{\partial^2\psi_{\mathrm{el}}}{\partial C_{33}\partial C_{\alpha\beta}} J_o^{-2} g^{\gamma\delta} \\ &- 4\frac{\partial^2\psi_{\mathrm{el}}}{\partial C_{33}\partial C_{\gamma\delta}} J_o^{-2} g^{\alpha\beta} + 2\frac{\partial\psi_{\mathrm{el}}}{\partial C_{33}} J_o^{-2}\left(2g^{\alpha\beta}g^{\gamma\delta} + g^{\alpha\gamma}g^{\beta\delta} + g^{\alpha\delta}g^{\beta\gamma}\right).\end{aligned} \tag{A.22}$$

A.3 Discussion of the Wrinkle and Principal Directions

In Section 4.4.2, the procedure for determining the wrinkle direction for arbitrary materials is presented in Equation (4.43). This appendix discusses the relation between the wrinkle direction and the principal directions of stress or strain. The Equation (4.43) can be also reformulated as:

$$f(\theta) = \mathbf{T}\cdot\mathbf{SW} - \frac{(\mathbf{W}\cdot\mathbf{SW})}{(\mathbf{W}\otimes\mathbf{W}) : \mathbb{C} : (\mathbf{W}\otimes\mathbf{W})}\ ((\mathbf{T}\otimes\mathbf{W}) : \mathbb{C} : (\mathbf{W}\otimes\mathbf{W})) = 0, \tag{A.23}$$

where $\mathbf{W}$ is the wrinkle direction vector and $\mathbf{T}$ is the direction vector orthogonal to $\mathbf{W}$, both related to the angle θ. The terms appearing in Equation (A.23) can be given a clear physical interpretation. The first term, $\mathbf{T} \cdot \mathbf{SW}$, represents the shear stress component acting in the direction $\mathbf{T}$ corresponding to the traction in the direction $\mathbf{W}$. The second term, $\mathbf{W} \cdot \mathbf{SW}$, denotes the normal stress acting along the wrinkle direction $\mathbf{W}$. The denominator $(\mathbf{W} \otimes \mathbf{W}) : \mathbb{C} : (\mathbf{W} \otimes \mathbf{W})$ corresponds to the effective normal stiffness in the $\mathbf{W}$-direction, extracted from the constitutive tensor $\mathbb{C}$. Finally, the term $(\mathbf{T} \otimes \mathbf{W}) : \mathbb{C} : (\mathbf{W} \otimes \mathbf{W})$ quantifies the shear–normal coupling stiffness between the orthogonal directions $\mathbf{T}$ and $\mathbf{W}$. This term vanishes identically for isotropic materials, since the constitutive tensor $\mathbb{C}$ does not couple orthogonal directions. However, for anisotropic materials, it generally remains nonzero. For this reason, it is often referred to as the anisotropic coupling term.

To illustrate this point, consider isotropic elastic materials such as the St. Venant–Kirchhoff model under plane stress conditions. The material tensor $\mathbb{C}$ can be expressed as $\mathbb{C} = \left(\lambda - \frac{\lambda^2}{\lambda+2\mu}\right) \mathbf{I} \otimes \mathbf{I} + 2\mu\, \mathbb{I}$, where λ and μ are the Lamé constants, $\mathbf{I} \otimes \mathbf{I}$ denotes the volumetric (hydrostatic) contribution, and $\mathbb{I}$ represents the symmetric fourth-order identity tensor corresponding to the deviatoric part. Substituting it into the tensor form of $f(\theta)$ shows that the anisotropic coupling term, $(\mathbf{T} \otimes \mathbf{W}) : \mathbb{C} : (\mathbf{W} \otimes \mathbf{W})$, vanishes identically for the St. Venant–Kirchhoff material. since $\mathbf{T} \cdot \mathbf{W} = 0$. Consequently, the equation $f(\theta) = 0$ reduces to $\mathbf{T} \cdot \mathbf{SW} = 0$, which implies that $\mathbf{SW}$ is collinear with $\mathbf{W}$. Therefore, the wrinkle direction $\mathbf{W}$ coincides with the principal direction of stress (and equivalently with that of strain, since the two tensors are coaxial).

This conclusion likewise holds for isotropic hyperelastic materials. Although the material tensor becomes deformation-dependent, the constitutive law remains isotropic in form and does not couple orthogonal directions. This means that, under finite deformation, the components of the material tensor may differ in magnitude due to the current stretch state, but this does not imply material anisotropy.

Let $\mathbf{C} = \lambda_i^2\, \mathbf{N}_i \otimes \mathbf{N}_i$ be the spectral decomposition with orthonormal eigenvectors $\mathbf{N}_i$, and the projectors $\mathbf{M}_i = \mathbf{N}_i \otimes \mathbf{N}_i$. According to [117, 123, 134], for an isotropic hyperelastic energy $\psi = \psi(\lambda_1,\lambda_2,\lambda_3)$, the chain rule yields

$$\frac{\partial(\cdot)}{\partial \mathbf{C}} = \frac{\partial(\cdot)}{\partial \lambda_i^2} \frac{\partial \lambda_i^2}{\partial \mathbf{C}} = \frac{1}{2\lambda_i} \frac{\partial(\cdot)}{\partial \lambda_i}\, \mathbf{N}_i \otimes \mathbf{N}_i. \tag{A.24}$$

Hence the second Piola–Kirchhoff stress is

$$\mathbf{S} = 2\, \frac{\partial \psi}{\partial \mathbf{C}} = \left(\frac{1}{\lambda_i} \frac{\partial \psi}{\partial \lambda_i}\right) \mathbf{N}_i \otimes \mathbf{N}_i \;= S_i\, \mathbf{N}_i \otimes \mathbf{N}_i, \tag{A.25}$$

which is diagonal in the eigenbasis of $\mathbf{C}$. Therefore, $\mathbf{S}$ and $\mathbf{C}$ are coaxial for any finite deformation.

Differentiating (A.25) with respect to $\mathbf{C}$ gives the material tensor in spectral form,

$$\mathbb{C} = \frac{\partial S_i}{\partial \mathbf{C}}\, (\mathbf{N}_i \otimes \mathbf{N}_i) + S_i\, \frac{\partial (\mathbf{N}_i \otimes \mathbf{N}_i)}{\partial \mathbf{C}}. \tag{A.26}$$

Neglecting scalar coefficients and focusing only on the tensorial directions, the first term produces combinations of the type $\mathbf{N}_i \otimes \mathbf{N}_i \otimes \mathbf{N}_j \otimes \mathbf{N}_j$ (by using chain rule), while the second term, through the derivative of the eigenprojections, contributes four directional tensors, $\mathbf{N}_i \otimes \mathbf{N}_j \otimes \mathbf{N}_i \otimes \mathbf{N}_j$, $\mathbf{N}_i \otimes \mathbf{N}_j \otimes \mathbf{N}_j \otimes \mathbf{N}_i$, $\mathbf{N}_j \otimes \mathbf{N}_i \otimes \mathbf{N}_i \otimes \mathbf{N}_j$, $\mathbf{N}_j \otimes \mathbf{N}_i \otimes \mathbf{N}_j \otimes \mathbf{N}_i$. These four correspond to the operators $\mathbb{G}_{ij} + \mathbb{G}_{ji}$ introduced in Equation (5.4) [134].

If $\mathbf{W}$ and $\mathbf{T}$ are taken as the eigenvectors of $\mathbf{C}$, that is, $\mathbf{W} = \mathbf{N}_j$ and $\mathbf{T} = \mathbf{N}_i$ with $i \neq j$, the contraction $(\mathbf{T} \otimes \mathbf{W}) : \mathbb{C} : (\mathbf{W} \otimes \mathbf{W})$ can be evaluated using the general identity

$$(\mathbf{A} \otimes \mathbf{B}) : (\mathbf{C} \otimes \mathbf{D} \otimes \mathbf{E} \otimes \mathbf{F}) : (\mathbf{G} \otimes \mathbf{H}) = (\mathbf{A} \cdot \mathbf{C})\,(\mathbf{B} \cdot \mathbf{D})\,(\mathbf{E} \cdot \mathbf{G})\,(\mathbf{F} \cdot \mathbf{H}). \tag{A.27}$$

Accordingly, for example,

$$(\mathbf{T} \otimes \mathbf{W}) : (\mathbf{T} \otimes \mathbf{T} \otimes \mathbf{W} \otimes \mathbf{W}) : (\mathbf{W} \otimes \mathbf{W}) = (\mathbf{T} \cdot \mathbf{T})(\mathbf{W} \cdot \mathbf{T})(\mathbf{W} \cdot \mathbf{W})(\mathbf{W} \cdot \mathbf{W}) = 0. \tag{A.28}$$

since $(\mathbf{W} \cdot \mathbf{T}) = 0$ for orthogonal eigenvectors. Consequently, $(\mathbf{T} \otimes \mathbf{W}) : \mathbb{C} : (\mathbf{W} \otimes \mathbf{W}) = 0$. This result demonstrates that when $\mathbf{W}$ and $\mathbf{T}$ coincide with the principal directions of $\mathbf{C}$ (or equivalently of $\mathbf{S}$), the coupling term in the wrinkle-direction equation vanishes, and the wrinkle direction aligns with the principal stress or strain direction.

In contrast, for anisotropic materials, the coupling term $(\mathbf{T} \otimes \mathbf{W}) : \mathbb{C} : (\mathbf{W} \otimes \mathbf{W})$ does not generally vanish. This is because the constitutive tensor $\mathbb{C}_{\text{ani}}$ couples orthogonal directions through its direction-dependent stiffness components. In other words, stretching along $\mathbf{W}$ can produce shear stress in the orthogonal direction $\mathbf{T}$, reflecting the inherent anisotropic coupling of the material. As a result, the stress and strain tensors are generally non-coaxial, and the wrinkle direction must be obtained from the full equation $f(\theta) = 0$.

List of Figures

1.1 Illustrative examples of wrinkling phenomena across different contexts and scales [1]: (a) buckling pattern observed in the stem of a green alga (Acetabularia schenckii); (b) undulated petal edge of Dendrobium helix orchid; (c) growth-induced marginal wrinkles in a lotus leaf; (d) body-surface folds of the free-swimming sea slug (Hexabranchus sanguineus); (e) surface morphology of E. coli AR3110 biofilm; (f) lateral wrinkling in a polyethylene film subjected to uniaxial stretching; (g) wavy patterns on adhesive tape generated by torsional loading; (h) time-dependent instability in an elastic ring under dynamic conditions; (i) pull-in-induced wrinkling of a dielectric elastomer membrane; (j) skin-mounted epidermal electronic sensor; (k) wrinkle formation in a photovoltaic thin film; (l) patterned deformations in a three-dimensional flexible integrated circuit; (m) microscale light-emitting diode device exhibiting surface instabilities. 2

2.1 Schematic view of a membrane [114]. The vectors $\mathbf{X}$ and $\mathbf{x}$ denote the positions on the midsurface in the reference and deformed configurations, respectively, with $\mathbf{u}$ as the displacement vector. 21

3.1 Instabilities in Newton's method [131]: (a) a system unstable under load control (snap–through), (b) a system unstable under displacement control (snap–back), (c) a system unstable under both load and displacement control. . 41

4.1 Illustration of membrane states [115]: (a) taut, (b) wrinkled, and (c) slack. . . 47

4.2 Classification of membrane states in the principal strain space based on different wrinkling criteria. 48

4.3 Transformations among the various configurations of a membrane. 49

5.1 Gradient magnitude $\|\nabla\psi_{\text{eff}}\|$ and minimum Hessian eigenvalue $\lambda_{\min}(\mathbf{H})$ of the effective energy function $\psi_{\text{eff}}(E_1, E_2)$ with $\eta = 0$ for three wrinkling models. 72

5.2 Gradient magnitude $\|\nabla\psi_{\text{eff}}\|$ and minimum Hessian eigenvalue $\lambda_{\min}(\mathbf{H})$ of the effective energy function $\psi_{\text{eff}}(E_1, E_2)$ with $\eta = 10^{-4}$ for mixed- criterion-based model. 73

6.1 In-plane pure bending of a pre-tensioned rectangular membrane [115]. . . . 78

6.2 Numerical simulation settings for the right half of the rectangular membrane under in-plane bending [115]. 79

6.3 Normal stress σ_x predicted by the strain-criterion-based model and compared with the analytical solution for various $2M/PH$ values: (a) $\nu = 0.3$, (b) $\nu = 0$ [114]. 79
6.4 Normal stress σ_x predicted by (a) the stress-criterion-based model and (b) the mixed-criterion-based model, compared with the analytical solution for various $2M/PH$ values at Poisson's ratio $\nu = 0.3$ [115]. 80
6.5 Comparison of model predictions with the analytical solution [115]: (a) moment–curvature relation, and (b) moment–wrinkling height relation. . . . 80
6.6 Convergence behavior of the proposed models [115]: number of iterations required during the second load step to reach the residual tolerance for (a) strain-, (b) stress-, and (c) mixed-criterion-based models. 81
6.7 Mesh convergence study of the proposed wrinkling model (mixed-criterion-based, $p = 2$, $\nu = 0.3$): distribution of normalized normal stress σ_x/σ_0 along the membrane height y/H under different moment-load ratio $\alpha = 2M/PH$. From left to right, results are shown for meshes with 11×5, 23×11, and 43×21 elements. The analytical solution (Ref.) is shown as a solid line. . . 82
6.8 Mesh convergence study of the proposed wrinkling model (mixed-criterion-based, $p = 1$, $\nu = 0.3$): distribution of normalized normal stress σ_x/σ_0 along the membrane height y/H under different load parameters $\alpha = 2M/PH$. From left to right, results are shown for meshes with 11×5, 23×11, and 43×21 elements. The analytical solution (Ref.) is shown as a solid line. . . 83
6.9 Wrinkle formation in the annular membrane under torsion. 85
6.10 Comparison of the first (a) and second (b) principal stresses obtained from the mixed-criterion-based model with analytical solutions for various R/a ratios. 86
6.11 Comparison of the first (a) and second (b) principal stresses obtained from the strain-criterion-based model with analytical solutions for various R/a ratios. . 87
6.12 Comparison of the first (a) and second (b) principal stresses obtained from the stress-criterion-based model with analytical solutions for various R/a ratios. . 87
6.13 Representative convergence behavior of the mixed-criterion-based model for various wrinkle radii R/a in the wrinkling simulation. 88
6.14 Geometry and boundary conditions of the rectangular membrane under simple shear [115]. 89
6.15 Wrinkling patterns observed in a Kapton® membrane under different levels of shear displacement [68]: (a) $u_x = 0.5\,\text{mm}$, (b) $u_x = 1.0\,\text{mm}$, (c) $u_x = 2.0\,\text{mm}$, and (d) $u_x = 3.0\,\text{mm}$. 90
6.16 Distribution of principal stresses along the horizontal midline (section A–A) of the membrane under different shear displacements [115]. 91
6.17 Reaction force versus displacement response of the rectangular membrane under in-plane shear loading [115]. 92
6.18 Convergence behavior of the mixed-criterion-based model at prescribed displacements $u_x = 1.6$ mm and 3.0 mm in the simple shear test. 92
6.19 Visualization of wrinkling intensity and trajectories in the membrane under simple shear, computed using the mixed-criterion-based model. 93

6.20 Experimental and numerical configurations for analyzing the wrinkling behavior of a square membrane under diagonal corner loads. 94
6.21 Comparison of the first principal stress distributions (in MPa) predicted by different models under load ratios T_1/T_2 = 1–4. The top row shows the reference solution obtained from a shell model reported in [68]; the middle row displays the results from the mixed-criterion-based model [115]; and the bottom row corresponds to the strain-criterion-based model [114]. 95
6.22 Comparison of the wrinkling intensity and trajectories predicted by different models under load ratios T_1/T_2 = 1–4. The top row presents the experimental observations reported in [141]; the middle row displays the results from the mixed-criterion-based model; and the bottom row corresponds to the strain-criterion-based model [114]. 96
6.23 Convergence behavior of the mixed-, and strain-criterion-based models in the biaxial corner stretching test. 97
6.24 Geometric and material properties of the square membrane used for inflation simulations [114]. 98
6.25 Comparison of the convergence behavior of different models with mesh 10 ×10 during the final step. 99
6.26 Mesh convergence analysis of the vertical displacement at point M: (a) predicted displacement under different mesh resolutions; (b) relative error with respect to normalized mesh size. 100
6.27 Self-penetration at point B of the airbag with a 32×32 mesh ($\eta = 0$) [114]. . 101
6.28 Displacements at points M and B under different values of η [114]. 102
6.29 Deformation near point B for the 32×32 mesh with various values of η [114]. 102
6.30 Hanging blanket under self-weight [115]. 103
6.31 Comparison of the convergence behavior of different models during the final step with various Poisson's ratios [115]. 104
6.32 Predictions by the mixed-criterion-based model. 104
6.33 Observed skirt deformation in the towing tank test: (a) initial submerged configuration, (b) intermediate stage during towing, and (c) steady-state deformation. The upstream face collapses inward, while the rear surface shows slight outward bulging. 106
6.34 Schematic of the simulation setup: Boundary conditions and applied loads (left) and illustration of the directional surface load $\mathbf{f}_{\text{drag}}$ (right). 107
6.35 Time evolution of the skirt deformation in side view obtained with different models. 108
6.36 Time evolution of the skirt deformation in top view obtained with different models. 109
6.37 Time histories of the reaction forces extracted at the top edge. 110
6.38 Influence of η in the simple shear test (Section 6.1.3): (a) reaction force–displacement; (b) residual norm history. 111
6.39 Influence of η in the biaxial corner stretching test (Section 6.1.4): (a) displacement at upper-left corner; (b) residual norm history. 112

6.40 Influence of η in the airbag inflation test (Section 6.1.5): (a) center displacement; (b) residual norm history. 112
6.41 Influence of η in the free fall of blanket (Section 6.1.6): (a) center displacement; (b) residual norm history. 113
6.42 Geometry and boundary conditions of an airbag subjected to inflation pressure. 114
6.43 Geometry and boundary conditions of a rectangular membrane under stretching. 116
6.44 Comparison of reaction forces between the KL-shell model and the current model under varying strain. 117
6.45 Wrinkle amplitude evolution under increasing strain predicted by the KL-shell model (in m). 117
6.46 Comparison of the width of the wrinkled region under increasing strain between the KL-shell model and the new model. The wrinkling width is measured along the boundary Γ_1 of the membrane. 118
6.47 Geometry and boundary conditions of a rectangular membrane under shear deformation. 119
6.48 Shear force–displacement response. 120
6.49 Geometry and boundary conditions of a trapezoidal membrane subjected to stretching and twisting. 121
6.50 Torque–rotation response. 122
6.51 Comparison of wrinkling evolution under increasing rotation: KL-shell results (top) and proposed model (bottom). Red indicates wrinkled regions; white indicates taut or slack zones. 122

List of Tables

4.1 Overview of wrinkling criteria for different membrane states. 47

6.1 Comparison of results from literature and present work for mesh refinements 4×4 and 5×5. 99
6.2 Comparison of results from literature and present work for mesh refinements 8×8 and 10×10. 99
6.3 Comparison of the displacements and first principal stress with $\nu = 0.3$. . . 103
6.4 Comparison of results from literature and current model (CM). 115

Bibliography

[1] T. Wang, Y. Yang, and F. Xu. Mechanics of tension-induced film wrinkling and restabilization: a review. *Proceedings of the Royal Society A*, 478(2263):20220149, 2022.

[2] H.M. Verhelst. *Isogeometric Analysis of Wrinkling*. Dissertation, Delft University of Technology, 2024.

[3] B. Li, Y. P. Cao, X. Q. Feng, and H. Gao. Mechanics of morphological instabilities and surface wrinkling in soft materials: a review. *Soft Matter*, 8(21):5728–5745, 2012.

[4] L. Ma, L. He, and Y. Ni. Tunable hierarchical wrinkling: From models to applications. *Journal of Applied Physics*, 127(11), 2020.

[5] J. D. Paulsen. Wrapping liquids, solids, and gases in thin sheets. *Annual Review of Condensed Matter Physics*, 10(1):431–450, 2019.

[6] Y. Tan, B. Hu, J. Song, Z. Chu, and W. Wu. Bioinspired multiscale wrinkling patterns on curved substrates: An overview. *Nano-Micro Letters*, 12(1):101, 2020.

[7] N. Friedl, F. G. Rammerstorfer, and F. D. Fischer. Buckling of stretched strips. *Computers & Structures*, 78(1-3):185–190, 2000.

[8] E. Cerda, K. Ravi-Chandar, and L. Mahadevan. Wrinkling of an elastic sheet under tension. *Nature*, 419(6907):579–580, 2002.

[9] E. Cerda and L. Mahadevan. Geometry and physics of wrinkling. *Physical Review Letters*, 90(7):074302, 2003.

[10] N. Jacques and M. Potier-Ferry. On mode localisation in tensile plate buckling. *Comptes Rendus. Mécanique*, 333(11):804–809, 2005.

[11] E. Puntel, L. Deseri, and E. Fried. Wrinkling of a stretched thin sheet. *Journal of Elasticity*, 105:137–170, 2011.

[12] M. Xin and B. Davidovitch. Stretching hookean ribbons part i: relative edge extension underlies transverse compression and buckling instability. *The European Physical Journal E*, 44(7):92, 2021.

[13] N. Silvestre. Wrinkling of stretched thin sheets: Is restrained poisson's effect the sole cause? *Engineering Structures*, 106:195–208, 2016.

[14] W. Wong and S. Pellegrino. Wrinkled membranes ii: analytical models. *Journal of Mechanics of Materials and Structures*, 1(1):27–61, 2006.

[15] L. Pocivavsek, R. Dellsy, A. Kern, S. Johnson, B. Lin, K. Y. C. Lee, and E. Cerda. Stress and fold localization in thin elastic membranes. *Science*, 320(5878):912–916, 2008.

[16] E. Jambon-Puillet, D. Vella, and S. Protière. The compression of a heavy floating elastic film. *Soft Matter*, 12(46):9289–9296, 2016.

[17] T. J. W. Wagner and D. Vella. Floating carpets and the delamination of elastic sheets. *Physical Review Letters*, 107(4):044301, 2011.

[18] F. Brau, P. Damman, H. Diamant, and T. A. Witten. Wrinkle to fold transition: influence of the substrate response. *Soft Matter*, 9(34):8177–8186, 2013.

[19] B. Audoly. Localized buckling of a floating elastica. *Physical Review E—Statistical, Nonlinear, and Soft Matter Physics*, 84(1):011605, 2011.

[20] M. Rivetti. Non-symmetric localized fold of a floating sheet. *Comptes Rendus Mécanique*, 341(3):333–338, 2013.

[21] M. Rivetti and S. Neukirch. The mode branching route to localization of the finite-length floating elastica. *Journal of the Mechanics and Physics of Solids*, 69:143–155, 2014.

[22] D. P. Holmes and A. J. Crosby. Draping films: A wrinkle to fold transition. *Physical Review Letters*, 105(3):038303, 2010.

[23] D. Vella, J. Huang, N. Menon, T. P. Russell, and B. Davidovitch. Indentation of ultrathin elastic films and the emergence of asymptotic isometry. *Physical Review Letters*, 114 (1):014301, 2015.

[24] F. Box, D. Vella, R. W. Style, and J. A. Neufeld. Indentation of a floating elastic sheet: geometry versus applied tension. *Proceedings of the Royal Society A: Mathematical, Physical and Engineering Sciences*, 473(2206):20170335, 2017.

[25] D. Vella and B. Davidovitch. Regimes of wrinkling in an indented floating elastic sheet. *Physical Review E*, 98(1):013003, 2018.

[26] J. D. Paulsen, E. Hohlfeld, H. King, J. Huang, Z. Qiu, T. P. Russell, N. Menon, D. Vella, and B. Davidovitch. Curvature-induced stiffness and the spatial variation of wavelength in wrinkled sheets. *Proceedings of the National Academy of Sciences*, 113 (5):1144–1149, 2016.

[27] J. D. Paulsen, V. Démery, K. B. Toga, Z. Qiu, T. P. Russell, B. Davidovitch, and N. Menon. Geometry-driven folding of a floating annular sheet. *Physical Review Letters*, 118(4):048004, 2017.

[28] R. D. Schroll, M. Adda-Bedia, E. Cerda, J. Huang, N. Menon, T. P. Russell, K. B. Toga, D. Vella, and B. Davidovitch. Capillary deformations of bendable films. *Physical Review Letters*, 111(1):014301, 2013.

[29] J. Huang, M. Juszkiewicz, W. H. De Jeu, E. Cerda, T. Emrick, N. Menon, and T. P. Russell. Capillary wrinkling of floating thin polymer films. *Science*, 317(5838): 650–653, 2007.

[30] D. Vella, A. Ajdari, A. Vaziri, and A. Boudaoud. Wrinkling of pressurized elastic shells. *Physical Review Letters*, 107(17):174301, 2011.

[31] M. Taffetani and D. Vella. Regimes of wrinkling in pressurized elastic shells. *Philosophical Transactions of the Royal Society A: Mathematical, Physical and Engineering Sciences*, 375(2093):20160330, 2017.

[32] E. Siéfert, J. Bico, E. Reyssat, and B. Roman. Geometry and mechanics of inextensible curvilinear balloons. *Journal of the Mechanics and Physics of Solids*, 143:104068, 2020.

[33] E. Siéfert, E. Reyssat, J. Bico, and B. Roman. Bio-inspired pneumatic shape-morphing elastomers. *Nature Materials*, 18(1):24–28, 2019.

[34] E. Siéfert, E. Reyssat, J. Bico, and B. Roman. Programming curvilinear paths of flat inflatables. *Proceedings of the National Academy of Sciences*, 116(34):16692–16696, 2019.

[35] J. C. Thomas and C. Wielgosz. Deflections of highly inflated fabric tubes. *Thin-Walled Structures*, 42(7):1049–1066, 2004.

[36] C. Wielgosz and J. C. Thomas. Deflections of inflatable fabric panels at high pressure. *Thin-Walled Structures*, 40(6):523–536, 2002.

[37] C. Wielgosz and J. C. Thomas. An inflatable fabric beam finite element. *Communications in Numerical Methods in Engineering*, 19(4):307–312, 2003.

[38] J. Guo, X. Qiu, Z. Zhang, L. Zhang, and C. Wang. Inflated pillow with flexible bistable kink: snap design and application. *AIAA Journal*, 60(11):6500–6505, 2022.

[39] Q. Wang and X. Zhao. A three-dimensional phase diagram of growth-induced surface instabilities. *Scientific Reports*, 5(1):8887, 2015.

[40] N. Stoop, R. Lagrange, D. Terwagne, P. M. Reis, and J. Dunkel. Curvature-induced symmetry breaking determines elastic surface patterns. *Nature Materials*, 14(3): 337–342, 2015.

[41] F. Xu, S. Zhao, C. Lu, and M. Potier-Ferry. Pattern selection in core-shell spheres. *Journal of the Mechanics and Physics of Solids*, 137:103892, 2020.

[42] F. Xu, C. Fu, and Y. Yang. Water affects morphogenesis of growing aquatic plant leaves. *Physical Review Letters*, 124(3):038003, 2020.

[43] L. Zheng. *Wrinkling of dielectric elastomer membranes*. California Institute of Technology, 2009.

[44] V. Nayyar, K. Ravi-Chandar, and R. Huang. Stretch-induced stress patterns and wrinkles in hyperelastic thin sheets. *International Journal of Solids and Structures*, 48(25-26): 3471–3483, 2011.

[45] T. J. Healey, Q. Li, and R. B. Cheng. Wrinkling behavior of highly stretched rectangular elastic films via parametric global bifurcation. *Journal of Nonlinear Science*, 23: 777–805, 2013.

[46] Q. Li and T. J. Healey. Stability boundaries for wrinkling in highly stretched elastic sheets. *Journal of the Mechanics and Physics of Solids*, 97:260–274, 2016.

[47] C. Fu, T. Wang, F. Xu, Y. Huo, and M. Potier-Ferry. A modeling and resolution framework for wrinkling in hyperelastic sheets at finite membrane strain. *Journal of the Mechanics and Physics of Solids*, 124:446–470, 2019.

[48] A. A. Sipos and E. Fehér. Disappearance of stretch-induced wrinkles of thin sheets: a study of orthotropic films. *International Journal of Solids and Structures*, 97-98: 275–283, 2016.

[49] F. Liu, F. Xu, and C. Fu. Orientable wrinkles in stretched orthotropic films. *Extreme Mechanics Letters*, 33:100579, 2019.

[50] Y. Yang, C. Fu, and F. Xu. A finite strain model predicts oblique wrinkles in stretched anisotropic films. *International Journal of Engineering Science*, 155:103354, 2020.

[51] H. M. Verhelst, M. Möller, J. H. Den Besten, A. Mantzaflaris, and M. L. Kaminski. Stretch-based hyperelastic material formulations for isogeometric kirchhoff–love shells with application to wrinkling. *Computer-Aided Design*, 139:103075, 2021.

[52] D. J. Steigmann. A well-posed finite-strain model for thin elastic sheets with bending stiffness. *Mathematics and Mechanics of Solids*, 18(1):103–112, 2013.

[53] M. Taylor, K. Bertoldi, and D. J. Steigmann. Spatial resolution of wrinkle patterns in thin elastic sheets at finite strain. *Journal of the Mechanics and Physics of Solids*, 62: 163–180, 2014.

[54] M. Taylor, B. Davidovitch, Z. Qiu, and K. Bertoldi. A comparative analysis of numerical approaches to the mechanics of elastic sheets. *Journal of the Mechanics and Physics of Solids*, 79:92–107, 2015.

[55] M. Taylor, M. Shirani, Y. Dabiri, J. M. Guccione, and D. J. Steigmann. Finite elastic wrinkling deformations of incompressible fiber-reinforced plates. *International Journal of Engineering Science*, 144:103138, 2019.

[56] M. Taylor and M. Shirani. Simulation of wrinkling in incompressible anisotropic thin sheets with wavy fibers. *International Journal of Non-Linear Mechanics*, 127:103610, 2020.

[57] C. Fu, H. H. Dai, and F. Xu. Computing wrinkling and restabilization of stretched sheets based on a consistent finite-strain plate theory. *Computer Methods in Applied Mechanics and Engineering*, 384:113986, 2021.

[58] C. Fu, Y. Yang, T. Wang, and F. Xu. A consistent finite-strain plate model for wrinkling of stretched anisotropic hyperelastic films. *Thin-Walled Structures*, 179:109643, 2022.

[59] T. Wang, Y. Yang, C. Fu, F. Liu, K. Wang, and F. Xu. Wrinkling and smoothing of a soft shell. *Journal of the Mechanics and Physics of Solids*, 134:103738, 2020.

[60] T. Wang, F. Liu, C. Fu, X. Zhang, K. Wang, and F. Xu. Curvature tunes wrinkling in shells. *International Journal of Engineering Science*, 164:103490, 2021.

[61] T. Wang, Y. Yang, C. Fu, and F. Xu. Competition between mullins and curvature effects in the wrinkling of stretched soft shells. *International Journal of Solids and Structures*, 241:111473, 2022.

[62] T. Wang, Z. Dai, M. Potier-Ferry, and F. Xu. Curvature-regulated multiphase patterns in tori. *Physical Review Letters*, 130(4):048201, 2023.

[63] W. Huang, Q. Huang, Y. Liu, J. Yang, H. Hu, F. Trochu, and P. Causse. A fourier based reduced model for wrinkling analysis of circular membranes. *Computer Methods in Applied Mechanics and Engineering*, 345:1114–1137, 2019.

[64] H. M. Verhelst, M. Möller, and J. H. Den Besten. A wrinkling model for general hyperelastic materials based on tension field theory. *Computer Methods in Applied Mechanics and Engineering*, 441:117955, 2025.

[65] A. Jarasjarungkiat, R Wüchner, and K. U. Bletzinger. A wrinkling model based on material modification for isotropic and orthotropic membranes. *Computer Methods in Applied Mechanics and Engineering*, 197(6-8):773–788, 2008.

[66] T. Iwasa, M. C. Natori, and K. Higuchi. Evaluation of tension field theory for wrinkling analysis with respect to the post-buckling study. *Journal of Applied Mechanics*, 71(4): 532–540, 2004.

[67] A. Diaby, C. Wielgosz, and A. Le-van. Buckling and wrinkling of prestressed membranes. *Finite elements in Analysis and Design*, 42(11):992–1001, 2006.

[68] W. Wong and S. Pellegrino. Wrinkled membranes iii: numerical simulations. *Journal of Mechanics of Materials and Structures*, 1(1):63–95, 2006.

[69] F. Xu, M. Potier-Ferry, S. Belouettar, and H. Hu. Multiple bifurcations in wrinkling analysis of thin films on compliant substrates. *International Journal of Non-Linear Mechanics*, 76:203–222, 2015.

[70] K. Nakashino, A. Nordmark, and A. Eriksson. Geometrically nonlinear isogeometric analysis of a partly wrinkled membrane structure. *Computers & Structures*, 239:106302, 2020.

[71] H. Wagner. Ebene blechwandtrager mit sehr dunnem stegblech (metal beams with very thin webs). *Zeitschrift für Flugtechnik und Motorloftschiffahr*, 20(8), 1929.

[72] E. Reissner. On tension field theory. *Proceedings of the Fifth International Congress for Applied Mechanics, Harvard University and Massachusetts Institute of Technology*, pages 88–92, 1938.

[73] M. Stein and J. M. Hedgepeth. *Analysis of partly wrinkled membranes*. National Aeronautics and Space Administration, 1961.

[74] M. M. Mikulas. *Behavior of a flat stretched membrane wrinkled by the rotation of an attached hub*. National Aeronautics and Space Administration, 1964.

[75] D. A. Danielson and S. Natarajan. Tension field theory and the stress in stretched skin. *Journal of Biomechanics*, 8(2):135–142, 1975.

[76] A. C. Pipkin. The relaxed energy density for isotropic elastic membranes. *IMA Journal of Applied Mathematics*, 36(1):85–99, 1986.

[77] D. J. Steigmann. Tension-field theory. *Proceedings of the Royal Society of London. A. Mathematical and Physical Sciences*, 429(1876):141–173, 1990.

[78] A. C. Pipkin. Convexity conditions for strain-dependent energy functions for membranes. *Archive for Rational Mechanics and Analysis*, 121:361–376, 1993.

[79] A. C. Pipkin. Relaxed energy densities for large deformations of membranes. *IMA Journal of Applied Mathematics*, 52(3):297–308, 1994.

[80] M. Epstein. On the wrinkling of anisotropic elastic membranes. *Journal of Elasticity*, 55:99–109, 1999.

[81] Y. Miyazaki. Wrinkle/slack model and finite element dynamics of membrane. *International Journal for Numerical Methods in Engineering*, 66(7):1179–1209, 2006.

[82] C. Liu, Q. Tian, D. Yan, and H. Hu. Dynamic analysis of membrane systems undergoing overall motions, large deformations and wrinkles via thin shell elements of ancf. *Computer Methods in Applied Mechanics and Engineering*, 258:81–95, 2013.

[83] S. Kang and S. Im. Finite element analysis of dynamic response of wrinkling membranes. *Computer Methods in Applied Mechanics and Engineering*, 173(1-2):227–240, 1999.

[84] Z. Chen, H. Y. Chen, D. M. Kaufman, M. Skouras, and E. Vouga. Fine wrinkling on coarsely meshed thin shells. *ACM Transactions on Graphics (TOG)*, 40(5):1–32, 2021.

[85] J. Montes, B. Thomaszewski, S. Mudur, and T. Popa. Computational design of skintight clothing. *ACM Transactions on Graphics (TOG)*, 39(4):105–1, 2020.

[86] H. Le Meitour, G. Rio, H. Laurent, A. S. Lectez, and P. Guigue. Analysis of wrinkled membrane structures using a plane stress projection procedure and the dynamic relaxation method. *International Journal of Solids and Structures*, 208:194–213, 2021.

[87] A. Niewiarowski, S. Adriaenssens, and R. M. Pauletti. A conic programming approach to the wrinkling of pneumatic membranes using convex potentials. *Computers & Structures*, 292:107231, 2024.

[88] P. Contri and B. A. Schrefler. A geometrically nonlinear finite element analysis of wrinkled membrane surfaces by a no-compression material model. *Communications in Applied Numerical Methods*, 4(1):5–15, 1988.

[89] T. Nishima, N. Tosaka, and T. Honma. Membrane structure analysis using the finite element technique, shells, membranes and space frames. In *Proceedings IASS Symposium*, volume 2, 1986.

[90] B. Tabarrok and Z. Qin. Nonlinear analysis of tension structures. *Computers & Structures*, 45(5-6):973–984, 1992.

[91] R. K. Miller, J. M. Hedgepeth, V. I. Weingarten, P. Das, and S. Kahyai. Finite element analysis of partly wrinkled membranes. *Computers & Structures*, 20(1):631–639, 1985.

[92] R. K. Miller and J. M. Hedgepeth. An algorithm for finite element analysis of partly wrinkled membranes. *AIAA Journal*, 20(12):1761–1763, 1982.

[93] X. Liu, C. H. Jenkins, and W. W. Schur. Large deflection analysis of pneumatic envelopes using a penalty parameter modified material model. *Finite Elements in Analysis and Design*, 37(3):233–251, 2001.

[94] R. Rossi, M. Lazzari, R. Vitaliani, and E. Oñate. Simulation of light-weight membrane structures by wrinkling model. *International Journal for Numerical Methods in Engineering*, 62(15):2127–2153, 2005.

[95] X. W. Feng, Q. S. Yang, and S. S. Law. Wrinkled membrane element based on the wrinkling potential. *International Journal of Solids and Structures*, 51(21-22): 3532–3548, 2014.

[96] K. Nakashino and M. C. Natori. Efficient modification scheme of stress-strain tensor for wrinkled membranes. *AIAA Journal*, 43(1):206–215, 2005.

[97] C. H. Wu. Nonlinear wrinkling of nonlinear membranes of retolution. *Journal of Applied Mechanics, Transactions ASME*, 45(3):533–538, 1978.

[98] C. H. Wu and T. R. Canfield. Wrinkling in finite plane-stress theory. *Quarterly of Applied Mathematics*, 39(2):179–199, 1981.

[99] D. G. Roddeman, J. Drukker, C. W. J. Oomens, and J. D. Janssen. The wrinkling of thin membranes: part i—theory. *Journal of Applied Mechanics*, 54(4):884–887, 12 1987.

[100] D. G. Roddeman, J. Drukker, C. W. J. Oomens, and J. D. Janssen. The wrinkling of thin membranes: Part ii—numerical analysis. *Journal of Applied Mechanics*, 54(4): 888–892, 12 1987.

[101] D. G. Roddeman. Finite-element analysis of wrinkling membranes. *Communications in Applied Numerical Methods*, 7(4):299–307, 1991.

[102] F. Muttin. A finite element for wrinkled curved elastic membranes, and its application to sails. *Communications in Numerical Methods in Engineering*, 12(11):775–785, 1996.

[103] D. G. Jeong and B. M. Kwak. Complementarity problem formulation for the wrinkled membrane and numerical implementation. *Finite Elements in Analysis and Design*, 12 (2):91–104, 1992.

[104] K. Lu, M. Accorsi, and J. Leonard. Finite element analysis of membrane wrinkling. *International Journal for Numerical Methods in Engineering*, 50(5):1017–1038, 2001.

[105] S. Kang and S. Im. Finite element analysis of wrinkling membranes. *Journal of Applied Mechanics*, 64(2):263–269, 06 1997.

[106] K. Woo, H. Igawa, and C. H. Jenkins. Analysis of wrinkling behavior of anisotropic membrane. *Computer Modeling in Engineering and Sciences*, 6:397–408, 2004.

[107] T. Akita, K. Nakashino, M. C. Natori, and K. C. Park. A simple computer implementation of membrane wrinkle behaviour via a projection technique. *International Journal for Numerical Methods in Engineering*, 71(10):1231–1259, 2007.

[108] A. Jarasjarungkiat, R Wüchner, and K. U. Bletzinger. Efficient sub-grid scale modeling of membrane wrinkling by a projection method. *Computer Methods in Applied Mechanics and Engineering*, 198(9-12):1097–1116, 2009.

[109] H. Le Meitour, G. Rio, H. Laurent, A. S. Lectez, and P. Guigue. Analysis of wrinkled membrane structures using a plane stress projection procedure and the dynamic relaxation method. *International Journal of Solids and Structures*, 208:194–213, 2021.

[110] J. Mosler. A novel variational algorithmic formulation for wrinkling at finite strains based on energy minimization: application to mesh adaption. *Computer Methods in Applied Mechanics and Engineering*, 197(9-12):1131–1146, 2008.

[111] J. Mosler and F. Cirak. A variational formulation for finite deformation wrinkling analysis of inelastic membranes. *Computer Methods in Applied Mechanics and Engineering*, 198(27-29):2087–2098, 2009.

[112] R. de Rooij and M. M. Abdalla. A finite element interior-point implementation of tension field theory. *Computers & Structures*, 151:30–41, 2015.

[113] Y. Kanno. *Nonsmooth mechanics and convex optimization*. 2011. ISBN 9781420094244.

[114] D. Zhang and J. Kiendl. A variationally consistent membrane wrinkling model based on spectral decomposition of the strain tensor. *Computer Methods in Applied Mechanics and Engineering*, 432:117386, 2024.

[115] D. Zhang and J. Kiendl. A variationally consistent membrane wrinkling model based on spectral decomposition of the strain and stress tensors. *Journal of the Mechanics and Physics of Solids*, 205:106331, 2025.

[116] J. Kiendl. *Isogeometric analysis and shape optimal design of shell structures*. PhD thesis, Technische Universität München, 2011.

[117] G. A. Holzapfel. *Nonlinear solid mechanics: a continuum approach for engineering science*. Kluwer Academic Publishers Dordrecht, 2002.

[118] Y. Basar and D. Weichert. *Nonlinear continuum mechanics of solids: fundamental mathematical and physical concepts*. Springer Science & Business Media, 2013.

[119] J. Kiendl, K. U. Bletzinger, J. Linhard, and Roland Wüchner. Isogeometric shell analysis with kirchhoff–love elements. *Computer Methods in Applied Mechanics and Engineering*, 198(49-52):3902–3914, 2009.

[120] M. Bischoff, K. U. Bletzinger, W. A. Wall, and E. Ramm. Models and finite elements for thin-walled structures. *Encyclopedia of Computational Mechanics*, 2004.

[121] J. Kiendl, M. Ambati, L. De Lorenzis, H. Gomez, and A. Reali. Phase-field description of brittle fracture in plates and shells. *Computer Methods in Applied Mechanics and Engineering*, 312:374–394, 2016.

[122] J. Kiendl, M. C. Hsu, M. C. H. Wu, and A. Reali. Isogeometric kirchhoff–love shell formulations for general hyperelastic materials. *Computer Methods in Applied Mechanics and Engineering*, 291:280–303, 2015.

[123] H. M. Verhelst, M. Möller, J. H. Den Besten, A. Mantzaflaris, and M. L. Kaminski. Stretch-based hyperelastic material formulations for isogeometric kirchhoff–love shells with application to wrinkling. *Computer-Aided Design*, 139:103075, 2021.

[124] Y. Bazilevs, M. C. Hsu, D. J. Benson, S. Sankaran, and A. L. Marsden. Computational fluid–structure interaction: methods and application to a total cavopulmonary connection. *Computational Mechanics*, 45(1):77–89, 2009.

[125] S. Klinkel and S. Govindjee. Using finite strain 3d-material models in beam and shell elements. *Engineering Computations*, 19(3):254–271, 2002.

[126] J. A. Cottrell, T. J. R. Hughes, and Y. Bazilevs. *Isogeometric analysis: toward integration of CAD and FEA*. John Wiley & Sons, 2009.

[127] B. Oesterle, F. Geiger, D. Forster, M. Fröhlich, and M. Bischoff. A study on the approximation power of nurbs and the significance of exact geometry in isogeometric pre-buckling analyses of shells. *Computer methods in applied mechanics and engineering*, 397:115144, 2022.

[128] J. A. Cottrell, A. Reali, Y. Bazilevs, and T. J. R. Hughes. Isogeometric analysis of structural vibrations. *Computer methods in applied mechanics and engineering*, 195 (41-43):5257–5296, 2006.

[129] T. J. R. Hughes, J. A. Evans, and A. Reali. Finite element and nurbs approximations of eigenvalue, boundary-value, and initial-value problems. *Computer Methods in Applied Mechanics and Engineering*, 272:290–320, 2014.

[130] T. J. R. Hughes, J. A. Cottrell, and Y. Bazilevs. Isogeometric analysis: Cad, finite elements, nurbs, exact geometry and mesh refinement. *Computer Methods in Applied Mechanics and Engineering*, 194(39-41):4135–4195, 2005.

[131] N. Vasios. Nonlinear analysis of structures. *The Arc-Length method. Harvard*, 2015.

[132] M. Crisfield. An arc-length method including line searches and accelerations. *International Journal for Numerical Methods in Engineering*, 19(9):1269–1289, 1983.

[133] C. Miehe, M. Hofacker, and F. Welschinger. A phase field model for rate-independent crack propagation: Robust algorithmic implementation based on operator splits. *Computer Methods in Applied Mechanics and Engineering*, 199(45-48):2765–2778, 2010.

[134] C. Miehe and M. Lambrecht. Algorithms for computation of stresses and elasticity moduli in terms of seth–hill's family of generalized strain tensors. *Communications in Numerical Methods in Engineering*, 17(5):337–353, 2001.

[135] S. Zhang, W. Jiang, and M. R. Tonks. A new phase field fracture model for brittle materials that accounts for elastic anisotropy. *Computer Methods in Applied Mechanics and Engineering*, 358:112643, 2020.

[136] R. Kruse, N. Nguyen-Thanh, L. De Lorenzis, and T. J. R. Hughes. Isogeometric collocation for large deformation elasticity and frictional contact problems. *Computer Methods in Applied Mechanics and Engineering*, 296:73–112, 2015.

[137] X. W. Feng, J. Ma, S. S. Law, and Q. Yang. Numerical analysis of wrinkle-influencing factors of thin membranes. *International Journal of Solids and Structures*, 97:458–474, 2016.

[138] H. Ding, B. Yang, M. Lou, and H. Fang. New numerical method for two-dimensional partially wrinkled membranes. *AIAA Journal*, 41(1):125–132, 2003.

[139] D. G. Jeong and B. M. Kwak. Complementarity problem formulation for the wrinkled membrane and numerical implementation. *Finite Elements in Analysis and Design*, 12 (2):91–104, 1992.

[140] N. P. van Dijk, J. J. Espadas-Escalante, and P. Isaksson. Strain energy density decompositions in phase-field fracture theories for orthotropy and anisotropy. *International Journal of Solids and Structures*, 196:140–153, 2020.

[141] W. Wong and S. Pellegrino. Wrinkled membranes i: experiments. *Journal of Mechanics of Materials and Structures*, 1(1):3–25, 2006.

[142] N. Bauer. *Zur Darstellung von Falten in Membranen mit Hilfe der Methode der finiten Elemente*. SFB 64, Stuttgart, 1975.

[143] S. Kang and S. Im. Finite element analysis of dynamic response of wrinkling membranes. *Computer Methods in Applied Mechanics and Engineering*, 173(1-2):227–240, 1999.

[144] E. S. Lee and S. K. Youn. Finite element analysis of wrinkling membrane structures with large deformations. *Finite Elements in Analysis and Design*, 42(8-9):780–791, 2006.

[145] A. J. Gil and J. Bonet. Finite element analysis of partly wrinkled reinforced prestressed membranes. *Computational Mechanics*, 40:595–615, 2007.

[146] L. Zhang, K. Dong, M. Lu, and H. Zhang. A wrinkling model for pneumatic membranes and the complementarity computational framework. *Computational Mechanics*, 65: 119–134, 2020.

[147] A. J. Herrema, E. L. Johnson, D. Proserpio, M. C. H. Wu, J. Kiendl, and M. C. Hsu. Penalty coupling of non-matching isogeometric kirchhoff–love shell patches with application to composite wind turbine blades. *Computer Methods in Applied Mechanics and Engineering*, 346:810–840, 2019.

[148] T. Wang, C. Fu, F. Xu, Y. Huo, and M. Potier-Ferry. On the wrinkling and restabilization of highly stretched sheets. *International Journal of Engineering Science*, 136:1–16, 2019.

[149] A. Panaitescu, M. Xin, B. Davidovitch, J. Chopin, and A. Kudrolli. Birth and decay of tensional wrinkles in hyperelastic sheets. *Physical Review E*, 100(5):053003, 2019.

[150] H. M. Verhelst, A. Mantzaflaris, M. Möller, and J. H. Den Besten. Goal-adaptive meshing of isogeometric kirchhoff–love shells. *Engineering with Computers*, 40: 3595–3622, 2024.